NUCLEAR STRUCTURE OF ^{190,192,194}Ir

By

Paul Edward Garrett

A Thesis

Submitted to the School of Graduate Studies

in Partial Fulfillment of the Requirements

for the Degree

Doctor of Philosophy

McMaster University

NUCLEAR STRUCTURE OF ^{190,192,194}Ir

Doctor of Philosophy (1993) McMaster University
(Physics) Hamilton, Ontario

TITLE: Nuclear Structure of ^{190,192,194}Ir

AUTHOR: Paul Edward Garrett, B.Sc. (Queen's University)
M.Sc. (McMaster University)

SUPERVISOR: Professor D.G. Burke

NUMBER OF PAGES: xiii, 264

ABSTRACT

The nuclear structures of ^{190,192,194}Ir were investigated with single-nucleon transfer reactions. The (d,t) reactions into ^{190,192}Ir used 18 MeV deuterons beams, and the (d,p) reactions into ^{192,194}Ir utilized beams of 16 MeV deuterons. Single-proton transfer experiments were also performed on targets of ^{189}Os. The (α,t) reaction employed beams of 30 MeV α-particles, and the (^{3}He,d) reactions used a 28 MeV ^{3}He beam. The reaction products were analyzed with a magnetic spectrograph, and detected with photographic plates. The energy resolutions (FWHM) of the detected particles were typically $\simeq$ 5.7 keV for (d,t), $\simeq$ 8.9 keV for (d,p), $\simeq$ 10 keV for (α,t), and $\simeq$ 15 keV for (^{3}He,d) reactions. For the single-neutron transfer reactions, spectra were recorded at a large number of angles ($\geq$ 15). The angular distributions of cross sections were fitted with theoretical distributions from DWBA calculations, and the spectroscopic factors were obtained. For the (d,t) reactions, the fits to the angular distributions were performed in many cases with 2 l-values. By comparing the ratios of (α,t) and (^{3}He,d) cross sections, the dominant transferred l-value was determined. Level energies, parities, spectroscopic strengths, and possible spin values were determined up to approximately 1 MeV excitation energy in ^{190,192}Ir and 700 keV in ^{194}Ir. In order to obtain more information regarding the spins of levels in ^{192}Ir, multi-dimensional scaling programs were applied to known γ-ray intensities. The method appeared to be successful, and spins were suggested for many low-lying levels. The experimental results were compared with the IBFFM for ^{192,194}Ir, ESUSY for ^{192}Ir, and the Nilsson model for ^{190,192}Ir. The formalism for dealing with mixed configurations in the target ground state was developed, and significant effects were found for the single-proton transfer cross sections since the ^{189}Os target had significant admixed amplitudes. It was found that the models can only approximate the structure of odd-odd Ir nuclei.

ACKNOWLEDGEMENTS

Now that this project is finished and my term at McMaster is coming to a close, it is time to reflect back on my stay here and acknowledge those people with whom I have interacted.

Firstly, I must thank my wife, Debbie, for all that she has done. She gave me the encouragement to start this work, and always had confidence that I could complete the thesis, and even be a successful researcher. She has also been of great assistance in the writing of this thesis, since she drew *all* of the angular distributions! Now that the thesis is finished, she will no longer have to compete with a paper for my time.

Daniel Prévost, our former system manager, is one of the most unselfish people whom I have ever met. He always had time to correct bugs in our TEXfiles, improve the operating conditions of the Vax, and just be of general assistance, even at the cost of delaying his own work. There are certain images of him that will remain with me forever, such as his constant cursing at the terminal, and his passion for killing Nazi's in Wolf3D!

I would like to thank the members of my supervisory committee: Prof. D. Burke for suggesting this project, and for providing the opportunities for travel. His contacts have opened up many new possibilities for me; Prof. J. Waddington and Prof. S. Poehlman for sitting through my boring committee meeting when I am sure that they would sooner be doing other things. I especially want to thank Jim for essentially treating me like part of the group.

Some of the most precious memories that I carry away from here are those involving the friends that I have made over the past 4 years. In the beginning, there were Jeffry Johannson, Tao Qu, and Burton Valpy. Tao especially was very helpful since he participated in many of the experiments that were reported in the thesis (and he seemed to have a preference for night shifts). Jose Rodriguez was also here from the start, and was always trying to engage everyone else in some sort

of philosophical discussion on every topic under the sun, from politics ("So Daniel, what about Quebec?") to mathematics. Many good friends arrived after I had started, Daniel Prévost, Ahmed Omar, Leif Persson, and Greg Hackman. Then, of course, there are Dr. Simon Mullins and Scott McMaster. I especially want to thank them for their generous hospitality when I needed a place to stay. Simon contributed in many ways to the environment here, providing comic relief with his great mimicking ability, and reminded us that there are a number of real losers in this world who desperately need to be made fun of. Scott has proven to be a good friend over the years, and we both benefitted from being able to bounce ideas off one another, and well as being a good outlet when we wanted to complain about some aspect of our programs we hated.

I also want to express my appreciation to other people who in one way or another helped me or contributed to my mental well being. Helen Yardley had the tedious job of counting all the photographic plates used in the experiments. Needless to say, I don't think I would have had the patience to do this. Cheryl Johnston was always there to lend a helping hand to fill out forms, etc., and was always ready to spend a few minutes discussing the real serious issues of the day. Jim Stark, with his expertise with the accelerator, provided the beautiful stable beams that we needed, and also was a skilled target maker. Carol McMaster had the awful job of proofreading the draft version of this thesis, and made many suggestions which improved the content and presentation of the work appreciably. Pete Hofstra provided a convenient benchmark for me, as he may have been the only person in the lab who was in a worse situation than I was. I generally had too much data, whereas Pete, for a long time, simply could not get any (due to no fault of his own). In closing, I also want to express my appreciation to my parents, who, above all else, were always concerned with my well being.

I have probably missed serval people who also deserve mentioning, and I hope that they will not be offended.

Finally, I want to warn all those who may read this thesis. Transferasaurus Rex, a creature long thought to be extinct, has recently been sighted rearing its ugly head. To all those who may cross its path, BEWARE!

Table of Contents

List of Figures

List of Tables

Chapter 1.
Introduction

The study of nuclear physics has been an ongoing process for many decades, and the basic nature of nuclear structure has been ascertained. However, there are regions of the periodic chart that have not been fully explored, and may exhibit new features. In the past, the $A \simeq 190$ mass region was not studied in detail, but recently has been receiving attention. The present work is a study of three odd-odd nuclei, ^{190,192,194}Ir, utilizing single-nucleon transfer reactions.

Nuclei that have the numbers of protons and neutrons at or near the magic numbers, 2, 8, 20, 28, 50, 82, and 126, are described by spherical shapes. As the number of nucleons changes from these magic numbers, static deformations of the nuclear shape can set in, and this has very important consequences on the structure. At midshell, the deformations in the ground state can have quite large values, and these decrease as the magic numbers (or shell closures) are approached. As well, nuclei away from the closed shells usually have rigid shapes, which are characterized by deep minima in the potential energy surfaces. The most common shape in deformed nuclei is the prolate (football) shape. However, there may also be oblate (hamburger) shapes. For pure prolate and oblate shapes, the nuclei are axially symmetric, with the lengths along two axes the same, and the third having a different length. For prolate shapes, the length along the third axis is longer than the other two, whereas for oblate shapes, the length along the third axis is shorter. These shapes can be described approximately by the introduction of β and γ, which are quadrupole distortion parameters, where β represents the extent of quadrupole deformation, and γ represents the degree of axial asymmetry. As the number of nucleons changes towards closed-shell values, there is a transition region between the rigid, well-deformed shape, and the spherical shape. Nuclei in the transitional regions usually do not have well-defined shapes. When the shape is such that all the lengths along the axes are different, the axial symmetry is lost and the nuclei are

described as having triaxiality. In the transitions regions it is often found that nuclei are γ-soft, which means that the shape is not rigid and can be easily changed from prolate to oblate, triaxial, etc., and vice versa. These nuclei are characterized by potential energy surfaces that have shallow minima in the potential energy surface, and there may be several minima per nucleus.

As a consequence of quantum mechanics, rotations cannot occur about a symmetry axis. Therefore, an axially symmetric nucleus may rotate only about an axis perpendicular to the symmetry axis. For a single-particle orbiting a core there is no such restriction, and the projection of the single-particle angular momentum onto the symmetry axis, Ω, is, in many cases, a good quantum number. If the core retains its axial symmetry, the projection of the total angular momentum onto the symmetry axis, K, is also a good quantum number and $K = \Omega$.

Not only can the nucleus rotate, but it may also undergo shape vibrations. Quadrupole vibrations, classified as β- and γ-vibrations which are shown in Figure 1.1, are commonly observed in deformed nuclei. Rotations can be built on the vibrations, resulting in a β-band or a γ-band. The energies at which these bands occur depends to a great extent on the shape of the potential energy surface. For instance, if the potential energy surface has a deep, well-defined minimum, the vibrations are relatively high in energy. For a shallow minimum, the vibrations are relatively low in energy. The vibrations can also interact with the single-particle degrees of freedom such that there may be a mixing of the single-particle and collective (involving many nucleons) behaviour. Therefore, by studying both the collective motion and the single-particle motion, knowledge of the potential energy surface can be obtained, and this can be compared with the theoretical predictions. The predictions are often in the form of contour maps in the β-γ plane. There are many other ways of expressing the deformation parameters, such as a_0 and a_2, where $a_0 = \beta \cos\gamma$ and $a_2 = (\beta \sin\gamma)/\sqrt{2}$.

Nuclei with atomic numbers in the range $\sim 150 < A < 190$, are typically well-deformed, whereas those near the doubly magic ^{208}Pb are spherical in shape.

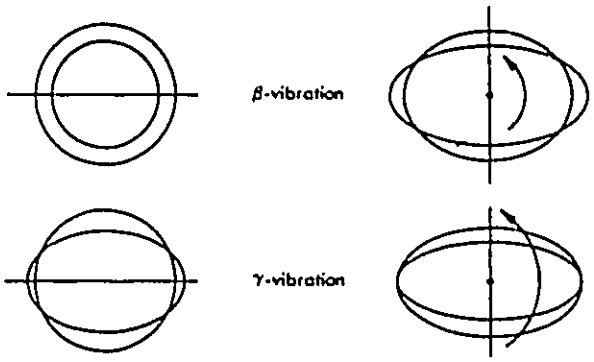

Figure 1.1: Schematic view of β- and γ-vibrations. The figures on the left are cross sections perpendicular to the symmetry axis, and the figures on the right are views parallel to the symmetry axis. The arrows indicate the direction of rotation in a possible rotational state. (From Preston and Bhaduri, 1975)

Thus, there is a transition region near $A \simeq 190$ where nuclei may exhibit a wide variety of shapes. Nuclei with mass numbers ~ 180 appear to be well described by a prolate shape, whereas those with atomic numbers $\sim$195 appear to be more oblate in shape. As well, there is evidence that the shapes are γ-soft, and there may be triaxiality. Recent studies[1–2] of the tungsten isotopes have provided evidence for both γ-softness and triaxiality, with the shape depending on mass and on the spin. Systematic surveys of the energies of the γ-bands in even-even nuclei show a trend towards lower energies as the atomic number increases from ~ 180 to ~ 194, indicating that the nuclei are becoming increasingly soft to vibrations in the γ-direction. In the odd iridium isotopes, $^{185-193}$Ir, there is a low-lying single-particle state that appears to have significant admixtures of a γ-vibration. Not only are the nuclei in $A \simeq$190 mass region soft in the γ-direction, but there has also been evidence for hexadecapole softness. Single-particle transfer studies[3], as well as the large $E4$ matrix elements found from (α, α') inelastic scattering measurements[4], indicated that 4^+ states at $\simeq$1 MeV in ^{188,190,192}Os were vibrational and two quasiparticle in nature, thus implying hexadecapole vibrations. Nuclei may also exhibit shape coexistence,

with some rotational bands built on prolate shapes, but also have bands built on oblate shapes. This has been demonstrated in ^{191}Os, where it was suggested that a decoupled positive parity band was built on an oblate shape[5]. Theoretical studies within the context of the General Collective Model (see Eisenberg and Greiner, 1987) predict that the nuclear shape is sensitive to the number of valence nucleons, and that nuclei in the $A \simeq 190$ region can be expected to exhibit many shapes. This is illustrated[6] in Figure 1.2 and Figure 1.3 for the even-even osmium and platinum isotopes, respectively, where the potential energy surfaces are plotted in the a_0 and a_2 plane. A minimum which occurs along the a_0 axis implies an axially symmetric prolate shape. Contours that are stretched out in an angular direction at a constant radius from the origin are showing γ-softness, and thus the shape is not well-defined. As can be seen, the figures demonstrate that the energy surface, and thus the underlying shape and structure, are sensitive to the number of nucleons and change rapidly from one nucleus to another.

The Interacting Boson Model[7](IBM), which has received much attention since its introduction, attempts to classify nuclei according to the dynamical symmetry they are supposed to possess. In the basic version of the model, valence particles are paired up to form s and d bosons. The Hamiltonian is studied from a group theoretic point of view, and three dynamical symmetries are found. The $U(5)$ limit, appropriate for vibrational nuclei, the $SU(3)$ limit, appropriate for axially symmetric deformed nuclei, and the $SO(6)$ limit, appropriate for γ-soft nuclei. The $SU(3)$ limit has been applied to the well-deformed rare-earth region, and the $SO(6)$ limit has been applied in the $A \simeq 196$ mass region. The best, and first, example[8] of an $SO(6)$ nucleuswas ^{196}Pt. However, even though ^{196}Pt was considered to obey $SO(6)$ symmetry, the $SO(6)$ limit cannot explain all of the features of this nucleus. For instance, in the $SO(6)$ limit, the quadrupole moment of the first 2^+ state is strictly zero, whereas experimentally it has been measured to have a relatively large value[9]. The problem with the quadrupole moment persists in the IBM-2, where the neutron and proton bosons are handled separately. Nuclei at

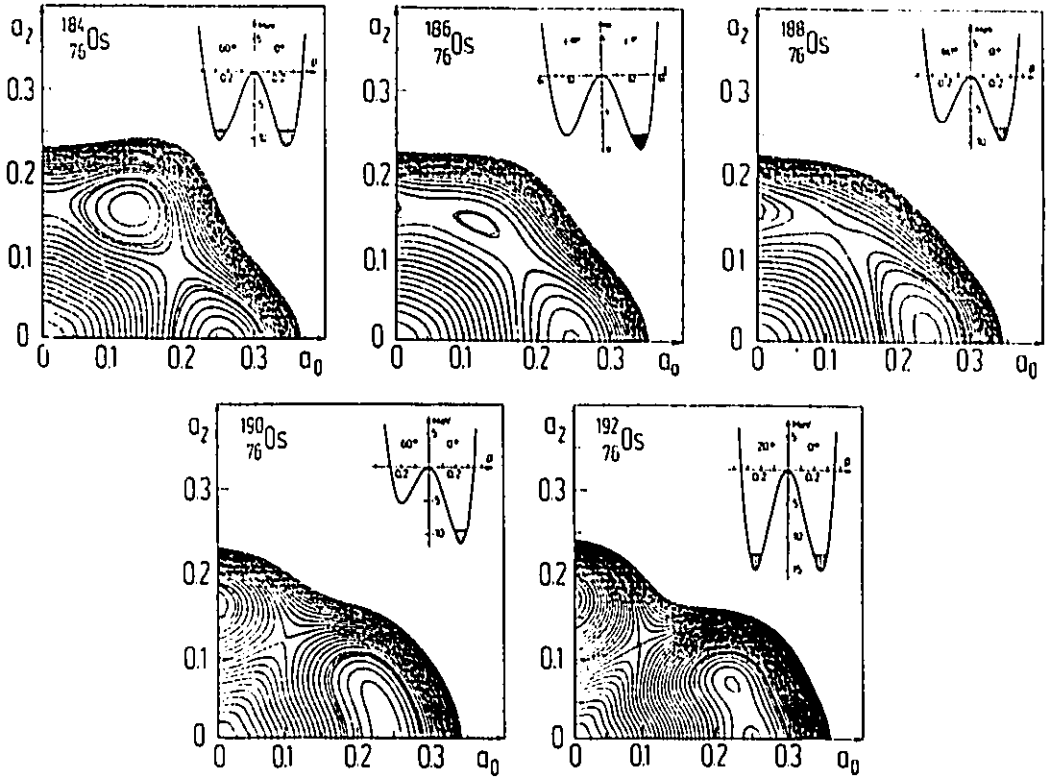

Figure 1.2: A series of potential energy surfaces in the a_0 and a_2 plain for even-even Os nuclei. The insets show the potential energy for specific values of γ. (From ref.[6])

atomic numbers $A \simeq 190$ are in a transitional region between the $SU(3)$ and $SO(6)$ symmetries, and this transition has been demonstrated in the osmium isotopes. It has recently been shown[10] that the 4^+ hexadecapole states in the Os isotopes at $\simeq$1 MeV can be described in the IBM by incorporating g bosons. Therefore, *sd* IBM is expected to only approximately describe the low-lying structures in even-even nuclei with $A \simeq 190$.

The $A \simeq 190$ transitional region has not been well studied. Some even-even nuclei, for example ^{190}Os, and odd-A nuclei, such as ^{191}Os, have recently

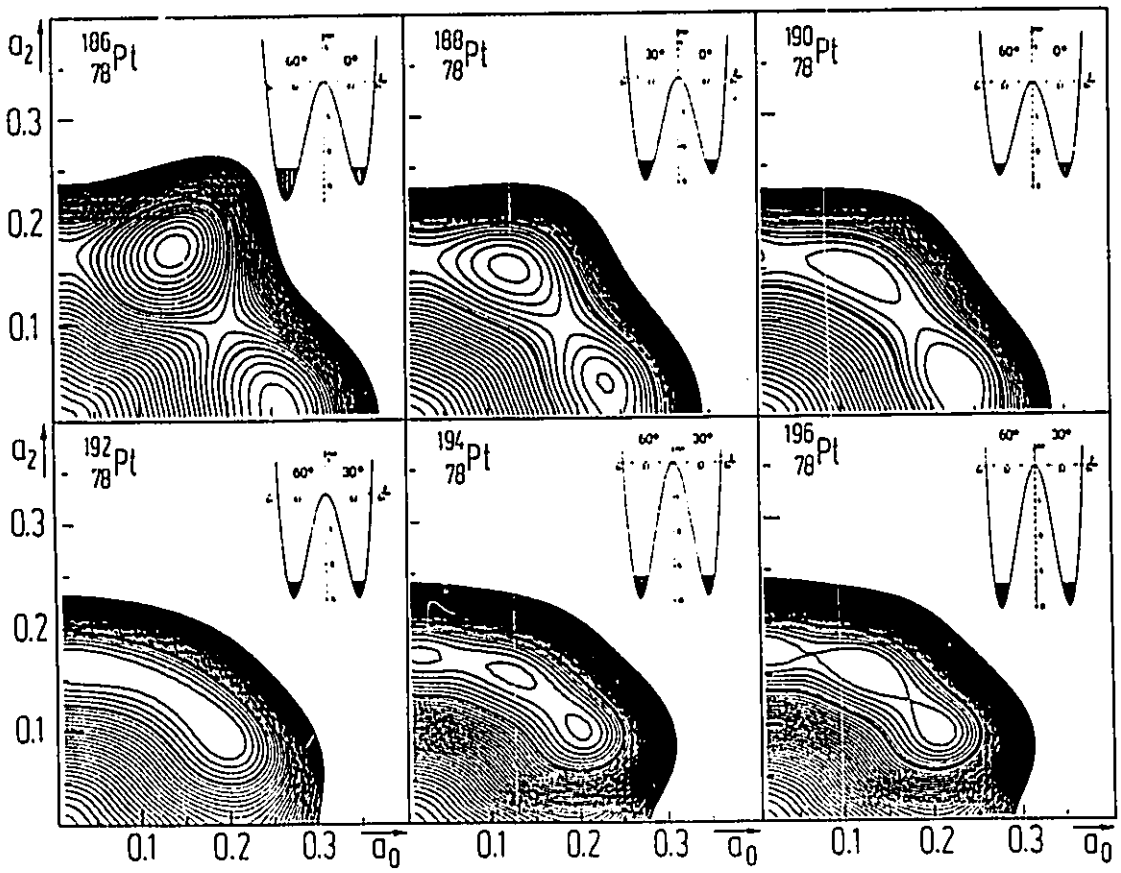

Figure 1.3: A series of potential energy surfaces in the a_0 and a_2 plain for even-even Pt nuclei. The insets show the potential energy for specific values of γ. (From ref.[6])

been the subject of intense investigations, and some interesting effects have been observed. Odd-odd nuclei have not been studied as intensely, and this is due to two reasons. Firstly, the high density of levels makes the performance of experiments very difficult, since high resolution must be achieved, and the analysis of the data is very difficult. Secondly, the theoretical description of transitional odd-odd nuclei is not complete. Recently, an extension of the IBM, the Interacting Boson Fermion Fermion Model (IBFFM), and the symmetry limit of the Extended Supersymmetry (ESUSY) model applicable in the transitional region have been investigated. These

models have not been well tested, and the range of their validity is an open question. More traditional models, such as the Nilsson model and the Rotation-Vibration Model, which have enjoyed considerable success in the rare-earth region, are known to encounter difficulties in explaining the structure in transitional nuclei.

One of the most powerful ways to examine nuclear structure is with single-nucleon transfer reactions. Unlike work involving γ-rays, the peaks observed in transfer reactions correspond directly to the nuclear levels, whereas the peaks observed in γ-spectra are transitions between two levels. The intensities of peaks in the particle spectra are directly related to the squares of the amplitudes of the wave functions for the states. By performing distorted wave Born approximation (DWBA) calculations, the dependence of the cross section on the reaction kinematics can be removed (assuming a single-step process), leaving information on the structure in the form of spectroscopic strengths. The experimental spectroscopic strengths can be compared with the predictions of different nuclear models to assign levels to specific configurations and to the test models.

In the present work, states in ^{190,192,194}Ir are studied via single-nucleon transfer reactions. The principle aims of this study were to establish the level energies and measure angular distributions of cross sections for levels below $\sim$ 1 MeV excitation energy, populated via single-nucleon transfer. Nuclear structure information in the form of parities, possible spin values, and spectroscopic strengths was obtained from the fits to the angular distributions of cross sections. The data from the study were used to test three nuclear models; the IBFFM, the ESUSY model, and a simple Nilsson model approach. Ultimately, it is the hope of the author that this work will serve as a guide to the modification of existing theories, such as the IBFFM, or to encourage work on extensions of older theories. For instance, a theoretical study of two odd particles orbiting a core that has a potential energy surface like those shown in Figure 1.2 and Figure 1.3 may be needed before a full understanding of the odd-odd iridium nuclides can be achieved.

In Chapter 2, the various nuclear models used in this work are discussed. The notation used in the IBM, IBFFM, and the ESUSY models can be somewhat complicated. In order to present the notation used in a more familar context, the rotation-vibration and Nilsson model are discussed first. The IBM and its extensions are then presented with the hope that the basics of the model are transparent once the reader is familiar with the notation that was introduced with the geometrical models. In Chapter 3, the experimental and analysis techniques are discussed, with the experimental results presented in Chapter 4. Chapter 5 contains the discussions of the experimental results, and the comparisons of the data with the IBFFM, ESUSY, and Nilsson model predictions. Finally, in Chapter 6, a summary of the work and its conclusions are given.

Chapter 2.
Nuclear Models

2.1. Introduction

Many different models have been applied to various nuclei. Each model has enjoyed some success in a particular region, but currently no model in existence can predict or explain all observable nuclear phenomena. The task of finding a model to describe all nuclei and their properties is a formidable one indeed. Considering the richness and complexity of the nuclear many-body system, a general model may be too ambitious an objective at the present time.

The basic problem with attempting to model nuclei is that nature is "too smart" for us to comprehend. Usually when we feel that we are understanding some particular phenomenon of nature, it is time to be humbled by the display of a behaviour we never imagined. This forces us to abandon or modify our current theory or, as is sometimes done, to state that the particular behaviour is outside the scope of the theory. Unfortunately, this statement often accompanies a claim that the model is very successful, when no such claim can legitimately be made.

When we examine nuclei, it is of little surprise that models have difficulty in explaining or predicting all nuclear properties. This is best illustrated by considering the ranges over which some of the properties fluctuate. The number of nucleons ranges from A=1 to A$\simeq$265. The nuclear decay lifetime, τ ranges from $\simeq 10^{-22}$ s to $\simeq 10^{21}$ yr., (not including stable nuclei) a span of 50 orders of magnitude. The angular momentum of the nucleus, I, ranges from 0 to $\simeq 70\hbar$. The nuclear shape ranges from prolate to oblate, spherical to triaxial, superdeformed and perhaps hyperdeformed. The excitations of the nucleus can be collective, single-particle, or a combination of both. The list could continue, but the point has probably been made: any theory that could give accurate predictions over the above ranges of

values would be truly remarkable. Thus, when a claim is made that a model can predict and explain certain nuclear properties, the reader should always reserve some skepticism, and not assume that it can explain other properties as well.

In this chapter, various nuclear models that are used in this work will be discussed. The geometric model is discussed in some length, since much of the notation used is similar to that used in the Interacting Boson Model (IBM). In section 2.2 the geometric models are discussed, such as the rotation-vibration model and Nilsson model, and in section 2.3 the algebraic models, the interacting boson model, interacting boson fermion model, interacting boson fermion-fermion model , and the supersymmetry model, are discussed. The material presented in this chapter is based heavily on the following textbooks; Eisenberg and Greiner[11](1987), Preston and Bhaduri[12](1975), Casten[13](1990), and Ring and Schuck[14](1980).

2.2. Geometric Models

2.2.1 Collective Coordinates and the RVM

Any discussion of geometric collective models must begin with a discussion of the collective coordinates. The collective coordinates are established by a classical picture of the nucleus as a kind of liquid drop with a vibrating or rotating surface. The collective variables, α, are complicated functions of the individual nucleon coordinates $\vec{x}_i$, but the form of this function is not, nor does it need to be, known explicitly. It is possible to construct the model without knowing its microscopic basis. The most important collective variables (i.e., those variables used most often in nuclear structure theories) are those describing the nuclear surface, $\alpha^{[\lambda]}$.

The notation $\alpha^{[\lambda]}$ actually implies the whole set

$$\alpha^{[\lambda]} \equiv \{\alpha_{\lambda\mu}\} \tag{2.2.1}$$

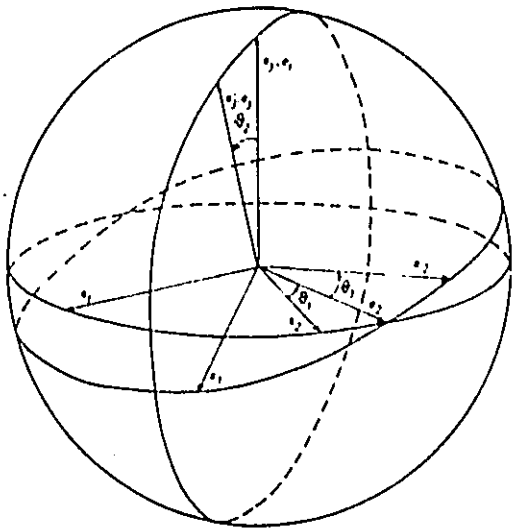

Figure 2.2.1: Definition of the Euler angles θ_j. The quantities $\vec{x}_i$ are the unit vectors in the laboratory system, $\vec{x}'_i$ are the unit vectors in the of the final rotated system. (From Eisenberg and Greiner, 1987)

with $\mu = -\lambda, -\lambda+1, ..., \lambda-1, \lambda$ such that $\alpha^{[\lambda]}$ are spherical tensors and they are time dependent. Since the nuclear surface must be invariant under rotation, the tensor $\alpha^{[\lambda]}$ must transform under rotations as

$$a_{\lambda\mu} = \sum_{\nu} \mathcal{D}^{\lambda}_{\nu\mu}(\theta_j)\, \alpha_{\lambda\nu} \tag{2.2.2}$$

or

$$\alpha_{\lambda\mu} = \sum_{\nu} \mathcal{D}^{\lambda *}_{\mu\nu}(\theta_j)\, a_{\lambda\nu} \tag{2.2.3}$$

(More formally $\alpha^{[\lambda]}$ are tensors of rank λ that transform under the $(2\lambda+1)$-dimensional representation of SO(3).) The coordinates $a_{\lambda\mu}$ now define the nuclear surface in the rotated frame. The quantities θ_j are the set of Euler angles as described in Figure 2.2.1.

The coordinates $\alpha^{[\lambda]}$ are defined by the expansion of the nuclear surface into spherical harmonics

$$R(\vartheta,\phi,t) = R_\alpha\Big(1+\sum_{\lambda,\mu}(-1)^\mu\,\alpha_{\lambda-\mu}(t)\,Y_{\lambda\mu}(\vartheta,\phi)\Big) \tag{2.2.4}$$

Since nuclear matter is incompressible (the incompressibility, K, is defined as

$$K = 9\rho_o^2\left(\frac{d^2(E/A)}{d\rho^2}\right)_o \tag{2.2.5}$$

for nuclear matter, and has a value of >120 MeV), there is a restriction on the radius such that volume must be conserved. Therefore,

$$\frac{4}{3}\pi R_o^3 = \int_0^{2\pi}d\phi\int_0^{\pi}\sin\vartheta d\vartheta\int_0^{R(\vartheta,\phi)}r^2dr \tag{2.2.6}$$

which yields

$$\frac{4}{3}\pi R_o^3 = \frac{4}{3}\pi R_\alpha^3\Big[1+\frac{3\alpha_{00}}{\sqrt{4\pi}}+\frac{3}{4\pi}\sum_{\lambda\mu}|\alpha_{\lambda\mu}|^2+O\left(\alpha^3\right)+\ldots \tag{2.2.7}$$

Deformations of the type α_{00} give a change of volume and may be associated with "breathing" modes of the nucleus. Because of the high incompressibility of nuclear matter, these breathing modes are expected to lie at high energies, 10 to 15 MeV. Since we will not be interested in such effects, α_{00} can be set to zero. The $\lambda = 1$ terms give a translation of the center of mass and if the origin is defined to coincide with the center of mass, these terms can also be set to zero. (It should be noted that this argument applies only if $\alpha_{1\mu}$ are small. For large $\alpha_{1\mu}$, the center of mass is shifted and the shape is deformed as well.) The radius can now be written as

$$R(\vartheta,\phi) = \frac{R_o}{\xi}\Big(1+\sum_{\lambda=2}^{\infty}\sum_{\mu=-\lambda}^{\lambda}\alpha_{\lambda\mu}(-1)^\mu\,Y_{\lambda\mu}(\vartheta,\phi)\Big) \tag{2.2.8}$$

The factor ξ is required for volume conservation and takes the value

$$\xi \simeq 1+\frac{1}{4\pi}\sum_{\lambda=2}^{\infty}\sum_{\mu}|\alpha_{\lambda\mu}|^2 \tag{2.2.9}$$

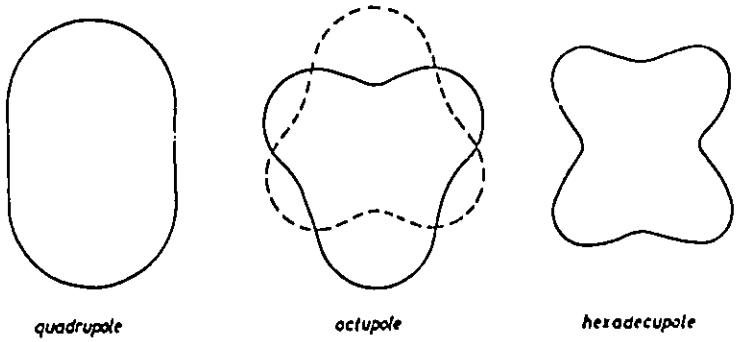

Figure 2.2.2: Effects on the shape of the terms in the surface expansion involving $\lambda = 2, 3$ and 4. (From Eisenberg and Greiner, 1987)

As long as the $\alpha_{\lambda\mu}$ terms are small, then $\xi \simeq 1$. The $\lambda = 2$ terms give rise to quadrupole deformations, $\lambda = 3$ terms yield octupole deformations, and $\lambda = 4$ terms give hexadecapole deformations. These are shown schematically in Figure 2.2.2. It can be argued that λ should have an upper bound. The maxima that occur in the surface due to $Y_{\lambda\mu}$ should have at least one nucleon associated with them. The number of maxima in the shape is proportional to λ^3. Therefore, for a nucleus with A nucleons, $\lambda < A^{\frac{1}{3}}$. For $A \simeq 190$, this argument yields $\lambda \leq 6$.

It is usually assumed that the $\lambda = 2$ terms are the most important for describing the surface, therefore the expression for the radius now becomes

$$R = R_o\Big(1 + \sum_{\mu} \alpha^*_{2\mu} Y_{2\mu}\Big) \tag{2.2.10}$$

The instantaneous values of α describe the shape of the nucleus in the laboratory frame. However this is not the most convenient frame. It is desirable to make a transformation to the intrinsic system, with the axes coinciding with the principal axes of the nucleus. This implies that the coordinates $a_{2\mu}$, which are related to $\alpha_{2\mu}$ by Eq. (2.2.2), should be used. Therefore,

$$a_{2\mu} = \sum_{\nu} \mathcal{D}^{2}_{\nu\mu}(\theta_j)\, \alpha_{2\nu} \tag{2.2.11}$$

where $a_{21} = a_{2-1} = 0$ and $a_{22} = a_{2-2}$ and the three Euler angles, θ_j, give the orientation of the nucleus in space. Now, a_{20} and a_{22} describe the shape of the intrinsic nucleus. It was at this point that A. Bohr introduced the β and γ parameters by

$$a_{20} = \beta \cos\gamma \tag{2.2.12a}$$

$$a_{22} = \frac{\beta \sin\gamma}{\sqrt{2}} \tag{2.2.12b}$$

Because of the symmetry of the trigonometric functions, and the fact that a cyclic permutation of the axes 1, 2, 3 leave the nuclear surface unaltered, it is only necessary to consider the wedge defined by $\gamma = 0° - 60°$. This wedge defines all possible quadrupole shapes. (It should be pointed out, however, that oblate nuclei are usually specified as having $\beta < 0$ and $\gamma = 0°$. This is equivalent to $\beta > 0$ and $\gamma = 60°$ as a cyclic permutation of the axes will transform one into the other.)

Nuclei away from closed shells often exhibit permanent deformations away from the spherical symmetry. Using the simplest form of the collective quadrupole kinetic energy operator,

$$\hat{T} = \frac{1}{2} B_2 \sum_{\mu} \dot{\hat{\alpha}}^*_{2\mu} \dot{\hat{\alpha}}_{2\mu} \tag{2.2.13}$$

it can be transformed into the operator in the intrinsic frame

$$\hat{T} = \frac{1}{2} \sum_{k} \tilde{\omega}_k^2 \mathcal{J}_k (\hat{a}_0, \hat{a}_2) + \frac{1}{2} B_2 \sum_{\nu} \dot{\hat{a}}^*_{\nu} \dot{\hat{a}}_{\nu} \tag{2.2.14}$$

where B_2 is the inertia parameter, $\mathcal{J}_k$ are the moments of inertia, and $\tilde{\omega}_k$ are the rotational frequencies about the origin. The moments of inertia take the values (in terms of the variables β and γ defined previously)

$$\mathcal{J}_1 = 4 B_2 \beta^2 \sin^2\left(\gamma - \frac{2\pi}{3}\right) \tag{2.2.15}$$

$$\mathcal{J}_2 = 4 B_2 \beta^2 \sin^2\left(\gamma - \frac{4\pi}{3}\right) \tag{2.2.16}$$

$$\mathcal{J}_3 = 4 B_2 \beta^2 \sin^2\gamma \tag{2.2.17}$$

The part of the kinetic energy operator $\hat{T}$ in Eq. (2.2.14) that depends on $\mathcal{J}_k$ might be called the rotational energy but it also contains an interaction with the

shape vibrations due to the dependence of $\mathcal{J}_k$ on β and γ (or on a_0 and a_2). The second part of $\hat{T}$ can be interpreted as the kinetic energy of the shape oscillations.

The kinetic energy of a rigid body with three moments of inertia $\mathcal{J}_1, \mathcal{J}_2$, and $\mathcal{J}_3$, which rotates about its center of mass is

$$\hat{T}_{RO} = \frac{\hbar^2}{2}\mathcal{J}_1\tilde{\omega}_1^2 + \frac{\hbar^2}{2}\mathcal{J}_2\tilde{\omega}_1^2 + \frac{\hbar^2}{2}\mathcal{J}_3\tilde{\omega}_1^2 \tag{2.2.18}$$

or, writing $R_k = \mathcal{J}_k\hbar\tilde{\omega}_k$,

$$\hat{T}_{RO} = \frac{R_1^2 + R_2^2}{2\mathcal{J}_0} + \frac{R_3^2}{2\mathcal{J}_3} \tag{2.2.19}$$

for a symmetric rotor with $\mathcal{J}_1 = \mathcal{J}_2 = \mathcal{J}_0$. This can be rewritten as

$$\hat{T}_{RO} = \frac{R^2 - R_3^2}{2\mathcal{J}_0} + \frac{R_3^2}{2\mathcal{J}_3} \tag{2.2.20}$$

where $R^2 = R_1^2 + R_2^2 + R_3^2$. In the rotational-vibrational model, which is appropriate for axially symmetric deformed nuclei, the collective potential energy is expanded around the equilibrium position

$$a_0 = \beta_0 + \xi \tag{2.2.21a}$$

$$a_2 = 0 + \eta \tag{2.2.21b}$$

The potential energy is written as

$$\hat{V}(\xi, \eta) = \frac{1}{2}C_0\xi^2 + C_2\eta^2 \tag{2.2.22}$$

where C_0 and C_2 are the potential (or stiffness) parameters.

The expressions above for $\hat{T}$ and $\hat{V}$ are still classical expressions that must be quantized (even though the variables satisfy commutation relations). The full Hamiltonian in the Rotation-Vibration Model (RVM) is

$$\hat{H} = \hat{H}_{rot} + \hat{H}_{vib} + \hat{H}_{rot-vib} \tag{2.2.23}$$

where

$$\hat{H}_{rot} = \frac{R^2 - R_3^2}{2\mathcal{J}_0} + \frac{R_3^2}{16\beta\eta^2} \tag{2.2.24}$$

$$\hat{H}_{vib} = \frac{-\hbar^2}{2B_2}\left[\frac{\partial^2}{\partial\xi^2} + \frac{1}{2}\frac{\partial^2}{\partial\eta^2}\right] + \frac{1}{2}C_2\xi^2 + C_2\eta^2 - \frac{\hbar^2}{16B\eta^2} \tag{2.2.25}$$

$$\begin{aligned}\hat{H}_{rot-vib} = &\frac{R^2 - R_3^2}{2\mathcal{J}_0}\left[\frac{2\eta^2}{\beta_0^2} - \frac{2\xi}{\beta_0} + \frac{3\xi^2}{\beta_0^2}\right] \\ &+ \frac{R_+^2 - R_-^2}{4\mathcal{J}_0}\left[\frac{2\sqrt{6}\xi\eta}{\beta_0^2} - \frac{2\sqrt{6}\eta}{3\beta_0}\right]\end{aligned} \tag{2.2.26}$$

The Hamiltonian diagonalized is usually that for $\hat{H}_{rot} + \hat{H}_{vib}$, and $\hat{H}_{rot-vib}$ is treated as a perturbation. The total wave function for $\hat{H}_{rot} + \hat{H}_{vib}$ must be invariant under $\hat{R}_1$ and $\hat{R}_2$, where $\hat{R}_1$ gives rotations of π about θ_1 and θ_2, and $\hat{R}_2$ gives rotations of $\pi/2$ about θ_3. The total wave function for a state with angular momentum I, projection M onto the laboratory $\hat{z}$-axis, projection K onto the intrinsic 3-axis, and with n_0 β-phonons and n_2 γ-vibrations is

$$|IMKn_2, n_0\rangle = \sqrt{\frac{2I+1}{16\pi^2(1+\delta_{K0})}}\left[\mathcal{D}^{I*}_{MK}(\theta_j) + (-1)^I \mathcal{D}^{I*}_{M-K}(\theta_j)\right]|\chi_{K,n_2}\rangle|n_0\rangle \tag{2.2.27}$$

Because of the invariance of the wave function under $\hat{R}_1$ and $\hat{R}_2$, there are limitations on the values that I and K can take

$$K = 0, 2, 4, \ldots \tag{2.2.28a}$$

$$I = 0, 2, 4, \ldots \qquad K = 0 \tag{2.2.28b}$$

$$I = K, K+1, K+2, \ldots \qquad K \neq 0 \tag{2.2.28c}$$

The energy of the states is given by

$$E_{IKn_2n_0} = \frac{\hbar^2\left(I(I+1) - K^2\right)}{2\mathcal{J}_0} + \left(\frac{1}{2}|K| + 1 + 2n_2\right)E_\gamma + \left(n_0 + \frac{1}{2}\right)E_\beta \tag{2.2.29}$$

The states can be labelled by the quantum numbers I, K, n_2 and n_0. The ground state band is $|I000\rangle$, the β-band is $|I001\rangle$ and the γ-band is $|I200\rangle$. The state $|I200\rangle$ is called a γ-band even though $n_2 = 0$ because of the strong rotation-vibration term $R^2/16B_2\eta^2$ which has been included in $\hat{H}_{rot}$. This term forces the γ-vibration

to be present in an excited state as soon as $K \neq 0$. The term $R_3/16B_2\eta^2$acts like a centrifugal term that pulls the γ-vibrational wave function from the origin. This also occurs for the ground state for the γ-vibrations, i.e. $n_2 = 0$, due to the term $\hbar^2/16B_2\eta^2$ in $\hat{H}_{vib}$. Thus, even though the initial conditions are that of an axially symmetric γ-vibrator ($\bar{a}_2 = 0$), the dynamics pull the wave function away from the origin and make the nucleus effectively dynamically triaxial.

The RVM is often used to describe the core of odd and odd-odd nuclei, and the extra-core particles are then coupled to it. The coupling may be strong or weak, as will be explained in the next section which discusses the Nilsson model.

2.2.2 Nilsson Model

The Nilsson model is basic to any discussion of deformed nuclei, and is one of the most successful models ever developed. It is usually one of the first models that new experimental data are compared with, and its nature is such that it is easy to develop a good "intuitive feel" of it.

The Nilsson model is essentially a single-particle model, except that there is an interaction between the collective and single-particle degrees of freedom. The coupling of the single-particle to the core is extremely important, as it determines many of the properties of the single-particle. Considering a classical picture for the moment, if the single-particle orbits the core at a much faster frequency than the core rotates, then the potential that the particle feels will be the instantaneous potential of the core. This is referred to as the adiabatic limit, or the strong coupling limit. If the rotational frequency of the particle is much less than that of the core, then the particle feels the time averaged potential of the core, which will then be oblate. Thus for very high rotational frequencies the strong coupling limit can be expected to break down. For nearly spherical nuclei, where the amplitudes of the surface collective variables are small, the coupling between the particle and the core is weak. This is the weak coupling limit.

The Hamiltonian for the system where there is a single-particle coupled to a core is

$$\hat{H} = \hat{H}_{coll} + \hat{H}_{sp} + \hat{H}_{int} \tag{2.2.30}$$

where $\hat{H}_{coll}$ is the collective Hamiltonian of the core, $\hat{H}_{sp}$ is the single-particle Hamiltonian, and $\hat{H}_{int}$ is the interaction between the collective and single-particle degrees of freedom. The collective Hamiltonian that can be used is that of the rotation-vibration model introduced previously. It contained terms involving the angular momentum of the core, $\vec{R}$. Now, the total angular momentum is that of the core and that of the particle, such that $\vec{I} = \vec{R} + \vec{j}$, and so Eq. (2.2.20) must now be rewritten making the substitution $\vec{R} = \vec{I} - \vec{j}$.

For nuclei with permanent deformations, the coupling between the single-particle and collective degrees of freedom becomes quite strong (at least for low rotational frequencies) and thus the strong-coupling limit is realized. In this limit, the projections of the single-particle angular momentum, $\vec{j}$, and the total angular momentum, $\vec{I}$, along the intrinsic $\hat{z}$-axis become approximate constants of motion, and are given the labels Ω and K, respectively.

The single-particle Hamiltonian and the interaction Hamiltonian are usually written in terms of an oscillator shell model, and take the form

$$\begin{aligned}\hat{H}_{sp} + \hat{H}_{int} = &\frac{p'^2}{2m} + \frac{1}{2}m\omega^2 r'^2 + C\vec{l}' \cdot \vec{s}' + Dl'^2 \\ &- m\omega^2 r'^2 \{a_0 Y_{20} + a_2 (Y_{22} + Y_{2-2})\}\end{aligned} \tag{2.2.31}$$

for an isotropic oscillator. The prime on the coordinates for the single-particle indicate that these are with respect to the intrinsic frame. The $\vec{l}' \cdot \vec{s}'$ term is the familiar spin-orbit coupling, which has been shown to arise from relativistic Hartree-Fock calculations of one-boson-exchange potentials. The l'^2 term arises from the fact that actual single-particle potential should be more "flat-bottomed" than that of the harmonic oscillator. The difference between the harmonic oscillator and a more realistic potential, like a Woods-Saxon, increases with radial distance from the center, i.e. with increasing l. The l'^2 term acts like an interpolation between a

harmonic oscillator and a square well, which is often used in the shell model. The last term represents the interaction between the single-particle and the collective degrees of freedom. Making the substitutions $\vec{R} = \vec{I} - \vec{j}$, and rearranging terms, the total Hamiltonian is written as

$$\hat{H} = \hat{H}_{o_{coll}} + \hat{H}_{o_{sp}} + \hat{H}' \tag{2.2.32}$$

where

$$\begin{aligned}\hat{H}_{o_{coll}} =& \frac{\hbar^2}{2\mathcal{J}_0}\left[\hat{I}^2 - \left(\hat{I}'_3 - \hat{j}'_3\right)^2\right] + \frac{\hbar^2}{16B_2\eta^2}\left[\left(\hat{I}'_3 - \hat{j}'_3\right)^2 - 1\right] \\ & - \frac{\hbar^2}{2B_2}\left[\frac{\partial^2}{\partial\xi^2} + \frac{1}{2}\frac{\partial^2}{\partial\eta^2}\right] + \frac{1}{2}C_o\xi^2 + C_2\eta^2\end{aligned} \tag{2.2.33}$$

is the collective part of the Hamiltonian,

$$\hat{H}_{o_{sp}} = \frac{p'^2}{2m} + \frac{1}{2}m\omega^2 r'^2 + C\vec{l}' \cdot \vec{s}' + Dl'^2 - m\omega^2 r'^2\beta_0 Y_{20} \tag{2.2.34}$$

is the single-particle Hamiltonian, and

$$\begin{aligned}\hat{H}' =& \frac{\hbar^2}{2\mathcal{J}_o}\hat{j}^2 - \frac{\hbar^2}{2\mathcal{J}_o}\left[\hat{I}'_+\hat{j}'_- + \hat{I}'_-\hat{j}'_+ + 2\hat{I}'_3\hat{j}'_3\right] \\ & + \frac{\hbar^2}{2\mathcal{J}_o}\left[\hat{I}^2 - \hat{I}'^2_3 + \hat{j}^2 - \hat{j}'^2_3 - \hat{I}'_+\hat{j}'_+\right]\left(\frac{2\eta^2}{\beta_0^2} - \frac{2\xi}{\beta_0} + \frac{3\xi^2}{\beta_0^2}\right) \\ & + \frac{\hbar^2}{4\mathcal{J}_0}\left[\hat{I}'^2_+ + \hat{I}'^2_- + \hat{j}'^2_+ + \hat{j}'^2_- - 2\left(\hat{I}'_+\hat{j}'_+ + \hat{I}'_-\hat{j}'_-\right)\right]\left[2\sqrt{6}\frac{\xi\eta}{\beta_0^2} - \frac{2\sqrt{6}}{3}\frac{\eta}{\beta_0}\right] \\ & - m\omega^2 r'^2\left[\xi Y_{20} + \eta\left(Y_{22} + Y_{2-2}\right)\right]\end{aligned} \tag{2.2.35}$$

is the interaction between the collective and single-particle degrees of freedom. The primed coordinates refer to quantities with respect to the intrinsic frame and the unprimed coordinates refer to the laboratory frame.

The $\hat{H}_{0_{coll}}$ term describes the rotating and vibrating core and corresponds closely to $\hat{H}_{vib} - \hat{H}_{rot}$ as in Eq. (2.2.24) and Eq. (2.2.25). $\hat{H}_{0_{sp}}$ is the shell model Hamiltonian for a particle moving in a deformed axially symmetric potential. Most of the terms in $\hat{H}'$ are small and hence are neglected. However, the second term in particular is very important as it is the Coriolis or rotation-particle coupling term,

and may also be written as $(\hbar^2/\mathcal{J}_o)\vec{I}' \cdot \vec{j}'$. The Coriolis term is the most important of the terms contained in $\hat{H}'$ and will be discussed later.

The solutions to the collective part of the Hamiltonian have been discussed previously, but some slight modifications must be made. The K quantum number for those solutions should now be replaced by $K - \Omega$. The energy of the states now becomes

$$\begin{aligned} E_{IK\Omega n_2 n_0} =& \mathcal{E}_\Omega + \left(I(I+1) - (K-\Omega)^2\right) \frac{\hbar^2}{2\mathcal{J}_0} \\ &+ \left(\frac{1}{2}|K-\Omega| + 1 + 2n_2\right) E_\gamma + \left(n_0 + \frac{1}{2}\right) E_\beta \end{aligned} \tag{2.2.36}$$

where $\mathcal{E}_\Omega$ are the single particle energies obtained from

$$\hat{H}_{0,p}\psi_\Omega = \mathcal{E}_\Omega \psi_\Omega. \tag{2.2.37}$$

The single particle Hamiltonian can be rewritten as

$$\begin{aligned} \hat{H}_{0,p} =& \frac{p'^2}{2m} + \frac{1}{2} m \left(\omega_\perp^2 \left(x'^2 + y'^2\right) + \omega_z^2 z'^2\right) \\ & C\vec{l}' \cdot \vec{s}' + D\left(l'^2 - < l'^2 >_{shell}\right) \end{aligned} \tag{2.2.38}$$

where the term in Y_{20} has been expanded into Cartesian coordinates, and

$$\omega_\perp^2 = \omega^2 \left(1 + \sqrt{\frac{5}{4\pi}}\beta_0\right) \tag{2.2.39a}$$

$$\omega_z^2 = \omega^2 \left(1 - 2\sqrt{\frac{5}{4\pi}}\beta_0\right) \tag{2.2.39b}$$

The term $-D < l'^2 >_{shell}$ has also been introduced in order to maintain the distance between the centers of gravity of different N shells. For a given shell, the term equals $-\frac{1}{2}DN(N+3)$.

The deformation parameter, δ_2, is introduced via the relations

$$\omega_\perp^2 = \omega_0^2(\delta_2)\left(1 + \frac{2}{3}\delta_2\right) \tag{2.2.40a}$$

$$\omega_z^2 = \omega_0^2(\delta_2)\left(1 - \frac{4}{3}\delta_2\right) \tag{2.2.40b}$$

where $\omega_0(\delta_2)$ is a function of the deformation.

The coordinates $\vec{r}\,'$ can be transformed to dimensionless coordinates, $\vec{r}$, by

$$x = \sqrt{\frac{m\omega_0}{\hbar}}x' \tag{2.2.41}$$

and similarly for y' and z'. The parameters C and D are usually expressed as

$$C = -2\hbar\mathring{\omega}\kappa \tag{2.2.42a}$$

$$D = -\hbar\mathring{\omega}\mu\kappa \tag{2.2.42b}$$

where $\mathring{\omega}$ is $\omega_0(\delta_2 = 0)$.

The Hamiltonian can now be rewritten as

$$\begin{aligned}\hat{H}_{0_{sp}} =& \frac{1}{2}\hbar\omega_0(\delta_2)\left(-\nabla_r^2 + r^2\right) - \delta_2\hbar\omega_0(\delta_2)\frac{4}{3}\sqrt{\frac{\pi}{5}}r^2Y_{20} \\ & - 2\hbar\mathring{\omega}\kappa\left(\vec{l}\cdot\vec{s}\right) - \hbar\mathring{\omega}\mu\kappa\left(l^2 - < l^2 >_{shell}\right)\end{aligned} \tag{2.2.43}$$

The usual choice of basis for evaluation of the matrix elements of $\hat{H}_{0_{sp}}$ is $|N l \Lambda\Sigma\rangle$ where N is the principle quantum number, l the orbital angular momentum, Λ the projection of l onto the intrinsic $\hat{z}$-axis, and Σ is the projection of the single-particle spin onto the $\hat{z}'$-axis. The projection of the single-particle angular momentum on to the $\hat{z}'$-axis is $\Omega = \Lambda + \Sigma$. With this choice of basis, the part of the Hamiltonian given by

$$\frac{1}{2}\hbar\omega_0(\delta_2)\left(-\nabla_r^2 + r^2\right)$$

is diagonal in the basis, and has eigenvalues $(N + \frac{3}{2})\hbar\omega_0(\delta_2)$. The matrix elements of the operator $\vec{l}\cdot\vec{s}$, $\langle N l \Lambda' \Sigma' | \vec{l}\cdot\vec{s} | N l \Lambda\Sigma\rangle$, have the selection rules that $\Lambda' = \Lambda \pm 1$ when $\Sigma' = \Sigma \mp 1$ and $\Lambda' = \Lambda$ when $\Sigma' = \Sigma$. Thus, Ω remains a good quantum number. The l^2 term obviously does not mix the different basis states. The remaining term in $\hat{H}_{0_{sp}}$ is proportional to r^2Y_{20} and mixes states with $l' = l \pm 2$ and $N' = N \pm 2$. While the selection rules imply that there is a mixing of states with different N, the assumption is usually made that these mixings are small, since the $N + 2$ shell has a large energy separation from the N shell. This can become important, however,

when downward sloping $N+2$ orbitals, i.e. those with the largest value of n_z, cross upward sloping N orbitals, i.e. those with $n_z = 0$. At the particular deformation where the crossing occurs, the effects can become important.

For small deformations, a single j component dominates the Nilsson wave function. At $\delta_2 = 0$, the spherical shell model is recovered and the Nilsson wave function is exactly the spherical shell-model wave function. The Nilsson wave function is labelled as $\Omega^\pi[Nn_z\Lambda]$ where Ω, N, Λ have been introduced previously, π is the parity and n_z is the $\hat{z}$-axis quantum number. Strictly speaking, only N, Ω and π are good quantum numbers, however at large deformations n_z and Λ become good quantum numbers. This occurs because the l^2 and $\vec{l} \cdot \vec{s}$ terms become negligible. The Hamiltonian in this limit reduces to that of a three dimensional anisotropic harmonic oscillator and the energy eigenvalues are simply

$$E = \hbar\omega\,(N - n_z + 1) + \hbar\omega_z \left(n_z + \frac{1}{2}\right)$$

The projections of the orbital and spin angular momenta, Λ and Σ, are also now constants of the motion. Hence, the Nilsson wave functions are labelled with these quantum numbers, which, strictly speaking, are only good for large deformations.

Calculations to determine the energies and wave functions of the Nilsson states have been performed by many people using slightly different schemes (such as a Woods-Saxon instead of the modified harmonic oscillator, with or without δ_4, including octupole deformation, etc.) but the resulting diagrams[15] bear a remarkable similarity to those in Figure 2.2.3. While these diagrams appear to be complicated, many features have a simple physical origin. Consider the case where a single nucleon orbits a deformed prolate core as in Figure 2.2.4. An orbital that lies along the equatorial plane (labelled K_1) is, on average, closer to the nuclear matter than an orbital perpendicular to the plane. Since the nuclear force has an overall attractive nature, the orbit that has time-averaged less separation from the nuclear matter distribution will be lower in energy. Therefore, it should be expected that low Ω orbits are lower in energy than high Ω orbits. As the prolate deformation

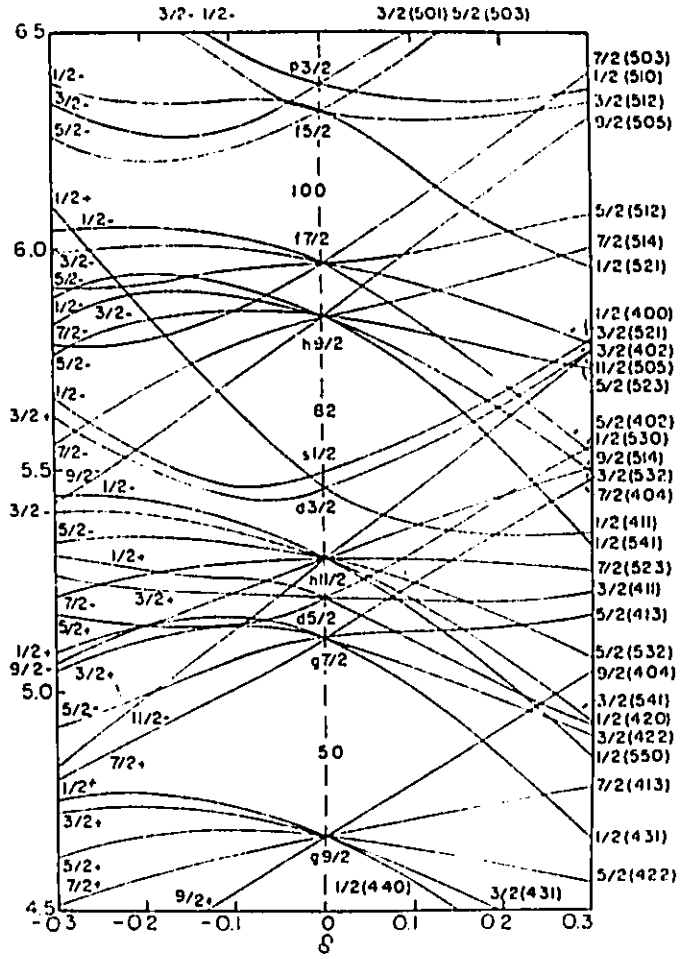

Figure 2.2.3a: Nilsson diagram[15] of proton states for 50< Z <82. (From Chi, 1966)

becomes greater, this effect should become stronger. Therefore, the low Ω orbitals decrease in energy as $\beta > 0$ increases, and high Ω orbits increase in energy as $\beta > 0$ increases. For oblate nuclei the effect is reversed, with high Ω orbitals decreasing in energy and low Ω increasing in energy as the deformation increases. The spacing between the levels increases with Ω and there are many more downward sloping orbitals (for prolate nuclei) than there are upward sloping orbitals.

As the deformation increases, the orbitals from different shell-model states approach one another. Orbitals with the same Ω and parity cannot cross one another

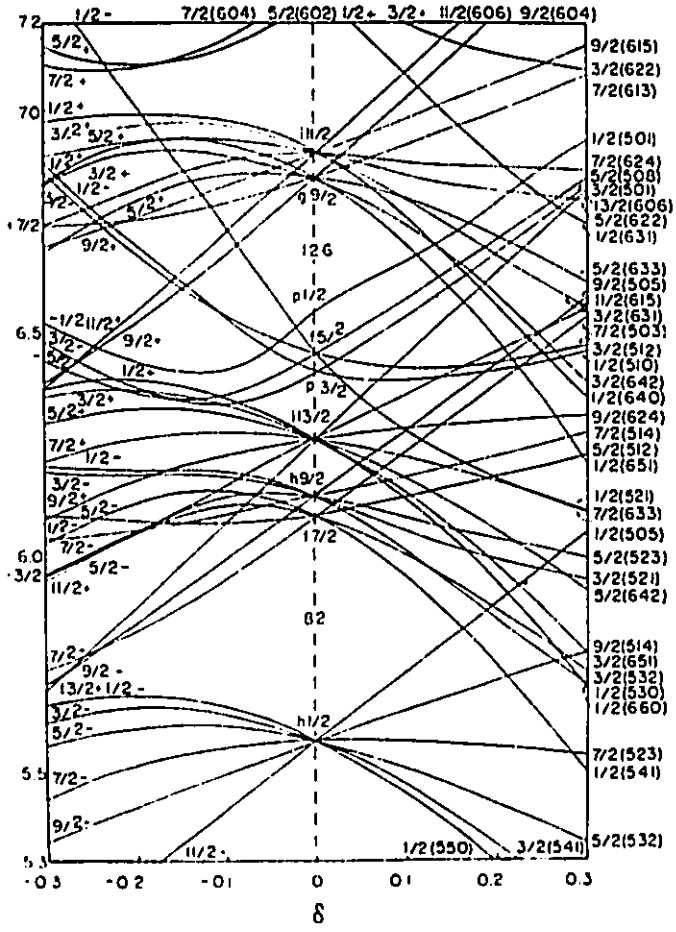

Figure 2.2.3b: Nilsson diagram[15] for neutron states for 82< N <126. (From Chi, 1966)

since even an infinitesimal interaction will cause them to repel. Therefore two orbitals with the same Ω and parity will curve away from each other.

When the deformation is zero, the Nilsson wave functions are a pure spherical shell model j state. As the deformation increases, the term in the Hamiltonian proportional to Y_{20} mixes different j shell configurations. The most favoured mixing occurs between configurations where $l' = l \pm 2$. Therefore, in the 50-82 major shell, the $d_{\frac{5}{2}}$ and $s_{\frac{1}{2}}$ states mix more than the $d_{\frac{5}{2}}$ and $d_{\frac{3}{2}}$ states, even though the latter are

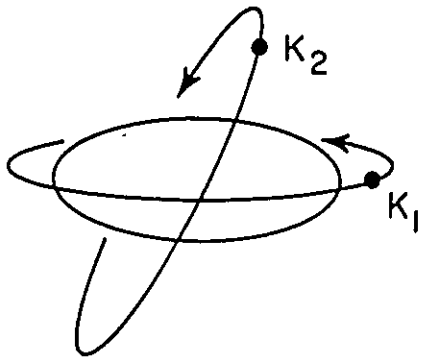

Figure 2.2.4: Classical picture of a two single-particle trajectories with different K-values orbiting a prolate core. (From Casten, 1990)

closer together than the former. Likewise, the $p_{\frac{3}{2}}$ and $f_{\frac{5}{2}}$ states mix very strongly in the 82-126 major shell. Intruder levels, which are those shell-model states which originate in the $N+1$ shell but because of their high angular momentum ($N+1=l$) are lowered into the N shell due to the l^2 term, have very pure wave functions and consist of almost entirely of a single j component until very large deformations. An example of these are the $i_{\frac{13}{2}}$ neutron states in the 82-126 major shell.

The Nilsson wave functions are often expressed in the spherical basis as opposed to the $|Nl\Lambda\Sigma\rangle$ basis. The coefficients for the spherical basis are the familar C_{jl}^{Ω} numbers given by

$$C_{jl}^{\Omega} = \sum_{\Lambda\Sigma} (l\Lambda\tfrac{1}{2}\Sigma|j\Omega)\, a_{l\Lambda\Omega} \tag{2.2.44}$$

such that

$$|\Psi_\Omega\rangle = \sum_j C_{jl}^{\Omega}|\phi_{j\Omega}\rangle = \sum_{l\Lambda} a_{l\Lambda\Omega}|\phi_{l\Lambda\Omega}\rangle \tag{2.2.45}$$

The C_{jl}^{Ω} coefficients have the property that

$$C_{jl}^{-\Omega} = (-1)^{j-\frac{1}{2}}(\pi)\, C_{jl}^{\Omega} \tag{2.2.46}$$

For axially symmetric nuclei, rotations can only occur about an axis perpendicular to the symmetry axis. Therefore, $\Omega = K$. The complete properly

symmetrized wave function is then

$$|IMK\Omega n_2 n_0\rangle = \sqrt{\frac{2I+1}{16\pi^2}}\Big[\mathcal{D}^{I*}_{MK}(\theta_j)\,|\Psi_\Omega\rangle + (-1)^{I+\frac{1}{2}-2K}(\pi)\,\mathcal{D}^{I*}_{M\,K}(\theta_j)\,|\Psi_{-\Omega}\rangle\Big]\chi_{|K-\Omega|n_2}(\eta)\,|n_0\rangle \tag{2.2.47}$$

The allowed values of the total angular momentum are

$$I = K, K+1, K+2, \ldots \tag{2.2.48}$$

The β- and γ-vibrations can still occur in the core. The β-vibrations have $n_0 = 1$ and $K = \Omega$. The γ-vibrations have a projection of their angular momentum onto the symmetry axis of 2 units, thus $K - \Omega = \pm 2$. In odd-A nuclei two γ-bands are always present, the lower band, with $K = \Omega - 2$ and energy

$$E = (-4\Omega - 2)\frac{\hbar^2}{2\mathcal{J}_0} + E_\gamma \tag{2.2.49}$$

and the higher band with $K = \Omega + 2$, and energy

$$E = (4\Omega + 2)\frac{\hbar^2}{2\mathcal{J}_0} + E_\gamma. \tag{2.2.50}$$

The most important part of $\hat{H}'$ are the terms giving rise to Coriolis coupling, or Rotational-Particle Coupling (RPC). The matrix elements are given by

$$\begin{aligned}\langle IMK'\Omega' n_2 n_0|\hat{H}_{RPC}|IMK\Omega n_2 n_0\rangle = \frac{\hbar^2}{2\mathcal{J}_0}\sum_j C^{\Omega'*}_{jl}C^{\Omega}_{jl}\Big[\Big[\delta_{K'K-1}\delta_{\Omega'\Omega} \\ + (-1)^{I+\frac{1}{2}}(-1)^{j-\frac{1}{2}}\,\delta_{K'-(K-1)}\delta_{\Omega'-(\Omega-1)}\Big] \\ \times\Big[(I+K)(I-K+1)(j+\Omega)(j-\Omega+1)\Big]^{\frac{1}{2}} \\ + \Big[\delta_{K'K+1}\delta_{\Omega'\Omega+1} + (-1)^{I+\frac{1}{2}}(-1)^{j-\frac{1}{2}}\,\delta_{K'-(K+1)}\delta_{\Omega'-(\Omega+1)}\Big] \\ \times\Big[(I-K)(I+K+1)(j-\Omega)(j+\Omega+1)\Big]^{\frac{1}{2}}\Big] \\ - \frac{\hbar^2}{2\mathcal{J}_0}2K\Omega\delta_{K'K}\delta_{\Omega'\Omega}\end{aligned} \tag{2.2.51}$$

and are calculated from the relations for the angular momentum ladder operators. The angular momentum part of the matrix element mixes states with different K and Ω except for $K = \Omega = \frac{1}{2}$ bands. In this case the Coriolis matrix elements are diagonal and are usually expressed in terms of the decoupling parameter,

$$\langle IM\frac{1}{2}\frac{1}{2}n_2n_0|\hat{H}_{RPC}|IM\frac{1}{2}\frac{1}{2}n_2n_0\rangle = -\frac{\hbar^2}{2\mathcal{J}_0}(-1)^{I+\frac{1}{2}}\left(I+\frac{1}{2}\right)a - \frac{\hbar^2}{4\mathcal{J}_0} \qquad (2.2.52)$$

where

$$a = \sum_j (-1)^{j-\frac{1}{2}}\left(j+\frac{1}{2}\right)|C_{j\bar{l}}^{\frac{1}{2}}|^2. \qquad (2.2.53)$$

This has been named the decoupling parameter since it corresponds to a partial decoupling of the particle motion from the rotator.

The sign of the decoupling parameter can be positive or negative, depending on which term dominates in the expression above. If a is negative, then states with spins $\frac{3}{2}$, $\frac{7}{2}$, $\frac{11}{2}$, etc., are lowered in energy while the other states are raised. For $a = -1$, the $\frac{1}{2}$ and $\frac{3}{2}$ states are degenerate in energy. If a is positive, then states with spins $\frac{1}{2}$, $\frac{5}{2}$, $\frac{9}{2}$ are lowered in energy, while the remaining states are raised. The effect of the decoupling parameter on the sequence of spins is shown in Figure 2.2.5, where the energy of the rotational states is shown as a function of a.

The non-diagonal Coriolis terms mix different K and Ω values, and since K is only a good quantum number for axially symmetric nuclei, the Coriolis coupling effectively introduces triaxiality into the system. The values of the matrix elements are maximum for intruder state mixing, and are somewhat lower for normal parity states. The matrix elements are larger for orbitals where both n_z and Λ change by one unit, but their sum remains constant, i.e. $\Delta n_z = -\Delta\Lambda$. Examples of this are the $\frac{5}{2}^-[503]$ and $\frac{3}{2}^-[512]$ orbitals. The intruder orbitals are also in this class. The other orbitals have matrix elements that are much smaller, usually by an order of magnitude or so.

It has been found that the actual Coriolis matrix elements are usually somewhat less than predicted by Eq. (2.2.51), and thus it is common that the matrix elements are multiplied by a factor, ρ, called the Coriolis attenuation factor, having

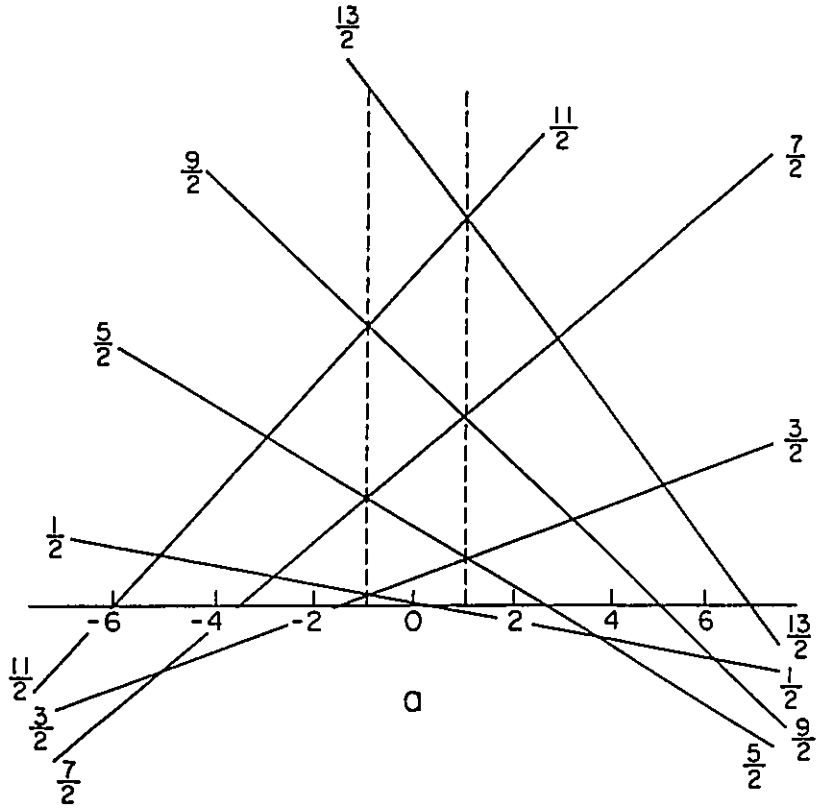

Figure 2.2.5: The dependence of rotational energy levels on the decoupling parameter a in a $K = \frac{1}{2}$ band in an odd-A nucleus. (From Casten, 1990)

a value of 0.5 to 0.8. The origin of the attenuation factor is not clear theoretically, although some possible explanations are that it is related to the proper treatment of the terms

$$\frac{\hbar^2}{2\mathcal{J}_o}\left(\hat{j}_1^2 + \hat{j}_2^2\right) \tag{2.2.54}$$

often called the recoil term, or the proper treatment of single-particle components in the vibrational wave functions.

2.2.3 Odd-Odd Nuclei

Odd-odd nuclei are the most difficult to understand both theoretically and experimentally. They have a high level density that results from the coupling of the odd proton and the odd neutron, and there is a rich interplay between the odd particles. However, to a first approximation, the properties of the nucleus can be considered to arise from the odd particles.

The Hamiltonian for the system can be obtained from a generalization of that for an odd-A nucleus, as given in Eq. (2.2.43). The single-particle angular momentum, $\vec{j}$, must now be replaced with $\vec{j_\pi}$ and $\vec{j_\nu}$, and also the single-particle Hamiltonian is now the sum over both particles. Therefore, the collective Hamiltonian becomes

$$\begin{aligned}\hat{H}_{o_{coll}} =& \frac{\hbar^2}{2\mathcal{J}_0}\left[\hat{I}^2 - \left(\hat{I}'_3 - \hat{j}'_{3(\pi)} - \hat{j}'_{3(\nu)}\right)^2\right] + \frac{\hbar^2}{16B_2\eta^2}\left[\left(\hat{I}'_3 - \hat{j}'_{3(\pi)} - \hat{j}'_{3(\nu)}\right)^2 - 1\right] \\ & - \frac{\hbar^2}{2B_2}\left[\frac{\partial^2}{\partial\xi^2} + \frac{1}{2}\frac{\partial^2}{\partial\eta^2}\right] + \frac{1}{2}C_o\xi^2 + C_2\eta^2\end{aligned} \tag{2.2.55}$$

and the single-particle part becomes

$$\hat{H}_{o_{sp}} = \sum_{\pi\nu}\frac{p'^2}{2m} + \frac{1}{2}m\omega^2 r'^2 + C\vec{l}'\cdot\vec{s}' + Dl'^2 - m\omega^2 r'^2\beta_0 Y_{20}. \tag{2.2.56}$$

The perturbations acting on the system are much more complex now, however, only the Coriolis, particle-particle, and residual interaction forces will be considered. Before these are investigated, the wave functions for $\hat{H}_{o_{coll}} + \hat{H}_{o_{sp}}$ will be explored. These are constructed as in the case for a single particle. Assuming that K is still a good quantum number (the nuclei are axially symmetric), K is now either

$$K_{\sigma=+} = \Omega_\pi + \Omega_\nu \tag{2.2.57}$$

or

$$K_{\sigma=-} = |\Omega_\pi - \Omega_\nu| \tag{2.2.58}$$

The single-particle wave function is the product of the wave functions of the proton and neutron, and the total wave function is

$$|IMK\Omega_\pi\Omega_\nu n_2 n_0\rangle = \sqrt{\frac{2I+1}{16\pi^2}}\Big[\mathcal{D}^{I*}_{MK}(\theta_j)\,|\Omega_\pi\rangle|\Omega_\nu\rangle - (-1)^{I-2K}(\pi_\pi)(\pi_\nu) \times \mathcal{D}^{I*}_{MK}(\theta_j)\,|-\Omega_\pi\rangle|-\Omega_\nu\rangle|\chi_{|K-\Omega_\pi-\Omega_\nu|n_2}\rangle|n_0\rangle \tag{2.2.59}$$

where

$$K-\Omega_\pi-\Omega_\nu = 0,\pm2,\pm4,\ldots \tag{2.2.60}$$

are the allowed values of K, and the total angular momentum is given by

$$I = |K|,|K|+1,|K|+2,\ldots \tag{2.2.61}$$

The K value is defined so that it is always positive. With the wave function written as in Eq. (2.2.59), Ω_π and Ω_ν can be positive or negative, with the greater one being positive. The intrinsic wave functions can be distinguished in the two cases by the label σ, where $\sigma = \pm$ for the cases

$$|K\sigma = +\rangle = |\rho_\pi\Omega_\pi\rangle|\rho_\nu\Omega_\nu\rangle \tag{2.2.62a}$$

$$|K\sigma = -\rangle = |\rho_\pi \pm \Omega_\pi\rangle|\rho_\nu \mp \Omega_\nu\rangle \tag{2.2.62b}$$

When $K = 0$, a special situation occurs such that the single-particle wave functions must be properly symmetrized. In this case the total wave function becomes

$$|IM\Omega - \Omega n_2 n_0\rangle = \sqrt{\frac{2I+1}{16\pi^2}}\mathcal{D}^{I*}_{M0}(\theta_j)\left[|\Omega_\pi\rangle|-\Omega_\nu\rangle - (-1)^I|-\Omega_\pi\rangle|\Omega_\nu\rangle|\chi_{0n_2}\rangle|n_0\rangle\right] \tag{2.2.63}$$

The energies of the states are given by

$$E_{IK\Omega_\pi\Omega_\nu n_2 n_0} = \mathcal{E}_{\Omega_\pi} + \mathcal{E}_{\Omega_\nu} + \frac{\hbar^2}{2\mathcal{J}_0}\Big[I(I+1) - (K-\Omega_\pi-\Omega_\nu)^2\Big] + \Big[\frac{1}{2}|K-\Omega_\pi-\Omega_\nu| + 1 + 2n_2\Big]E_\gamma + \left(n_0+\frac{1}{2}\right)E_\beta \tag{2.2.64}$$

The Coriolis interaction, written as in Eq. (2.2.51) except that $j_+ = j_\pi^+ + j_\nu^+$ and similarly for j_-, again mixes terms with $K' = K \pm 1$, and has matrix elements[16]

$$\begin{aligned}
\langle IMK\Omega_\pi\Omega_\nu|\hat{H}_{RPC}|IMK'\Omega'_\pi\Omega'_\nu\rangle = -\frac{\hbar^2}{\mathcal{J}_0}\Big[&\left((I+K')\,(I-K'+1)\right)^{\frac{1}{2}}\delta_{KK'-1}\\
&\Big[\delta_{\sigma+}\delta_{\sigma'+}(\langle\rho'_\pi\Omega'_\pi|j_\pi^+|\rho_\pi\Omega_\pi\rangle\delta_{\Omega'_\pi\Omega_\pi+1}\delta_{\rho_\nu\rho'_\nu}\delta_{\Omega_\nu\Omega_{\nu'}}\\
&+\langle\rho'_\nu\Omega'_\nu|j_\nu^+|\rho_\nu\Omega_\nu\rangle\delta_{\Omega'_\nu\Omega_\nu+1}\delta_{\rho_\pi\rho'_\pi}\delta_{\Omega_\pi\Omega_{\pi'}})\\
&\delta_{\sigma-}\delta_{\sigma'+}(\langle\rho'_\pi\Omega'_\pi|j_\pi^+|\rho_\pi-\Omega_\pi\rangle\delta_{\Omega_\pi\frac{1}{2}}\delta_{\Omega'_\pi\frac{1}{2}}\delta_{\rho_\nu\rho'_\nu}\delta_{\Omega_\nu\Omega_{\nu'}}\\
&+\langle\rho'_\nu\Omega'_\nu|j_\nu^+|\rho_\nu-\Omega_\nu\rangle\delta_{\Omega'_\nu\frac{1}{2}}\delta_{\Omega_\nu\frac{1}{2}}\delta_{\rho_\pi\rho'_\pi}\delta_{\Omega_\pi\Omega_{\pi'}})\\
&\delta_{\sigma-}\delta_{\sigma'-}(\langle\rho'_\pi\Omega'_\pi|j_\pi^+|\rho_\pi\Omega_\pi\rangle\delta_{\Omega'_\pi\Omega_\pi+1}\delta_{\rho_\nu\rho'_\nu}\delta_{\Omega_\nu\Omega_{\nu'}}\\
&+\langle\rho'_\nu\Omega'_\nu|j_\nu^+|\rho_\nu\Omega_\nu\rangle\delta_{\Omega'_\nu\Omega_\nu+1}\delta_{\rho_\pi\rho'_\pi}\delta_{\Omega_\pi\Omega_{\pi'}})\Big]\delta_{K\neq0}\\
&\delta_{K0}\frac{1}{2}\Big[\delta_{\sigma-}\delta_{\sigma'-}(\langle\rho'_\pi\Omega'_\pi|j_\pi^+|\rho_\pi\Omega\rangle\delta_{\Omega'_\pi\Omega+1}\delta_{\Omega'_\nu\Omega}\delta_{\rho_\nu\rho'_\nu}\\
&+(-1)^{I+1}\langle\rho'_\nu\Omega'_\nu|j_\nu^+|\rho_\nu\Omega\rangle\delta_{\Omega'_\nu\Omega+1}\delta_{\Omega'_\pi\Omega}\delta_{\rho_\pi\rho'_\pi})\\
&\delta_{\sigma-}\delta_{\sigma'+}(\langle\rho'_\nu\Omega'_\nu|j_\nu^+|\rho_\nu-\Omega\rangle\delta_{\Omega'_\pi\Omega}\delta_{\Omega'_\nu\frac{1}{2}}\delta_{\Omega\frac{1}{2}}\delta_{\rho_\pi\rho'_\pi}\\
&+(-1)^{I+1}\langle\rho'_\pi\Omega'_\pi|j_\pi^+|\rho_\pi-\Omega\rangle\delta_{\Omega'_\nu\Omega}\delta_{\Omega'_\pi\frac{1}{2}}\delta_{\Omega\frac{1}{2}}\delta_{\rho_\nu\rho'_\nu})\Big]\Big]\\
&+\frac{-\hbar^2}{\mathcal{J}_0}\Big[\left((I-K')\,(I+K'+1)\right)^{\frac{1}{2}}\delta_{KK'+1}\\
&\Big[\delta_{\sigma+}\delta_{\sigma'+}(\langle\rho_\pi\Omega_\pi|j_\pi^+|\rho'_\pi\Omega'_\pi\rangle\delta_{\Omega_\pi\Omega'_\pi+1}\delta_{\rho_\nu\rho'_\nu}\delta_{\Omega_\nu\Omega_{\nu'}}\\
&+\langle\rho_\nu\Omega_\nu|j_\nu^+|\rho_{\nu'}\Omega'_\nu\rangle\delta_{\Omega_\nu\Omega'_\nu+1}\delta_{\rho_\pi\rho'_\pi}\delta_{\Omega_\pi\Omega_{\pi'}})\\
&\delta_{\sigma'-}\delta_{\sigma+}(\langle\rho_\pi\Omega_\pi|j_\pi^+|\rho'_\pi-\Omega'_\pi\rangle\delta_{\Omega_\pi\frac{1}{2}}\delta_{\Omega'_\pi\frac{1}{2}}\delta_{\rho_\nu\rho'_\nu}\delta_{\Omega_\nu\Omega_{\nu'}}\\
&+\langle\rho_\nu\Omega_\nu|j_\nu^+|\rho'_\nu-\Omega'_\nu\rangle\delta_{\Omega'_\nu\frac{1}{2}}\delta_{\Omega_\nu\frac{1}{2}}\delta_{\rho_\pi\rho'_\pi}\delta_{\Omega_\pi\Omega_{\pi'}})\\
&\delta_{\sigma-}\delta_{\sigma'-}(\langle\rho_\pi\Omega_\pi|j_\pi^+|\rho'_\pi\Omega'_\pi\rangle\delta_{\Omega_\pi\Omega'_\pi+1}\delta_{\rho_\nu\rho'_\nu}\delta_{\Omega_\nu\Omega_{\nu'}}\\
&+\langle\rho_\nu\Omega_\nu|j_\nu^+|\rho'_\nu\Omega'_\nu\rangle\delta_{\Omega_\nu\Omega'_\nu+1}\delta_{\rho_\pi\rho'_\pi}\delta_{\Omega_\pi\Omega_{\pi'}})\Big]\delta_{K'\neq0}\\
&\delta_{K'0}\frac{1}{2}\Big[\delta_{\sigma-}\delta_{\sigma'-}(\langle\rho_\pi\Omega_\pi|j_\pi^+|\rho'_\pi\Omega'\rangle\delta_{\Omega_\pi\Omega'+1}\delta_{\Omega_\nu\Omega'}\delta_{\rho_\nu\rho'_\nu}\\
&+(-1)^{I+1}\langle\rho_\nu\Omega_\nu|j_\nu^+|\rho'_\nu\Omega'\rangle\delta_{\Omega_\nu\Omega'+1}\delta_{\Omega_\pi\Omega'}\delta_{\rho_\pi\rho'_\pi})\\
&\delta_{\sigma+}\delta_{\sigma'-}(\langle\rho_\nu\Omega_\nu|j_\nu^+|\rho'_\nu-\Omega'\rangle\delta_{\Omega_\pi\Omega'}\delta_{\Omega_\nu\frac{1}{2}}\delta_{\Omega'\frac{1}{2}}\delta_{\rho_\pi\rho'_\pi}\\
&+(-1)^{I+1}\langle\rho_\pi\Omega_\pi|j_\pi^+|\rho'_\pi-\Omega'\rangle\delta_{\Omega_\nu\Omega'}\delta_{\Omega_\pi\frac{1}{2}}\delta_{\Omega'\frac{1}{2}}\delta_{\rho_\nu\rho'_\nu})\Big]\Big]
\end{aligned} \tag{2.2.65}$$

where $\sigma\pm$ stands for the two cases where $K = |\Omega_\pi \pm \Omega_\nu|$. The single-particle matrix element $\langle \rho'\Omega'|j^+|\rho\Omega\rangle$ is non-vanishing only when $\Omega' = \Omega - 1$ and $\rho' = \rho$ where ρ stands for other quantum numbers needed to label the state.

There is another coupling that arises from the replacement of $\vec{I} \rightarrow \vec{I} - \vec{j_\pi} - \vec{j_\nu}$, and is of the form

$$\hat{H}_{ppc} = \frac{\hbar^2}{2\mathcal{J}_0}\left(j_\pi^+ j_\nu^- + j_\pi^- j_\nu^+\right) \tag{2.2.66}$$

and is called particle-particle coupling. This term couples $\Delta K = 0$ bands, where $\Delta\Omega_\pi = \pm 1$ and $\Delta\Omega_\nu = \mp 1$. This term gives rise to matrix elements given by[16]

$$\begin{aligned}
\langle IMK\sigma|\hat{H}_{ppc}|IMK'\sigma'\rangle = \delta_{KK'}\frac{\hbar^2}{2\mathcal{J}_0}\Big[&\delta_{\sigma+}\delta_{\sigma'+}\Big(\langle\rho_\pi\Omega_\pi|j_\pi^+|\rho'_\pi\Omega'_\pi\rangle \\
&\langle\rho'_\nu\Omega'_\nu|j_\nu^+|\rho_\nu\Omega_\nu\rangle\delta_{\Omega_\pi\Omega'_\pi+1}\delta_{\Omega'_\nu\Omega_\nu+1} \\
&+ \langle\rho'_\pi\Omega'_\pi|j_\pi^+|\rho_\pi\Omega_\pi\rangle\langle\rho_\nu\Omega_\nu|j_\nu^+|\rho'_\nu\Omega'_\nu\rangle\delta_{\Omega'_\pi\Omega_\pi+1}\delta_{\Omega_\nu\Omega'_\nu+1}\Big) \\
&+ \delta_{\sigma+}\delta_{\sigma'-}\Big(\langle\rho'_\pi\Omega'_\pi|j_\pi^+|\rho_\pi\Omega_\pi\rangle\langle\rho_\nu\Omega_\nu|j_\nu^+|\rho'_\nu - \Omega'_\nu\rangle\delta_{\Omega'_\pi\Omega_\pi+1}\delta_{\Omega_\nu\frac{1}{2}}\delta_{\Omega'_\nu\frac{1}{2}} \\
&+ \langle\rho_\pi\Omega_\pi|j_\pi^+|\rho'_\pi - \Omega'_\pi\rangle\langle\rho'_\nu\Omega'_\nu|j_\nu^+|\rho_\nu\Omega_\nu\rangle\delta_{\Omega_\pi\frac{1}{2}}\delta_{\Omega'_\pi\frac{1}{2}}\delta_{\Omega'_\nu\Omega_\nu+1}\Big) \\
&+ \delta_{\sigma-}\delta_{\sigma'+}\Big(\langle\rho_\pi\Omega_\pi|j_\pi^+|\rho'_\pi\Omega'_\pi\rangle\langle\rho_\nu\Omega_\nu|j_\nu^+|\rho'_\nu - \Omega'_\nu\rangle\delta_{\Omega_\pi\Omega'_\pi+1}\delta_{\Omega_\nu\frac{1}{2}}\delta_{\Omega'_\nu\frac{1}{2}} \\
&+ \langle\rho_\pi\Omega_\pi|j_\pi^+|\rho'_\pi - \Omega'_\pi\rangle\langle\rho_\nu\Omega_\nu|j_\nu^+|\rho'_\nu\Omega'_\nu\rangle\delta_{\Omega_\pi\frac{1}{2}}\delta_{\Omega'_\pi\frac{1}{2}}\delta_{\Omega_\nu\Omega'_\nu+1}\Big) \\
&+ \delta_{K0}\delta_{\sigma-}\delta_{\sigma'-}\Big(-\langle\rho_\pi\Omega_\pi|j_\pi^+|\rho'_\pi\Omega'_\pi\rangle\langle\rho_\nu\Omega_\nu|j_\nu^+|\rho'_\nu - \Omega'_\nu\rangle\delta_{\Omega_\pi\Omega'_\pi+1}\delta_{\Omega_\nu\Omega_\nu+1} \\
&- \langle\rho'_\pi\Omega'_\pi|j_\pi^+|\rho_\pi\Omega_\pi\rangle\langle\rho'_\nu\Omega'_\nu|j_\nu^+|\rho_\nu\Omega_\nu\rangle\delta_{\Omega'_\pi\Omega_\pi+1}\delta_{\Omega'_\nu\Omega_\nu+1}\Big) \\
&+ (-1)^{I+1}\langle\rho_\pi\Omega_\pi|j_\pi^+|\rho'_\pi - \Omega'_\pi\rangle\langle\rho_\nu\Omega_\nu|j_\nu^+|\rho'_\nu - \Omega'_\nu\rangle\delta_{\Omega_\pi\frac{1}{2}}\delta_{\Omega_\nu\frac{1}{2}}\delta_{\Omega'_\pi\frac{1}{2}}\delta_{\Omega'_\nu\frac{1}{2}}\Big]
\end{aligned} \tag{2.2.67}$$

In axially symmetric nuclei, the K values are restricted to $K = |\Omega_\pi \pm \Omega_\nu|$. The band heads for the two rotational bands based on the two K values are separated in energy by the Gallagher-Moszkowski (GM) splitting[17], with the K values that arises when the particle spins are coupled parallel being lower in energy.

The GM splitting can be reproduced[18–19] by assuming a zero-range spin dependentresidual interaction between the odd proton and the odd neutron. The

residual interaction is usually taken as

$$V_{\pi\nu} = -4\pi g\delta\left(\vec{r}_\pi - \vec{r}_\nu\right)\left[(1-\alpha) + \alpha\left(\vec{\sigma}_\pi \cdot \vec{\sigma}_\nu\right)\right] \tag{2.2.68}$$

where g is the interaction parameter and α is the fractional strength of the spin-spin interaction. The interaction energy is

$$\Delta E_{\pi\nu} = \langle \chi_{\Omega_\pi}\chi_{\Omega_\nu}|V_{\pi\nu}|\chi_{\Omega_\pi}\chi_{\Omega_\nu}\rangle \tag{2.2.69a}$$

$$= (1-\alpha)\,W A_0(K) \pm \alpha W A_\sigma(K) + (-1)^I B\delta_{K0} \tag{2.2.69b}$$

where the parameter $W = (2\omega_0^3(\delta_2)/\pi)^{\frac{1}{2}}$ and A_0, A_σ are the GM matrix elements corresponding to the spin-independent and spin-dependent parts of $V_{\pi\nu}$. The GM splitting is the difference between the two unperturbed band head energies, and is

$$E_{GM} = \pm 2\alpha W|A_\sigma|. \tag{2.2.70}$$

The parameter $(-1)^I B$ in Eq. (2.2.69) is the odd-even shift coefficient, otherwise known as the Newby term[20]. The Newby matrix element is defined by

$$E_N = -(\pi)\langle \chi_{\Omega_\pi}\chi_{-\Omega_\nu}|V_{\pi\nu}|\chi_{-\Omega_\pi}\chi_{\Omega_\nu}\rangle \tag{2.2.71}$$

and has a value

$$E_N = -(\pi)\,\alpha W\left(A_0 - A_\sigma\right). \tag{2.2.72}$$

Sood and Ray[21] have suggested that the Newby matrix element incorporate a factor related to the total intrinsic spin, Σ, by

$$E_N = (-1)^\Sigma(\pi)\,\alpha W\left(|A_0| - |A_\sigma|\right) \tag{2.2.73}$$

and have found that this correctly reproduces the sign of the Newby shifts when the residual interaction is that of Eq. (2.2.68).

2.2.4 BCS Pairing Theory

In this section, the pairing formalism first used by Bardeen, Cooper, and Schrieffer (BCS pairing) in their study of superconductivity is briefly introduced. It was then applied to nuclei by Bohr, Mottleson, and Pines and also by Belyaev.

There are several experimental facts that naturally lead to the idea that there must be some sort of pairing energy occurring in nuclei.

1. The ground states of all even-even nuclei have spin 0.
2. The total binding energy of an odd-even nucleus is less than the mean of the binding energies of the neighbouring even-even nuclei, i.e.

$$M_{A\ odd} > \frac{M_{A-1} + M_{A+1}}{2}. \tag{2.2.74}$$

3. In even-even nuclei there occurs an "energy gap", such that below the energy gap the nuclear level density is low, but above the energy gap the level density is somewhat higher.

All of these facts lead to the idea that nucleons like to "pair-up" to angular momentum zero and lower their energy. In fact, as long as a potential is a short-ranged, two-body, attractive potential, the coupling of two nucleons in the same shell to total angular momentum zero will lower their energy, as they will have maximum overlap of their wave functions. For two nucleons to couple to angular momentum zero, their values of the projection quantum number, m_j, must be equal and opposite. Therefore if one nucleon has the wave function $|jm_j\rangle$ then its paired nucleon will have the wave function $|j - m_j\rangle$. In this way, one nucleon can be viewed as being in a time-reversed orbit with respect to the other.

The original ansatz for the BCS formalism was to try to represent the wave function for even-even nuclei as

$$|BCS\rangle = \prod_{\Omega} \left(U_\Omega + V_\Omega a^\dagger_\Omega a^\dagger_{\bar{\Omega}}\right) |0\rangle \tag{2.2.75}$$

where $a_\Omega^\dagger$ creates a fermion, and $a_{\bar{\Omega}}^\dagger$ creates a fermion in a time reversed orbit. The BCS wave function is actually a variational wave function, and U_Ω and V_Ω are variational parameters. The quantities V_Ω^2 and U_Ω^2 represent the probability that a pair state, $[\Omega, \bar{\Omega}]$, is or is not occupied, respectively. Thus, they are subject to the normalization that

$$U_\Omega^2 + V_\Omega^2 = 1 \tag{2.2.76}$$

and are given by

$$U_\Omega^2 = \frac{1}{2}\left(1 + \frac{E_\Omega - \lambda}{\sqrt{(E_\Omega - \lambda)^2 + \Delta^2}}\right) \tag{2.2.77}$$

$$V_\Omega^2 = \frac{1}{2}\left(1 - \frac{E_\Omega - \lambda}{\sqrt{(E_\Omega - \lambda)^2 + \Delta^2}}\right) \tag{2.2.78}$$

The parameter Δ is called the energy-gap parameter, since the energy gap observed in even-even nuclei is on the order of 2Δ. The value of V^2 versus the energy relative to the Fermi surface is shown in Figure 2.2.6.

It is far easier to work in a new basis, one in which $|BCS\rangle$ will act like a vacuum state. To transform to the new basis, a Bogolyubov-Valatin transformation is used, defined as

$$\alpha_\Omega = U_\Omega a_\Omega - V_\Omega a_{\bar{\Omega}}^\dagger \tag{2.2.79a}$$

$$\alpha_{\bar{\Omega}}^\dagger = U_\Omega a_{\bar{\Omega}}^\dagger - V_\Omega a_\Omega \tag{2.2.79b}$$

where α and $\alpha^\dagger$ are the quasiparticle annihilation and creation operators, respectively. The transformation is a unitary one, and so the anticommutation relations between the new quasiparticle operators are the same as between the fermion operators.

The effect of pairing is to "smear" out the Fermi surface. If there were no pairing, then the Fermi surface would be sharp, and below it there would be particles, and above it, holes. However, with a pairing interaction, the distinction between particles and holes is less clear, since the quasiparticles, defined above, are a

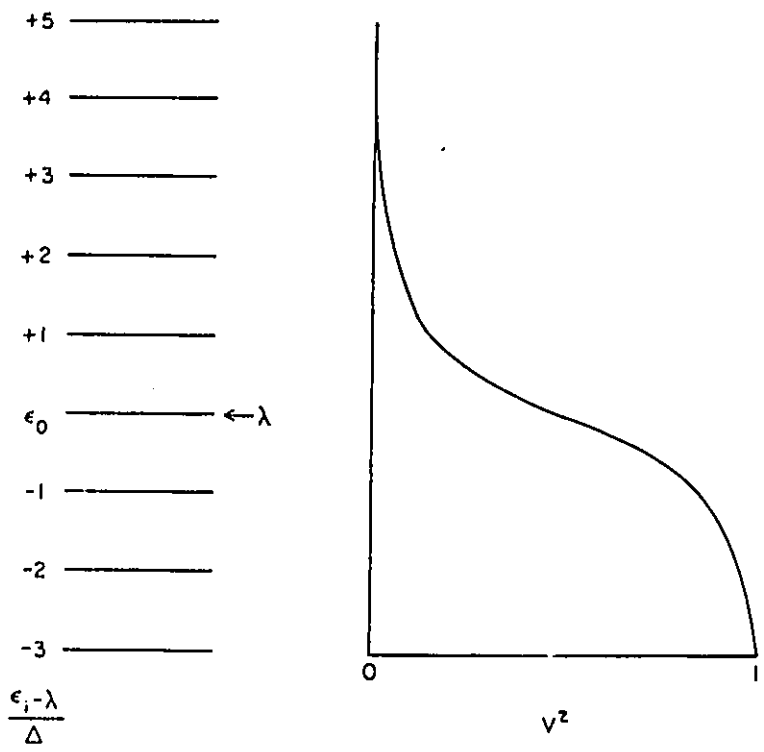

Figure 2.2.6: The occupation probably V^2 for orbitals where the energies are given in units of Δ, the pairing gap parameter, relative to the Fermi surface. In this figure, λ is the Fermi energy and ϵ_i is the single-particle energy. (From Casten, 1990)

mixture of both. The effect on all transition matrix elements is a slight modification with the introduction of factors U or V where appropriate. For instance, the Coriolis matrix elements introduced in section 2.3 now get multiplied by the factor $(U_1U_2 + V_1V_2)$, where the subscript 1 and 2 stand for the two states that are coupled by the matrix element.

2.3. Interacting Boson Model

Since the introduction of the Interacting Boson Model (IBM) by Arima and Iachello[7] in 1975, a great deal of work has been done on this model. Indeed, some researchers maintain that it is responsible for a rejuvenation of interest into

nuclear structure. Initially, the main advantages of the IBM was its group theoretical approach that allowed for ease of computation when various dynamical symmetries were realized. However, when serious tests of the model were made, the need for refinements and extensions became obvious. The IBM model was then extended to cover not only even-even nuclei, but also odd-A nuclei. Recently[22–23], an attempt hasbeen made to describe odd-odd nuclei with the Interacting Boson Fermion-Fermion Model (IBFFM). However, while these extensions have met with some success, the number of adjustable parameters has greatly increased, and the ease of computation has all but disappeared. Regardless of this, however, the IBM remains a beautiful model, being able to describe many aspects of nuclear structure quite naturally, and the idea of exploiting symmetries is an enticing one indeed. In this section, the basic IBM is explored, as are the extensions such as the IBFM, IBFFM, and Supersymmetry schemes.

2.3.1 The IBM-1

The original version of the IBM introduced by Arima and Iachello[7] assumed that low-lying collective states in even-even nuclei could be described by an interacting system of s and d bosons carrying angular momentum 0 and 2 respectively. This assumption was based on features of generalized seniority calculations in the shell model and the empirical structure of nuclei near the closed shells where 0^+ and 2^+ states lie much lower in energy than higher angular momentum states. The boson states can be viewed as correlated pairs of like nucleons that are valence particles. It is also assumed that there are no particle excitations out of the closed shell, and thus the number of bosons is a definite number for each nucleus, and is

$$\mathcal{N} = N_\pi + N_\nu = n_s + n_d \tag{2.3.1}$$

The number of bosons is determined by counting the number of valence particles, either particles or holes, to the nearest closed shell and dividing by two. The reason that the valence nucleons are counted to the nearest closed shell is the following. Consider a shell which consists of only 1 orbit, with angular momentum j. There

can be a maximum of $2j+1$ particles in the shell. The maximum angular momentum allowed in the shell is made by maximizing the alignment of all the particles, and is $J_{max} = nj - n(n-1)/2$ where n is the number of particles. The maximum angular momentum occurs when $n = j + \frac{1}{2}$. This state must, by definition, have seniority $\nu = n = j + \frac{1}{2}$, and this is the maximum seniority. (Seniority is the number of particles not coupled to angular momentum zero.) If the number of bosons were not counted to the nearest closed shell, then states would exist that would, in the fermionic space, have a seniority $\nu > j + \frac{1}{2}$ when $\mathcal{N} > (j + \frac{1}{2})/2$. This would, however, violate the Pauli principle.

The s and d bosons are created by the operators

$$\hat{b}^\dagger_{\lambda\mu} = \begin{cases} \hat{d}^\dagger_\mu & \lambda = 2 \\ \\ \hat{s}^\dagger & \lambda = 0 \end{cases}$$

The number of d bosons is defined by the operator

$$\begin{aligned} \hat{N} &= \sum_\mu \hat{d}^\dagger_\mu \hat{d}_\mu \\ &= \sqrt{5}\left[\hat{d}^\dagger \times \hat{d}\right]^{[0]} \end{aligned} \tag{2.3.2}$$

with the total number of bosons defined by

$$\hat{\mathcal{N}} = \hat{s}^\dagger \hat{s} + \hat{N} \tag{2.3.3}$$

The conventional form of the general Hamiltonian is

$$\begin{aligned} \hat{H} =& \mathcal{E}_s \hat{s}^\dagger \hat{s} + \mathcal{E}_d \hat{N} + \frac{1}{2} \sum_{L=0,2,4} \sqrt{2L+1}\; C_L \left[\left[\hat{d}^\dagger \times \hat{d}^\dagger\right]^{[L]} \times \left[\hat{d}^* \times \hat{d}^*\right]^{[L]}\right]^{[0]} \\ &+ \frac{1}{\sqrt{2}} \tilde{v}_2 \left(\left[\left[\hat{d}^\dagger \times \hat{d}^\dagger\right]^{[2]} \times \hat{d}^* \hat{s}\right]^{[0]} + h.c.\right) \\ &+ \frac{1}{2} \tilde{v}_0 \left(\left[\hat{d}^\dagger \times \hat{d}^\dagger\right]^{[0]} \hat{s}\hat{s} + h.c.\right) + u_2 \left[\hat{d}^\dagger \hat{s}^\dagger \times \hat{d}^* \hat{s}\right]^{[0]} + \frac{1}{2} u_0 \hat{s}^\dagger \hat{s}^\dagger \hat{s}\hat{s} \end{aligned} \tag{2.3.4}$$

The first two terms simply count the number of s and d bosons, assigning them energies $\mathcal{E}_s$ and $\mathcal{E}_d$ respectively. The next term describes interactions between d bosons, the next three terms interactions between s and d bosons, and the last term interactions between s bosons.

The s boson has only 1 magnetic substate, and the d boson has 5 substates, therefore the sd boson system can be viewed as spanning a 6-dimensional space, and the system can be described as having a group structure of $U(6)$.

The operator for the total boson number, $\hat{\mathcal{N}}$, commutes with the Hamiltonian and is a Casimir operator of $U(6)$. The collective states are labelled by $\mathcal{N}$ (total boson number), L (angular momentum), M (projection of L) and other quantum numbers which depend upon the dynamical symmetry. The operator $\hat{\Sigma}$ is defined by

$$\hat{\Sigma}^2 = \hat{T}^2 + \hat{N}^2\left(\hat{s}^\dagger\hat{s}+1\right) + \left(\hat{N}+5\right)\hat{s}^\dagger\hat{s} - \hat{P}^\dagger\hat{s}\hat{s} - \hat{s}^\dagger\hat{s}^\dagger\hat{P} \tag{2.3.5}$$

with

$$\hat{P}^\dagger = \sqrt{5}\left[\hat{d}^\dagger \times \hat{d}^\dagger\right]^{[0]} \tag{2.3.6}$$

and

$$\hat{T}^2 = \hat{N}\left(\hat{N}+3\right) - \hat{P}^\dagger\hat{P} \tag{2.3.7}$$

The operator $\hat{\Sigma}^2$ is called the generalized seniority operator in the 6-dimensional space and is a Casimir operator of the $SO(6)$ group. The Hamiltonian can now be expressed as

$$\begin{aligned}\hat{H} = {} & \mathcal{E}_n\hat{\mathcal{N}} + \mathcal{E}_\nu\hat{N} + v_n\hat{\mathcal{N}}\hat{N} + v_\nu\hat{N}^2 \\ & + v_\Sigma\hat{\Sigma}^2 + v_\tau\hat{T}^2 + v_L\hat{L}^2 + v_q\hat{Q}^2\end{aligned} \tag{2.3.8}$$

where

$$\hat{Q}^2 = \sqrt{5}\left[\hat{Q}\times\hat{Q}\right]^{[0]} \tag{2.3.9}$$

and

$$\hat{Q}_\mu = \hat{d}^\dagger_\mu\hat{s} + \hat{s}^\dagger\hat{d}^*_\mu \pm \frac{\sqrt{7}}{2}\left[\hat{d}^\dagger\times\hat{d}^*\right]^{[2]}_\mu \tag{2.3.10}$$

is the quadrupole operator.

The group $U(6)$ has various subgroups; however, only the subgroups that contain $SO(3)$ are physically realizable. There are three group chains that contain $SO(3)$

$$U(6) \supset U(5) \supset SO(5) \supset SO(3) \quad U(5)\,\text{chain} \tag{2.3.11a}$$

$$U(6) \supset SU(3) \supset SO(3) \quad SU(3)\,\text{chain} \tag{2.3.11b}$$

$$U(6) \supset SO(6) \supset SO(5) \supset SO(3) \quad SO(6)\,\text{chain} \tag{2.3.11c}$$

The $U(5)$ chain is realized when the assumption is made that some nuclei can be described with $v_{\Sigma} = v_q = 0$, i.e. the interaction between s, d bosons can be neglected. The Hamiltonian then becomes

$$H = \mathcal{E}_n \hat{\mathcal{N}} + \mathcal{E}_v \hat{N} + v_n \hat{\mathcal{N}}^2 + v_{nv} \hat{\mathcal{N}} \hat{N} + v_v \hat{N}^2 + v_\tau \hat{T}^2 + v_L \hat{L}^2 \tag{2.3.12}$$

The Casimir operator of $U(5)$ is $\hat{N}$, the d-boson number operator, and it has eigenvalue n_d. The $SO(5)$ group has $\hat{T}^2$ as a Casimir operator, which acts as the seniority operator in the d-boson space, and has eigenvalue $\tau(\tau+3)$ where τ is the number of d bosons not coupled pairwise to angular momentum zero. The energy eigenvalues can be written immediately as

$$E_{nv\tau L} = \mathcal{E}_n N + v_n N^2 + (\mathcal{E}_v + v_{nv})\, n_d + v_v n_d^2 + v_\tau \tau\,(\tau+3) + v_L L\,(L+1) \tag{2.3.13}$$

The Hamiltonian is diagonal in the basis

$$|\mathcal{N} - n_d\rangle |n_d \tau n_\Delta L M\rangle \tag{2.3.14}$$

where $\mathcal{N} - n_d$ is the number of s bosons, and n_Δ is the number of d-boson triplets coupled to angular momentum zero. This last quantum number arises in the reduction to $SO(5)$, as it is needed to label the different irreducible representations. The separation of the s-boson space from the d-boson space is possible because there are no terms in the Hamiltonian that mix the s and d bosons, or mix states with different d-boson numbers.

The spectrum generated by Eq. (2.3.13) above resembles that of a vibrator, and thus the $U(5)$ limit is often called the vibrational limit of the IBM. This is

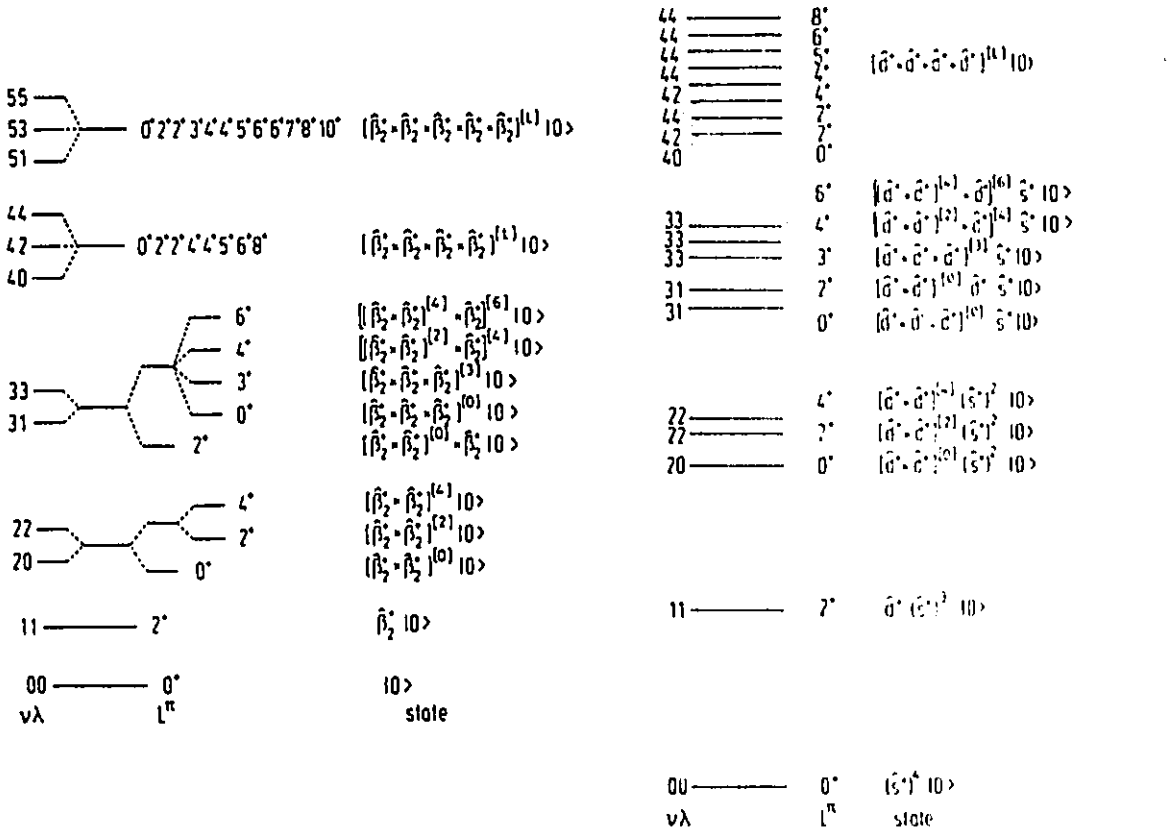

Figure 2.3.1: Comparison of a purely harmonic spectrum obtained from the RVM (left) to that of the $U(5)$ limit of the IBM for a total of 4 bosons (right). (From Eisenberg and Greiner, 1987)

shown in Figure 2.3.1, where the vibrational levels from the RVM are shown along with a spectrum from the $U(5)$ limit. The spectrum obtained from the RVM has many degenerate levels, and is, in principle, infinite, whereas in the IBM this degeneracy has been removed due to the boson-boson interaction, and the generated spectrum is finite due to the constraint on the number of bosons. The nuclear potential corresponding to the $U(5)$ limit has spherical symmetry with a minimum at a deformation $\beta = 0$.

The $SO(6)$ limit is realized when the Hamiltonian is assumed to be

$$H = \mathcal{E}_n\hat{\mathcal{N}} + v_n\hat{\mathcal{N}}^2 + v_\Sigma\hat{\Sigma}^2 + v_\tau\hat{T}^2 + v_L\hat{L}^2 \tag{2.3.15}$$

where all terms proportional to $\hat{N}$ have been neglected, i.e. $\mathcal{E}_\nu = v_\nu = v_{n\nu} = 0$. The Casimir operator of $SO(6)$ is $\hat{\Sigma}^2$, which is the generalized seniority operator in the *sd* boson space, and has eigenvalues of $\Sigma(\Sigma+4)$. The energy eigenvalues are

$$E_{n\Sigma\tau L} = \mathcal{E}_n\mathcal{N} + v_n\mathcal{N}^2 + v_\Sigma\Sigma(\Sigma+4) + v_\tau\tau(\tau+3) + v_L L(L+1) \tag{2.3.16}$$

The Hamiltonian is diagonal in the $|\mathcal{N}\Sigma\tau n_\Delta LM\rangle$ basis. The similarity between the $U(5)$ and the $SO(6)$ quantum numbers used to describe the states should be noted, which arises from the similarity in the chain decomposition. The operator $\hat{\Sigma}^2$ does not commute with $\hat{N}$, and therefore the numbers of s and d bosons can be changed. There are limits on the values of Σ and τ, with $\Sigma = n, n-2, \ldots 0$ or 1, and $\tau = 0, 1, \ldots, \Sigma$. The spectrum generated in this limit is very similar to that of a γ-unstable rotor, and thus the $SO(6)$ limit is often called the γ-unstable limit of the IBM. A typical spectrum generated by this limit is shown in Figure 2.3.2. The nuclear potential corresponding to the $SO(6)$ limit is that of an axially symmetric, deformed γ-soft rotor.

When the assumption is made that $\mathcal{E}_\nu = v_{n\nu} = v_\nu = v_\Sigma = v_\tau = 0$, then the Hamiltonian becomes

$$\hat{H} = \mathcal{E}_n\hat{\mathcal{N}} + v_n\hat{\mathcal{N}}^2 + v_L\hat{L}^2 + v_q\hat{Q}^2 \tag{2.3.17}$$

With this, the boson-boson interaction becomes dominant and the $SU(3)$ limit is realized. The Casimir operator for $SU(3)$ is

$$\hat{C}^2 = 2\hat{Q}^2 + \frac{3}{4}\hat{L}^2 \tag{2.3.18}$$

and has eigenvalues $\lambda^2 + \lambda\mu + \mu^2 + 3(\lambda+\mu)$. The energy levels are given by

$$E_{n\lambda\mu L} = \epsilon_n N + v_n N^2 + \frac{1}{2}v_q\left(\lambda^2 + \mu^2 + \lambda\mu + 3(\lambda+\mu)\right) + \left(v_L - \frac{3}{8}v_q\right)L(L+1) \tag{2.3.19}$$

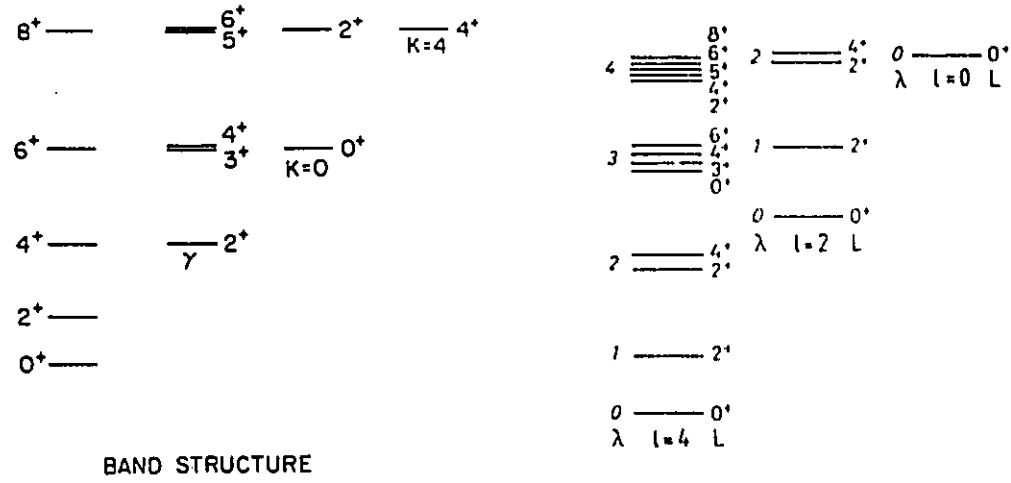

Figure 2.3.2: Comparison of a spectrum obtained from the Wilets-Jean model (left) for γ-unstable nuclei to that of the $SO(6)$ limit of the IBM for a total of 4 bosons (right). (From Casten, 1990, and Eisenberg and Greiner, 1987)

The quantum numbers (λ, μ) label the irreducible representations of $SU(3)$ and have values constrained by

$$\lambda = 2n - 6l - 4k \geq 0 \qquad (2.3.20a)$$

$$\mu = 2k \qquad \geq 0 \qquad (2.3.20b)$$

for $l, k = 0, 1, \ldots$.

When decomposing the chain $U(6) \supset SU(3) \supset SO(3)$, there are states that are degenerate for the same quantum numbers n, λ, μ, L, M, and these need to be distinguished with another quantum number, K'. The quantum number K' is not identical to the projection of the angular momentum on the intrinsic axis. In general, the state labelled by K' has several K values contained within it. However,

the amplitudes of these states with $K \neq K'$ are very small, and usually one uses $K' = K$. The values of allowed K are

$$K = 0, 2, 4, \ldots \min(\lambda, \mu) \tag{2.3.21}$$

The angular momentum L can take the values of

$$L = \begin{cases} 0, 2, 4, \ldots, \max(\lambda, \mu) & \text{for K} = 0 \\ \\ K, K+1, K+2, \ldots, K + \max(\lambda, \mu) & \text{for K} \neq 0 \end{cases}$$

The maximum projection of the angular momentum onto the laboratory $\hat{z}$-axis is $M_{max} = \lambda + \mu$.

On a more physical basis, λ is equivalent to $n_z - n_x$, where n_z, n_x are oscillator quanta in the $\hat{z}$ and $\hat{x}$-axis directions respectively. The quantum number μ is equivalent to $n_x - n_y$. For deformed prolate nuclei the orbitals with the greatest value of n_z lie lower in energy than other orbitals for the same principle quantum number N. Therefore, the ground states in the $SU(3)$ description have $(\lambda, \mu) = (2n, 0)$. The next highest representation in energy is $(\lambda, \mu) = (2n-4, 2)$, then $(2n-8, 4)$ and $(2n-6, 0)$ etc. These are labelled in Figure 2.3.3, which shows a spectrum in the $SU(3)$ limit for $\mathcal{N} = 8$. The rotational spectrum displays a termination of the bands, which is not a characteristic of the RVM, where a rotational band has no termination.

For all the above symmetry limits, $U(5), SO(6)$, and $SU(3)$, in performing calculations the basis states used are often those of $U(5)$, since these are usually the easiest to work with. The $U(5)$ limit has the structure that the number of d bosons, n_d, is constant, whereas the $SO(6)$ and $SU(3)$ limits have the structure that $\Delta n_d = 0, \pm 2$, and $\Delta n_d = 0, \pm 1, \pm 2$ respectively. Thus the $SU(3)$ wave function can have more terms in it compared to the $SO(6)$ wave function with respect to the $U(5)$ basis. In fact, many properties of the $SO(6)$ and $U(5)$ limits are identical since both chains contain the $SO(5)$ and $SO(3)$ subgroups. Properties that have to do with the seniority structure of the wave function are thus identical in both limits.

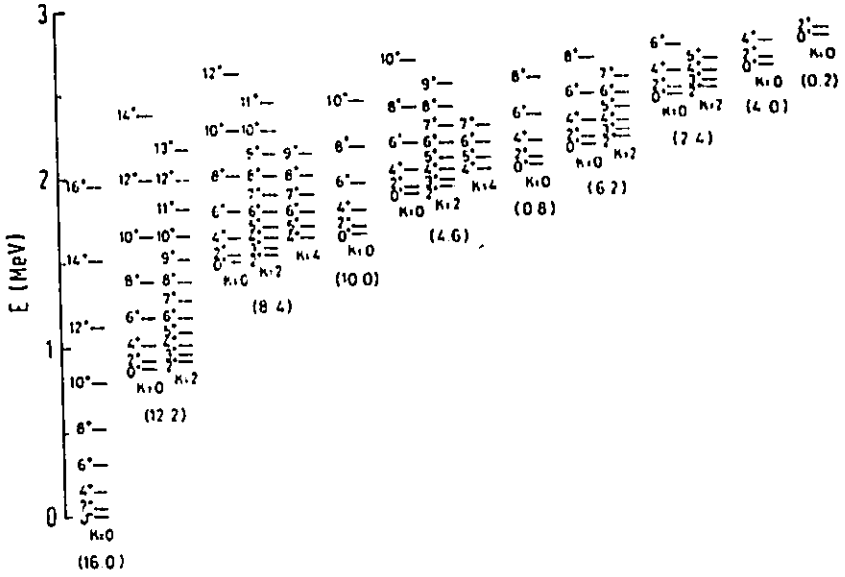

Figure 2.3.3: Typical energy spectrum of the $SU(3)$ limit of the IBM for a total of 8 bosons. The quantum numbers (λ, μ) are indicated under each band. (From Eisenberg and Greiner, 1987)

When performing realistic calculations on nuclei, there is often a departure from the strict limits or a transition from one symmetry limit to another. The three symmetry limits are often viewed as the apexes of a triangle as in Figure 2.3.4. The space enclosed by the triangle represents the most general solutions of the IBM-1 Hamiltonian. A transition between two of the symmetry limits, without invoking the characteristics of a third, would move along one of the sides. In this case, the transition would depend on a single parameter. Nuclei in the A$\simeq$190 region have been classified as having $SO(6)$ symmetry. Indeed, the first nucleus identified as processing $SO(6)$ symmetry was ^{196}Pt. There was a one-to-one correspondence between predicted and observed levels. As stated previously, the $SO(6)$ limit corresponds to a γ-unstable potential, and has the typical $2^+, (3^+, 4^+), (5^+, 6^+) \ldots$ γ-band staggering

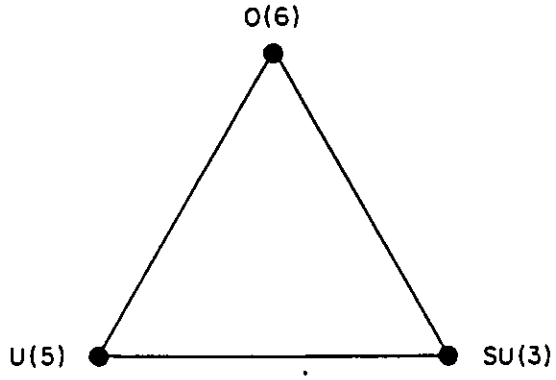

Figure 2.3.4: Symmetry triangle of the IBM. If a transition occurs from one symmetry limit to the next without invoking a third, then the mixed symmetry can be expressed in terms of a single parameter. (From Casten, 1990)

characteristic of γ-soft rotors. There appears to be an $SU(3) \rightarrow SO(6)$ transition[24] between ^{186}Os (predominately$SU(3)$) and ^{192}Os (predominately $SO(6)$).

2.3.2 Interacting Boson-Fermion Model

The Interacting Boson-Fermion Model (IBFM) was a logical extension to the IBM that attempts to describe odd-A nuclei. It was introduced by Arima and Iachello[25] in 1976 and developed extensively by Iachello and Scholten[26] and others[27]. The basic idea is the same as that for the IBM, except that a fermion is coupled to the IBM core. The Hamiltonian for the system becomes

$$\hat{H} = \hat{H}_B + \hat{H}_F + \hat{V}_{BF} \tag{2.3.22}$$

where $\hat{H}_B$ is the usual IBM Hamiltonian, $\hat{H}_F$ is the fermion Hamiltonian given by

$$\hat{H}_F = \sum_{j\mu} \mathcal{E}_j a^\dagger_{j\mu} a_{j\mu} + \sum_{jj'kk'L} \frac{1}{2} U^{(L)}_{jj'kk'} \left[\left[a^\dagger_j \times a^\dagger_j \right]^{[L]} \times \left[a^*_k \times a^*_{k'} \right]^{[L]} \right]^{[0]} \tag{2.3.23}$$

and $\hat{V}_{BF}$ is the boson-fermion interaction given by[27]

$$\begin{aligned}\hat{V}_{BF} = &\sum_j \bar{w}_j^{(0)} \left[\left[s^\dagger \times s^* \right]^{[0]} \times \left[a_j^\dagger \times a_j^* \right]^{[0]} \right]^{[0]} \\ &+ \sum_{jj'} \bar{w}_{jj'}^{(2)} \left[\left[d^\dagger \times s^* + s^\dagger \times d^* \right]^{[2]} \times \left[a_j^\dagger \times a_j^* \right]^{[2]} \right]^{[0]} \\ &+ \sum_{jj'L} w_{jj'}^{(L)} \left[\left[d^\dagger \times s^* + s^\dagger \times d^* \right]^{[L]} \times \left[a_j^\dagger \times a_j^* \right]^{[L]} \right]^{[0]}\end{aligned} \tag{2.3.24}$$

In the above expressions $s^\dagger, d^\dagger$ are the usual s and d boson creation operators and $a_j^\dagger, a_j$ are fermion creation and annihilation operators with time reversal property $a_j^* = (-1)^{j-\mu} a_{j-\mu}$. This is the general expression for the Hamiltonian. However, it has been noted[28] that $\hat{V}_{BF}$ can be simplified to

$$\begin{aligned}\hat{V}_{BF} = &\sum_j A_j \left[M_B^{[0]} \times M_{F_j}^{[0]} \right]^{[0]} + \sum_{jj'} \Gamma_{jj'} \left[Q_B^{[2]} \times Q_{F_{jj'}}^{[2]} \right]^{[0]} \\ &+ \sum_{jj'j''} \Lambda_{jj'}^{j''} : \left[F_j^{\dagger[j'']} \times F_{j'}^{[j'']} \right]^{[0]} :\end{aligned} \tag{2.3.25}$$

where

$$M_B^{[0]} = \left[d^\dagger \times d^* \right]^{[0]} \tag{2.3.26a}$$

$$M_{F_j}^{[0]} = \left[a_j^\dagger \times a_j^* \right]^{[0]} \tag{2.3.26b}$$

$$Q_B^{[2]} = \left[d^\dagger \times s^* + s^\dagger d^* \right]^{[2]} + \chi \left[d^\dagger + d^* \right]^{[2]} \tag{2.3.26c}$$

$$Q_{F_{jj'}}^{[2]} = \left[a^\dagger \times a_{j'}^* \right]^{[2]} \tag{2.3.26d}$$

$$F_j^{\dagger[j'']} = \left[a^\dagger \times d^* \right]^{[j'']} \tag{2.3.26e}$$

$$F_{j'}^{\dagger[j'']} = \left[d^\dagger \times a_{j'}^* \right]^{[j'']} \tag{2.3.26f}$$

The symbol : denotes normal ordering of the operators. The first term above is a monopole interaction, the second term a quadrupole interaction, and the last term is an exchange interaction. The parameters $A_j, \Gamma_{jj'}$, and $\Lambda_{jj'}^{j''}$ denote the strengths

of the various interactions, and correspond to a special choice of the parameters $w_{jj'}^{(L)}$.

In general, the Hamiltonian must be diagonalized numerically, but in certain special situations, analytic solutions can be obtained. The group structure for the general Hamiltonian is

$$U^B(6) \otimes U^F(m) \tag{2.3.27}$$

where m is the dimension of the fermion group, $m = \sum_i (2j_i + 1)$. There are many different ways to decompose the direct product in Eq. (2.3.27) that depend on the dimension of the fermion group, m. Studies of these decompositions are available in the literature[27,29–30].

2.3.3 The Interacting Boson Fermion-Fermion Model

The Interacting Boson Fermion-Fermion Model (IBFFM) is an extension of the IBFM where two fermions are coupled to the IBM core. This introduces another complication since the group structure is

$$U^B(6) \otimes U^F(m_\pi + m_\nu) \supset U^B(6) \otimes U^F(m_\pi) \otimes U^F(m_\nu) \tag{2.3.28}$$

If $m_\pi = m_\nu$, then the group can be decomposed further into various symmetry limits similar to those of the IBFM[23].

The Hamiltonian for the IBFFM is written[31–32] as

$$\hat{H}_{IBFFM} = \hat{H}^{\pi}_{IBFM} + \hat{H}^{\nu}_{IBFM} + \hat{H}^{\pi\nu}_{RES} - \hat{H}_{IBM} \tag{2.3.29}$$

The IBFM Hamiltonians for both protons and neutrons are added together, but since they both include contributions for the IBM core, $\hat{H}_{IBM}$ must be subtracted. The term $\hat{H}^{\pi\nu}_{RES}$ is a residual interaction between the proton and the neutron. The IBFM and IBM Hamiltonians are those given previously and $\hat{H}^{\pi\nu}_{RES}$ is given by[31]

$$\hat{H}^{\pi\nu}_{RES} = \hat{H}_\delta + \hat{H}_{\sigma\sigma\sigma} + \hat{H}_{\sigma\sigma} + \hat{H}_T + \hat{H}_{MM} \tag{2.3.30}$$

where

$$\hat{H}_\delta = 4\pi V_\delta \delta(\vec{r}_\pi - \vec{r}_\nu)\,\delta(r_\pi - R_0)\,\delta(r_\nu - R_0) \tag{2.3.31}$$

is a surface delta-function interaction between the proton and neutron,

$$\hat{H}_{\sigma\sigma\sigma} = 4\pi V_{\sigma\sigma\sigma}\delta\left(\vec{r}_\pi - \vec{r}_\nu\right)\left(\vec{\sigma}_\pi \cdot \vec{\sigma}_\nu\right)\delta\left(r_\pi - R_0\right)\delta\left(r_\nu - R_0\right) \tag{2.3.32}$$

is a surface contact spin-spin interaction,

$$\hat{H}_{\sigma\sigma} = -\sqrt{3}V_{\sigma\sigma}\vec{\sigma}_\pi \cdot \vec{\sigma}_\nu \tag{2.3.33}$$

is a spin-spin interaction,

$$\hat{H}_T = V_T\left[3\frac{\left(\vec{\sigma}_\pi\vec{r}_\pi\right)\cdot\left(\vec{\sigma}_\nu\vec{r}_\nu\right)}{r_{\pi\nu}^2} - \vec{\sigma}_\pi \cdot \vec{\sigma}_\nu\right] \tag{2.3.34}$$

is a tensor interaction, and

$$\hat{H}_{MM} = 4\pi\frac{\delta\left(r_\pi - r_\nu\right)}{r_\pi r_\nu}\sum_{\kappa m} V_\kappa Y^*_{\kappa m}\left(\theta_\pi, \phi_\pi\right)Y_{\kappa m}\left(\theta_\nu, \phi_\nu\right) \tag{2.3.35}$$

is a multipole-multipole interaction. In the above expressions, $\vec{r}_{\pi\nu} = \vec{r}_\pi - \vec{r}_\nu$ and $R_0 = 1.2A^{\frac{1}{3}}$. The parameters V_δ, $V_{\sigma\sigma\sigma}$, $V_{\sigma\sigma}$, V_T, and V_κ are constants, and determine the strength of the interactions.

For most comparisons with experimental data a dynamical symmetry in the IBFFM is not employed, but rather a full numerical calculation is performed. The Hamiltonian is diagonalized in the basis[33]

$$\left|\left(j_\pi, j_\nu\right)j_{\pi\nu}, n_d v J; I\right\rangle \tag{2.3.36}$$

where j_π and j_ν are the proton and neutron single-particle angular momenta, $j_{\pi\nu}$ is the resultant angular momentum of the coupling of j_π and j_ν, n_d is the number of d bosons coupled to angular momentum J, ν is a label for extra quantum numbers if needed, and I is the total angular momentum resulting from the coupling of $j_{\pi\nu}$ and J. The IBFFM wave function is then expressed in the form

$$\left|I_\tau\right\rangle = \sum \xi^{(I_\tau)}_{(j_\pi j_\nu)j_{\pi\nu}n_d J}\left|\left(j_\pi, j_\nu\right)j_{\pi\nu}, n_d v J; I\right\rangle \tag{2.3.37}$$

where the subscript τ denotes the r'th state of a particular angular momentum I.

The boson-fermion interaction dominates the spectrum generated by the IBFFM. The boson-fermion coupling generates considerable mixing in the wave functions, as the two quasiparticle zero d-boson amplitudes of the wave functions are typically $< 30\%$.

2.4. The Extended Supersymmetry Model

The idea of exploiting dynamical symmetries in nuclei has lead to many important results in the IBM and the IBFM. Indeed, the initial success of the various symmetries was important in establishing the models, and one of the major advantages often claimed was that the solutions were easy to determine once the group chains were worked out. However, as the need for extensions and refinements became apparent, the ease of computation all but vanished. The IBFFM, described in the previous section, requires numerical calculations in most cases[34]. The supersymmetry model attempts to describe both even A andodd A nuclei within the same group multiplet, with the result that the expressions for transition rates, transfer strengths, etc., are analytical. This has tremendous advantages in that it allows for easy comparisons with experimental data, and the effect of the various parameters in the model is much more transparent.

The basic idea of the supersymmetry scheme is to embed both the bosonic and fermionic groups into supergroups, and then to decompose the supergroups into the various groups chains[35]. One of the first supersymmetry schemes worked out for nuclei was the $U(6/4)$ supersymmetry[36-37]. The dimension of the boson group was 6, and a $j = \frac{3}{2}$ fermion was coupled to the boson core, hence the fermion group has dimension 4. The group supermultiplets, which describe both even-even and odd nuclei, are labelled with the quantum number N=$\mathcal{N} + m$. The $U(6/4)$ supersymmetry has been applied with some success[38-41] to the Os-Ir nuclei, where N=9 and ^{190}Os and ^{191}Ir belong to the same supermultiplet.

The group chain for the $U(6/4)$ supersymmetry is

$$U\,(6/4) \supset U^{(B)}\,(6) \otimes U^{(F)}\,(4) \tag{2.4.1}$$

For the Os-Ir region, the boson core is described by the $SO(6)$ limit, and thus the group chain above can be further decomposed

$$U\,(6/4) \supset U^{(B)}\,(6) \otimes U^{(F)}\,(4) \supset SO^{(B)}\,(6) \otimes SU^{(F)}\,(4) \tag{2.4.2}$$

A further decomposition at this point requires a specific symmetry limit. A similar decomposition can be given for the $U(6/12)$ supersymmetry[42], where the fermionic group has dimension 12, which allows for $j = \frac{1}{2}$, $\frac{3}{2}$, or $j = \frac{5}{2}$ particles coupled to the boson core. The $U(6/12)$ supersymmetry has been used with some success in the Os-Pt region[43–48].

In a natural extension of these ideas, Van Isacker[49–50] and co-workers have considered the extended supersymmetry involved with the coupling of the $U_\pi(6/4)$ and $U_\nu(6/12)$ groups, i.e.,

$$U_\pi(6/4) \otimes U_\nu(6/12) \tag{2.4.3}$$

The coupling order appropriate for neutron-transfer strengths in the $A \simeq 196$ region is[50]

$$\begin{aligned} U_\nu^{(B)}(6) \otimes U_\pi^{(B)}(6) \otimes U_\nu^{(F)}(12) \otimes U_\pi^{(F)}(4) & \\ \supset U_{\nu+\pi}^{(B)}(6) \otimes U_\nu^{(F)}(6) \otimes SU_\nu^{(F)}(2) \otimes SU_\pi^{(F)}(4) & \\ \supset O_{\nu+\pi}^{(B)}(6) \otimes O_\nu^{(F)}(6) \otimes SU_\nu^{(F)}(2) \otimes O_\pi^{(F)}(6) & \\ \supset \tilde{O}_{\nu+\pi}^{(B+F)}(6) \otimes O_\nu^{(F)}(6) \otimes SU_\nu^{(F)}(2) & \\ \supset O_{\nu+\pi}^{(B+F)}(6) \otimes SU_\nu^{(F)}(2) \otimes O_{\nu+\pi}^{(B+F)}(5) \otimes SU_\nu^{(F)}(2) & \\ \supset O_{\nu+\pi}^{(B+F)}(3) \otimes SU_\nu^{(F)}(2) \supset O(3) \supset O(2) & \end{aligned} \tag{2.4.4}$$

The labels for the irreducible representations of the above symmetry limit are used to label the states. The Hamiltonian is written in terms of the Casimir operators of the groups in the chain, and is given by[49]

$$\begin{aligned} H =& AC_2\left(U_{\nu+\pi}^{(B+F)}(6)\right) + BC_2\left(\tilde{O}_{\nu+\pi}^{(B+F)}(6)\right) + B'C_2\left(O_{\nu+\pi}^{(B+F)}(6)\right) \\ &+ CC_2\left(O_{\nu+\pi}^{(B+F)}(5)\right) + DC_2\left(O_{\nu+\pi}^{(B+F)}(3)\right) + EC_2\left(Spin(3)\right) \end{aligned} \tag{2.4.5}$$

where the irreducible representations have labels $[N_1, N_2, N_3]$, $< \Sigma_1, \Sigma_2, \Sigma_3 >$, $< \sigma_1, \sigma_2, \sigma_3 >$, (τ_1, τ_2), L, and I, respectively, for the groups in Eq. (2.4.5). The eigenvalues for the quadratic Casimir operators are well known[50], thus the energy

eigenvalues are given by[49]

$$\begin{aligned}\mathcal{E} =& A\left[N_1\left(N_1+5\right)+N_2\left(N_2+3\right)+N_3\left(N_3+1\right)\right] \\ &+B\left[\Sigma_1\left(\Sigma_1+4\right)+\Sigma_2\left(\Sigma_2+2\right)+\Sigma_3^2\right] \\ &+B'\left[\sigma_1\left(\sigma_1+4\right)+\sigma_2\left(\sigma_2+2\right)+\sigma_3^2\right] \\ &+C\left[\tau_1\left(\tau_1+3\right)+\tau_2\left(\tau_2+1\right)\right]+DL\left(L+1\right)+EI\left(I+1\right)\end{aligned} \tag{2.4.6}$$

The supermultiplets based on the extended supersymmetry are capable of describing even-even, odd, and odd-odd nuclei. For example, the supermultiplet first considered[49,51] contained ^{196}Pt, ^{197}Pt, ^{197}Au, and ^{198}Au. With one set of parameters, the energy spectra of all four nuclei were reasonably reproduced, and thus if the even-even spectra and neighbouring odd A spectra can be fitted, then predictions for the energy spectrum for the odd-odd member of the supermultiplet can be made.

Expressions for transitions rates and the transfer strengths have been determined for certain group chains. As pointed out by Van Isacker[50], the expressions obtained are dependent on the way that the coupling is performed, and expressions for single-neutron transfer will differ from those for single-proton transfer even if the transfer operator is the same.

Chapter 3.
Experimental Techniques

Since transfer reactions are such a well known and established technique, it is not necessary to explore the details in depth because these are described elsewhere[52]. However, an overview will be given of the experimental technique.

3.1. Target Chamber and Enge Spectrometer

Beam particles obtained from the accelerator are focused and steered into the target chamber, the base plate of which is fixed to a central post. The target ladder, which can be rotated and elevated or lowered as desired, is positioned in the center of the chamber. Apertures are fixed to the base plate between the entrance port and the target position. Also fastened on the base plate is the silicon monitor counter assembly. This consists of a base, which is in good thermal contact with the cooled brass base plate of the target chamber; a thermoelectric cooler; and on top, the monitor counter holder. The assembly is constructed so that the silicon monitor counter remains in electrical isolation from the target chamber, thus minimizing electrical noise.

The products of the reaction between the beam particles and the target are admitted into the Enge spectrometer by means of apertures that can be adjusted in both the vertical and horizontal planes. The spectrometer can be rotated about the target, from 0° to about 160°. The Enge spectrometer is described as a split-pole instrument since it has two separate pole pieces surrounded by a single coil. The purpose of the split between the poles is to provide second-order double focusing (focusing in both the vertical and horizontal planes)[53]. The reaction products are momentum analyzed by the spectrograph, and thus the particles are dispersed. The dispersion, D, depends on the radius of curvature, ρ, and at the high ρ end ($\rho_{max} \simeq 90$ cm), where the particle detectors are usually located, has the value

$\Delta d/\Delta\rho \simeq 2.5$, where d is the distance along the focal plane. Therefore, for a change in energy that corresponds to a change in the radius of curvature of 1 cm, the position along the focal plane can be expected to change by about 2.5 cm. The magnification of the spectrometer is defined as the ratio of the size of the image to the size of the object. Obviously, the most important is the horizontal magnification, since it is desired that the width of the beam spot not produce wide peaks on the focal plane. The Enge spectrometer has a horizontal magnification, M_H, of about 0.34, and a vertical magnification, M_V, that varies from 1 to 2.7 over the length of the focal plane. The resolving power of the instrument is defined as $p/\Delta p$ where Δp is the momentum spread corresponding to the image width, and can obtain a value of approximately 5000 for beam spot widths of about 1 mm.

When the particles emerged from the magnetic field, they entered the detector chamber. In this chamber the photographic plates, which were used as particle detectors, were placed. More than one plate can be placed in the focal plane at a time, so that particles with different radii of curvature can be investigated. This was used in the (d,t) reactions to find the excitation energy of the first state populated, by comparing the energy of the particles in the elastic scattered peak to the energy of the tritons. The cassette holder can be moved both perpendicular and parallel to the focal plane. The perpendicular movement allows for more than one exposure to be made on a photographic plate, while the horizontal movement allows for the correction in focusing due to the "kinematic shift". If the spectrograph were accepting particles from radioactive decay, for instance, then the particle energies are independent of angle, and all particles have the same radius of curvature. The focal plane is defined as the plane where the particle trajectories convergence. During a reaction, the acceptance of particles over the range of angles defined by the apertures implies that there are now a range of energies accepted (due to kinematics), and these particles have different radii of curvature. The plane where the particle trajectories converges is now different from the focal plane, and this difference is

the kinematic shift. As the spread in energy becomes greater, for instance for particles that originate from reactions on light nuclei such as the carbon backing, the kinematic shift can become quite large. The shift, δ, is given by[53]

$$\delta = F(\rho)\,\rho_{max} K \sin\theta \tag{3.1.1}$$

where

$$K = \frac{(M_i M_o)^{\frac{1}{2}}}{(M_R + M_o)} \left(\frac{T_i}{T_{o_{max}}}\right)^{\frac{1}{2}} \tag{3.1.2}$$

and $F(\rho)$ depends only on the geometry of the spectrograph, and is

$$F(\rho) = \frac{DM_H}{1 - \dfrac{(K\cos\theta)\,\rho_{max}}{\rho}} \tag{3.1.3}$$

In the above expressions, M_i, M_o, and M_R are the masses of the beam particles, reaction products, and residual nuclei, respectively, $T_{o_{max}}$ is the kinetic energy corresponding to the maximum radius of curvature, ρ_{max}, T_i is the kinetic energy of the beam particles, and D is the dispersion defined previously.

3.2. Particle Detection

The particle detectors used in the experiments were photographic plates. Since resolution was the prime concern, photographic plates were chosen, since with active counters there is always a contribution to the peak width from the electronic noise. There are various types of photographic plates that could be used, depending on the linear energy transfer (LET) of the particle. For example, for the detection of α-particles, which have a high LET, a photographic plate with an emulsion that was relatively insensitive to charged particles with a low LET would be used. In this way, background reduction is easily accomplished. Particles that had a lower LET, such as protons, deuterons, or tritons, would not leave tracks, or would leave very faint tracks, and thus would not be counted. However, if it were desired to detect light ions, then a photographic emulsion that would be sensitive to them would be required. For the detection of protons and tritons, either Kodak NTA,

NTB, or NTB2 emulsions were used. For α's, Illford K-1 emulsions were used. The NTA, NTB, and NTB2 plates were developed with a mixture of 30% D19 developer and 70% distilled water for 6 minutes, and then fixed for 6 minutes. The K-1 plates were also developed in a solution of 30% D19 for 6 minutes, but were left in the fixer for typically 30 minutes.

Since the plates used for the detection of protons or tritons were also sensitive to deuterons, α's, and other heavier ions, thin foils of aluminium or lead were placed over the plates to stop unwanted ions. For the detection of tritons, the Q-values for the reaction were such that it would not be expected that any protons or deuterons would strike the focal plane at the same point as the tritons. Therefore, 0.004 inch thick aluminium foils were placed over the plates to stop singly charged α's or ^{12}C ions from reaching the plate. When detecting protons, the Q-values were such that deuterons and tritons would also fall on the focal plane at the same point. Therefore, taking advantage of the fact that the protons have the greatest range, 0.010 inch thick lead foils were placed over the plates. Deuterons and tritons would be stopped by this thickness of lead, but the protons would go through, although with a reduced energy.

Once the plates were developed, they could be scanned. The plates were placed under a microscope which had a depth of focus < 50 μm, and counted in 0.25 mm strips. The tracks that were from particles originating in the reaction entered the emulsion at a 45° angle, and since the emulsion was approximately 50 microns thick, when one end of the track was in focus, the other end was not. Therefore, particles without the proper track direction could be discriminated against. Also, very long tracks or very short ones, as well as tracks that were not horizontal, were discriminated against. In this way, a further reduction in the background could be achieved.

3.3. Targets

Targets of ^{191,193}Ir labelled as FSU 61 and FSU 12, respectively, were obtained from Florida State University and used for some early (d,p) and (d,t) experiments. These targets were made by vacuum evaporation, as described below, and had thicknesses of about 30 μg/cm^2. The composition of the iridium targets, as indicated by the supplier of the samples, is given in Table 3.3.1.

Targets of ^{191,193}Ir, and ^{189}Os were made at McMaster University by J. Stark. These were produced by vacuum evaporation of the metal samples, obtained from the Isotope Sales Division of Oak Ridge National Laboratory, onto carbon foils. The carbon foils were approximately 30 μg/cm^2 thick. This thickness was chosen to balance the strength of the target against the degradation of resolution due to the backing. The process of evaporation of the sample material onto the backing was achieved in several steps. Firstly, the sample, which was in the form of a metal powder, was placed into a tungsten boat in the vacuum chamber, heated by an electron beam, and melted into a sphere. When enough material had been incorporated into the sphere, the carbon backing foils were loaded into the vacuum chamber. The electron beam was again focused onto the metal sphere, and the intensity was slowly increased. Care was essential because the carbon foils ruptured if they became too hot. Therefore, the evaporation was carried out in several stages, until the desired thickness of material was reached. The targets of ^{191,193}Ir made in this manner had thicknesses of approximately 40 and 45 μg/cm^2, respectively, and were mounted on frames labelled as Y 134 and M 48, respectively. The ^{189}Os targets had thicknesses of approximately 33 μg/cm^2, and had compositions of 0.06% ^{186}Os, 0.41% ^{187}Os, 1.23% ^{188}Os, 81.14% ^{189}Os, 14.10% ^{190}Os, and 3.06% ^{192}Os.

The ^{195}Pt target was obtained from Los Alamos National Laboratory, and had a thickness of 120 μg/cm^2.

Table 3.3.1: Composition of Targets

Target	% ^{191}Ir	% ^{193}Ir
FSU 61	94.66	5.34
FSU 12	1.3	98.7
Y 134	96.19	3.81
M 48	0.65	99.35

3.4. Experiments Performed

The single-nucleon transfer experiments that are reported in this work were carried out at McMaster University. The beam energy chosen for the (d,t) reactions was 18 MeV, since many other (d,t) experiments performed in this mass region used this energy, and the angular distributions of cross sections have more structure than if the reactions were carried out at lower beam energies. The (d,p) reaction used 16 MeV deuterons. The (d,p) Q-values are positive ($\simeq$3 to 4 MeV), and to decrease the full width half maximum (FWHM) in energy, the beam energy was reduced from that used for the (d,t) reactions. Distorted wave Born approximation (DWBA) calculations indicated that the structure in angular distributions would still be sufficient to allow the determination of the dominant l-transfer in the transition.

In order to fine-tune the magnets so that the beamspot on target would have a small horizontal size, apertures (with a horizontal opening of 0.33 mm) were placed in the target location and the beam was focused through these. The objective was to reduce the current on the apertures as much as possible while maximizing the current on the Faraday cup located behind the target position. The currents to the quadrupole magnets on the beamline were adjusted, and for some experiments 90% of the beam reached the Faraday cup through the apertures. Once the focusing of the beam was satisfactory, the apertures were removed and the targets positioned.

Depending on the experiment, the targets were placed such that the carbon backing was facing the beam (for (d,t) and (p,α) experiments) or facing away from the beam (for the (d,p), (^{3}He,d), and (α,t) experiments). In this way the effects of energy straggling, which increases with the atomic number and decreases the resolution that can be achieved, were minimized.

The silicon surface-barrier monitor detector was placed at an angle of 30° to the beam, and used to measure the number of elastically scattered deuterons. A tantalum disk, with a 1.51 mm diameter aperture, was placed immediately in front of the detector. The aperture was 127 mm away from the center of the chamber. Therefore, the solid angle subtended by the aperture was 0.1110 msr. Several monitor detectors, which ranged in thickness from 1000 to 2000 microns, were used since with prolonged exposure the resolution would deteriorate. The resolution was required to be of sufficient quality to separate the elastic peak of the target from that of the carbon foil backing or other impurities. The output from the monitor detector was amplified and analyzed with a multichannel analyzer. The net counts in the elastic scattered peak were determined, from which a normalization value necessary for the conversion to absolute cross sections was obtained.

The apertures for particle acceptance to the Enge spectrometer could be adjusted in both the vertical and horizontal directions independently. The choice of setting was a compromise between good resolution and count rate. In order to have the maximum count rate, the apertures had to be opened as far as possible. However, if the horizontal and vertical apertures were set too wide, the resolution would be degraded through third order aberrations. The apertures were set as listed in Table 3.4.1.

The beam current on the targets was typically 1 particle μA, and for the single-neutron transfer reactions gave a sufficient exposure of the photographic plates after 1 or 2 hours. The exposures were usually stopped after 2×10^6 monitor counts. Spectra were taken at 15 angles for the ^{191}Ir(d,p), ^{193}Ir(d,p), and ^{191}Ir(d,t) reactions, in 2° steps from 6° to 10°, in 2.5° steps from 10° to 20°, in 5° steps from

Table 3.4.1: Apertures Set for Enge Spectrograph Experiments

Experiment	Setting		Solid Angle msr
	Vertical	Horizontal	
^{191}Ir(d,p)	50	60	0.759
^{191}Ir(d,t)	50	60	0.759
^{193}Ir(d,p)	50	60	0.759
^{193}Ir(d,t)	50	60	0.759
^{189}Os(α,t)	60	120	1.821
^{189}Os(^{3}He,d)			
35°,60°	60	120	1.821
10°,15°,20°,30°	70	90	1.593
^{195}Pt(p,α)	60	100	1.517
^{193}Ir(^{3}He,α)	60	120	1.821

20° to 50°, and in 10° steps from 50° to 70°. The ^{191}Ir(d,t), ^{193}Ir(d,p) reactions had an additional spectrum taken at 22.5°, and the ^{193}Ir(d,t) reaction had additional spectra taken at 22.5° and 27.5°. For the ^{189}Os(α,t) experiment only two spectra were recorded, at 50° and 60°. Spectra recorded at smaller angles would probably have a large number of impurity peaks, thus reducing the amount of information gained, and DWBA calculations indicated that the angular distributions are somewhat structureless. A total of 6 spectra were recorded for the ^{189}Os(^{3}He,d) reaction, at 10°, 15°, 20°, 30°, 35° and 60°. In the ^{195}Pt(p,α) experiment, only two spectra were recorded at 10° and 15°.

3.5. Experimental Analysis Techniques

After the plates were scanned, the counts were used as input to the program SPECTR. The program performed a fit to the peaks with the function

$$y = H\left[\exp\left[\frac{-(x-x_0)^2(4\ln 2)}{G^2}\right] + S\exp\left[-\left(\frac{\ln 2}{A}\right)(|x-x_0-GG|)\right] \times \left(1-\exp\left[\frac{-(x-x_0)^2(4\ln 2)}{GG^2}\right]\right)\right] \tag{3.5.1}$$

where y is the observed count, x is the position along the plate. The peak shape parameters, A, S, G, and GG were determined by fitting strongly populated, well resolved peaks, and then kept constant for the fit to the entire spectrum. The function is a gaussian, centered at x_0 with full width at half maximum (FWHM) G, with an exponential tail added to it. The exponential tail, which has a decay rate of $1/A$, is also multiplied by another gaussian function such that the contribution of the tail at x_0 is zero. The height of the peak is given by H, and the height of the exponential tail at a distance GG away from x_0 is $H \times S$. The peak shape is shown in Figure 3.5.1.

The number of counts in the elastic scattering peak is given by

$$N_{mon} = \frac{d\sigma}{d\Omega}\Big)_{el} d\Omega_{mon}\epsilon_{mon}N_t N_b\,(DTC) \tag{3.5.2}$$

where $\frac{d\sigma}{d\Omega}\Big)_{el}$ is the elastic scattering cross section at the angle of the monitor counter, $d\Omega_{mon}$ is the solid angle subtended by the monitor counter, N_t is the number of target atoms in the beam path, and N_b is the number of beam projectiles. The dead time correction (DTC) and the efficiency for detection of the elastic scattered events (ϵ_{mon}) were essentially 1 for all experiments. The number of counts observed in a peak by the detector in the spectrograph is

$$N_{sp} = \frac{d\sigma}{d\Omega}\Big)_{sp} d\Omega_{sp}\epsilon_{sp}N_t N_b\,(TP) \tag{3.5.3}$$

where $\frac{d\sigma}{d\Omega}\Big)_{sp}$ is the reaction cross section, $d\Omega_{sp}$ is the solid angle subtended by the spectrograph, ϵ_{sp} is the detection efficiency for the detector (equal to 1 for

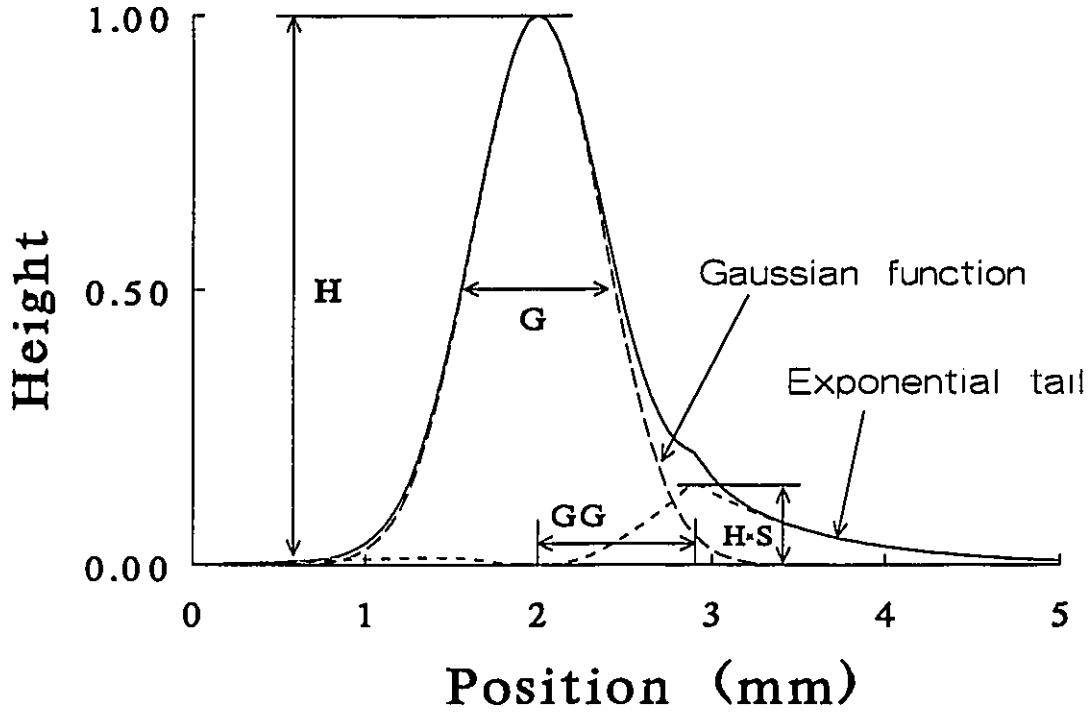

Figure 3.5.1: The peak-fitting function used in the analysis of the particle data. The meaning of the parameters G, GG, H, and S that describe the shape are shown.

photographic plates), and TP is the target purity. By dividing Eq. (3.5.2) by Eq. (3.5.3), the reaction cross section can be obtained in terms of known quantities

$$\frac{d\sigma}{d\Omega}\Big)_{sp} = \frac{d\sigma}{d\Omega}\Big)_{cl} \frac{d\Omega_{mon}}{d\Omega_{sp}} \frac{1}{N_{mon}} \frac{1}{TP} N_{sp} = \mathcal{Y}_{norm} N_{sp} \tag{3.5.4}$$

and thus the peak intensities found by SPECTR can be converted to absolute cross sections by multiplying by the normalization factor, $\mathcal{Y}_{norm}$.

The calibration polynomial relating the distance along the plate to the radius of curvature is accurately known, and was determined by D. Burke and C.R. Hirning[54] by examining the variation with magnetic field of the distance along the plates for peaks due to α-particles from a radioactive source of ^{212}Pb. The

calibration polynomial was found to be

$$\rho = 89.3031 - 0.405073d + 0.242966 \times 10^{-3}d^2 - 0.751076 \times 10^{-5}d^3 + 0.834861 \times 10^{-7}d^4 \quad (3.5.5)$$

where d is the distance from the end of the plate in cm, and ρ is the radius of curvature in cm. A nuclear magnetic resonance (NMR) probe was used to determine the magnetic field in the Enge spectrograph. This, combined with knowledge of the mass and charge of the detected particles, allowed their energy to be determined. From relativistic kinematics, with knowledge of the beam particle mass and energy, the reaction Q-values can be found. For the (d,t) reactions, two photographic plates were sometimes placed in the focal plane, one to detect the tritons, and the other to detect the elastically scattered deuterons. A precise value of the energy difference between the elastic peaks and the reaction peaks can be determined. If the ground state Q-value is well known, then the excitation energy can be measured.

Angular distributions of cross sections from single-neutron transfer reactions have shapes which depend upon the transferred l-values of the transition. Since angular momentum coupling allows for more than one l-value to be transferred to a particular state, the angular distributions can be fitted with several DWBA curves for different l-values simultaneously. The fits were carried out by a least squares procedure. In a two-parameter fit, an attempt was made to reproduce the observed angular distribution with

$$y = af_1(\theta) + bf_2(\theta) \quad (3.5.6)$$

where $f(\theta)$ is a theoretical angular distribution for a particular l-value. To find the values of the coefficients, the value of χ^2, defined by

$$\chi^2 = \sum_i \left(\frac{y_i - af_1(\theta_i) - bf_2(\theta_i)}{\sigma_i} \right)^2 \quad (3.5.7)$$

was minimized with respect to both a and b, yielding

$$\sum_i \left(\frac{y_i - af_1(\theta_i) - bf_2(\theta_i)}{\sigma_i^2} \right) f_1(\theta_i) = 0 \quad (3.5.8)$$

$$\sum_i \left(\frac{y_i - af_1(\theta_i) - bf_2(\theta_i)}{\sigma_i^2} \right) f_2(\theta_i) = 0 \quad (3.5.9)$$

The sums in the above expressions are over all data points, where y_i is the observed value of the cross section at angle θ_i. The solution of the above equations gives the values of a and b to be

$$a = \frac{\sum_i \frac{y_i f_1(\theta_i)}{\sigma_i^2} - b\sum_i \frac{f_1(\theta_i) f_2(\theta_i)}{\sigma_i^2}}{\sum_i \frac{(f_1(\theta_i))^2}{\sigma_i^2}} \tag{3.5.10}$$

$$b = \frac{\sum_i \frac{y_i f_2(\theta_i)}{\sigma_i^2} - \frac{\left(\sum_i \frac{y_i f_1(\theta_i)}{\sigma_i^2}\right)\left(\sum_i \frac{f_1(\theta_i) f_2(\theta_i)}{\sigma_i^2}\right)}{\sum_i \frac{(f_1(\theta_i))^2}{\sigma_i^2}}}{\sum_i \frac{(f_2(\theta_i))^2}{\sigma_i^2} - \frac{\left(\sum_i \frac{f_1(\theta_i) f_2(\theta_i)}{\sigma_i^2}\right)^2}{\sum_i \frac{(f_1(\theta_i))^2}{\sigma_i^2}}} \tag{3.5.11}$$

To determine the errors on the coefficients, any systematic errors, such as errors in the angles, shall be ignored. As well, uncertainties are introduced by the optical model parameters used in the DWBA calculations, and these also will not be treated here. Assuming only statistical errors then

$$\sigma_f^2 = \sum_i \left(\frac{\partial f}{\partial x_i}\right)^2 \sigma_{x_i}^2 \tag{3.5.12}$$

where x_i are the variables of function f. The error on a is found using

$$\frac{\partial a}{\partial y_i} = \frac{\frac{f_1(\theta_i)}{\sigma_i^2}}{\sum_i \frac{(f_1(\theta_i))^2}{\sigma_i^2}} \tag{3.5.13a}$$

$$\frac{\partial a}{\partial b} = \frac{\sum_i \frac{f_1(\theta_i) f_2(\theta_i)}{\sigma_i^2}}{\sum_i \frac{(f_1(\theta_i))^2}{\sigma_i^2}} \tag{3.5.13b}$$

and substituting into Eq. (3.5.12). Similarly, the error on b can be found by applying Eq. (3.5.12) with

$$\frac{\partial b}{\partial y_i} = \frac{\frac{f_2(\theta_i)}{\sigma_i^2} - \frac{\left(\frac{f_1(\theta_i)}{\sigma_i^2}\right)\left(\sum_i \frac{f_1(\theta_i) f_2(\theta_i)}{\sigma_i^2}\right)}{\sum_i \frac{(f_1(\theta_i))^2}{\sigma_i^2}}}{\sum_i \frac{(f_2(\theta_i))^2}{\sigma_i^2} - \frac{\left(\sum_i \frac{f_1(\theta_i) f_2(\theta_i)}{\sigma_i^2}\right)^2}{\sum_i \frac{(f_1(\theta_i))^2}{\sigma_i^2}}} \tag{3.5.14}$$

The uncertainties on the data points, σ_i, are found by

$$\sigma_i = \sqrt{\sigma_p^2 + (0.1 y_i)^2} \tag{3.5.15}$$

where σ_p is the statistical uncertainty in the cross section as given by the program SPECTR and depends on the number of counts in a peak, how well it is resolved from other peaks, etc. The uncertainty σ_i also includes an additional 10% of the cross section, which is a measure of the reproducibility, i.e. when experiments are repeated trying to match the same conditions, differences in cross sections as large as 10% may be found for the same levels.

The case where only one theoretical angular distribution was fit to the observed data is much simpler, with the fit coefficient

$$a = \frac{\sum_i \frac{y_i f(\theta_i)}{\sigma_i^2}}{\sum_i \frac{(f(\theta_i))^2}{\sigma_i^2}} \tag{3.5.16}$$

and uncertainty

$$\sigma_a = \sqrt{\frac{1}{\sum_i \frac{(f(\theta_i))^2}{\sigma_i^2}}} \tag{3.5.17}$$

All of the angular distributions were first fit with one theoretical l-value. If there appeared to be significant deviations between the data and the fit, then the fit was performed with two l-values. In order to test whether the two-parameter fit was justified, an F_χ test was performed. The statistic F_χ is defined as

$$F_\chi = \frac{\chi^2(n-1) - \chi^2(n)}{\frac{\chi^2(n)}{(N-n)}} \tag{3.5.18}$$

and is a test of how much the additional term in the fit improves the χ^2. The number of degrees of freedom is $N - n$, where N is the number of data points and n the number of parameters. The probabilities of F_χ exceeding a certain value due to random fluctuations of the data are tabulated [55]. For 16 data points, a value of $F_\chi > 2.46$ implies that the two-parameter fit is meaningful at the 95% confidence level, while for 17 data points, the corresponding value is 2.39. Therefore, if a value of $F_\chi < 2.4$ was observed, then the one parameter fit was favoured over the two-parameter fit.

Chapter 4.
Experimental Results

4.1. Introduction

In this chapter, the results from various experiments are presented. The techniques used to derive the plots and numbers that are seen here were described in the previous chapter.

A large number of levels below 1 MeV excitation energy are populated in the single-neutron transfer reactions. All of the levels observed have negative parity, as the transferred l-values were either 1, 3, or 5, and the targets have positive parity. The results from the (d,t) reactions are more precise than those from the (d,p) reactions, since there were impurity peaks present in the (d,p) spectra, and the resolution was slightly poorer. Indeed, with the (d,t) reaction results, it was often possible to determine the spectroscopic strengths for more than one l-value populating a state. The (α,t) and (^{3}He,d) studies provided information on the proton part of the configurations in ^{190}Ir, and in combination with the results of a (d,t) experiment, provide evidence for strong configuration mixing, but unfortunately there is very little complementary information regarding this nucleus.

4.2. Single-Neutron Transfer Reactions

The (d,t) and (d,p) reactions were performed using beams of 18 and 16 MeV deuterons, respectively. The resolutions obtained for the (d,t) spectra, typical examples of which are shown in Figure 4.2.1 and Figure 4.2.2 for the ^{191}Ir(d,t)^{190}Ir and ^{193}Ir(d,t)^{192}Ir reactions, respectively, were very impressive, being on average 0.38 mm, or 5.7 keV, with the best resolution of 4.5 keV. The average peak widths for the (d,p) reactions, slighter greater than for the (d,t) reactions, was 0.49 mm, and since the protons have greater energy due to the Q-value differences than the tritons, results in a greater FWHM in energy, 8.9 keV. Figure 4.2.3 and Figure 4.2.4 shows typical spectra obtained in the ^{191}Ir(d,p)^{192}Ir and ^{193}Ir(d,p)^{194}Ir reactions, respectively.

During the (d,t) experiments, extra photographic plates were sometimes put in the focal plane to detect the elastically scattered deuterons. The position on the focal plane of the peak due to elastic scattered particles was used to determine their radius of curvature using Eq. (3.5.5), and their kinetic energy was found using relativistic kinematics. Since the Q-value for elastic scattering is zero, the kinetic energy of the beam particles could also be found. The energy of the particles associated with the position of the first triton peak, combined with the knowledge of the beam kinetic energy, was used to determine the Q-values for the states populated in the reactions. With this method, the Q-value for the first populated state in ^{190}Ir is $Q = -1.767 \pm 0.002$ MeV. This result is consistent with the Q-value of -1.768 ± 0.006 MeV obtained by measuring the energy difference between between the first level populated in ^{190}Ir and the peaks from the 56.7, 84.3, 104.5, 116.8, and 128.3 keV levels in ^{192}Ir, present due to the 5.34% ^{193}Ir impurity in the target, observed in the spectra recorded at 12.5° and 50°. The uncertainty of $\pm$0.006 MeV includes the contribution of $\pm$0.004 MeV in the mass of the ^{191}Ir ground state [56]. Since the^{190}Ir ground state Q-value from the 1986 mass tables[56] has an uncertainty of $\pm$200 keV, the excitation energy of the first state populated in the reaction is unknown. From the mass tables[56], the ground state Q-value for ^{192}Ir is well known,

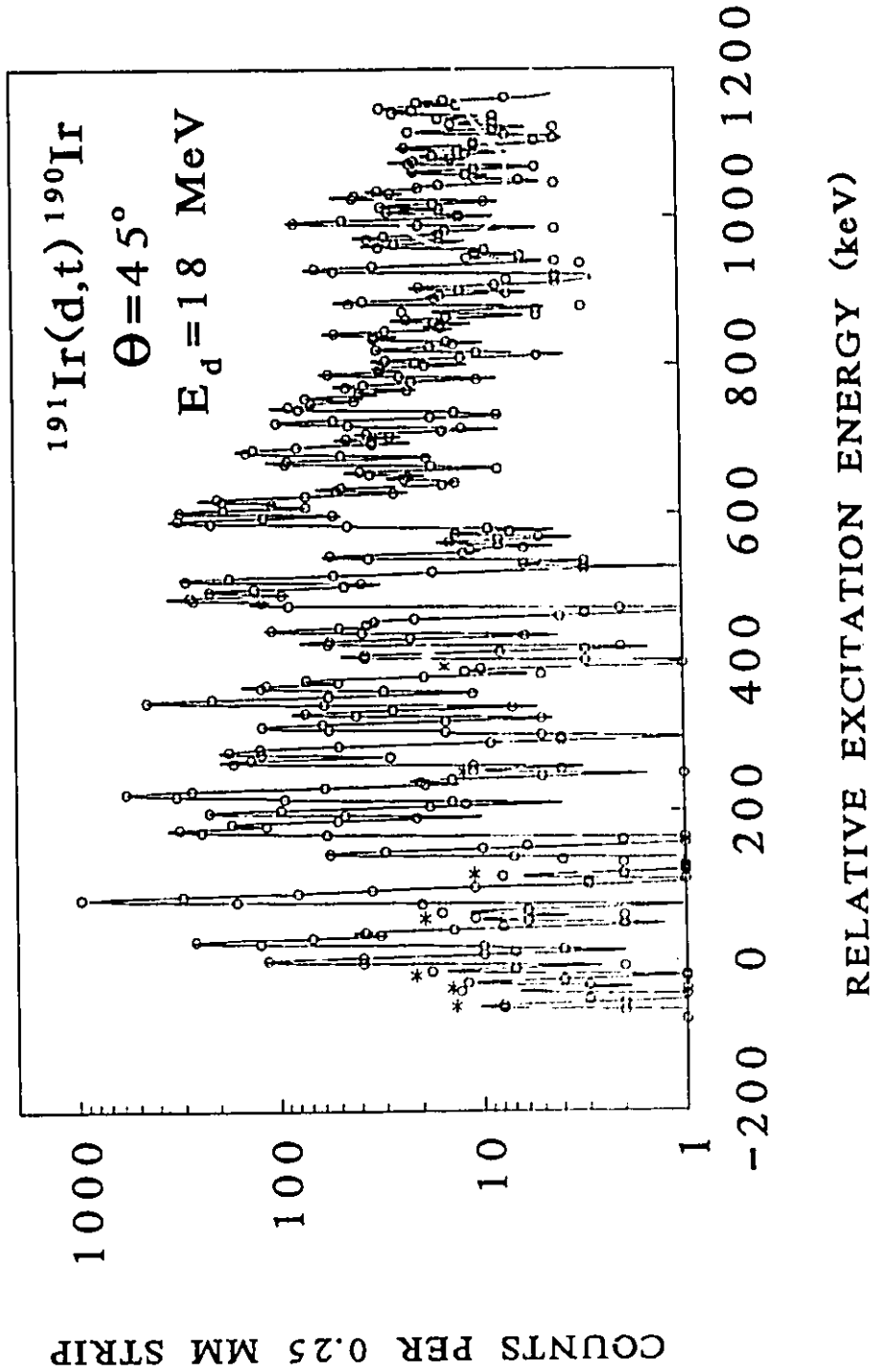

Figure 4.2.1: Spectrum obtained at an angle of $\theta = 45°$ for the ^{191}Ir(d,t) reaction with 18 MeV deuterons. Peaks labelled with asterisk marks are due to levels in ^{192}Ir.

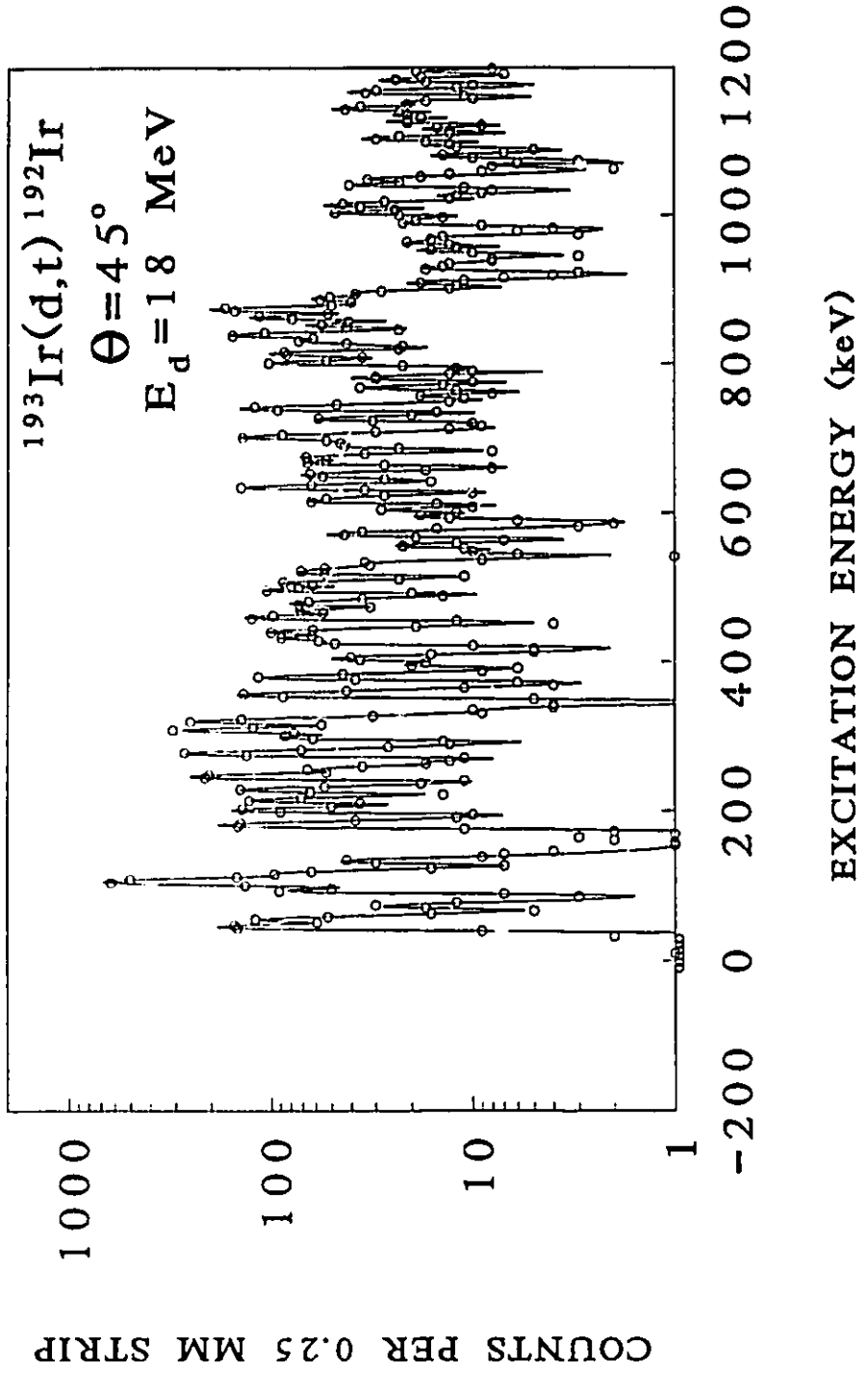

Figure 4.2.2: Spectrum obtained at an angle of $\theta = 45°$ for the ^{193}Ir(d,t) reaction with 18 MeV deuterons.

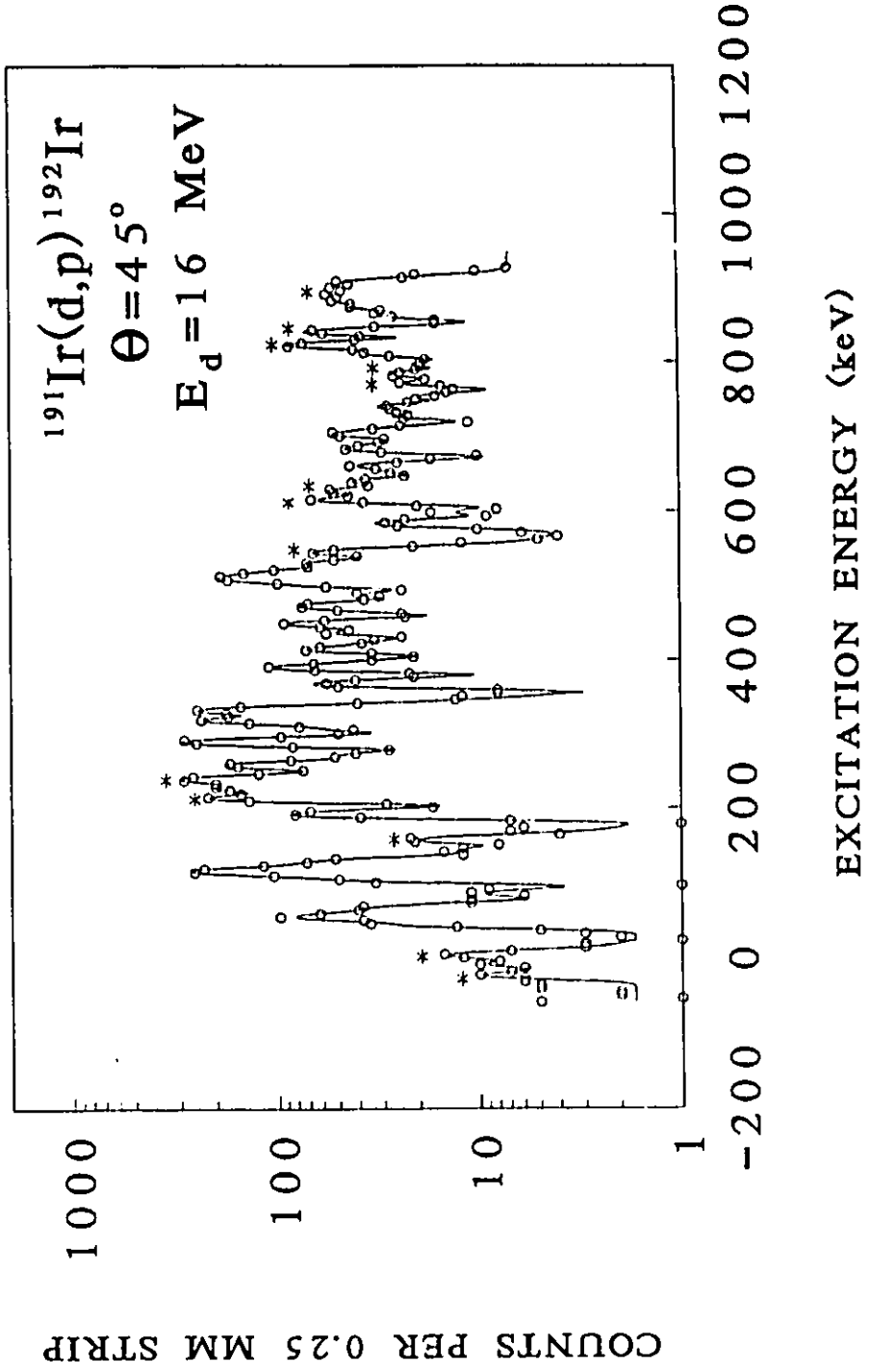

Figure 4.2.3: Spectrum obtained at an angle of $\theta = 45°$ for the ^{191}Ir(d,p) reaction with 16 MeV deuterons. Peaks labelled with asterisk marks are due to impurities.

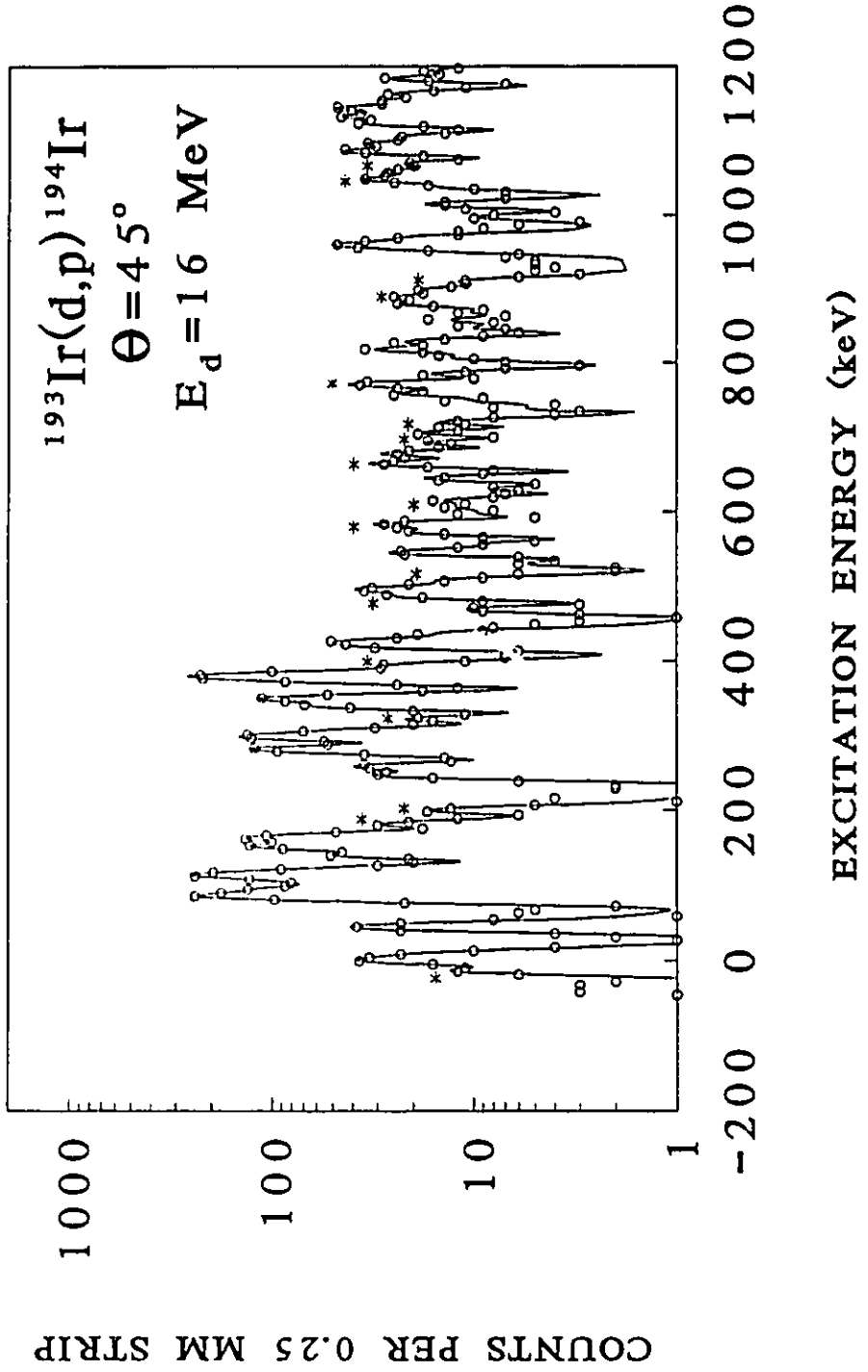

Figure 4.2.4: Spectrum obtained at an angle of $\theta = 45°$ for the ^{193}Ir(d,p) reaction with 16 MeV deuterons. Peaks labelled with asterisk marks are due to impurities.

and the excitation energy for the first peak populated in ^{192}Ir by the (d,t) reaction was determined to be 57.6 ± 1.2 keV, where the uncertainty does not take into account the 4 keV uncertainty [56] in the ground state Q-value. This agrees with the value of 56.72 keV reported by Kern et al[57] for the energy of the first excited state. An additional ±2 keV uncertainty, which has not been included, on all Q-values may be due to systematic error in the calibration of the spectrograph.

The peak intensities were converted to cross sections, and angular distributions were fitted with either one or two l-values as described in Section 3.5. The theoretical angular distributions for the transferred l-values for (d,t) and (d,p) reactions, shown in Figure 4.2.5 and Figure 4.2.6, respectively, were obtained from distorted wave Born approximation (DWBA) calculations using the computer code[58] DWUCK4 and the same optical model parameters as in a single-nucleon transfer study[48] of Pt nuclei. These parameters were chosen since the single-neutron transfer experiments on Pt nuclei, which are in the same mass region, were performed using the same beam energies as in the present work, and both the shape of the angular distributions and the analyzing powers for various transferred angular momenta, j, were successfully reproduced. The parameters are listed in Table 4.2.1. The normalization value, N, was equal to 3.33 for (d,t) reactions and 1.55 for (d,p) reactions as recommended by Kunz[58].

In single-nucleon transfer from an initial state with spin I_i, more than one j-value may be transferred to a final state with spin I_f. From angular momentum conservation the transferred j-value is restricted to the range between $|I_i - I_f|$ and $I_i + I_f$. However, usually one or two j-components will dominate the transfer, and in this work there were no angular distributions that gave reasonable evidence for more than two l components. The transfer of $j = \frac{1}{2}^-$ or $j = \frac{3}{2}^-$ is indicated by the presence of an $l = 1$ component in the angular distribution, and since the ground states of ^{191,193}Ir are $\frac{3}{2}^+$, the final state spin is 0^-, 1^-, 2^-, or 3^-. An $l = 3$ component indicates the transfer of $j = \frac{5}{2}^-$ or $j = \frac{7}{2}^-$, and could populate final spins of 1^-, 2^-, 3^-, 4^-, and 5^-. An $l = 5$ component, which would be the l-value

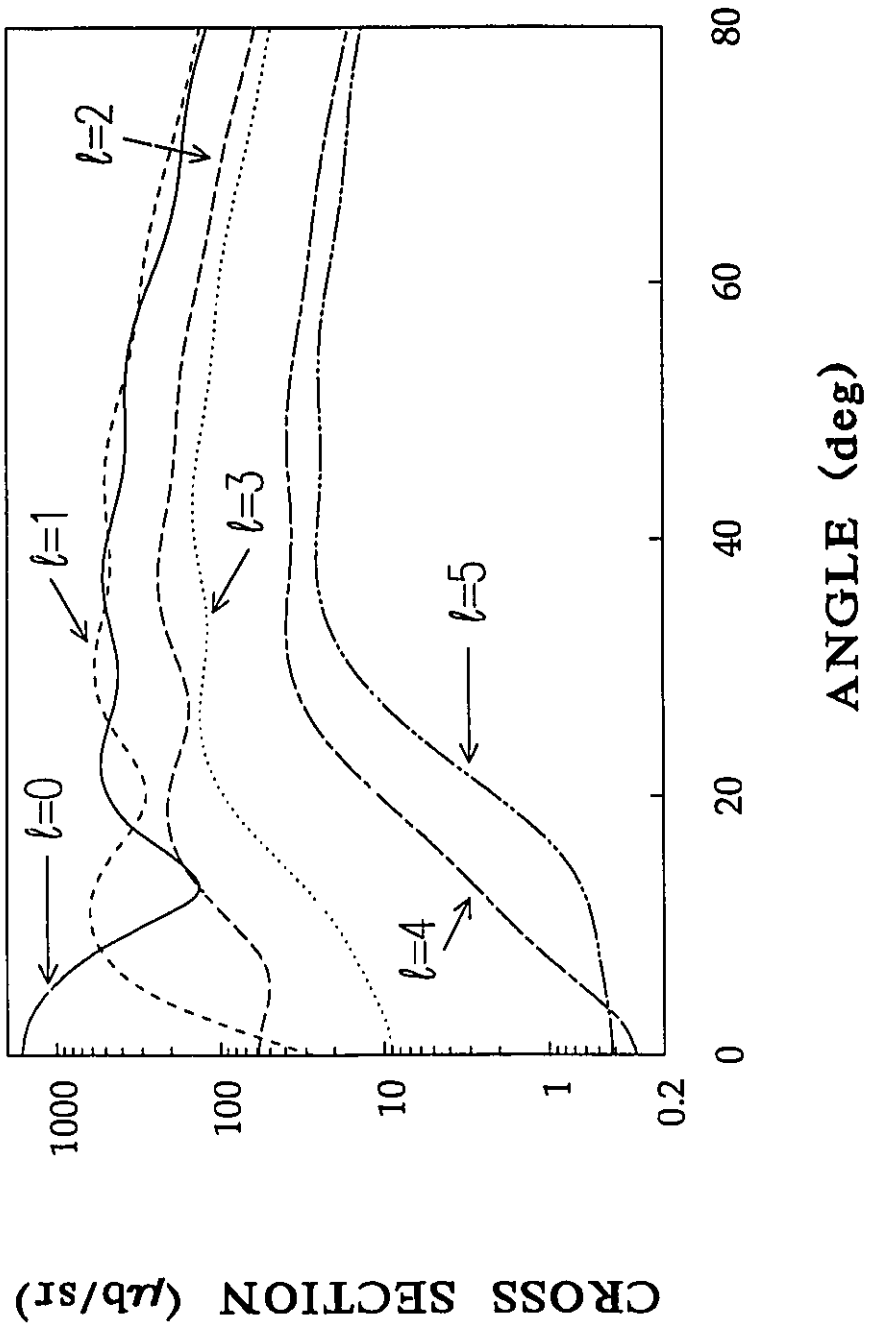

Figure 4.2.5: Angular distributions of (d,t) cross sections obtained from DWBA calculations using the program DWUCK4. The calculations were performed assuming a bombarding energy of 18 MeV.

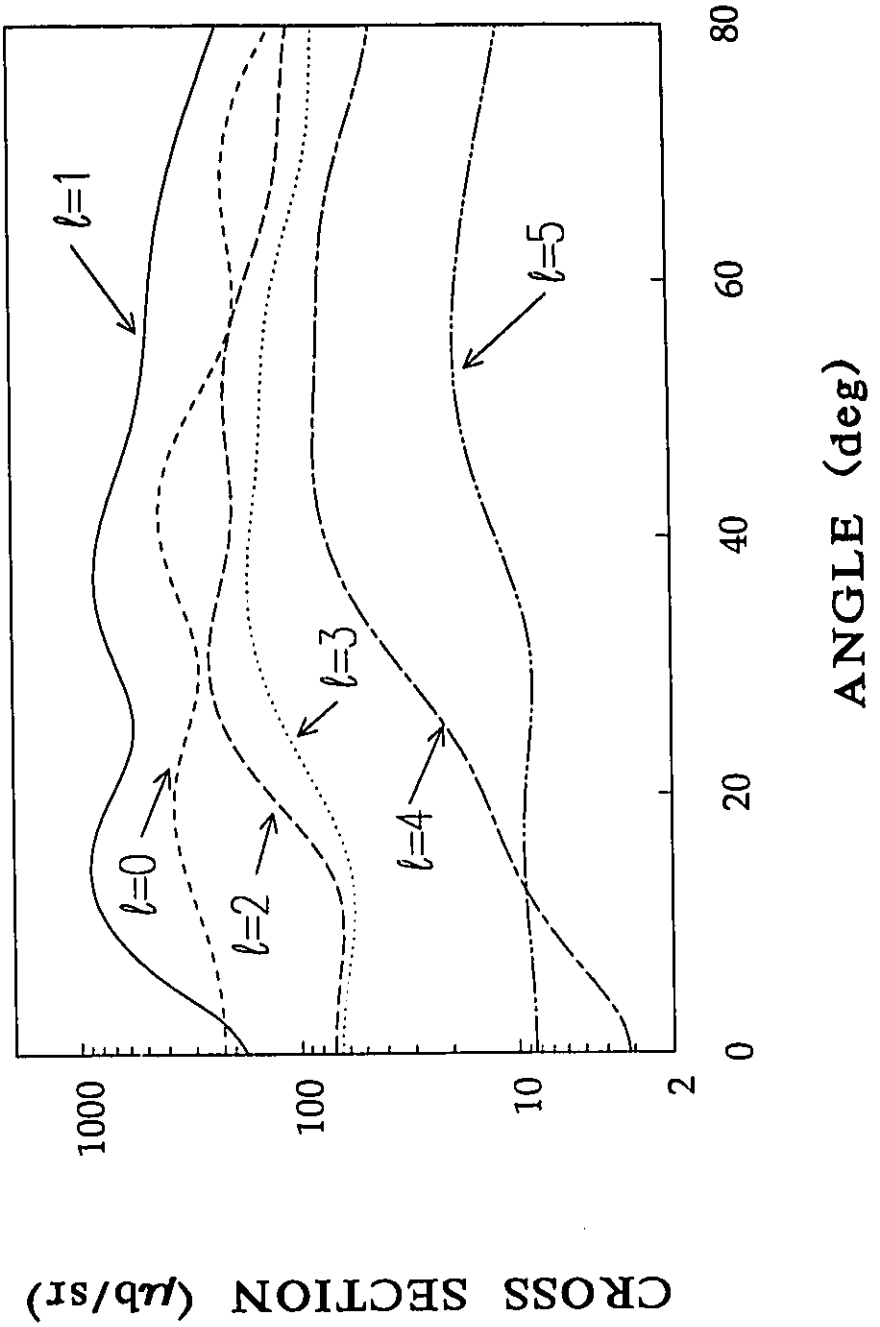

Figure 4.2.6: Angular distributions of (d,p) cross sections obtained from DWBA calculations using the program DWUCK4. The calculations were performed assuming a bombarding energy of 16 MeV.

Table 4.2.1: Optical Model Parameters for DWBA Calculations (d,t) and (d,p) Reaction[a])

Particle	V (MeV)	r_r (fm)	a_r (fm)	W (MeV)	$4W_D$ (MeV)	r_I (fm)	a_I (fm)	r_c (fm)	Nonlocal Parameter
deuteron	−103.8	1.15	0.81		74.9	1.34	0.68	1.15	0.54
triton	−151.7	1.24	0.685	−12.85		1.432	0.87	1.25	0.25
proton	−57.8	1.17	0.75	−1.92	24.2	1.32	0.66	1.17	0.85
neutron	[b])	1.17	0.75						

[a]) Finite range parameter and normalization constant used were 0.845, 0.650 and $N = 3.33$, $N = 1.55$ for the (d,t) and (d,p) reactions, respectively.

[b]) Well depth varied to reproduce the neutron binding energy. A spin-orbit strength corresponding to λ=8 was also used.

for transfer of $j = \frac{9}{2}^-$ or $j = \frac{11}{2}^-$, could populate final states with spin 3^-, 4^-, 5^-, 6^-, and 7^-. If an angular distribution has two l components, then clearly the spin of the state is restricted to the intersection of the spin range for each l-value.

The angular distributions of cross sections from the ^{191}Ir(d,t) reaction and the ^{193}Ir(d,t) reactions are shown in Figure 4.2.7 and Figure 4.2.8. The fits to the data are, in almost all cases, extremely good. There are several angular distributions that appear to be populated with pure $l = 1$ or $l = 3$ transitions, and these are well reproduced by the DWBA curves. Many of the plots have more than one curve on them, corresponding to a transfer of more than one l-value. The $F\chi$ test, described in Section 3.5, was used as a measure of the probability that the reduction in the χ^2 value for a two component fit was not due to random fluctuations in the data. The level of confidence chosen for the $F\chi$ test was 95%, and Table 4.2.2 and Table 4.2.3 lists the χ^2 and $F\chi$ values obtained for the fits to the angular distribution for the

^{191}Ir(d,t) and ^{193}Ir(d,t) reactions, respectively. The values of the fit coefficients are equal to the spectroscopic strengths, defined as

$$S_l = \frac{\frac{d\sigma}{d\Omega}\Big)_{exp}}{N\frac{d\sigma_l}{d\Omega}\Big)_{DWBA}} \tag{4.2.1}$$

where the experimental angular distribution is fitted with a single l-transition, and

$$\frac{d\sigma}{d\Omega}\Big)_{exp} = N\left[S_i\frac{d\sigma_i}{d\Omega}\Big)_{DWBA} + S_k\frac{d\sigma_k}{d\Omega}\Big)_{DWBA}\right] \tag{4.2.2}$$

where it is fitted with two l-components.

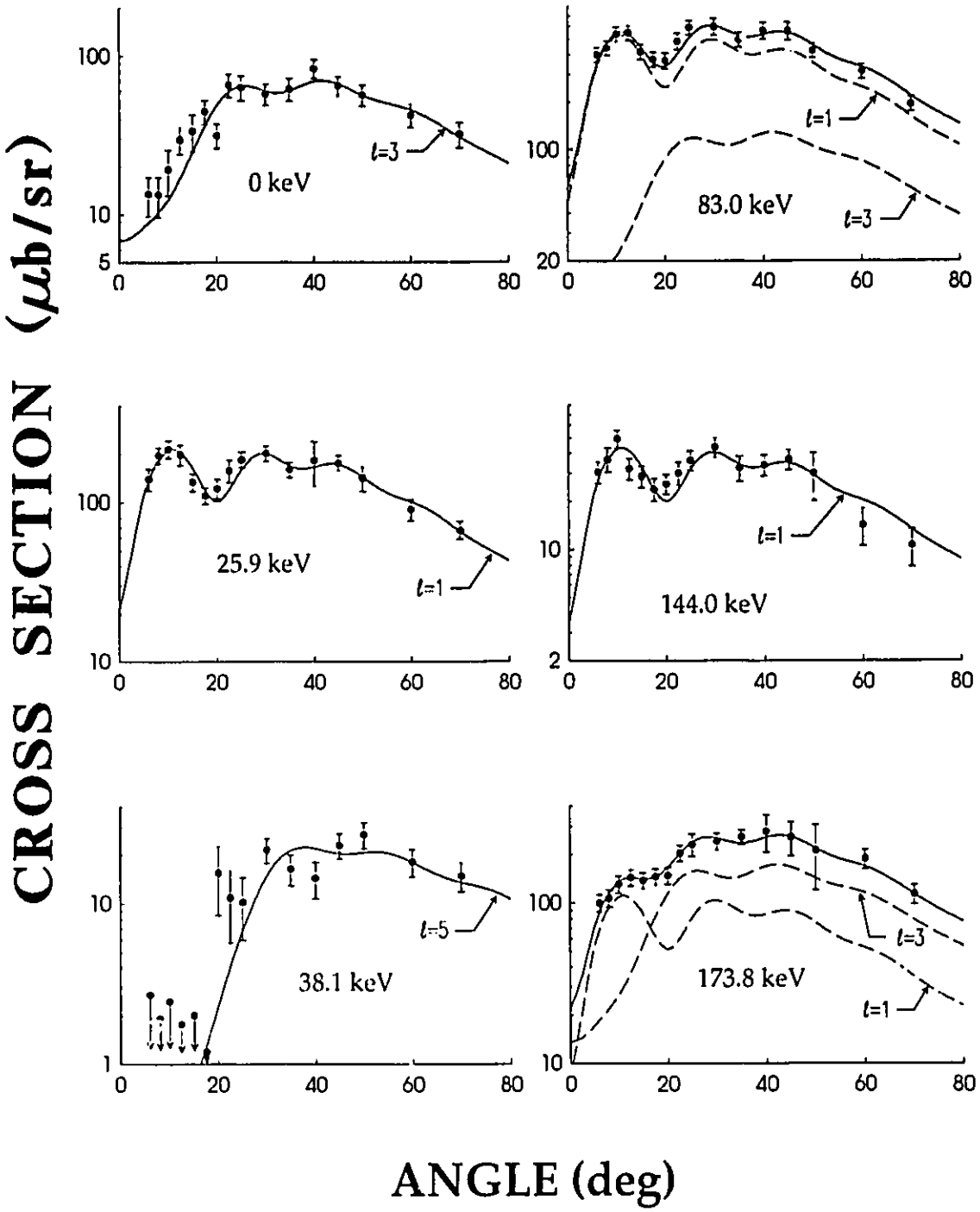

Figure 4.2.7a: Angular distributions of cross sections from the ^{191}Ir(d,t) reaction. The dashed curves are the results of a DWBA calculation for the transferred l-value indicated. The solid curves are the fits to the data.

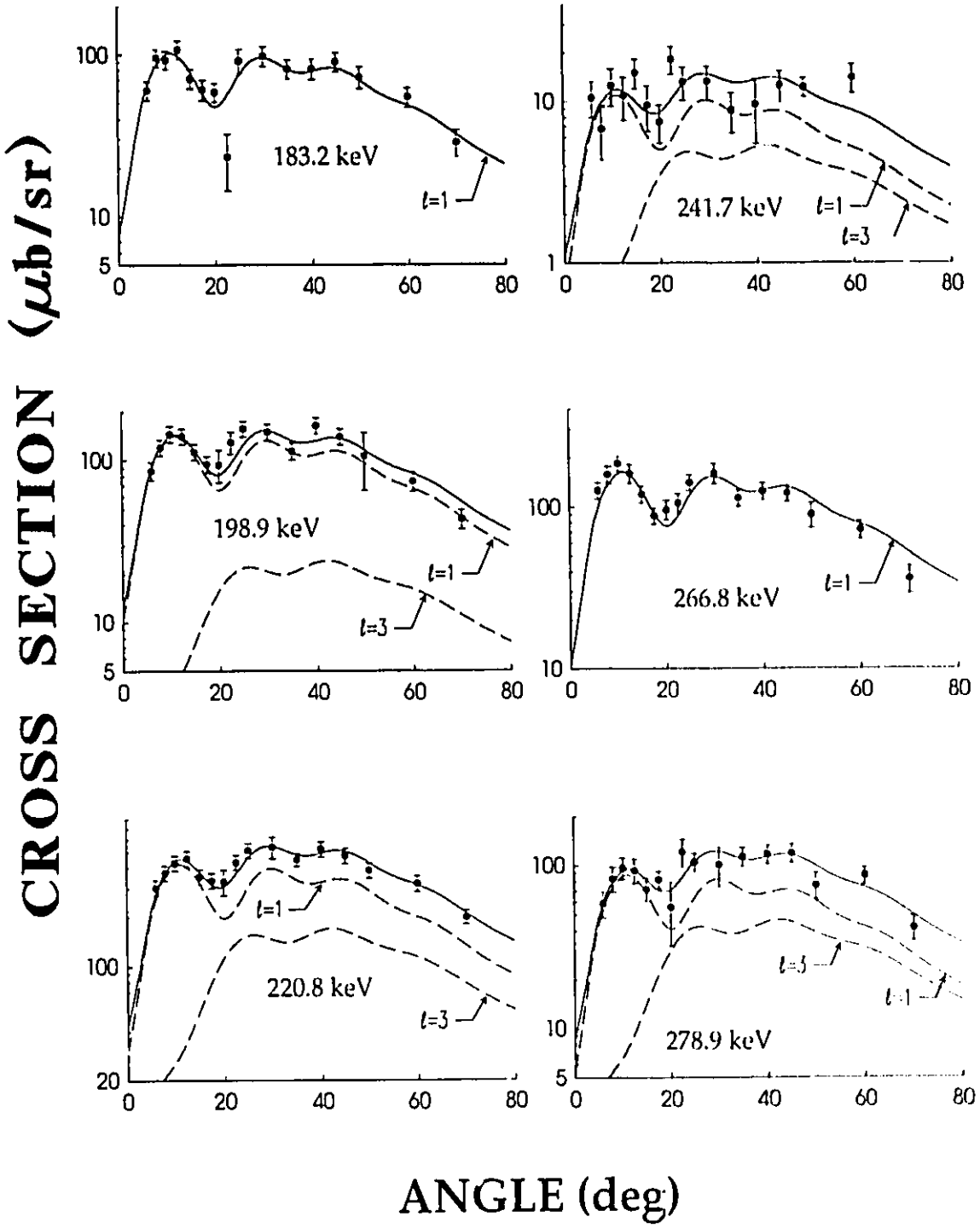

Figure 4.2.7b: See caption for Figure 4.2.7a.

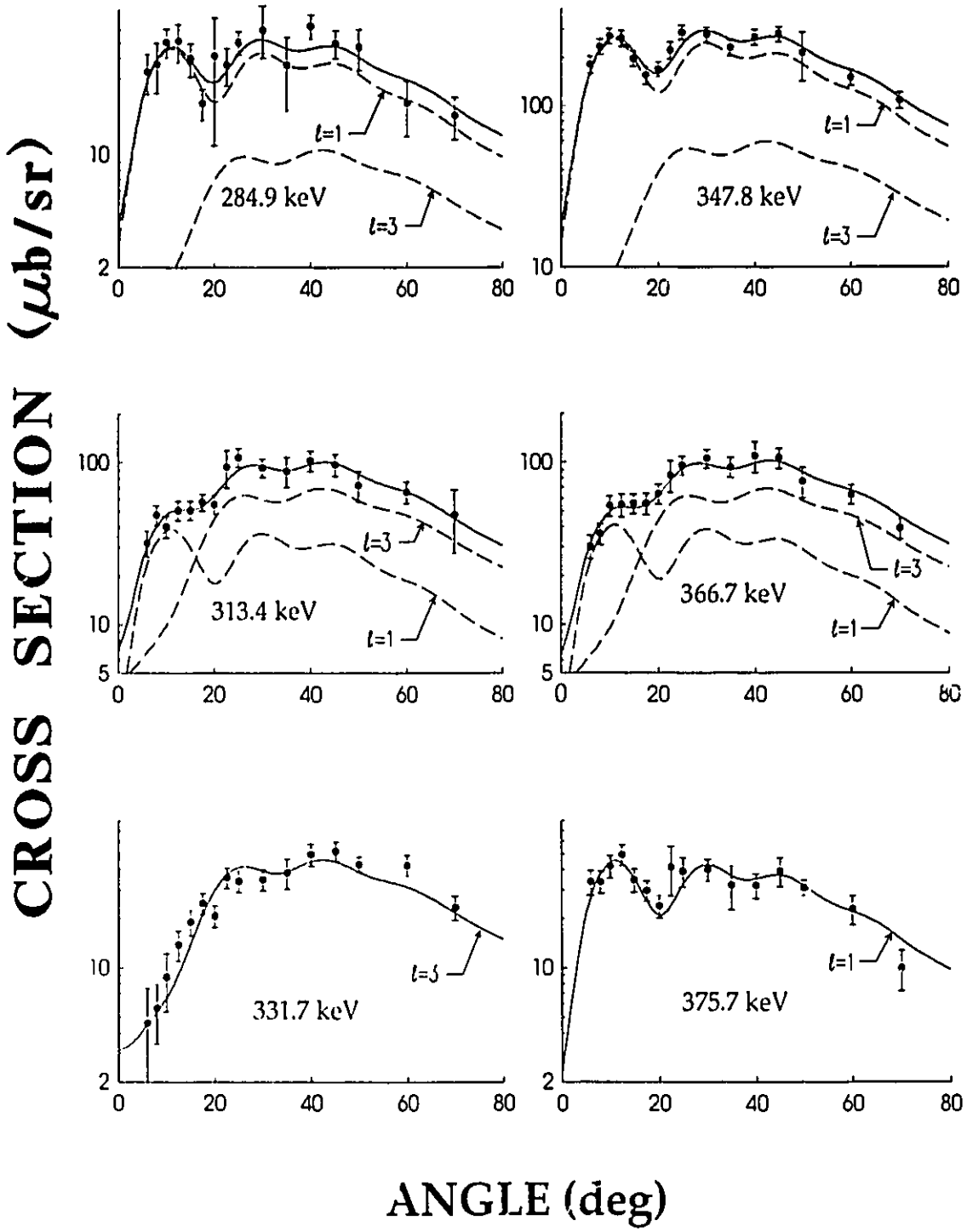

Figure 4.2.7c: See caption for Figure 4.2.7a.

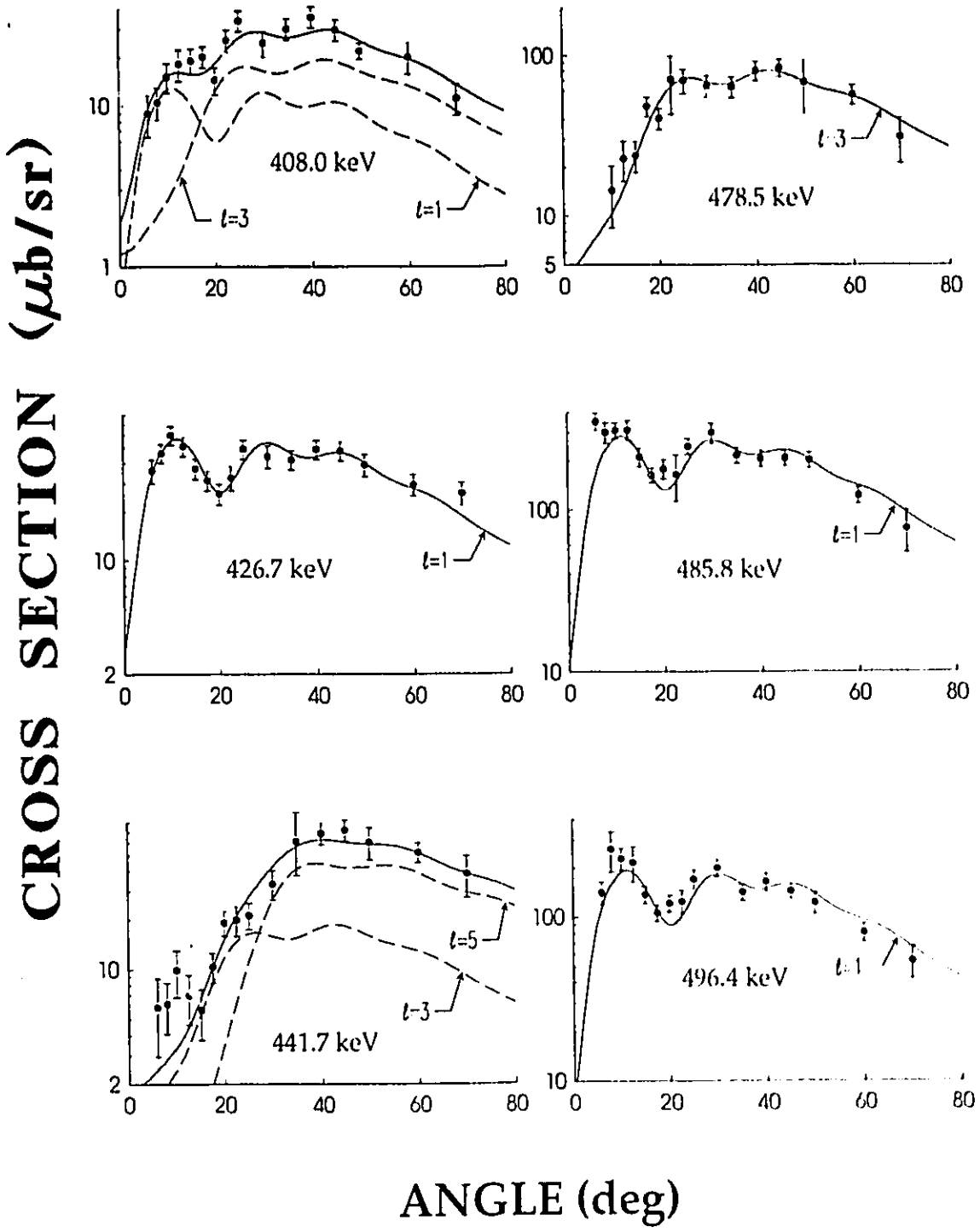

Figure 4.2.7d: See caption for Figure 4.2.7a.

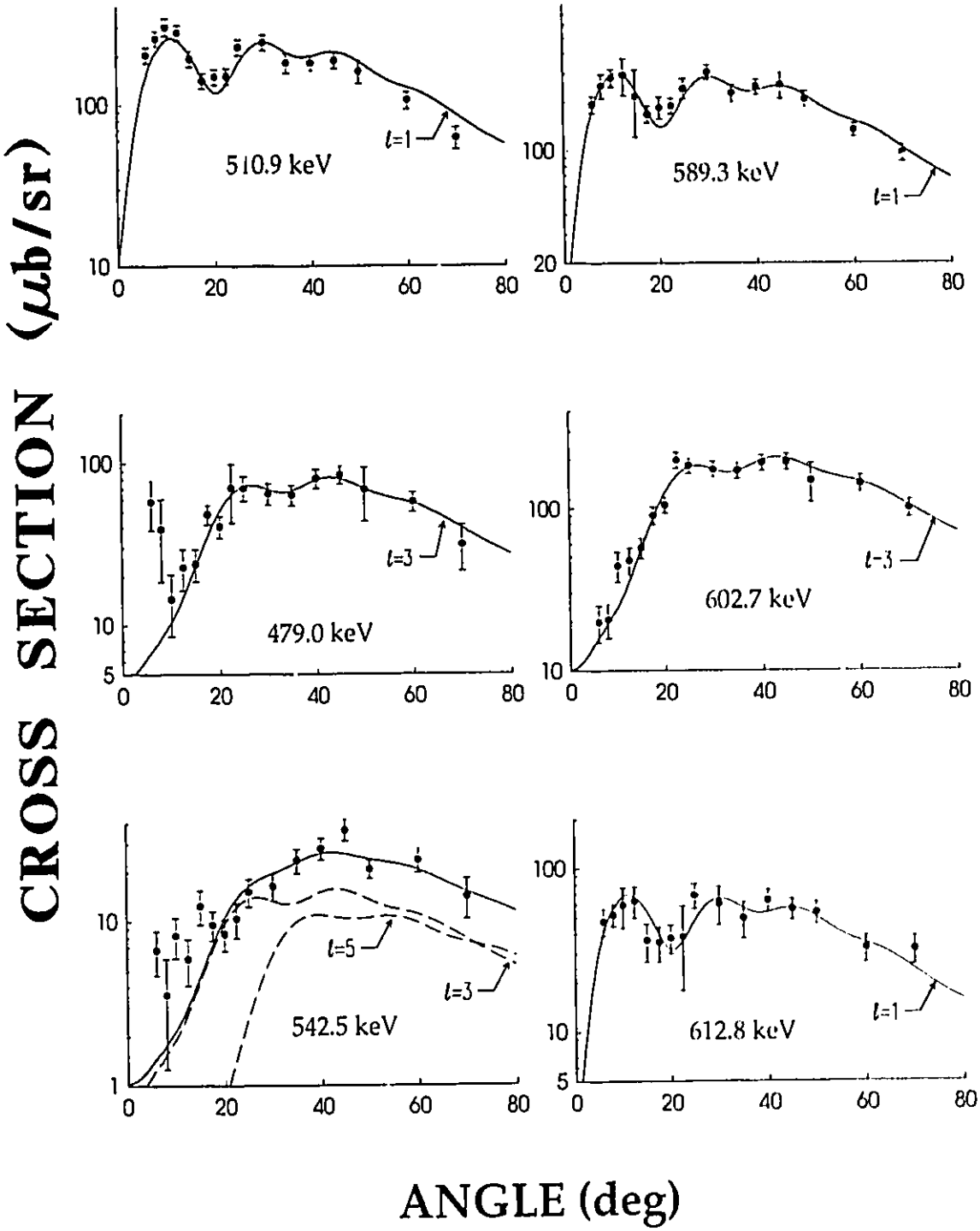

Figure 4.2.7e: See caption for Figure 4.2.7a.

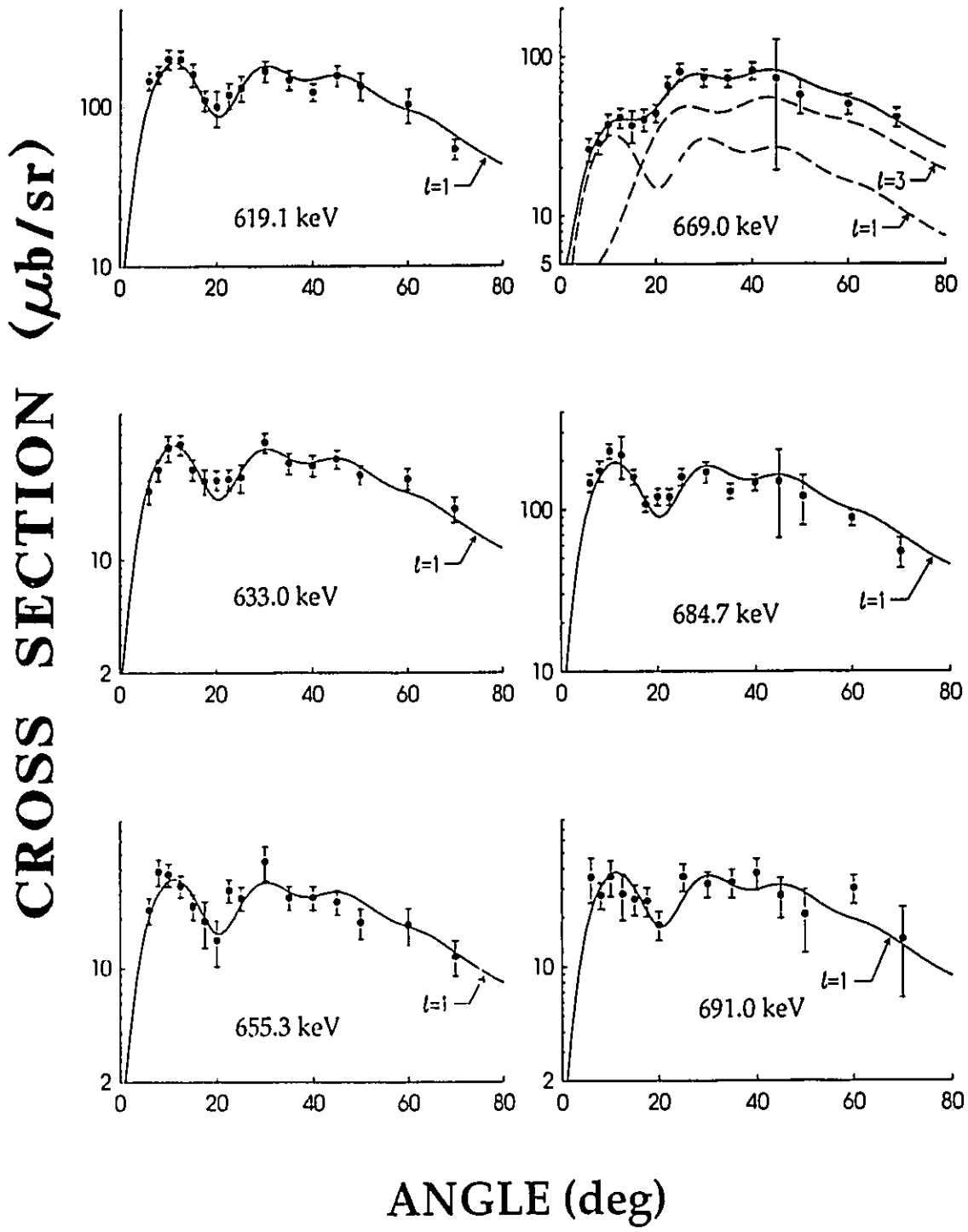

Figure 4.2.7f: See caption for Figure 4.2.7a.

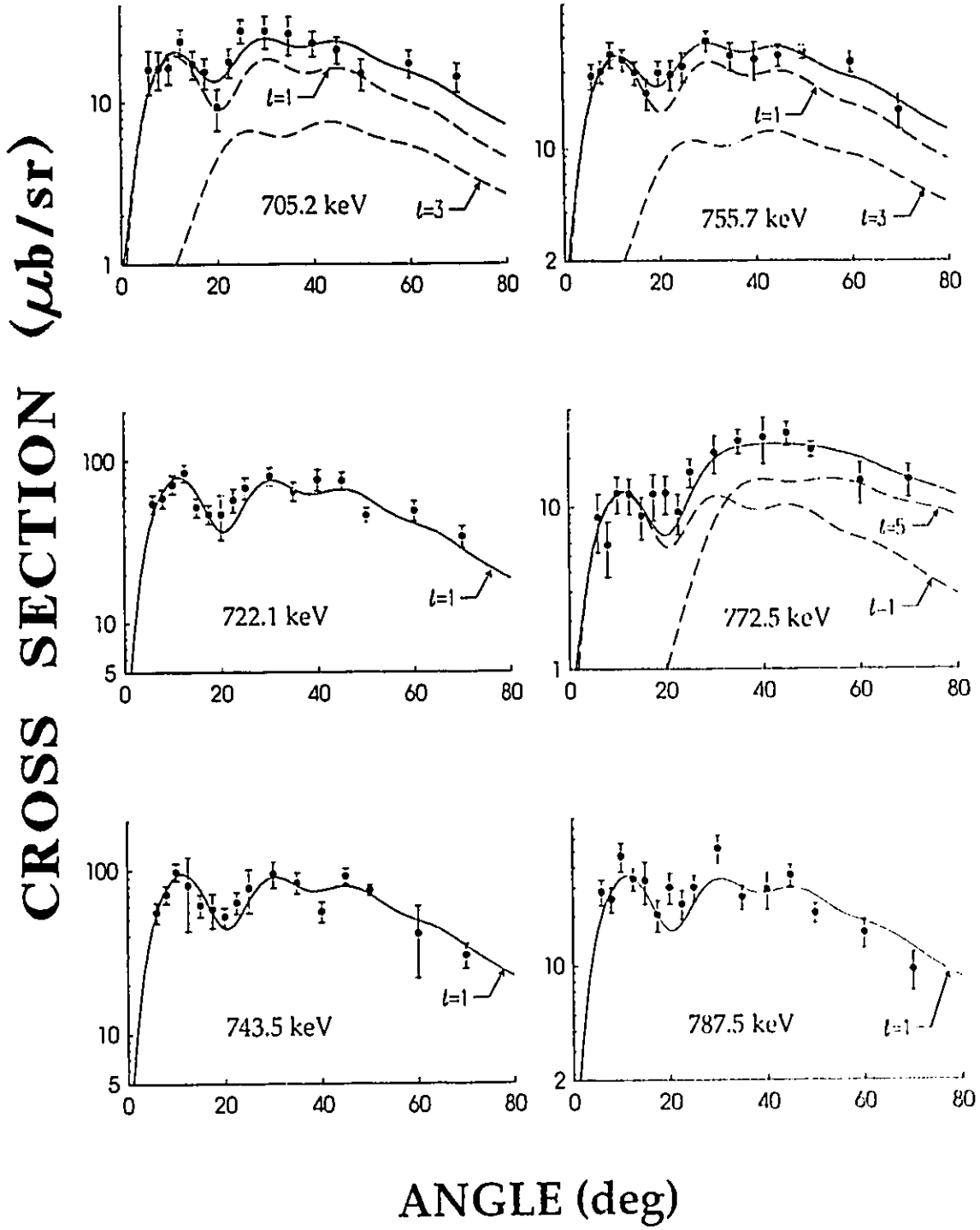

Figure 4.2.7g: See caption for Figure 4.2.7a.

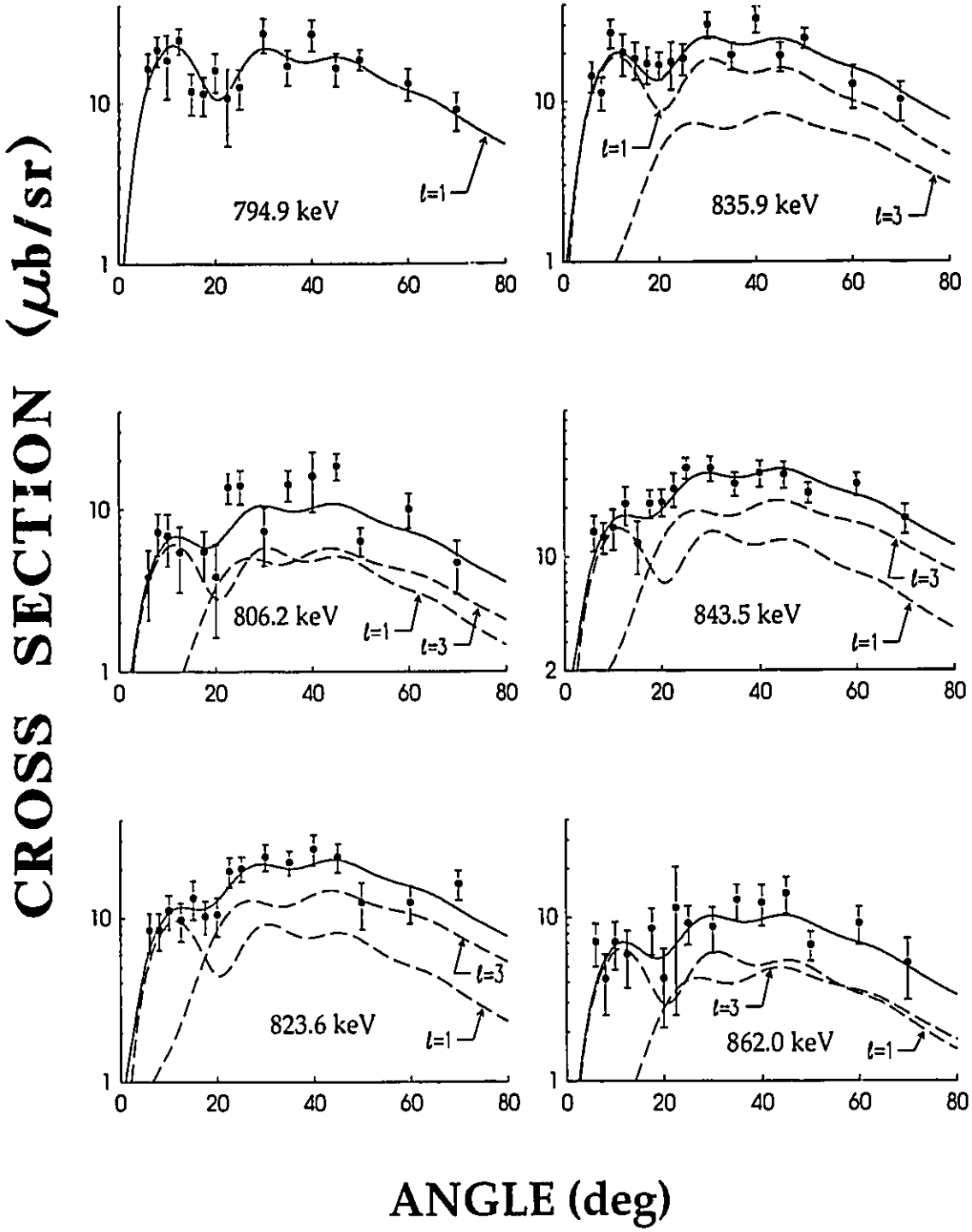

Figure 4.2.7h: See caption for Figure 4.2.7a.

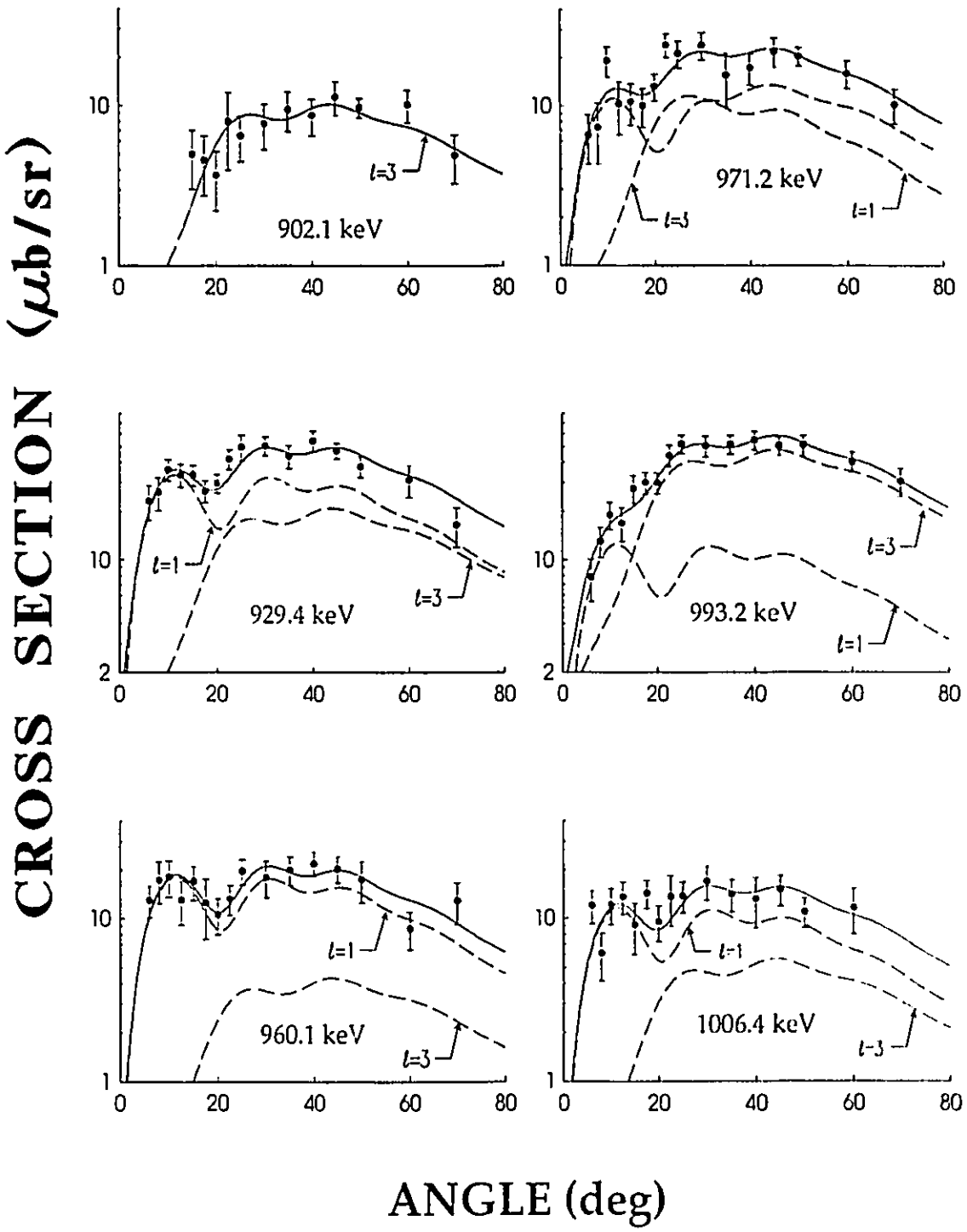

Figure 4.2.7i: See caption for Figure 4.2.7a.

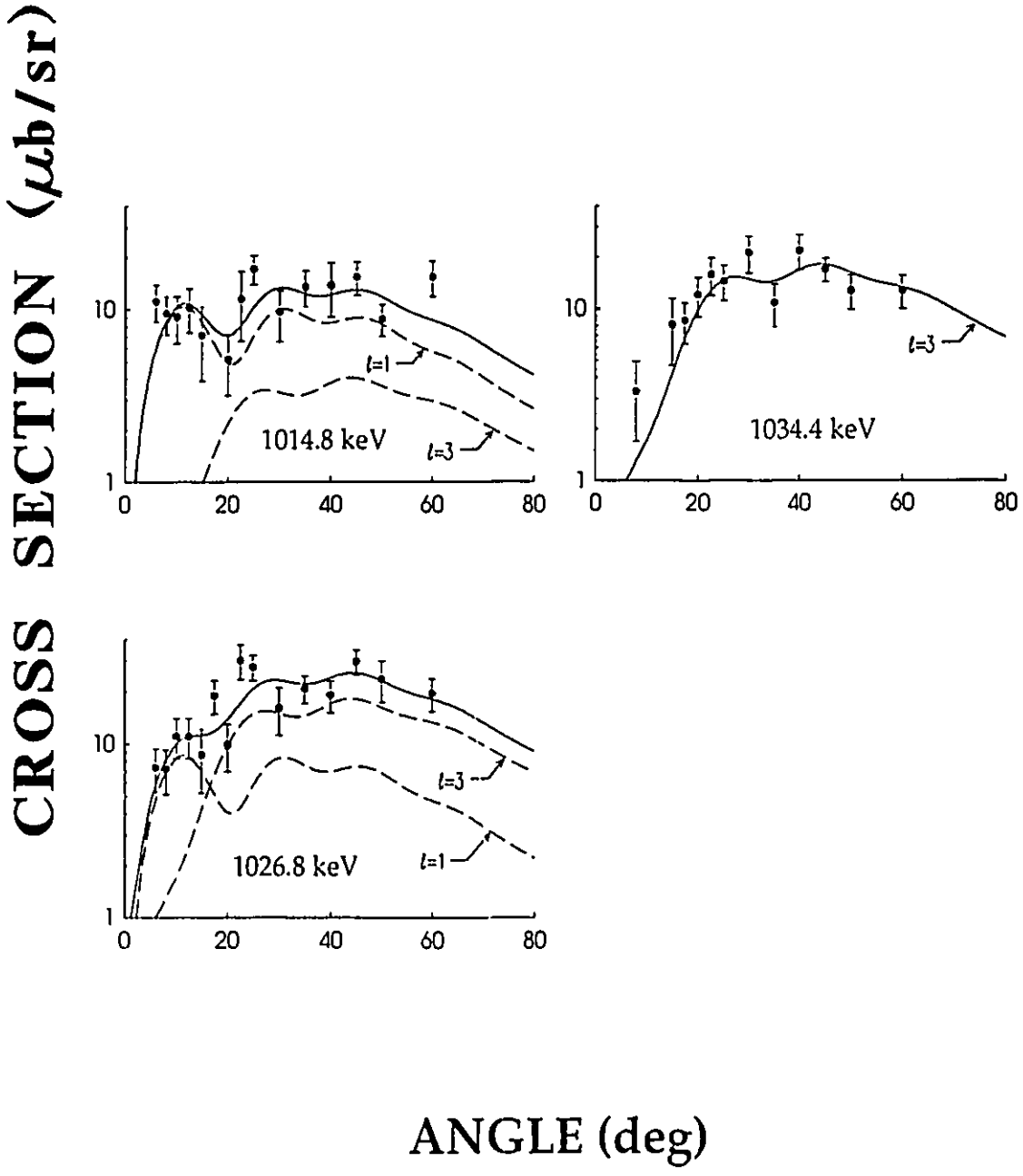

Figure 4.2.7j: See caption for Figure 4.2.7a.

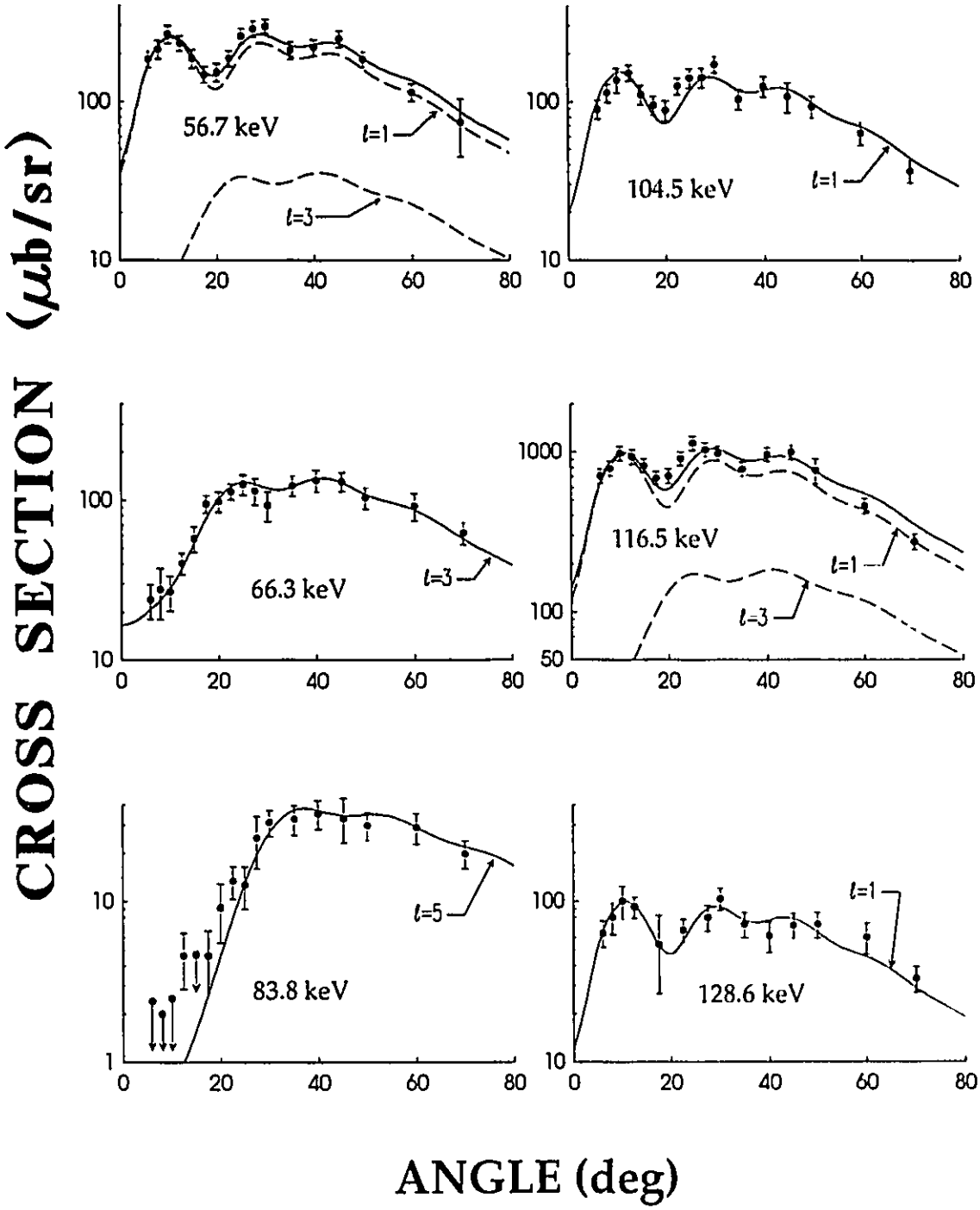

Figure 4.2.8a: Angular distributions of cross sections from the ^{193}Ir(d,t) reaction. The dashed curves are the results of a DWBA calculation for the transferred l-value indicated. The solid curves are the fits to the data.

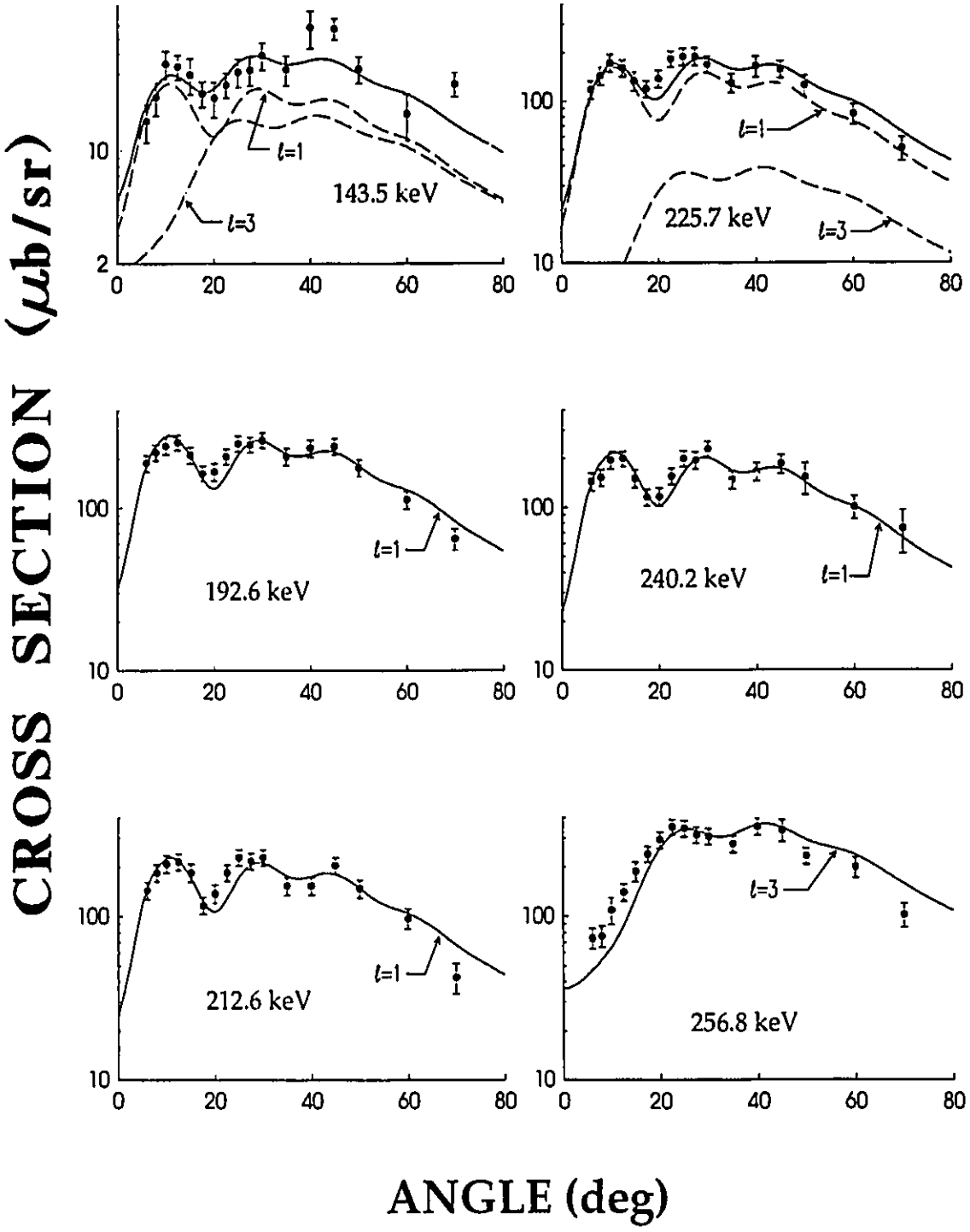

Figure 4.2.8b: See caption for Figure 4.2.8a.

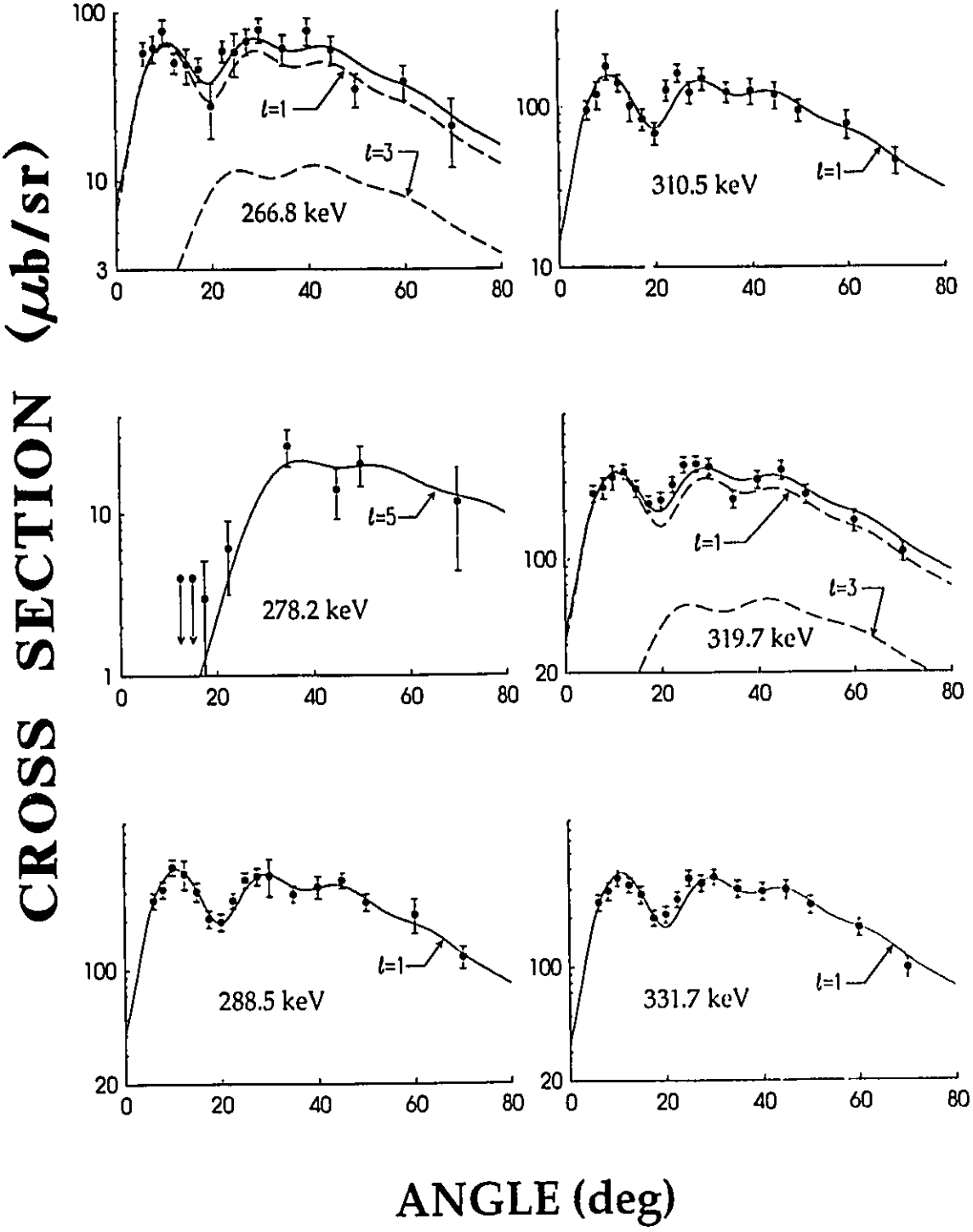

Figure 4.2.8c: See caption for Figure 4.2.8a.

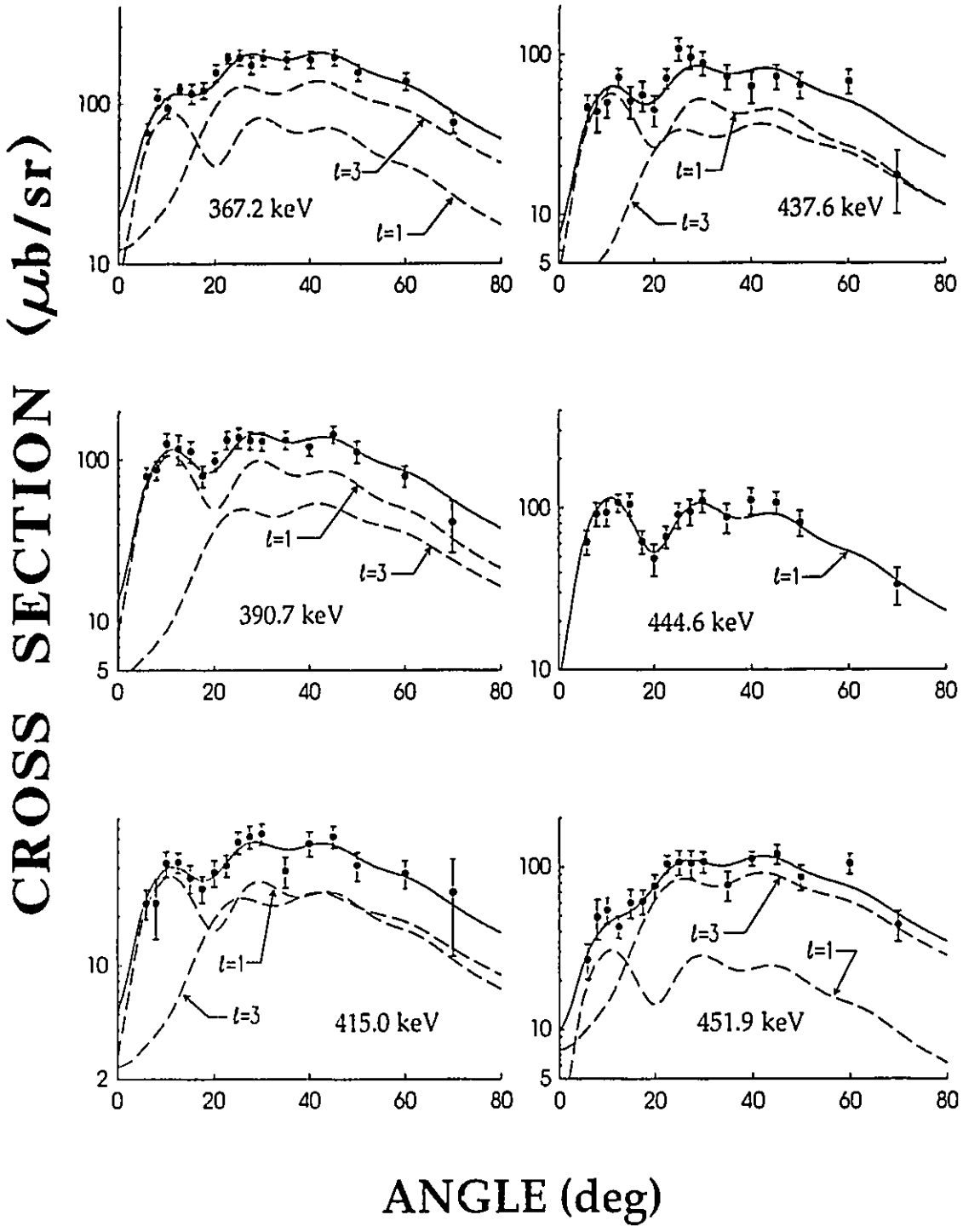

Figure 4.2.8d: See caption for Figure 4.2.8a.

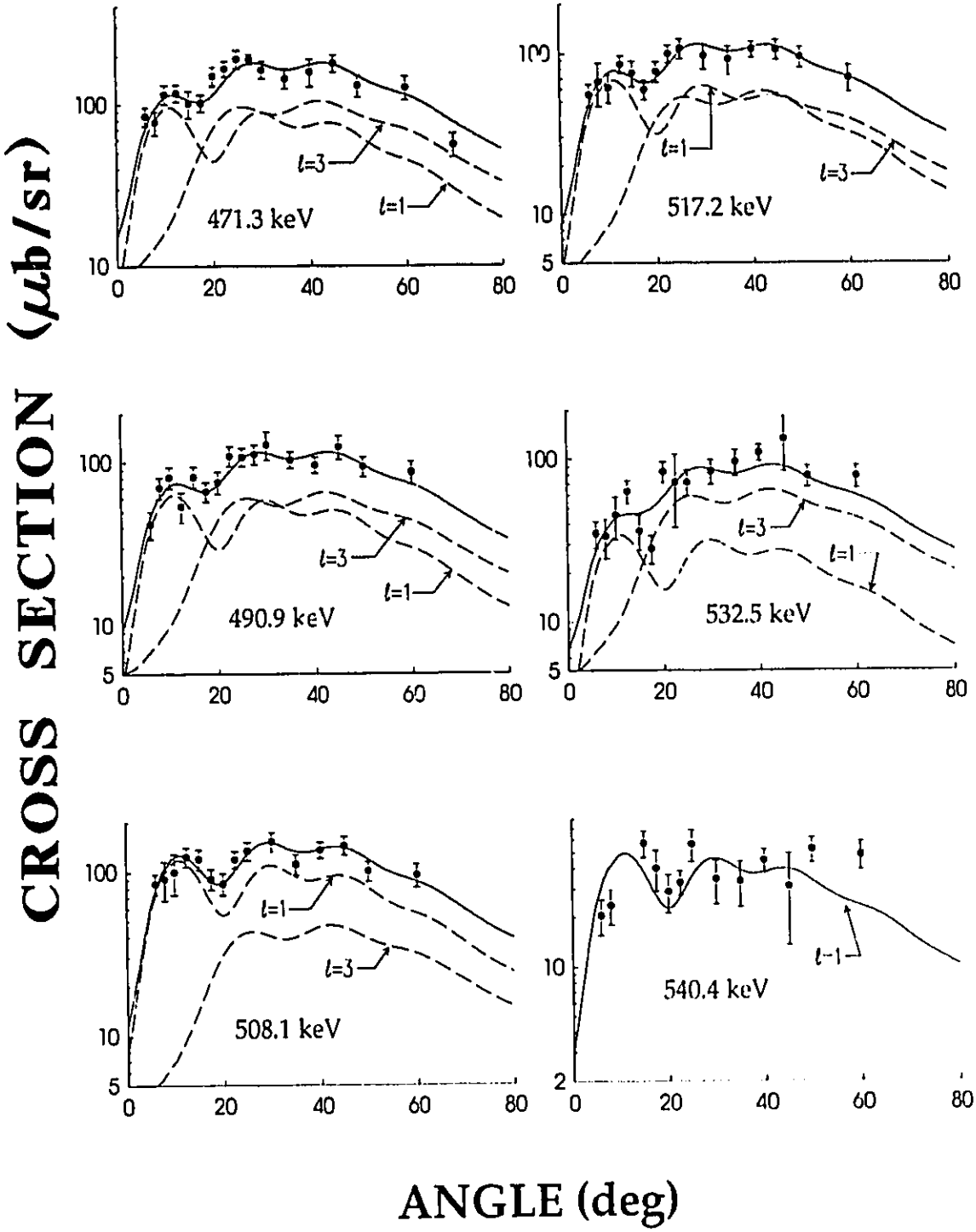

Figure 4.2.8e: See caption for Figure 4.2.8a.

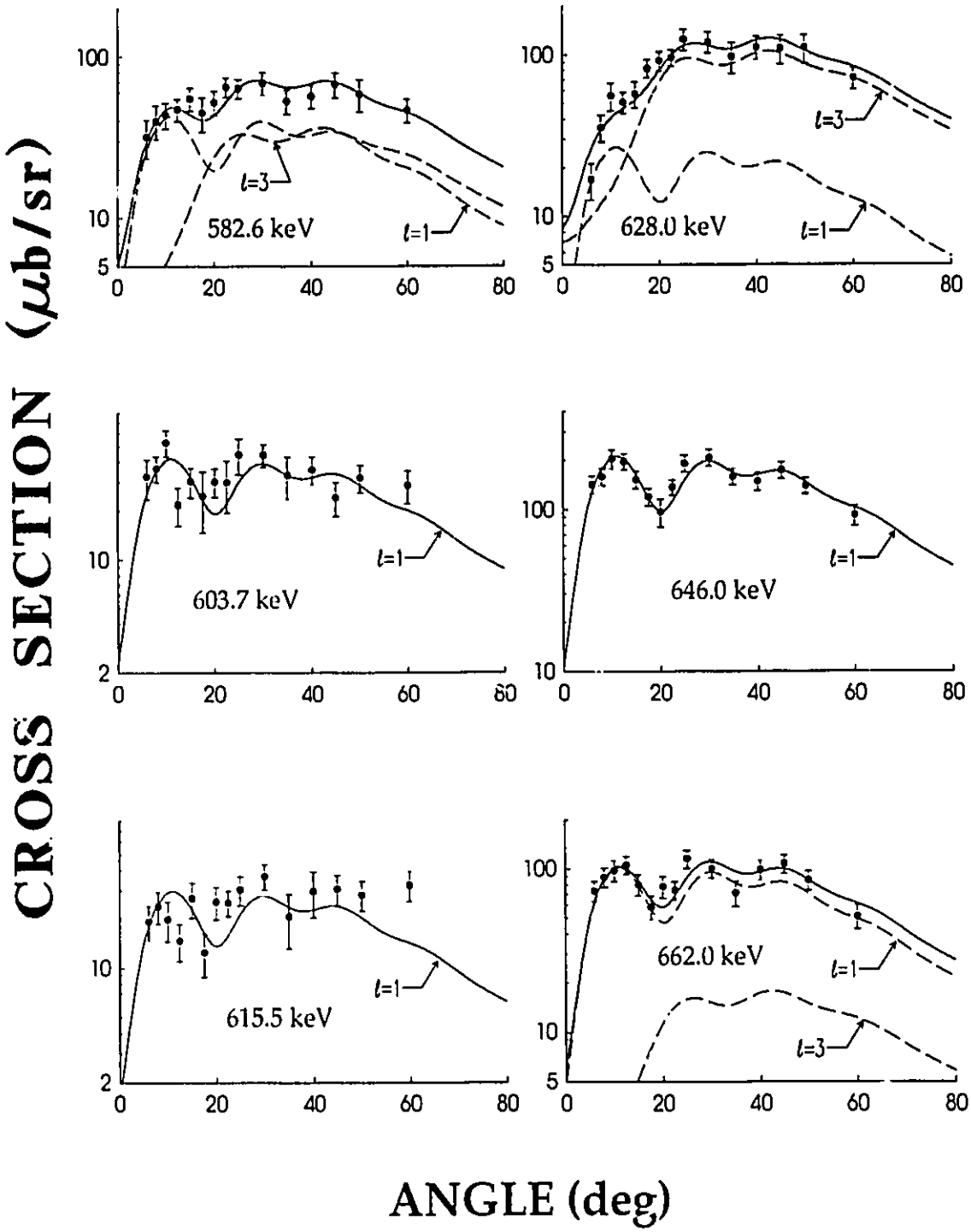

Figure 4.2.8f: See caption for Figure 4.2.8a.

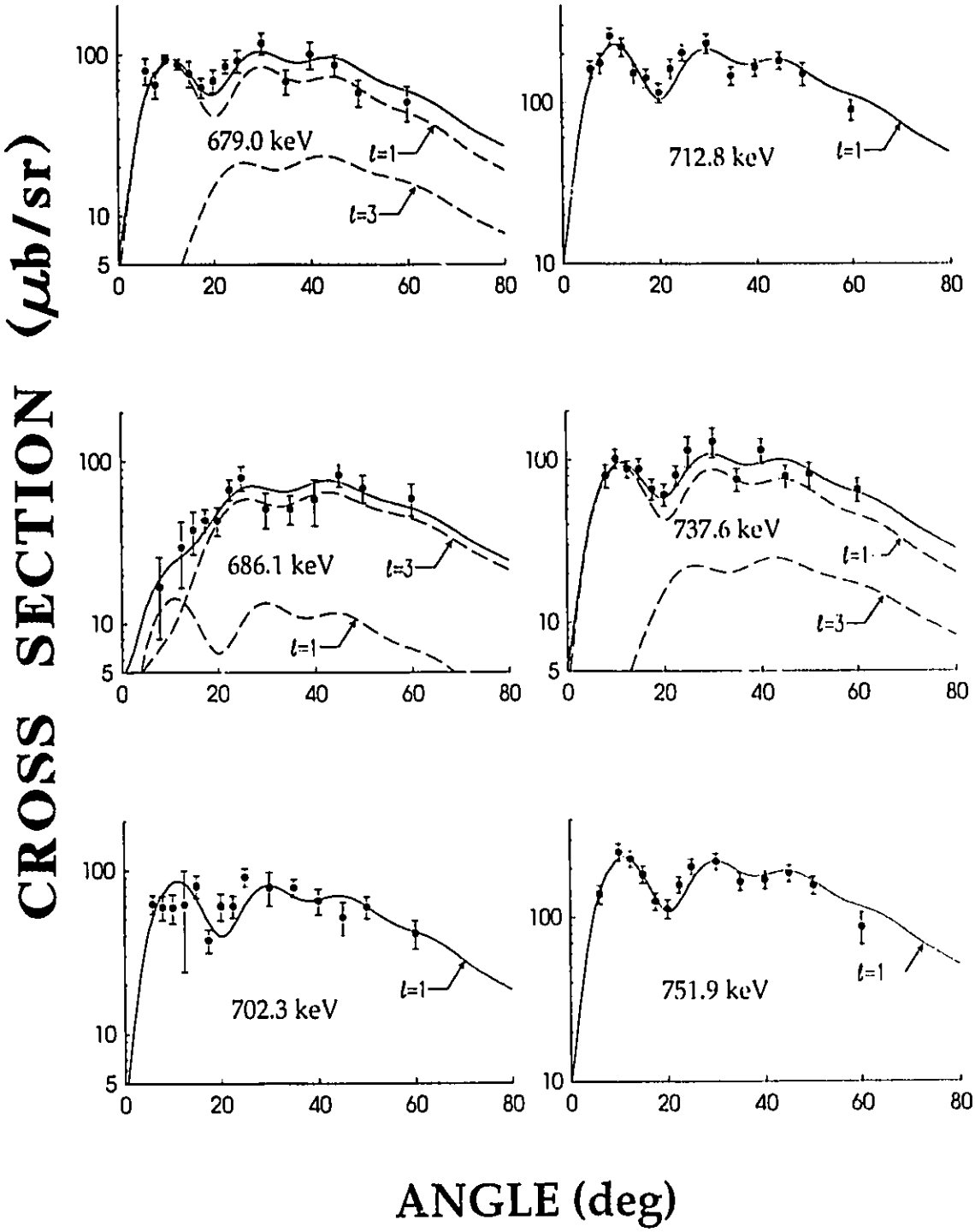

Figure 4.2.8g: See caption for Figure 4.2.8a.

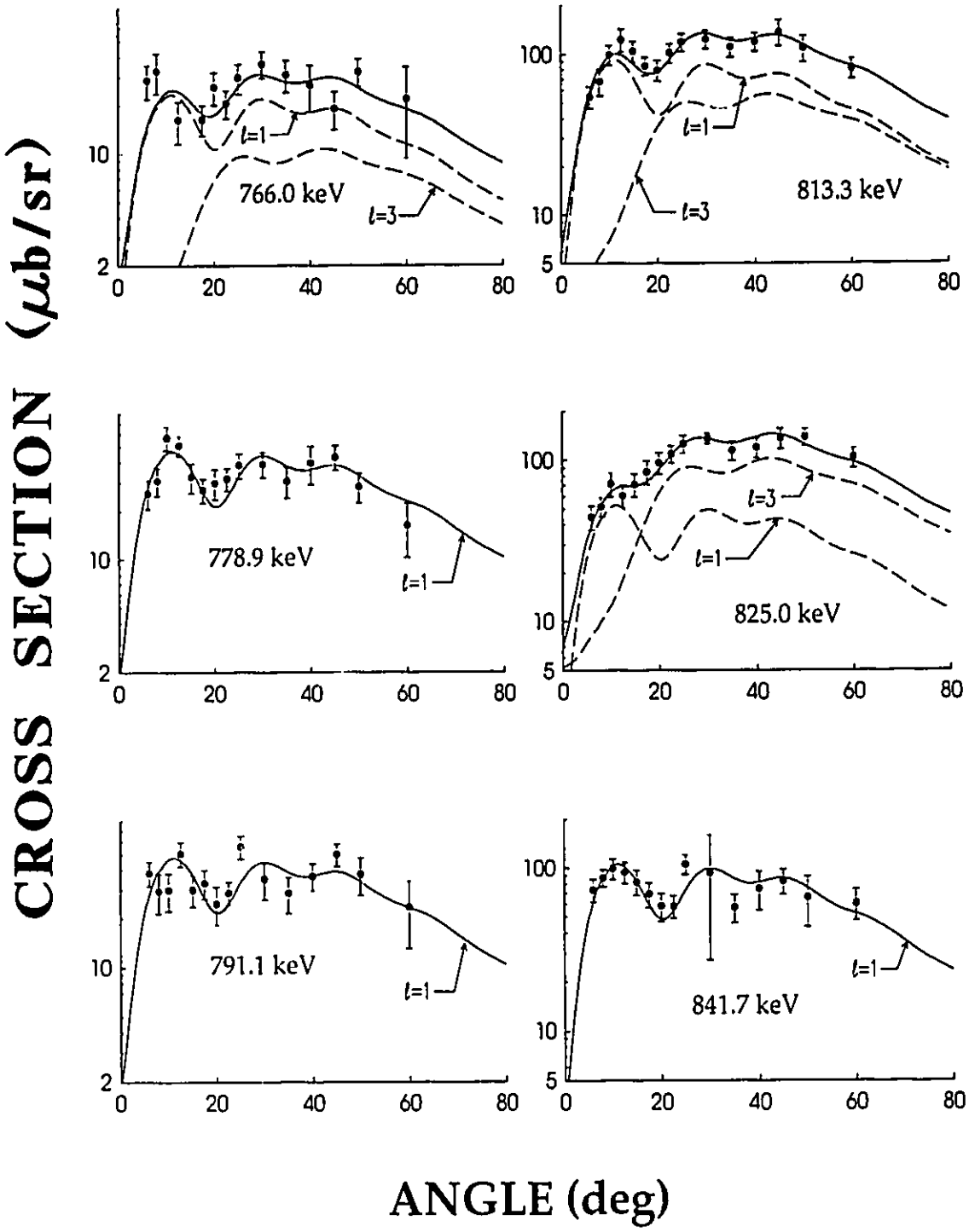

Figure 4.2.8h: See caption for Figure 4.2.8a.

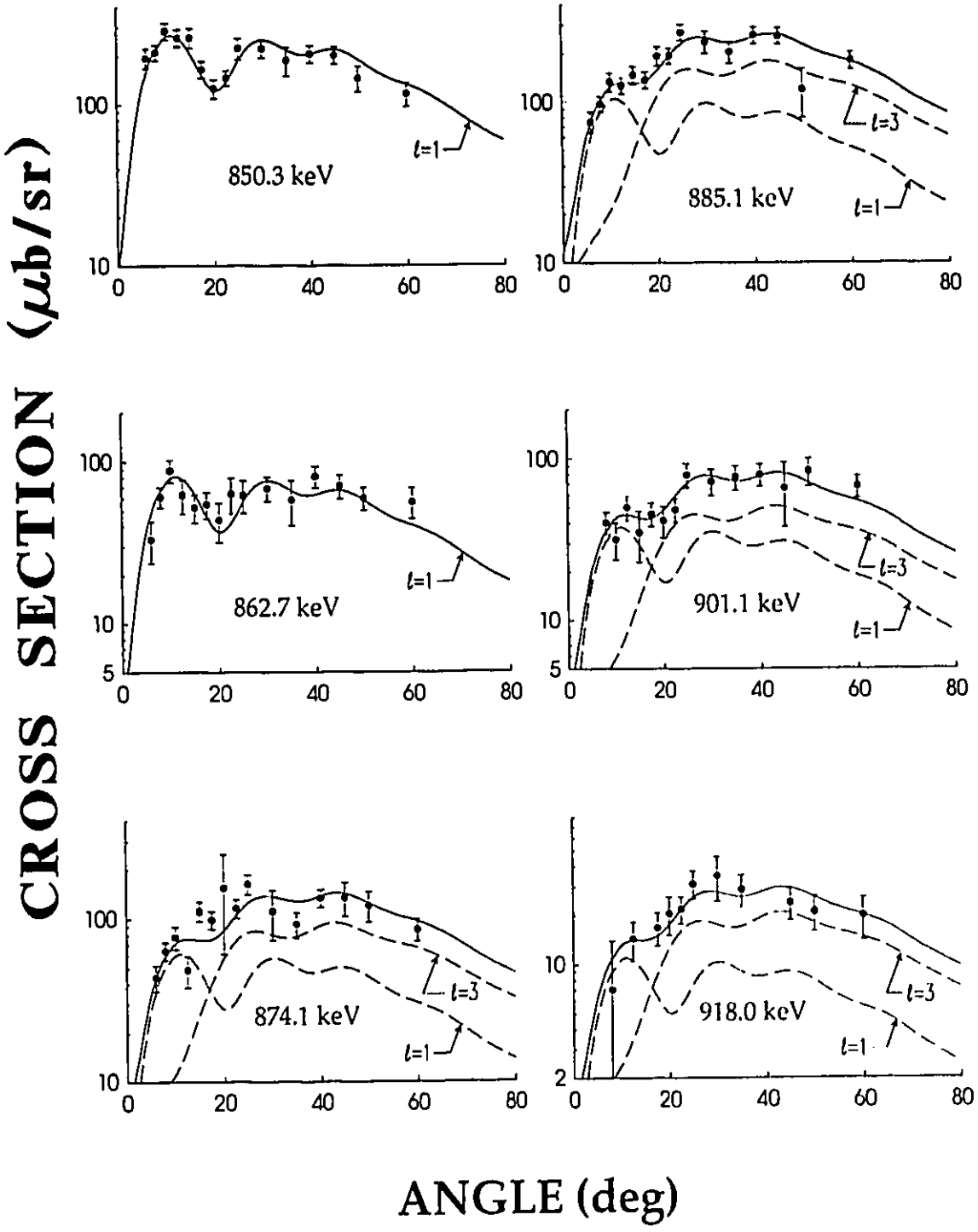

Figure 4.2.8i: See caption for Figure 4.2.8a.

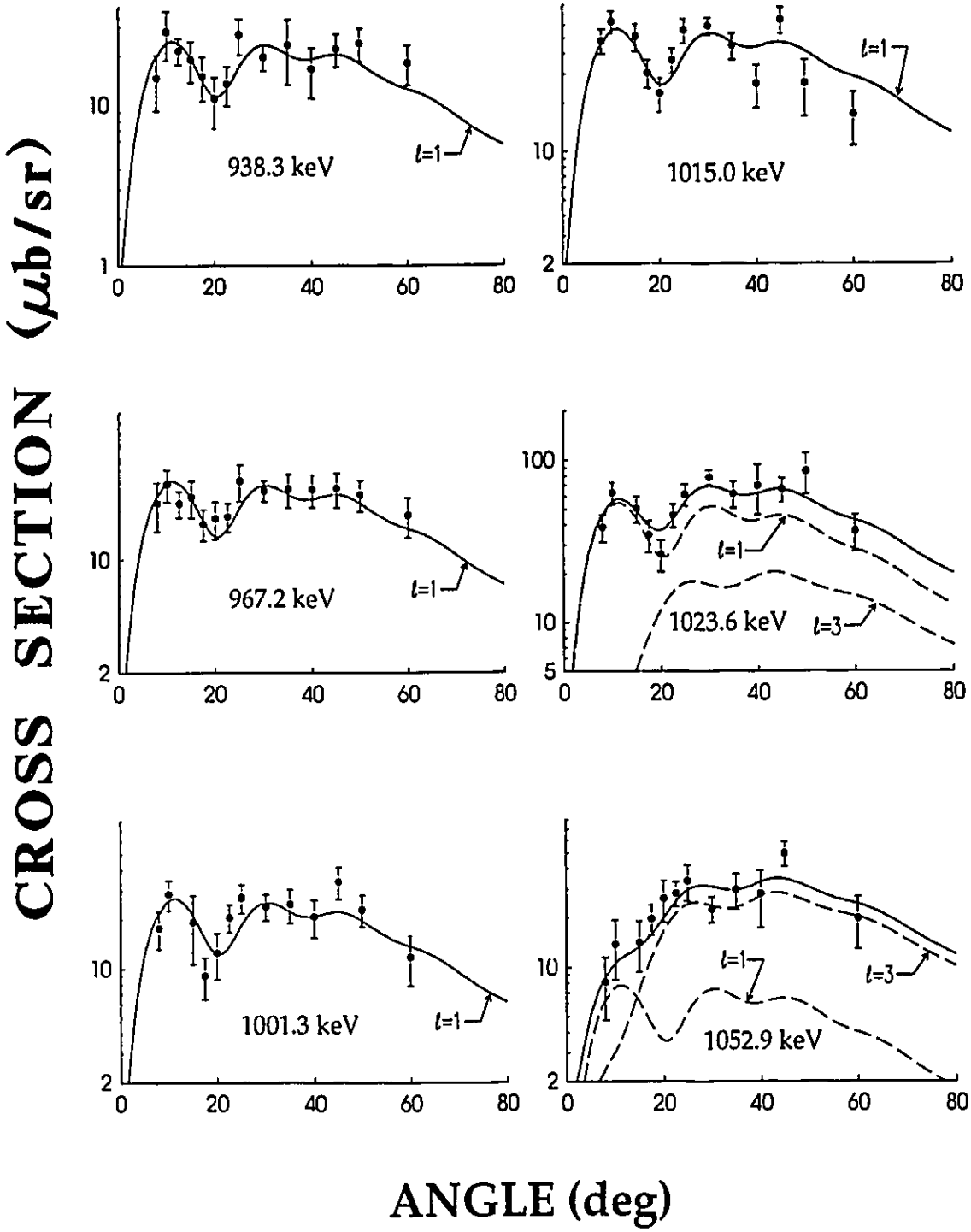

Figure 4.2.8j: See caption for Figure 4.2.8a.

Table 4.2.2: Values of χ^2_ν and F_χ from Fits to Angular Distributions from ^{191}Ir(d,t) Reaction

Relative Energy (keV)	χ^2_ν for one l-value	χ^2_ν for two l-values	F_χ
0	1.564	1.393	6.90
25.9	0.664	0.660	1.11
83.0	1.629	0.713	20.3
144.0	1.021	1.057	0.48
173.8	9.140	0.315	420
198.9	1.467	1.166	4.88
220.8	2.788	0.525	65.7
241.7	1.908	1.474	5.11
278.9	2.371	0.853	27.7
284.9	0.866	0.772	2.83
313.4	7.385	0.500	208
331.7	1.566	1.462	2.07
347.8	1.479	0.741	16.0
366.7	7.683	0.343	322
408.0	4.162	1.105	42.5
441.7	4.245	1.237	37.5
542.5	3.518	2.526	6.9
602.7	1.021	0.702	7.8
669.0	8.722	0.385	325
705.2	1.502	1.021	8.1
755.7	1.259	0.557	19.9
772.5	4.548	1.007	53.7
806.2	2.763	2.024	6.11

Table 4.2.2 -continued

Relative Energy (keV)	χ^2_ν for one l-value	χ^2_ν for two l-values	F_χ
823.6	3.768	0.853	52.3
835.9	1.615	1.073	8.5
843.5	4.331	0.769	70.5
862.0	1.526	0.923	9.9
929.4	7.561	0.790	129
960.1	0.868	0.728	3.89
971.2	3.331	0.906	41.2
993.2	2.886	0.454	81.3
1006.4	1.541	1.152	6.7
1014.8	1.745	1.562	2.52
1026.8	5.038	1.319	40.5

The relative excitation energies, and absolute cross sections at $\theta = 45°$, of levels observed in the (d,t) reactions are listed in Table 4.2.4 for ^{190}Ir and Table 4.2.5 for ^{192}Ir. The uncertainties on the energies are expressed for the least significant digit, and are given in the brackets. As can be seen, for strongly populated, well resolved peaks, the energy uncertainty is approximately 0.1 keV. The uncertainties on the cross sections are the addition in quadrature of the statistical uncertainty as given by the peak-fitting program, SPECTR, plus an additional 10%, found to be a reasonable estimate of the reproducibility error. Also listed in the tables are the strengths and possible spin values for the populated levels.

Table 4.2.3: Values of χ^2_ν and F_χ from Fits to Angular Distributions from ^{193}Ir(d,t) Reaction

Energy (keV)	χ^2_ν for one l-value	χ^2_ν for two l-values	F_χ
56.7	0.786	0.559	7.5
66.3	0.375	0.374	1.05
83.8	0.907	0.347	29.2
104.5	1.169	1.081	2.30
115.6	2.398	1.871	5.5
143.5	2.427	1.433	12.11
192.6	1.141	1.093	1.71
212.6	1.798	1.882	0.29
225.7	2.058	1.549	6.25
256.8	3.401	1.704	16.9
266.8	1.320	1.195	2.68
319.7	1.601	1.358	3.86
367.2	12.64	0.885	213.5
390.7	2.208	0.669	37.8
415.0	2.394	0.495	62.4
437.6	2.634	1.228	19.3
451.9	2.494	0.751	38.2
471.3	6.727	1.249	71.1
490.9	4.520	0.775	73.5
508.1	4.718	0.776	77.2
517.2	3.500	0.513	85.2
532.5	6.618	2.501	24.0
582.6	3.103	0.623	56.7
628.0	3.282	1.093	29.0

Table 4.2.3 -continued

Energy (keV)	χ^2_ν for one l-value	χ^2_ν for two l-values	F_χ
662.0	1.391	1.150	3.93
679.0	2.592	1.723	8.07
686.1	0.945	0.769	3.75
737.6	1.443	0.935	8.06
766.0	2.213	1.381	6.02
813.3	3.048	0.493	67.4
825.0	7.158	0.454	192.0
874.1	8.596	2.078	44.9
885.1	10.828	1.044	132.2
901.1	4.822	0.721	74.9
918.0	1.130	0.477	14.71
1023.6	1.426	0.845	9.25
1052.9	1.435	1.047	5.07

The Q-values involved in (d,p) reactions are such that protons from reactions on lighter materials often fall at the same position on the focal plane as protons from reactions on heavy targets. The impurity peaks that result from the reactions on lighter materials can sometimes obscure a peak that is of interest, although this normally occurs only for a few angles. The proton spectrum obtained for the ^{191}Ir(d,p) and ^{193}Ir(d,p) reactions, shown in Figure 4.2.3 and Figure 4.2.4, respectively, contain several impurity peaks which are labelled. However, for strongly populated levels, the presence of impurity peaks does not seriously hinder the extraction of spectroscopic strengths, although two-component fits to the data were rarely performed since the (d,p) data were not as sensitive to the presence of $l = 3$

Table 4.2.4: States in ^{190}Ir Populated with (d,t) Reactions

Relative Energy (keV)	Cross Section (μb/sr) at $\theta = 45°$	Transferred l	Final Spin	Transfer Strength $l = 1$	$l = 3$	$l = 5$
0[a])	74(9)	(1), 3	1^-–5^-	(<0.004)	0.100(8)	
25.9(1)	176(19)	1	0^-–3^-	0.089(3)		
38.1(2)[a])	23(4)	5	3^-–7^-			0.325(24)
83.0(1)	563(71)	1, 3	1^-–3^-	0.224(14)	0.224(59)	
144.0(1)	37(5)	1	0^-–3^-	0.019(1)		
173.8(1)[b])	257(62)	1, 3	1^-–3^-	0.048(4)	0.316(28)	
183.2(3)	90(12)	1	0^-–3^-	0.045(2)		
198.9(1)	140(16)	1, 3	1^-–3^-	0.062(4)	0.044(18)	
223.4(1)[b])	477(50)	1, 3	0^-–5^-	0.187(12)	0.313(53)	
241.7(5)	13(3)	1, 3	1^-–3^-	0.005(1)	0.010(4)	
266.8(1)	121(14)	1	0^-–3^-	0.074(2)		
278.9(1)	119(15)	1, 3	1^-–3^-	0.039(4)	0.088(18)	
284.9(2)	49(10)	1, 3	1^-–3^-	0.021(4)	0.020(13)	
313.4(2)	97(15)	1, 3	1^-–3^-	0.018(2)	0.134(13)	
331.7(2)	52(5)	3	1^-–5^-		0.089(4)	
347.8(1)	282(30)	1, 3	1^-–3^-	0.121(8)	0.116(34)	
366.7(1)	106(15)	1, 3	1^-–3^-	0.019(2)	0.134(13)	
375.7(2)	39(8)	1	0^-–3^-	0.021(1)		
408.0(2)	29(4)	1, 3	1^-–3^-	0.006(1)	0.039(5)	
426.7(1)	48(6)	1	0^-–3^-	0.027(1)		
441.7(3)[a])	72(10)	(3), 5	3^-–7^-		(<0.038)	0.87(11)
452.3(4)[c])	16(6)			<0.003	<0.006	<0.024
478.5(2)	84(11)	3	1^-–5^-		0.166(8)	

Table 4.2.4 - continued

Relative Energy (keV)	Cross Section (μb/sr) at $\theta = 45°$	Transferred l	Final Spin	Transfer Strength $l = 1$	$l = 3$	$l = 5$
485.8(2)	210(23)	1	0^-–3^-	0.140(5)		
496.4(2)	144(15)	1	0^-–3^-	0.096(3)		
510.9(2)	188(21)	1	0^-–3^-	0.128(4)		
542.5(4)	36(5)	3, 5	3^-–5^-		0.033(5)	0.226(58)
589.3(2)	256(47)	1	0^-–3^-	0.157(5)		
602.7(2)[a])	194(21)	(1), 3	1^-–5^-	(<0.007)	0.705(35)	
612.8(4)	155(17)	1	0^-–3^-	0.036(2)		
619.1(3)	42(6)	1	0^-–3^-	0.098(4)		
633.0(3)	15(4)	1	0^-–3^-	0.027(1)		
655.3(3)	25(4)	1	0^-–3^-	0.019(1)		
669.0(2)	73(10)	1, 3	1^-–3^-	0.017(2)	0.123(11)	
684.7(3)	150(17)	1	0^-–3^-	0.105(4)		
705.2(4)	21(4)	1, 3	1^-–3^-	0.011(1)	0.017(6)	
722.1(2)	75(10)	1	0^-–3^-	0.044(2)		
743.5(3)	92(10)	1	0^-–3^-	0.053(2)		
755.7(3)	39(6)	1, 3	1^-–3^-	0.020(2)	0.030(9)	
772.5(8)[a])	29(5)	(1), 5	3^-–7^-	(<0.007)		0.341(46)
787.5(4)	36(5)	1	0^-–3^-	0.020(1)		
794.9(4)	16(4)	1	0^-–3^-	0.013(1)		
806.2(5)	18(3)	1, 3	1^-–3^-	0.004(1)	0.014(4)	
823.6(5)	24(5)	1, 3	1^-–3^-	0.006(1)	0.035(5)	
835.9(4)	19(4)	1, 3	1^-–3^-	0.011(1)	0.020(7)	
843.5(3)	32(6)	1, 3	1^-–3^-	0.009(1)	0.053(7)	
862.0(6)	14(4)	1, 3	1^-–3^-	0.004(1)	0.012(1)	
902.1(4)	11(3)	3	1^-–5^-		0.025(2)	

Table 4.2.4 -continued

Relative Energy (keV)	Cross Section (μb/sr) at $\theta = 45°$	Transferred l	Final Spin	Transfer Strength $l = 1$	$l = 3$	$l = 5$
862.0(6)	14(4)	1, 3	1^-–3^-	0.004(1)	0.012(1)	
902.1(4)	11(3)	3	1^-–5^-		0.025(2)	
929.4(4)	47(5)	1, 3	1^-–3^-	0.020(2)	0.052(10)	
960.1(5)	20(4)	1, 3	1^-–3^-	0.011(2)	0.011(6)	
971.2(4)	22(5)	1, 3	1^-–3^-	0.006(1)	0.037(6)	
993.2(4)	51(7)	1, 3	1^-–3^-	0.008(1)	0.123(9)	
1006.4(10)	15(3)	1, 3	1^-–3^-	0.007(1)	0.015(5)	
1014.8(8)	15(3)	1	0^-–3^-	0.008(1)		
1026.8(8)	30(5)	1, 3	1^-–3^-	0.006(1)	0.047(6)	
1034.4(12)	17(3)	3	1^-–5^-		0.047(3)	
1062.9(14)	11(3)					
1082.8(6)	8(3)					
1092.4(11)	13(3)					
1115.6(12)	10(3)					
1135.9(15)	6(4)					
1143.0(14)	13(5)					

[a]) Peaks where there may be impurity contributions. At forward angles, the presence of an impurity peaks may masquerade as an $l = 1$ component.

[b]) Levels that are known to be, or may be, due to unresolved doublets.

[c]) A good fit to the angular distribution could not be obtained. The strengths listed are upper limits.

Table 4.2.5: States in ^{192}Ir Populated with (d,t) Reactions

Energy (keV)	Cross Section (μb/sr) at $\theta = 45°$	Transferred l-value	Possible Spin	Transfer Strength l=1	l=3	l=5
56.7[a])	248(29)	1, 3	1^-–3^-	0.097(7)	0.056(31)	
66.3(2)	131(17)	3	1^-–5^-		0.216(8)	
83.8(3)	33(10)	(3), 5	3^-–7^-		(<0.011)	0.553(38)
104.5(1)	109(23)	1	0^-–3^-	0.061(2)		
116.5(1)	1001(110)	1, 3	1^-–3^-	0.38(2)	0.30(9)	
128.6(3)	71(13)	1	0^-–3^-	0.039(2)		
143.5(2)	57(9)	1, 3	1^-–3^-	0.010(1)	0.027(6)	
192.6(1)	240(27)	1	0^-–3^-	0.114(3)		
212.6(1)	205(24)	1	0^-–3^-	0.093(3)		
225.7(2)	158(19)	1, 3	1^-–3^-	0.066(5)	0.065(21)	
240.2(2)	186(24)	1	0^-–3^-	0.089(3)		
256.8(1)	333(50)	(1), 3	1^-–5^-	(<0.022)	0.509(28)	
266.8(2)	60(12)	1, 3	1^-–3^-	0.026(3)	0.021(12)	
278.2(10)	14(5)	5	3^-–7^-			0.34(5)
288.5(1)	354(39)	1	0^-–3^-	0.173(5)		
310.5(2)	120(33)	1	0^-–3^-	0.066(3)		
319.7(2)	357(48)	1, 3	1^-–3^-	0.144(10)	0.098(43)	
331.7(2)	297(38)	1	0^-–3^-	0.159(5)		
367.2(2)	195(23)	1, 3	1^-–3^-	0.037(3)	0.245(18)	
390.7(2)	144(18)	1, 3	1^-–3^-	0.046(4)	0.096(19)	
415.0(3)	62(9)	1, 3	1^-–3^-	0.015(2)	0.051(9)	
437.6(3)	73(13)	1, 3	1^-–3^-	0.025(3)	0.067(14)	
444.6(3)	108(17)	1	0^-–3^-	0.050(2)		
451.9(3)	120(16)	1, 3	1^-–3^-	0.014(3)	0.170(14)	

Table 4.2.5 -continued

Energy (keV)	Cross Section (μb/sr) at $\theta = 45°$	Transferred l-value	Possible Spin	Transfer Strength l=1	l=3	l=5
471.3(2)	181(22)	1, 3	1^-–3^-	0.042(4)	0.194(21)	
490.9(3)	125(16)	1, 3	1^-–3^-	0.028(3)	0.122(16)	
508.1(2)	144(18)	1, 3	1^-–3^-	0.053(5)	0.089(22)	
517.2(3)	106(14)	1, 3	1^-–3^-	0.031(3)	0.110(17)	
532.5(4)	134(49)	1, 3	1^-–3^-	0.015(3)	0.123(16)	
540.4(5)	31(17)	1	0^-–3^-	0.022(2)		
582.6(3)	67(12)	1, 3	1^-–3^-	0.020(2)	0.070(12)	
603.7(4)	24(6)	1	0^-–3^-	0.019(1)		
615.5(4)	31(6)	1	0^-–3^-	0.014(1)		
628.0(4)	109(22)	1, 3	1^-–3^-	0.013(2)	0.209(16)	
646.0(2)	174(21)	1	0^-–3^-	0.101(3)		
662.0(3)	108(14)	1, 3	1^-–3^-	0.049(4)	0.036(17)	
679.0(3)	87(13)	1, 3	1^-–3^-	0.043(2)	0.048(13)	
686.1(3)	82(13)	1, 3	1^-–3^-	0.007(4)	0.131(18)	
702.3(5)	51(12)	1	0^-–3^-	0.042(2)		
712.8(3)	183(23)	1	0^-–3^-	0.112(4)		
737.6(3)	80(12)	1, 3	1^-–3^-	0.046(4)	0.051(19)	
751.9(3)	187(22)	1	0^-–3^-	0.118(4)		
766.0(6)	19(5)	1, 3	1^-–3^-	0.012(2)	0.022(9)	
778.9(3)	43(7)	1	0^-–3^-	0.023(1)		
791.1(4)	50(8)	1	0^-–3^-	0.024(1)		
813.3(3)	137(25)	1, 3	1^-–3^-	0.047(4)	0.121(21)	
825.0(5)	137(20)	1, 3	1^-–3^-	0.027(3)	0.219(18)	
841.7(4)	83(15)	1	0^-–3^-	0.054(2)		
850.3(3)	203(25)	1	0^-–3^-	0.138(5)		

Table 4.2.5 -continued

Energy (keV)	Cross Section (μb/sr) at $\theta = 45°$	Transferred l-value	Possible Spin	Transfer Strength l=1	l=3	l=5
850.3(3)	203(25)	1	0^-–3^-	0.138(5)		
862.7(18)	71(12)	1	0^-–3^-	0.042(2)		
874.1(15)	135(32)	1, 3	1^-–3^-	0.032(3)	0.208(23)	
885.1(14)	258(30)	1, 3	1^-–3^-	0.055(5)	0.399(33)	
901.1(20)	66(28)	1, 3	1^-–3^-	0.020(3)	0.113(15)	
918.0(19)	24(5)	1, 3	1^-–3^-	0.006(2)	0.047(10)	
938.3(14)	22(5)	1	0^-–3^-	0.013(1)		
967.2(20)	27(7)	1	0^-–3^-	0.017(1)		
1001.3(16)	34(7)	1	0^-–3^-	0.015(1)		
1015.0(15)	65(12)	1	0^-–3^-	0.031(2)		
1023.6(22)	66(11)	1, 3	1^-–3^-	0.031(4)	0.048(17)	
1052.9(26)	50(9)	1, 3	1^-–3^-	0.004(2)	0.067(10)	
1060.5(23)	36(9)					
1078.2(12)	8(4)					
1090.6(32)	19(5)					

[a]) An energy of 56.7 keV from the work of Kern et al[57] has been adopted for this state, and all other energies are relative to it.

or $l = 5$ components. The (d,p) angular distributions for ^{191}Ir(d,p) and ^{193}Ir(d,p) experiments are shown in Figure 4.2.9 and Figure 4.2.10, respectively. As can be seen, in almost all cases a one-component fit was sufficient to describe the experimental angular distribution. Since the $l = 1$ intrinsic cross section is much greater than that for $l = 3$ or $l = 5$, it is much more difficult to detect the $l = 3$ or 5

components. In fact, no $l = 5$ (d,p) angular distributions were obtained, and only a few peaks had definite $l = 3$ transitions.

The excitation energies and cross sections at an angle of $\theta = 45°$ are listed in Table 4.2.6 and Table 4.2.7 for ^{192}Ir and ^{194}Ir, respectively, along with the spectroscopic strengths obtained.

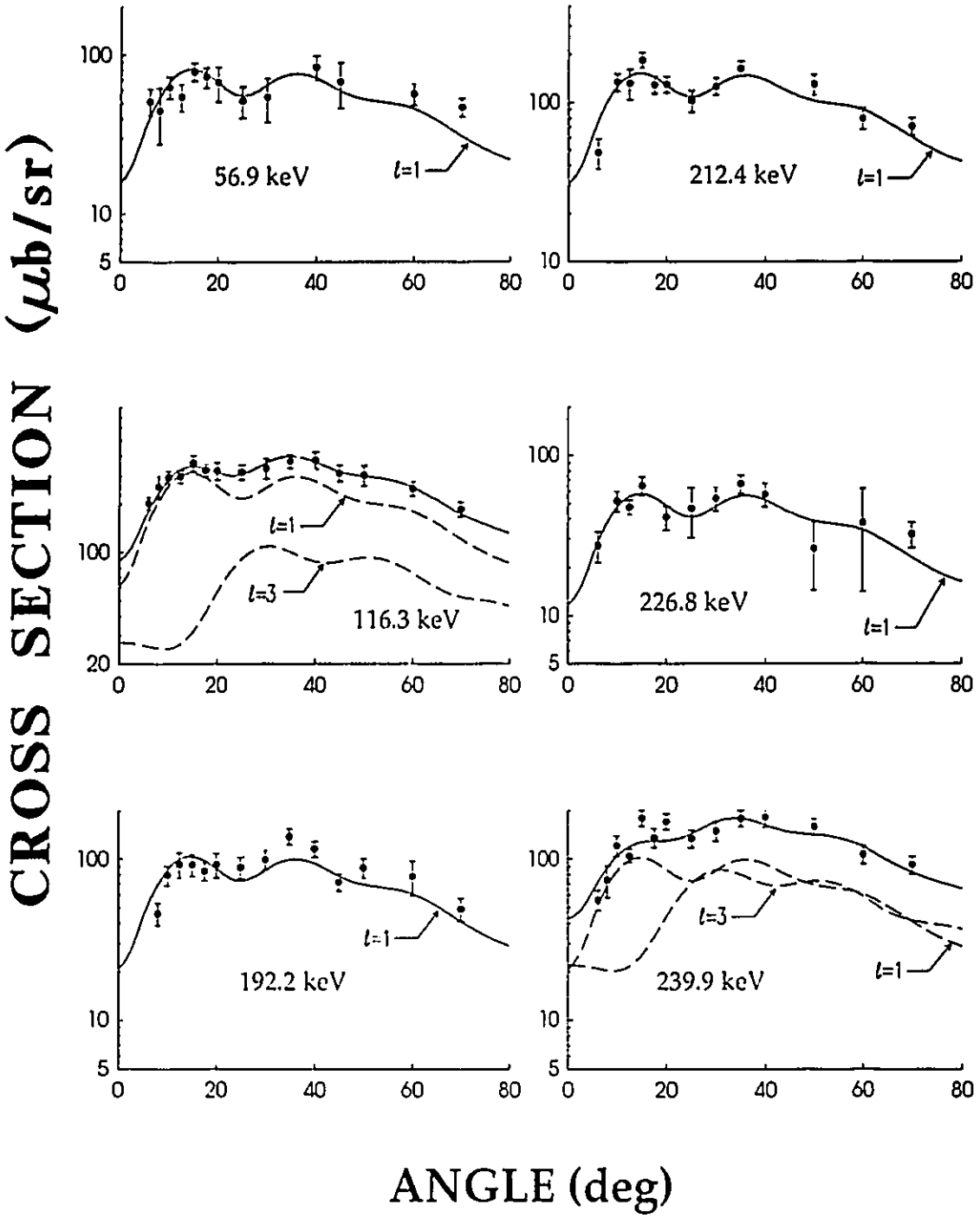

Figure 4.2.9a: Angular distributions of cross sections from the ^{191}Ir(d,p) reaction. The dashed curves are the results of DWBA calculation for the transferred l-value indicated. The solid curves are the fits to the data.

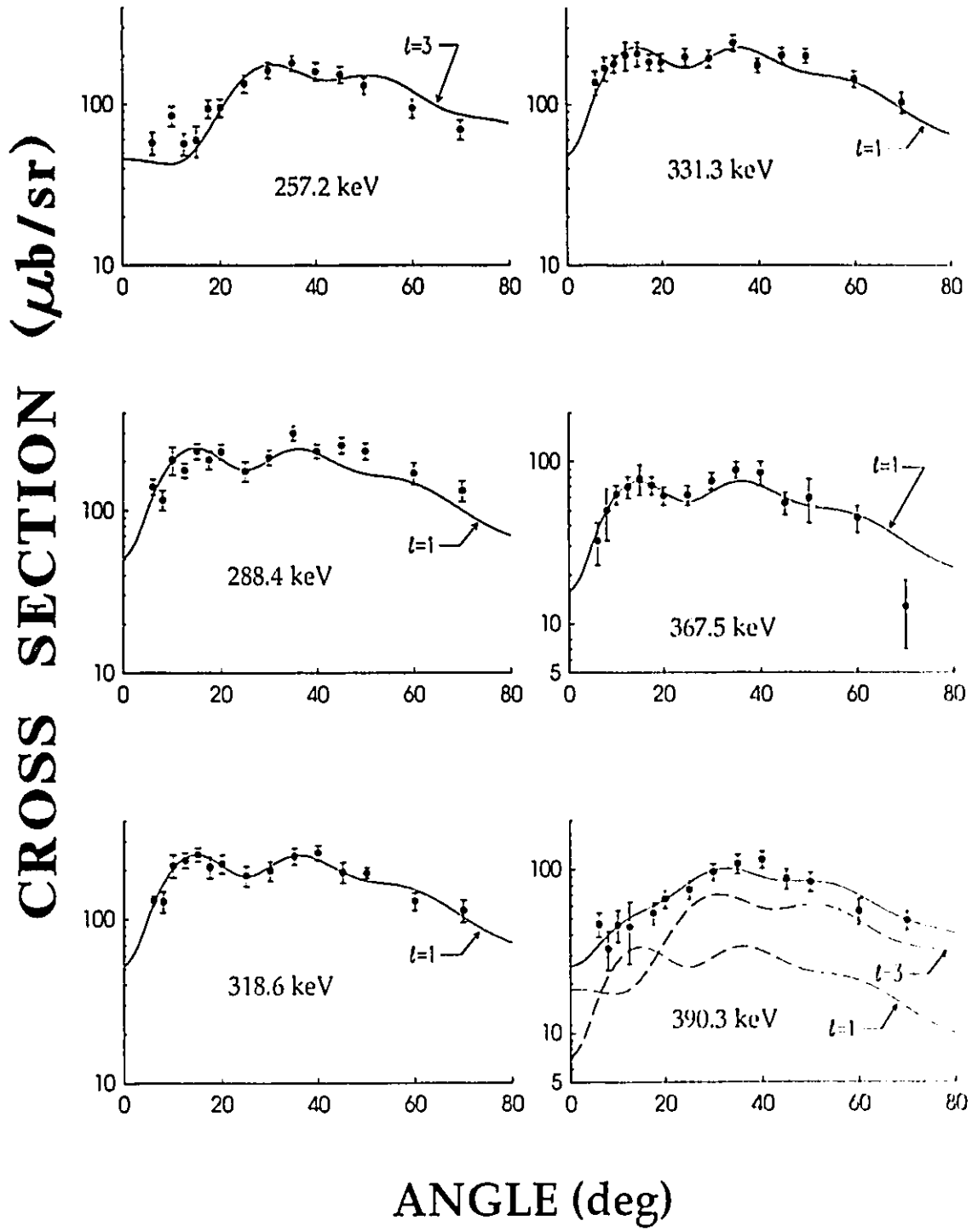

Figure 4.2.9b: See caption for Figure 4.2.9a.

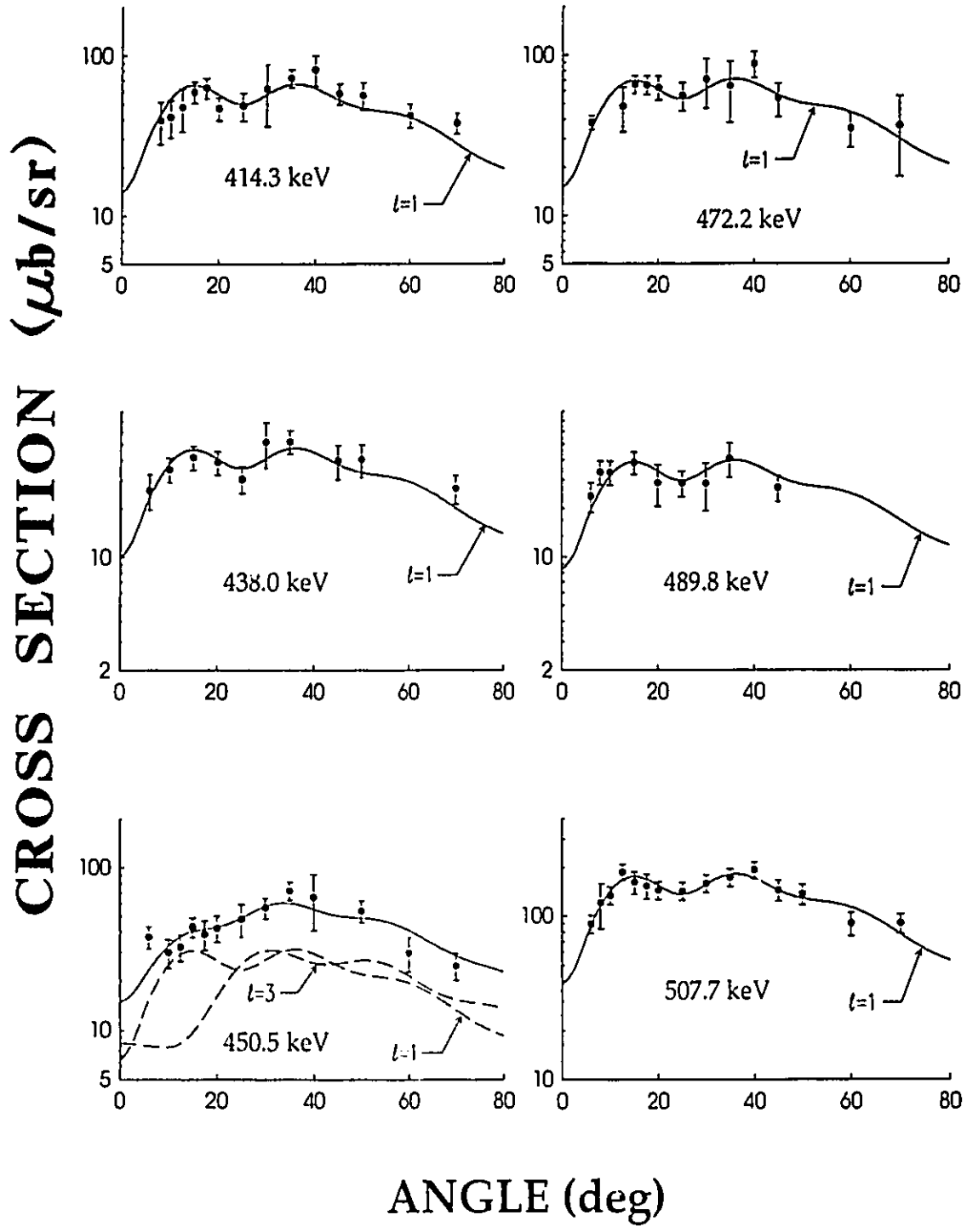

Figure 4.2.9c: See caption for Figure 4.2.9a.

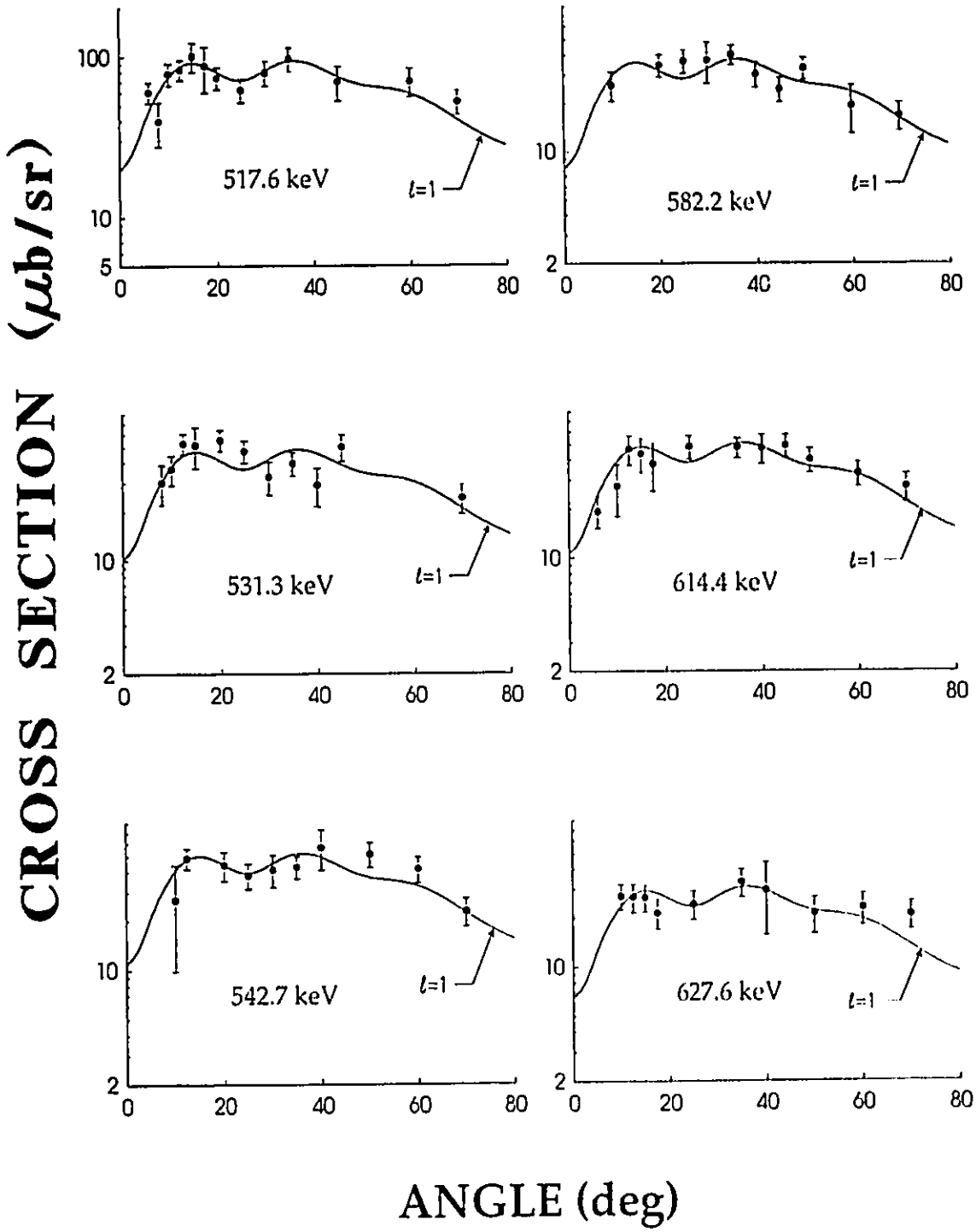

Figure 4.2.9d: See caption for Figure 4.2.9a.

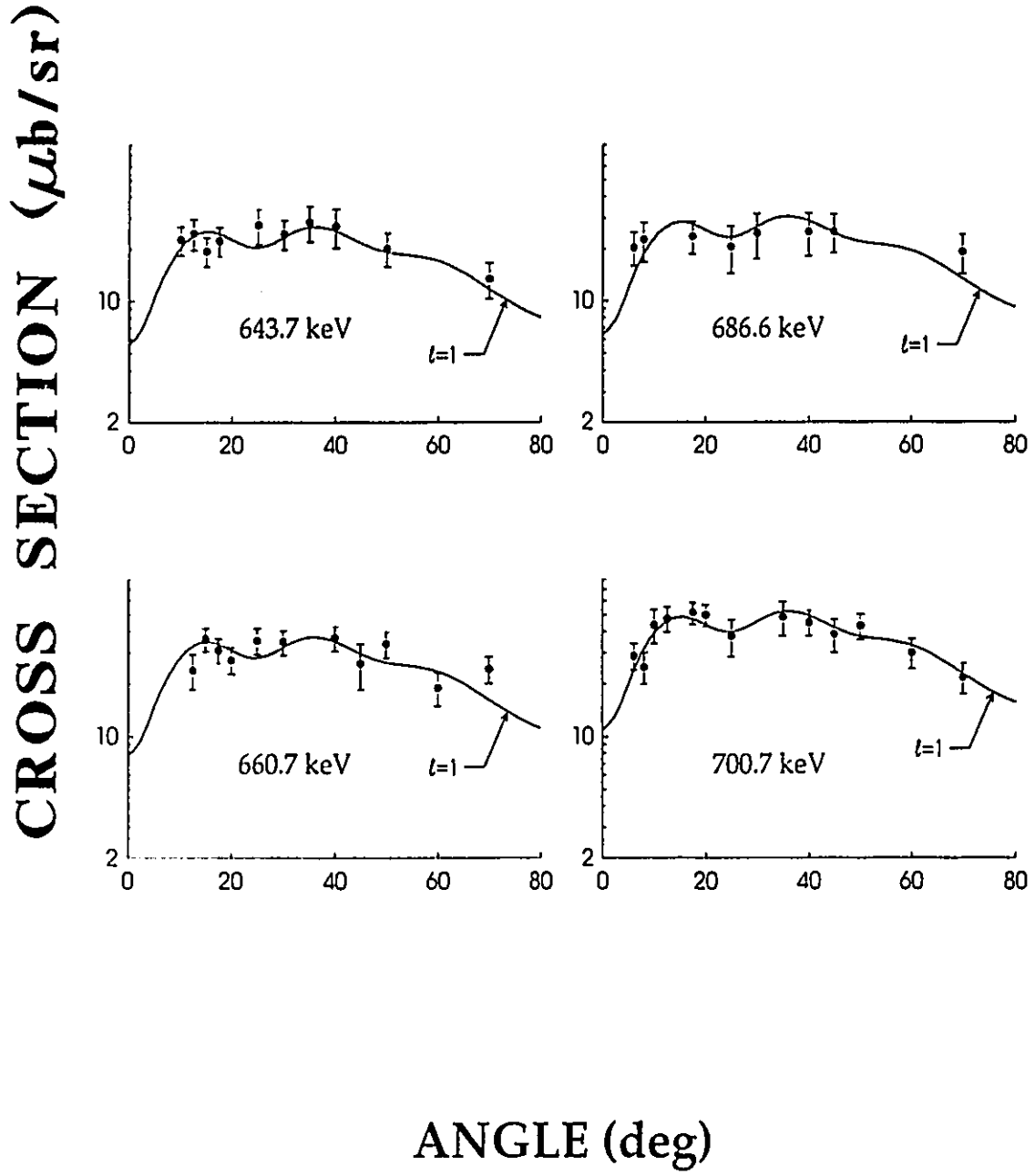

Figure 4.2.9e: See caption for Figure 4.2.9a.

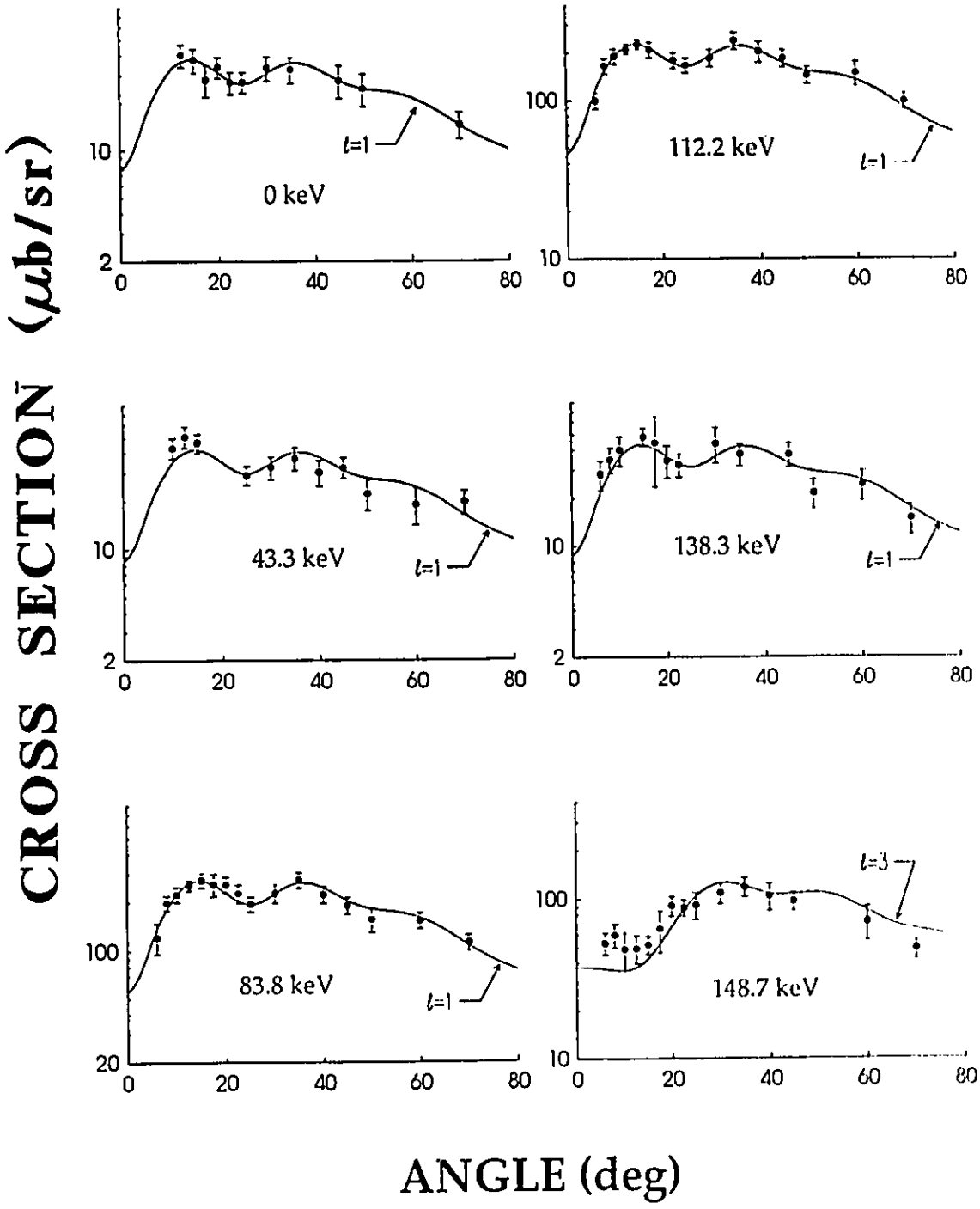

Figure 4.2.10a: Angular distributions of cross sections from the ^{193}Ir(d,p) reaction. The dashed curves are the results of DWBA calculation for the transferred l-value indicated. The solid curves are the fits to the data.

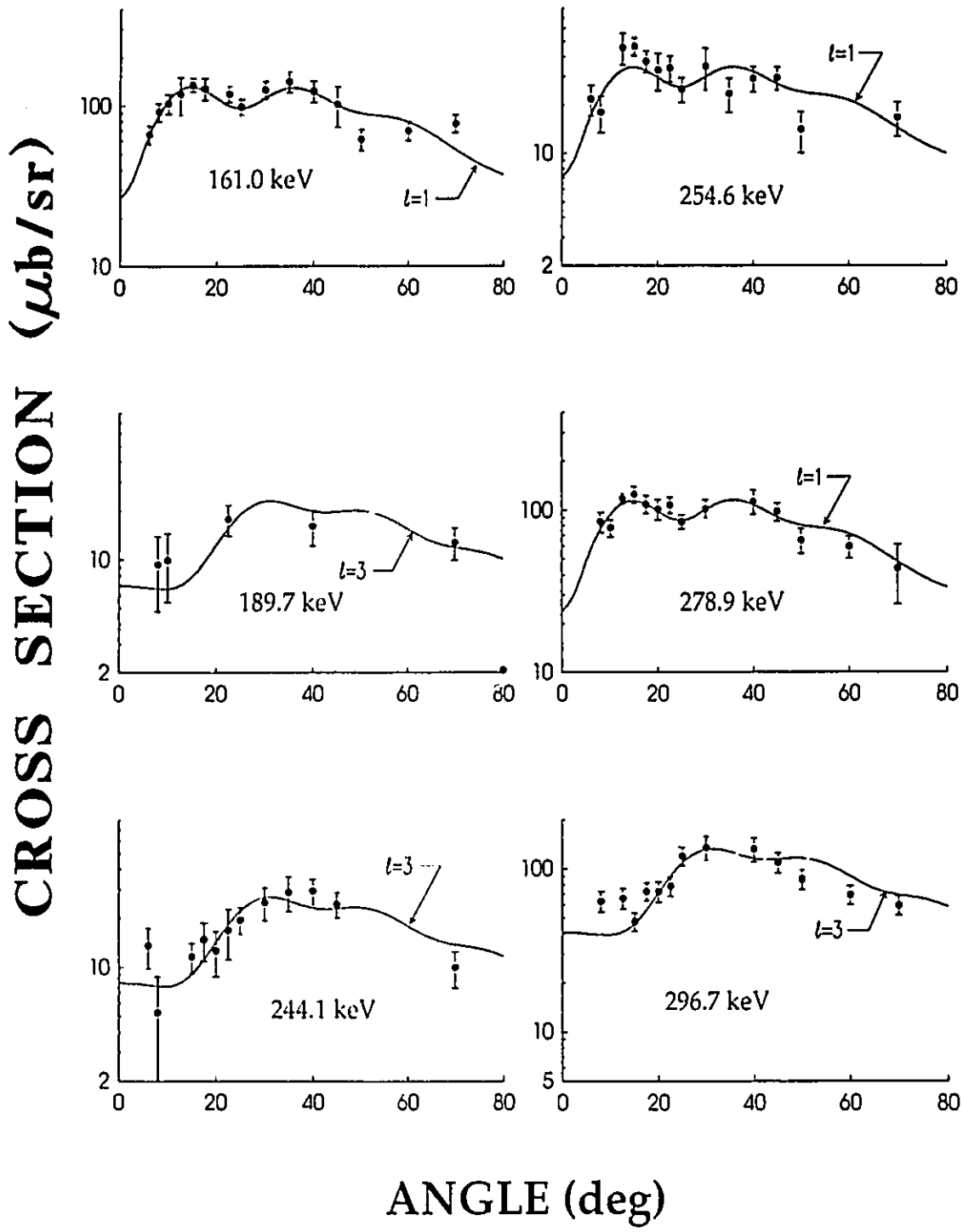

Figure 4.2.10b: See caption for Figure 4.2.10a.

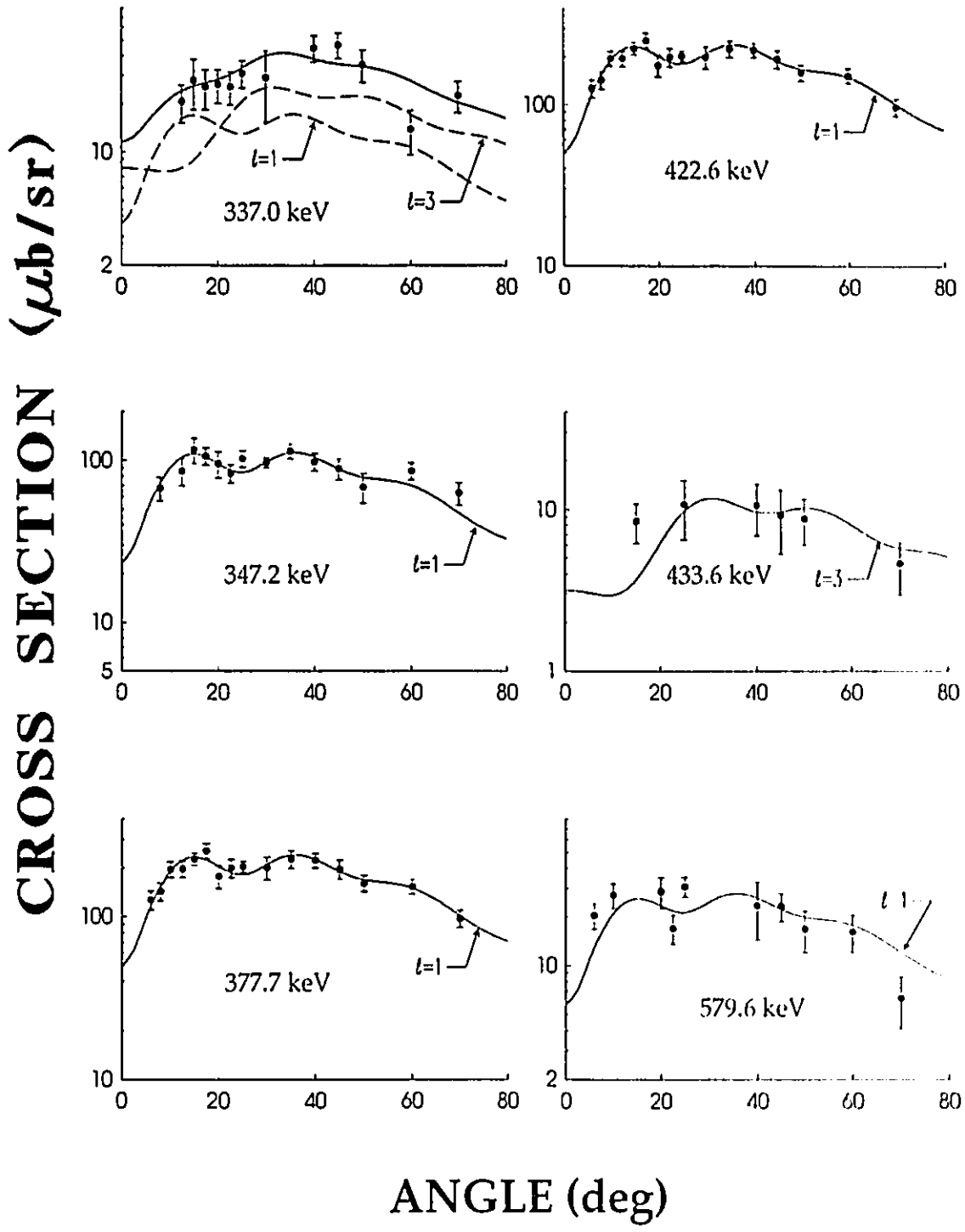

Figure 4.2.10c: See caption for Figure 4.2.10a.

Table 4.2.6: States in ^{192}Ir Populated With (d,p) Reactions

Energy[a] (keV)	Cross Section (μb/sr) at $\theta = 45°$	Transferred l-value	Transfer Strength l=1	l=3	l=5
56.9(4)	68(22)	1	0.058(3)		
66.3(11)	24(8)	3		< 0.1	
85.2(12)	[b])	5			< 0.25
104.5[c])			< 0.04		
116.3(2)	311(36)	1, 3	0.224(14)	0.27(7)	
128.3[c])			< 0.03		
144.8(10)	[b])		< 0.02		
192.2(2)	72(9)	1	0.075(3)		
212.4(2)	[b])	1	0.109(4)		
226.8(5)	[b])	1	0.041(2)		
239.9(2)	[b])	1, 3	0.073(7)	0.21(4)	
257.2(4)	154(18)	3		0.431(15)	
288.5	254(28)	1	0.175(6)		
318.6(3)	194(28)	1	0.178(5)		
331.3(2)	204(23)	1	0.164(6)		
367.5(4)	55(9)	1	0.054(2)		
390.3(3)	86(13)	1, 3	0.024(6)	0.165(25)	
414.3(4)	58(9)	1	0.047(2)		
438.0(4)	40(9)	1	0.034(2)		
450.5(3)	66(25)	1, 3	0.022(4)	0.072(17)	
472.2(4)	54(13)	1	0.050(3)		
489.8(4)	27(5)				
507.7(3)	145(21)	1	0.126(5)		

Table 4.2.6 -continued

Energy[a]) (keV)	Cross Section (μb/sr) at $\theta = 45°$	Transferred l-value	Transfer Strength l=1	l=3	l=5
517.6(6)	70(17)	1	0.066(3)		
531.3(5)	50(10)	1	0.034(2)		
542.7(6)	[b])	1	0.036(2)		
582.2(5)	25(4)	1	0.026(2)		
614.4(4)	49(8)	1	0.035(2)		
627.6(4)	[b])	1	0.035(2)		
643.7(3)	[b])	1	0.018(1)		
660.7(4)	26(8)	1	0.025(2)		
686.6(6)	25(6)	1	0.021(2)		
700.7(5)	38(8)	1	0.35(2)		

[a]) Energy is relative to 288.5 keV peak.

[b]) Peak obscured at this angle due to impurity peaks.

[c]) Peak was not observed. Strength given is an upper limit.

4.3. The ^{189}Os(α,t) and ^{189}Os(^{3}He,d) Reactions

The ^{189}Os(α,t) and ^{189}Os(^{3}He,d) reactions examined proton states in ^{190}Ir, typical spectra of which are shown in Figure 4.3.1 and Figure 4.3.2, and used beam energies of 30 MeV and 28 MeV, respectively. The resolution (FWHM) of the tritons was $\simeq$ 10 keV and that of the deuterons $\simeq$ 15 keV. Since the ^{189}Os target had an impurity of 14.1% ^{190}Os, and 3.06% ^{192}Os, states in both ^{191}Ir and ^{193}Ir were also populated in the reaction. The Q-values for these reactions are known[56] to $\pm$0.006 MeV, therefore the beam energies can be determined, and the Q-values

Table 4.2.7: States in ^{194}Ir Populated with (d,p) Reactions

Energy[a] (keV)	Cross Section (μb/sr) at $\theta = 45°$	Transferred l-value	Possible Spin	Transfer Strength l=1	l=3
−0.3(4)	26(6)	1	0^-–3^-	0.027(2)	
43.3(3)	32(5)	1	0^-–3^-	0.030(2)	
83.8(1)	192(23)	1	0^-–3^-	0.197(6)	
112.2	185(23)	1	0^-–3^-	0.164(5)	
138.3(4)	37(6)	1	0^-–3^-	0.031(2)	
148.7(2)	97(13)	3	1^-–5^-		0.290(10)
161.0(1)	102(29)	1	0^-–3^-	0.095(4)	
189.7(12)	[b])	(3)	1^-–5^-		(0.05)
244.1(4)	24(4)	3	1^-–5^-		0.030(2)
254.6(4)	29(5)	1	0^-–3^-	0.025(7)	
278.9(2)	98(13)	1	0^-–3^-	0.082(3)	
296.7(3)	109(15)	1, 3	0^-–3^-	<0.04	0.295(15)
312.1(14)	[b])				
337.0(4)	47(9)	1	0^-–3^-	0.012(3)	
347.2(2)	89(13)	1	0^-–3^-	0.079(3)	
377.7(3)	196(26)	1	0^-–3^-	0.168(5)	
422.6(5)	24(12)	1	0^-–3^-	0.029(2)	
433.6(15)	9(4)	(3)	1^-–5^-		(0.025)
467.5(10)	8(2)				
490.1(11)	28(7)				
500.2(10)	[b])				
545.7(11)	20(4)				
555.8(13)	5(2)				
579.6(6)	23(5)	1	0^-–3^-	0.019(1)	

Table 4.2.7 -continued

Energy[a]) (keV)	Cross Section (μb/sr) at $\theta = 45°$	Transferred Spin	Possible l-value	Transfer Strength l=1	l=3
591.9(13)	[b])				
640.7(12)	13(3)				
668.1(10)	[b])				
677.1(14)	21(4)				
760.7(14)	17(7)				
773.4(11)	[b])				
819.3(12)	23(7)				
879.0(13)	16(4)				

[a]) Energy is relative to 112.2 keV peak.

[b]) Peak obscured by impurity peak at this angle.

for the peaks in the spectra corresponding to states in ^{190}Ir can be found. Using the Q-value for the first ^{190}Ir state populated in the (d,t) reaction, the Q-values of this state for the (α,t) and (^{3}He,d) reactions were calculated to be -14.756 ± 0.005 MeV and -0.435 ± 0.005 MeV respectively. Subtracting these values from the Q-values obtained for all the peaks in the spectra allows the relative excitation energies to be determined, and they can be compared to those from the (d,t) reaction. The relative excitation energies obtained in this manner are listed in Table 4.3.1, along with the cross section at 50° for the (α,t) and 35° for the (^{3}He,d) reactions. It should be noted that the uncertainty quoted in the energies does not include the ± 0.005 uncertainty of the Q-value.

Table 4.3.1: Levels Populated with ^{189}Os(α,t) and ^{189}Os(^{3}He,d) Reactions

^{189}Os(α, t)		^{189}Os(^{3}He, d)		Transferred
Relative Energy (keV)	Cross Section (μb/sr) at $\theta = 50°$	Relative Energy (keV)	Cross Section (μb/sr) at $\theta = 35°$	l-value
26(1)	7.3(9)	29(2)	3.7(9)	2,3
84(1)	57(6)	86(1)	35(4)	2,3
145(1)	35(3)	147(1)	28(3)	1,2
173(1)	11(1)	175(2)	6.0(14)	2,3
184(1)	10(1)	187(2)	12(2)	1,2
200(1)	3.8(5)	205(2)	4.9(8)	
226(1)	8.5(10)	227(1)	13.4(17)	0,1
246(1)	9.9(14)	246(1)	9.0(13)	1,2
269(1)	5.7(8)	271(1)	9.5(14)	0,1
284(1)	7.1(10)	287(2)	8.4(16)	1,2
314(1)	31(4)	312(1)	16(2)	2,3
355(1)	6.5(20)	360(2)	9.9(13)	
381(1)	25(4)	380(1)	37(4)	1,2
428(2)	4.0(6)	425(2)	6.3(9)	0,1
441(1)	3.6(7)	440(2)	[a])	3,4
456(1)	13(3)	456(2)	4(3)	3,4,5
483(2)	2.2(6)	484(2)	[a])	
511(1)	3.2(7)	509(2)	4.1(7)	0,1
550(1)	1.9(4)	553(2)	3(1)	0,1
590(1)	5.0(6)	592(2)	3.1(16)	1,2
623(1)	4.1(6)	622(1)	6.0(9)	1,2
645(1)	26(3)	649(2)	5.8(9)	

Table 4.3.1 - continued

^{189}Os(α, t)		^{189}Os(^{3}He, d)		Transferred
Relative Energy (keV)	Cross Section (μb/sr) at θ = 50°	Relative Energy (keV)	Cross Section (μb/sr) at θ = 35°	*l*-value
672(1)	2.5(4)	671(1)	4.5(7)	1,2
696(2)	2.2(3)	703(2)	3.2(9)	
717(1)	9.1(11)	721(3)	3.3(6)	4,5
741(1)	8.5((12)	742(2)	6.5(9)	2,3
759(1)	34(5)	760(2)	8.9(13)	
817(1)	21(2)	819(2)	8.8(12)	4,5
847(1)	11(1)	848(2)	10(1)	2,3
869(1)	14(2)	868(2)	8(1)	3,4
891(1)	42(6)	892(2)	10.6(13)	4,5
924(2)	26(4)	928(2)	14(2)	3,4

[a]) Peak obscured by the presence of an impurity peak at this angle.

Ratios of the (^{3}He,d) to (α,t) cross sections, defined as

$$R = \frac{\left.\frac{d\sigma}{d\Omega}\right)_{(^3\mathrm{He,d})}}{\left.\frac{d\sigma}{d\Omega}\right)_{(\alpha,t)}} \qquad (4.3.1)$$

can be sensitive to the *l*-value of the transition. This arises from the different *l*-dependance of angular distributions for the two reactions. The angular distributions are shown in Figure 4.3.3, obtained from DWBA calculations using optical model parameters listed in Table 4.3.2. These parameters were used in the work of Price et al[59] where a similar study was made for ^{191,193}Ir. The results of the calculations are that as the *l*-value of the transition increases, the ratio *R* decreases. At certain

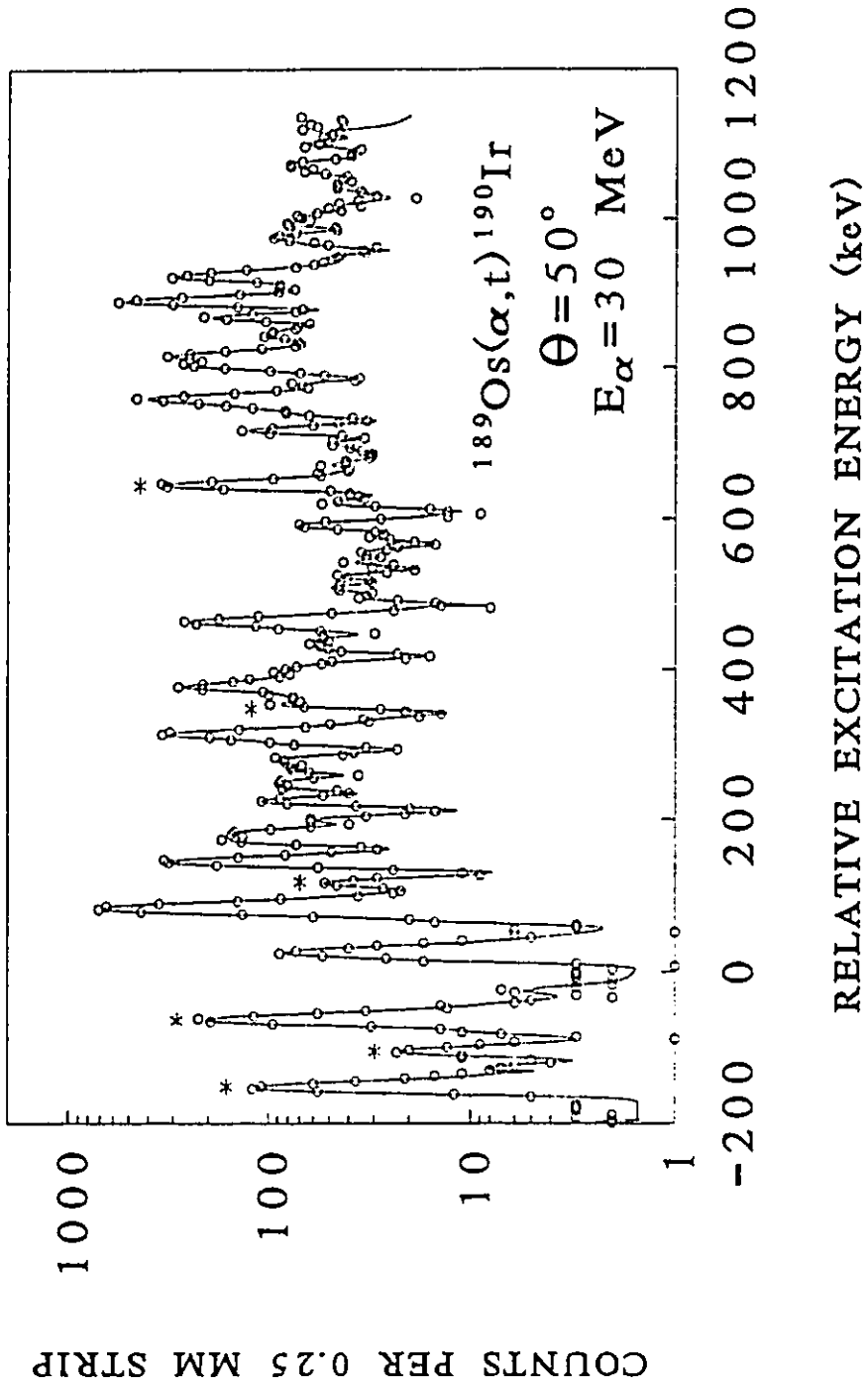

Figure 4.3.1: Spectrum obtained at $\theta = 50°$ from the ^{189}Os(α,t) reaction using a bombarding energy of 30 MeV. Peaks from the ^{190}Os(α,t) reaction are labelled by an asterisk.

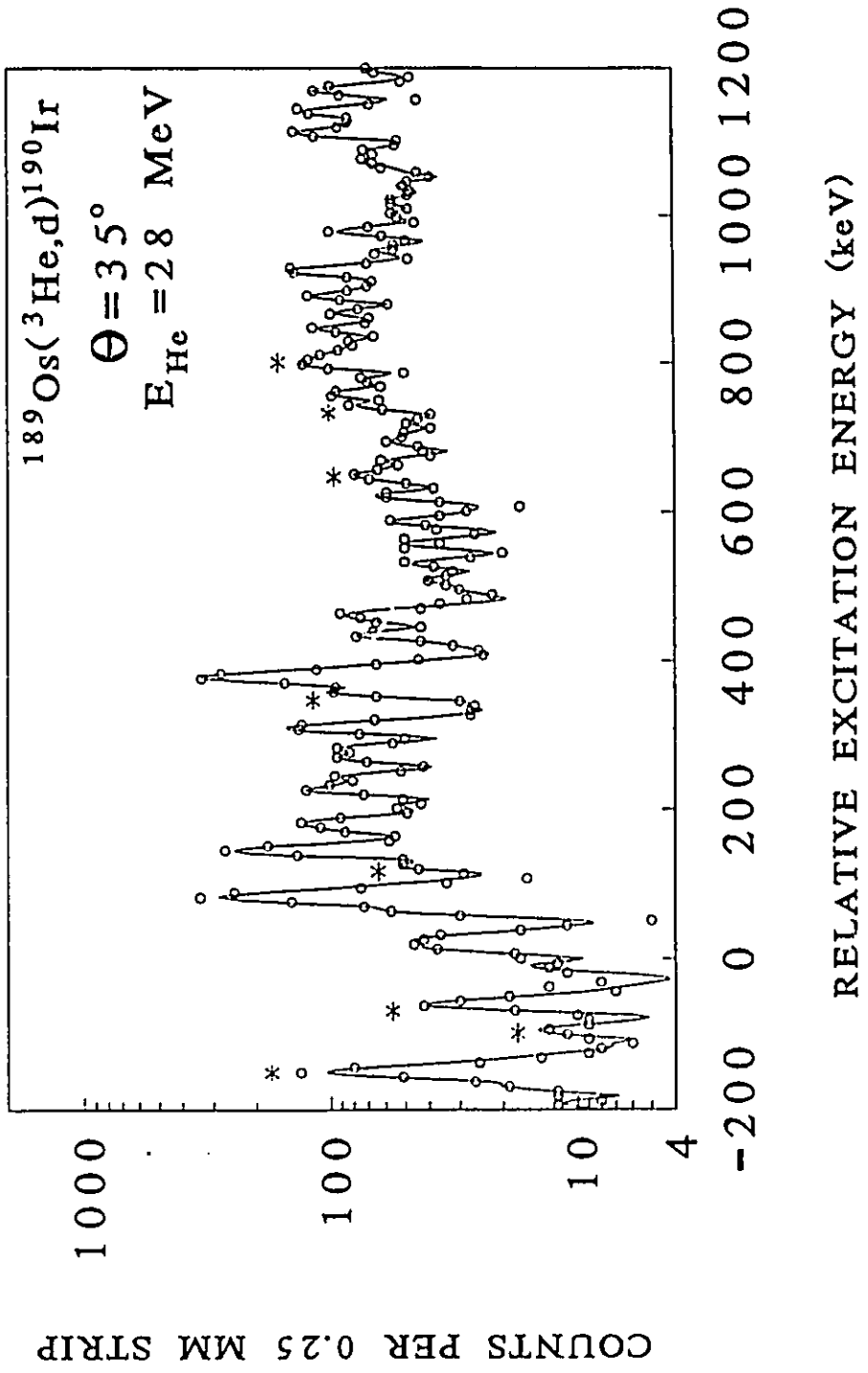

Figure 4.3.2: Spectrum obtained at $\theta = 35°$ from the ^{189}Os(^{3}He,d) reaction using a bombarding energy of 28 MeV. Peaks from the ^{190}Os(^{3}He,d) reaction are labelled by an asterisk.

Table 4.3.2: Optical Model Parameters for DWBA Calculations for ^{189}Os(α,t) and ^{189}Os(^{3}He,d) Reactions

Particle	V (MeV)	r_r (fm)	a_r (fm)	W (MeV)	$4W_D$ (MeV)	r_I (fm)	a_I (fm)	r_c (fm)
α	−200.0	1.40	0.60		−20.0	1.40	0.60	1.30
triton	−200.0	1.45	0.60	−50.0		1.45	0.60	1.30
proton	[a])	1.25	0.65					1.25
^{3}He	−175.0	1.14	0.723		−17.5	1.60	0.810	1.4
deuteron	−111.0	1.05	0.859		70.8	1.24	0.794	1.25
proton	[a])	1.25	0.625					1.25

[a]) Well depth was varied to reproduce the proton binding energy.

The normalization constant for the (^{3}He,d) reaction was $N = 4.42$ and for the (α,t) reaction $N = 118$.

angles, the difference between R for an $l = 0$ and an $l = 5$ transition may be an order of magnitude. The ratio's have a slight dependance on Q-value, increasing slightly as the excitation energy increases.

The theoretical values of R are sensitive to the DWBA normalization constants used, and since this is not well known for the (α,t) reaction, the overall normalization factor for R was determined empirically. The work of Price et al[59] studied proton states in ^{191}Ir by examining ratios of (α,t) to (^{3}He,d) cross sections, and found that states at 0 keV ($\frac{3}{2}\frac{3}{2}^+$[402] orbital), 83 keV ($\frac{1}{2}\frac{1}{2}^+$[400] orbital), and at 171 keV ($\frac{11}{2}\frac{1}{2}^-$[505] and $\frac{3}{2}\frac{1}{2}^+$[400] orbitals) had ratios indicative of $l = 2$, $l = 0$, and $l \geq 4$ transfer respectively. These same levels were also observed in the reactions carried out for this work since the target had a large impurity of ^{190}Os, and a normalization constant was found that would reproduce the proper R values for

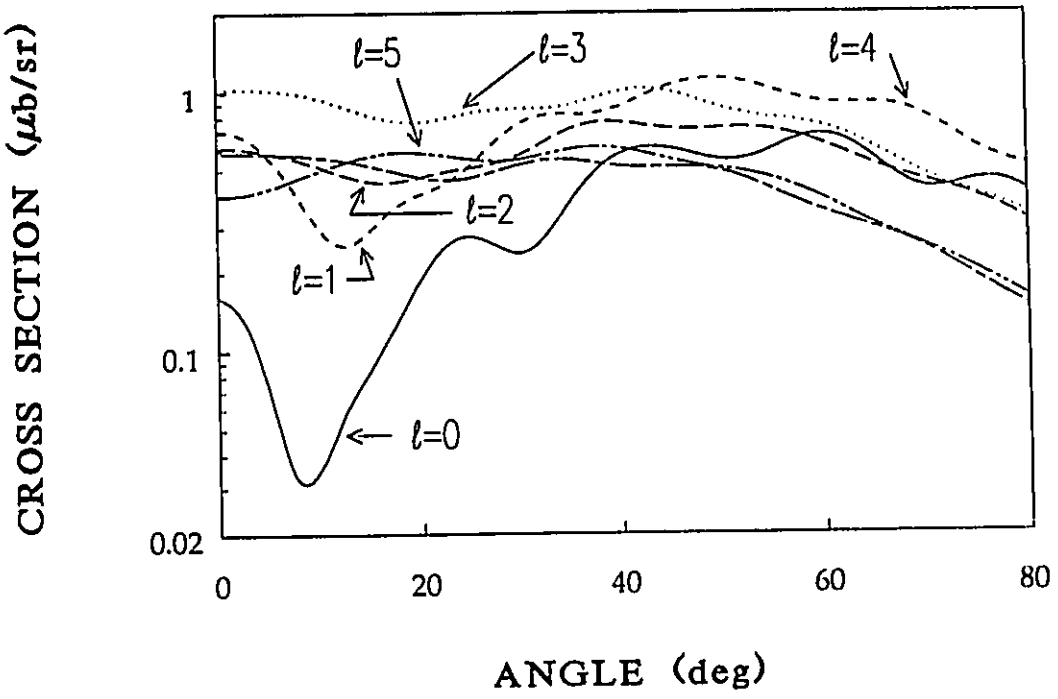

Figure 4.3.3a: Angular distributions of cross sections for the ^{189}Os(α,t) reaction obtained from a DWBA calculation assuming a beam energy of 30 MeV. The cross sections have not been multiplied by the normalization factor of $N = 118$.

these states. As a test of how well this procedure worked, states in ^{191}Ir at 591 keV ($\frac{5}{2}^{+}\frac{5}{2}^{+}$[402] orbital) and at 879 keV ($\frac{9}{2}^{-}\frac{1}{2}^{-}$[541] orbital and possibly a contribution from the $\frac{13}{2}^{+}\frac{1}{2}^{+}$[660] orbital) were resolved from other peaks in the spectra, and the values of R were consistent with an $l = 1$ or 2 transfer and an $l = 5$ transfer, respectively, as they should be.

Since the (^{3}He,d) and (α,t) spectra were recorded at various angles, values of R were determined for the various combinations of angles. A typical example of R versus relative excitation energy is plotted in Figure 4.3.4, where the (^{3}He,d) data were obtained at 30° and the (α,t) data at 50°. Before an l-value is assigned, the ratios had to be consistent for the majority of the angle combinations, i.e., two particular ratios may be disregarded due to impurities, but the others had to agree

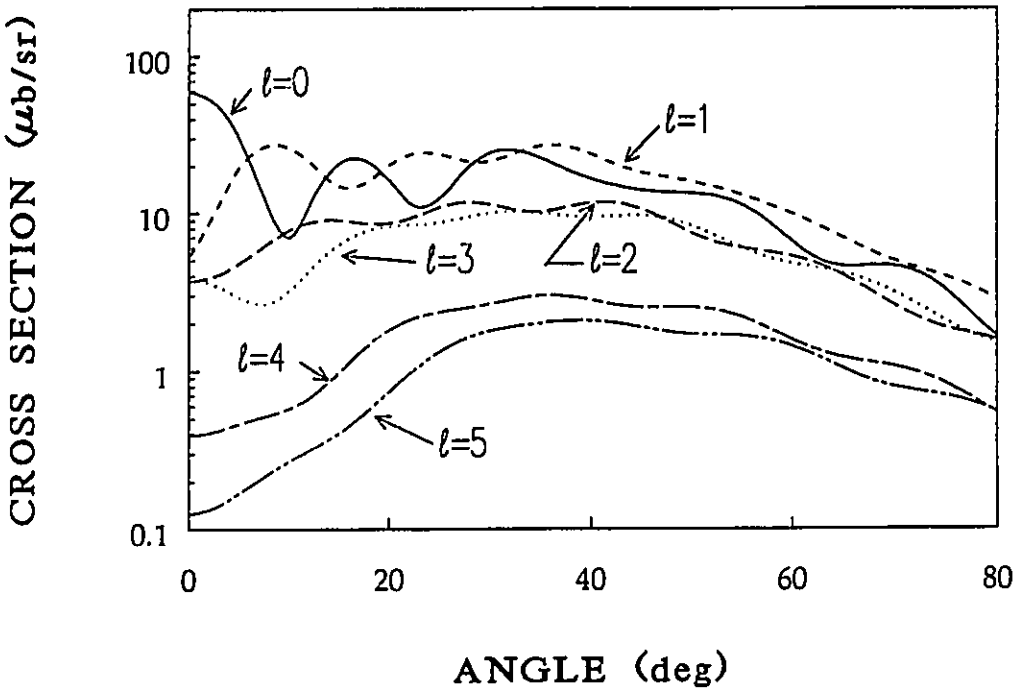

Figure 4.3.3b: Angular distributions of cross sections for the ^{189}Os(^{3}He,d) reaction obtained from a DWBA calculation assuming a beam energy of 28 MeV. The cross sections have not been multiplied by the normalization factor of $N = 4.42$.

within error. In all cases, the errors are large enough to allow more than one l-value to be assigned. Table 4.3.1 lists the l-values assigned for states in ^{190}Ir. It can be seen that the low l's dominate the transitions, with very few high l's being observed.

4.4. The ^{195}Pt(p,α) and ^{193}Ir(^{3}He,α) Reactions

Earlier studies[60] have shown that for nuclei in the rare-earth region, there is a good correlation between the (p,α) cross sections and those of the (t,α) reaction leading to the same final nucleus. Therefore, in an attempt to gain information regarding the similarity of the neutron configurations in ^{192}Ir to those in ^{195}Pt, a (p,α) experiment was performed. Spectra were recorded at 10° and 15° for the ^{195}Pt(p,α) reaction using an 18 MeV proton beam. The energies and relative cross

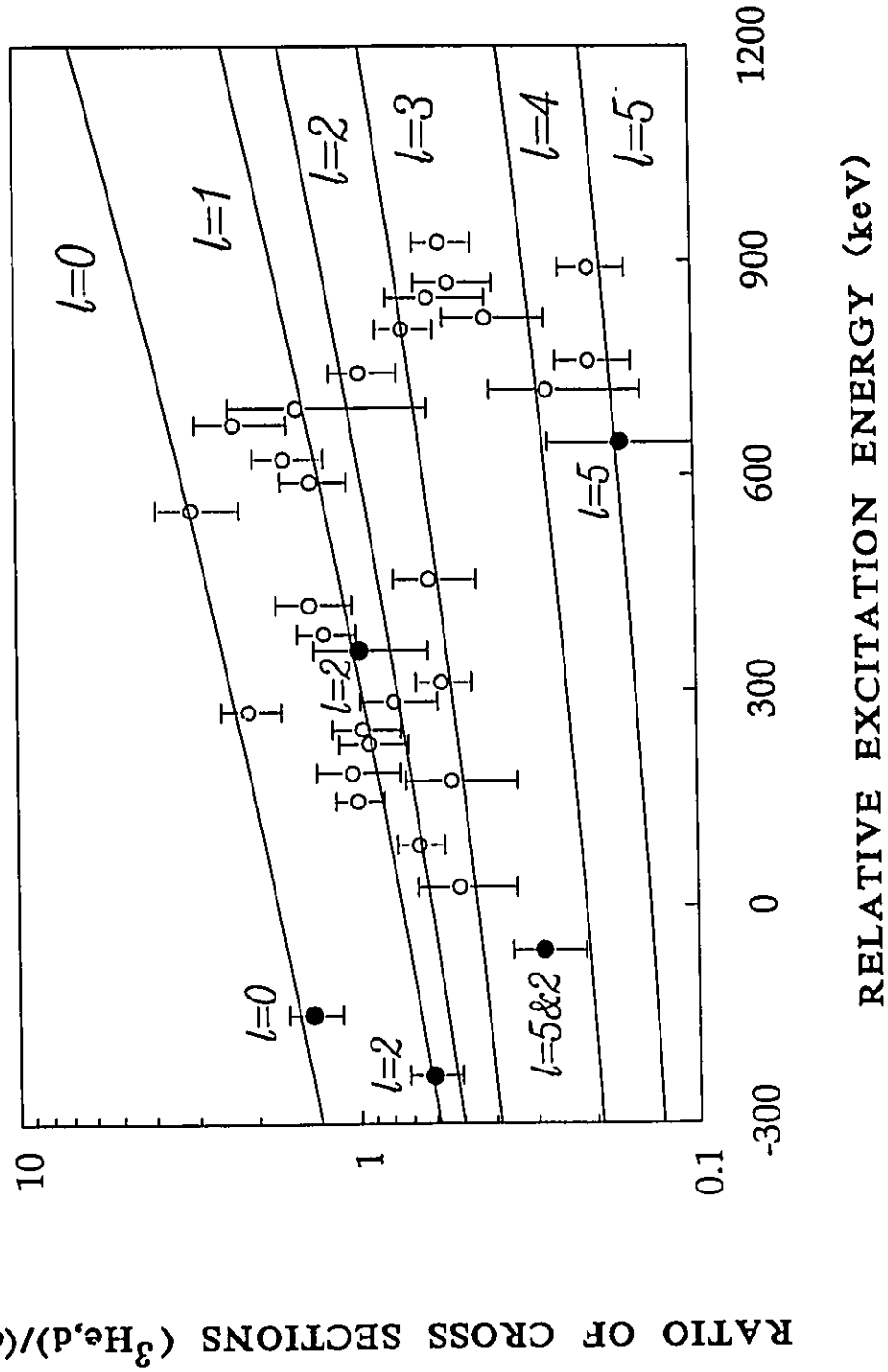

Figure 4.3.4: Ratios of cross sections from ^{189}Os(^{3}He,d) at 30° to ^{189}Os(α,t) at 50°. The curves are the results of DWBA calculations for the transferred l-value indicated. The solid data points are for peaks from ^{191}Ir due to isotopic impurities.

sections at 10° are listed in Table 4.4.1, and the spectrum is shown in Figure 4.4.1. The resolution (FWHM) of the peaks in the α spectrum was approximately 18 keV. As can be seen, the largest peaks in the spectrum occur above 400 keV. In the low-lying portion of the spectrum, the peak intensities are small, and thus the overlaps of the wave functions of the target and those in the final states are small. Therefore, the low-lying neutron configurations in ^{192}Ir do not have large admixtures of the neutron configuration of the ^{195}Pt ground state.

An older ^{193}Ir(^{3}He,α) spectrum, shown in Figure 4.4.2, was analyzed in the hope that it would yield some information on high-l transfers into ^{192}Ir. The (^{3}He,α) reaction preferentially populates higher angular momentum states than the (d,t) reaction. The α spectrum shown in Figure 4.4.2 was taken at an angle of 50° with a 25.5 MeV ^{3}He beam, and the energies and cross sections are listed in Table 4.4.2. The resolution obtained was 25 keV, and there is a large uncertainty on the absolute energies, perhaps as large as 30 keV. However, if the assumption is made that the energies are correct and that the main peaks in the (^{3}He,α) spectrum are due to transitions with $l = 3$ or higher, there is a fairly good correspondence between strong $l = 3$ transitions in the (d,t) spectra and the peaks in the (^{3}He,α) spectrum. There is a peak which is strongly populated in the (^{3}He, α) reaction but not in the (d,t) or (d,p) reactions, at 143 keV. This may indicate the presence of an $l = 5$ or perhaps an $l = 6$ transition, since the amount of $l = 3$ component is known to be quite small.

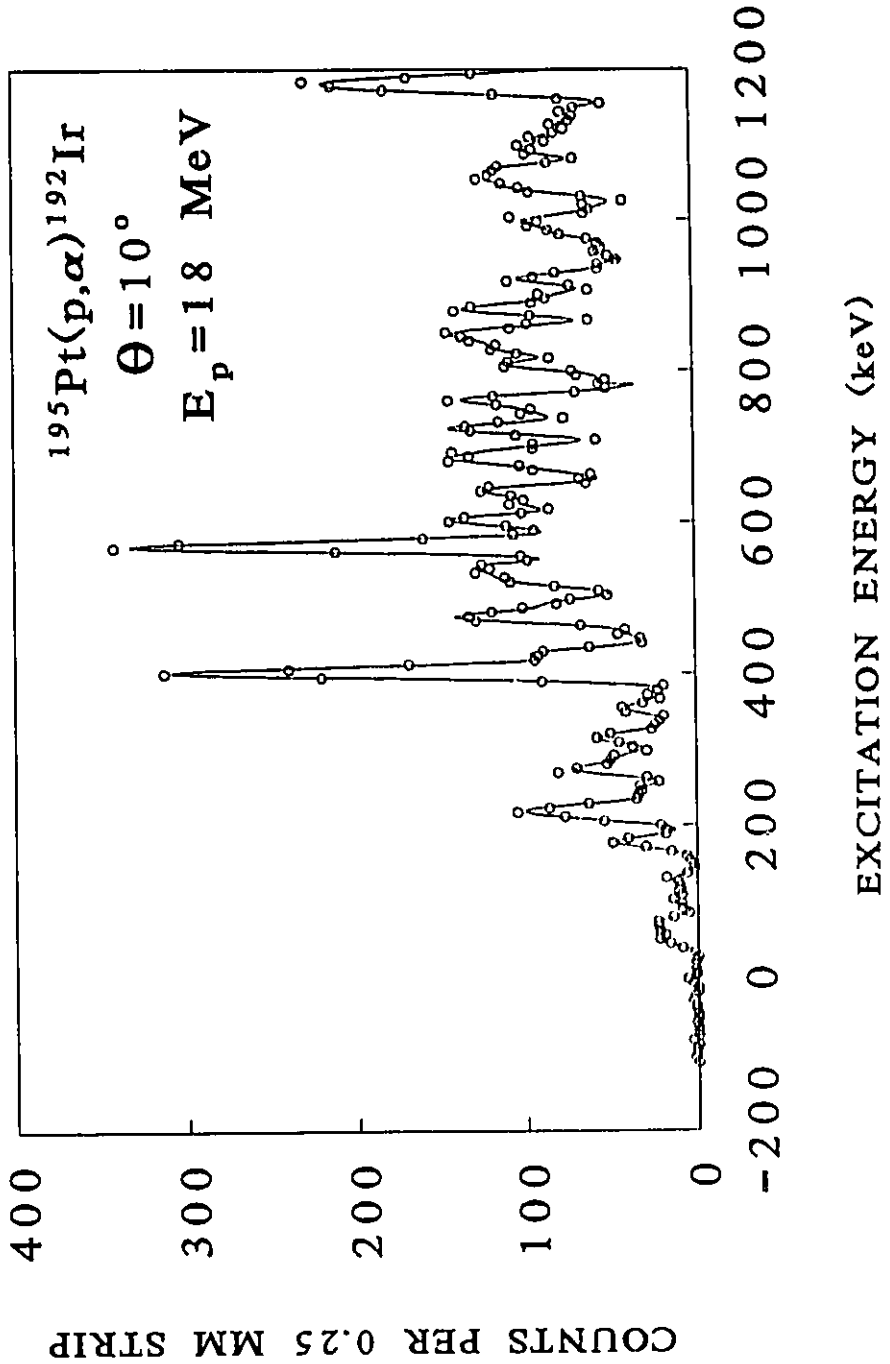

Figure 4.4.1: Spectrum obtained at $\theta = 10°$ from the ^{193}Ir(p,α) reaction using a bombarding energy of 18 MeV.

Table 4.4.1: Energies and Relative Cross Sections for States in ^{192}Ir Populated by the (p,α) Reaction

Excitation Energy (keV)	Relative Cross Section (μb/sr) at $\theta = 10°$	Excitation Energy (keV)	Relative Cross Section (μb/sr) at $\theta = 10°$
50(3)	7	426(2)	26
71(3)	8	474(2)	38
102(3)	4	493(3)	19
127(3)	4	524(4)	35
178(2)	14	542(3)	30
211(4)	15	568(2)	100
222(3)	24	604(3)	35
246(3)	9	624(3)	22
273(3)	20	642(3)	30
291(4)	10	683(4)	31
315(3)	15	697(4)	20
354(4)	9	723(2)	36
402(2)	95		

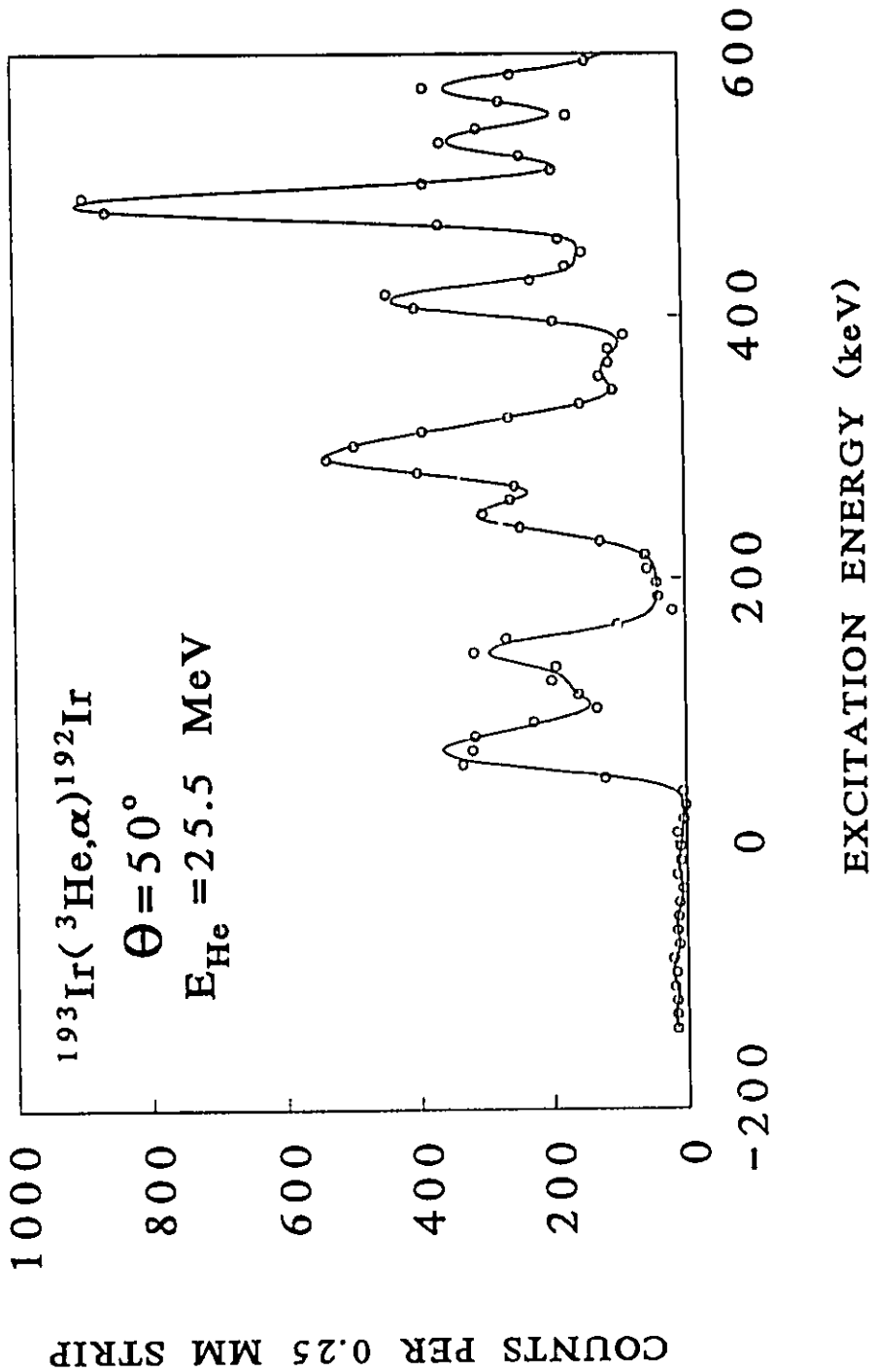

Figure 4.4.2: Spectrum obtained at $\theta = 50°$ from the ^{193}Ir(^{3}He,α) reaction using a bombarding energy of 25.5 MeV.

Table 4.4.2: Energies and Relative Cross Sections for States in ^{192}Ir Populated by (^{3}He,α) Reaction

Excitation Energy (keV)	Cross Section (μb/sr) at $\theta = 50°$	Excitation Energy (keV)	Cross Section (μb/sr) at $\theta = 50°$
65(5)	23	298(5)	22
84(10)	9	318(5)	9
114(10)	9	359(3)	4
143(4)	19	410(3)	26
212(10)	2	482(2)	59
245(2)	20	531(3)	20
281(3)	21	572(2)	20

Chapter 5.
Discussion and Interpretation of Results

5.1. Discussion of Experimental Results

Before proceeding with interpreting the data in terms of nuclear models, a discussion of some of the important experimental results is warranted. Levels in ^{192}Ir will be discussed first, since many complementary data are available for this nucleus, followed by an examination of states in ^{194}Ir and ^{190}Ir.

5.1.1 Levels in ^{192}Ir

Many of the levels below 500 keV in ^{192}Ir observed in this work have been investigated in the study by Kern et al[57]. Their work involved a series of experiments over a period of approximately 15 years, and a low-lying level scheme of ^{192}Ir was established. Their experiments included a study of the γ-rays and conversion electrons following the (n,γ) reaction, average resonance capture (ARC) measurements, and high resolution (d,t) and (d,p) measurements. The spins and parities of many levels were established, and very precise level energies were determined. However, the single-neutron transfer experiments were performed at only a few angles, and thus the transferred l-values and spectroscopic strengths could not be obtained. In the present work, complete angular distributions were measured for the purpose of determining both the transferred l-values, which yields the parity of the levels populated, and their spectroscopic strengths, which provides a very sensitive test of nuclear models. The energies of levels determined in the present study are in excellent agreement with those of Kern et al[57], who list the energies up to approximately 500 keV. The present work has also found many new levels above 500 keV.

When this work was undertaken, the spin of the ground state was known to be 4, but the parity was unknown. Conflicting assignments had appeared in the literature, and one aim of the present work was to establish clearly the parities of

many levels in ^{192}Ir. The ground state, which is not observed in single-neutron transfer experiments, must have its parity inferred from the multipolarities of γ-transitions feeding it and the parities of the parent states. The present work confirms the assignments of Kern et al[57] of negative parity for many excited states. Some of the negative parity excited states decay to the ground state with γ-transitions that involve parity changes, and thus the ground state has positive parity.

Kern et al[57] report the possible existence of a level at 62 keV as observed in their (d,t) spectra and report a significant cross section populating this level. In the present work there is no evidence of this state. While the resolution obtained in the work of Kern et al is slightly better than that achieved here, the resolution obtained in the present work was such that the peak at 62 keV should have been observed. Even if the cross section were much less than the value reported, it would at least cause a shoulder on the peak due to the 56.7 keV level, contrary to experiment. It is therefore concluded that this is a spurious peak in ref.[57].

The state at 66.3 keV was not observed in the average resonance capture (ARC) studies of Kern et al[57], and since the claim of completeness for spins 0 to 3 up to 200 keV has been made for the ARC measurements, it must have spin > 3. If the single-neutron transfer involves both $l = 1$ and 3 transitions, then the spin of the state is limited to be in the range of 1 to 3. However, a fit to the (d,t) angular distribution with both $l = 1$ and 3 transitions fails the $F\chi$ test, and thus there is no evidence for an $l = 1$ component. The (d,t) angular distribution can be reproduced with a pure $l = 3$ component, which limits the spin to 4 or 5. A probable $E5$ transition has been observed to feed the ground state from an isomeric level at 161 keV, which is tentatively assigned an I^π value of 9^-. If the I^π value of the 66.3 keV state were 5^-, then an $M4$ transition to it from the isomer would probably be observed; since this is not observed, the spin of 4 is favoured for the 66.4 keV level.

The level observed at 256.8 keV was not seen in the ARC experiments by Kern et al[57], but was observed in their (d,p) and (d,t) measurements. It appears to have an $l = 3$ angular distribution for both the (d,t) and (d,p) reactions, with

perhaps a small amount of $l = 1$ present. The (d,t) F_χ value favours a two-component fit over a one-component fit. The presence of $l = 1$ in the angular distribution would limit the spin to be at most 3. The amount of $l = 1$ found by the fit is very small, and it is very sensitive to any impurity peaks or unresolved levels present in the spectra at forward angles. The 256.8 keV peak occurs in a region where the level density is fairly high, so that small, unaccounted for, impurity peaks could be present. While the energy of this state is greater than the limit on completeness given by Kern et al[57], they do state that most of the spin 0 to 3 states below 400 keV would be observed. Therefore, it is assumed that the $l = 1$ component is spurious, and thus this state is either 4^- or 5^-.

An interesting situation occurs for the peak at 367.2 keV where the (d,t) angular distribution required a fit with a small $l = 1$ strength and a large $l = 3$ strength, while the (d,p) angular distribution required only an $l = 1$ component. When a two-component fit to the (d,p) angular distribution was performed, the result fails the F_χ test. However, this peak is due to an unresolved doublet at energies of 366.7 and 368.4 keV. It is suggested that one of the levels is below the Fermi surface, and is responsible for the $l = 3$ strength observed in the (d,t) reaction.

5.1.2 Levels in ^{194}Ir

An extensive study of ^{194}Ir, similar to the study of ^{192}Ir, is currently being made[61], but unfortunately only some preliminary results are available. Many of the levels have undetermined spins, or have their spins only tentatively assigned. Most of the level energies below 500 keV observed in the present work agree with the those of Balodis et al[61].

As in ^{192}Ir, all of the levels populated with the single-neutron transfer reaction have negative parity. The $l = 1$ transitions dominated the angular distributions, with only a few $l = 3$ transitions observed. This is not surprising since the intrinsic cross section decreases as the l-value increases. It is quite possible that there are

many other weaker $l = 3$ and $l = 5$ transitions that were not observed. The $l = 3$ transitions that are observed, such as those to the 148.7 keV and 296.7 keV levels, are quite strong.

The ground state, known to be $I^\pi = 1^-$, was observed in the reaction, and had a similar strength to the lowest 1^- state in ^{192}Ir, which suggests that they have a similar configuration.

The state at 296.7 keV has a $F\chi$ statistic that allows for a fit to the angular distribution with both $l = 1$ and $l = 3$ components. The presence of $l = 3$ is definite, whereas the presence of $l = 1$ is less certain. There are known impurity peaks in the spectra, which obscure the peak at some angles, and there may be others that are unaccounted for. An I^π value of 4^- is given for this state by Balodis[61], which would rule out the presence of $l = 1$ in the transition. Given this value for the spin, the assumption is made that the $l = 1$ component is due to impurity contributions at forward angles, and a fit is made with a pure $l = 3$ curve.

5.1.3 Levels in ^{190}Ir

The study of ^{190}Ir offers a unique opportunity in that both single-neutron and single-proton transfer data have been obtained. Unfortunately, very little complementary information exists for this nucleus. Many negative parity levels below 1 MeV excitation energy have been observed in the present study.

The ground state of ^{190}Ir has been assigned[62] as spin 4^+. The spin 4 assignment comes from the observation[63] that states in ^{190}Os of spin 3, 4, and 5 are fed by electron capture from the ^{190}Ir ground state. The positive parity assignment for the ground state is deduced from knowledge of the parities of isomeric levels in ^{190}Ir, as well as the multipolarities of γ-transitions from the isomeric levels. The 3.25 h isomeric state at 175 keV decays to the 10^- state at 1705.8 keV in ^{190}Os via electron capture with a $\log ft = 4.7$. In a recent study, Sood et al[64] have found that for allowed-unhindered decays, which have $\log ft$ values below 5.2, the proton→neutron or neutron→proton transition involves only a spin-flip of the

particle, with all other Nilsson quantum numbers remaining the same. They find no instances where this rule has been broken. For low-lying states in the $A \simeq 190$ mass region, only the $\frac{9}{2}^-[505]_\nu$ and $\frac{11}{2}^-[505]_\pi$ orbitals satisfy the spin-flip condition. The isomeric 10^- state in ^{190}Os has been assigned the $\frac{9}{2}^-[505]_\nu + \frac{11}{2}^+[615]_\nu$ configuration, which implies the isomeric level at 175 keV in ^{190}Ir is the $\frac{11}{2}^-[505]_\pi + \frac{11}{2}^+[615]_\nu$ configuration. This argument yields the assignment of 11^- for the isomeric level in ^{190}Ir, which also decays[65] by an $M4$ transition to the state at 26.3 keV in ^{190}Ir, which further decays to the ^{190}Ir ground state by an $M3$ transition[65]. This yields the positive parity assignment for the ground state.

The first level populated in the (d,t) reactions has an angular distribution that can be fit with an $l = 3$ curve, which would limit the spin to the range 1 to 5, although there may be some $l = 1$ present, which would reject the possibility of $I^\pi = 4^-$ or 5^-. The amount of $l = 1$ indicated by the experimental data is very sensitive to any impurity peaks present at forward angles. There is a contribution to the peak area from the 319.7 keV state in ^{192}Ir due to the isotopic impurity in the target, and this accounts for about 10% to 20% of the peak intensity. With this component subtracted, the angular distribution fit with both $l = 1$ and $l = 3$ curves is favoured by the $F\chi$ test, but the amount of $l = 1$ is very small. Therefore, the $l = 1$ strength is questionable, and the strength value of 0.004 in Table 4.2.4 is considered to be a realistic upper limit of the $l = 1$ strength. If the transition is assumed to be a pure $l = 3$, the final spin could be in the range of 1 to 5. Although not as strongly populated, this level bears a resemblance to the first 4^- state populated in ^{192}Ir, and therefore it is suggested that the spin for this level in ^{190}Ir is also 4^-.

Many of the levels populated in ^{190}Ir with the (d,t) reaction were also populated in the (α,t) and (^{3}He,d) reactions. Table 5.1.1 lists the levels that appear to be populated in all three reactions. It cannot be said with certainty that there is a one-to-one correspondence in the levels, as there is a fairly high level density such

that some states are probably within a few keV of others, and are not resolved in the experiments.

The ratios of (^{3}He,d) and (α,t) cross sections presented in the previous chapter do not precisely determine the l-value of the transition. However, levels that are populated in both the single-neutron and single-proton transfer reactions must involve the positive parity proton. The single-proton transfer work of Price et al[59] examined states in ^{191,193}Ir, and found that there are are no $l = 1$ transitions and only one $l = 3$ transition to low-lying states. Therefore, since the low-lying proton states in ^{190}Ir should be similar to those in ^{191,193}Ir, it can be assumed that ratios indicative of $l = 1$ are probably due to a transition that contains both $l = 0$ and $l = 2$. For states populated in common in both single-proton and single-neutron transfer, ratios consistent with $l = 2$ or $l = 3$ will be assigned as an $l = 2$ transition. Table 5.1.1 lists the assigned l-values based on these assumptions for levels that appear to be populated in both single-proton and single-neutron transfer reactions.

5.2. Similarity of γ-Decay Branching

It was suggested[66] a number of years ago that if a state of unknown spin decays to a number of lower levels with the same branching fractions as a nearby state with known spin, the spins of the two states are the same. The basis for this argument was the spin selectivity of the γ-transitions. This has been put on a more quantitative basis by J. Cameron[67–68] using the multidimensional scaling program MINISSA.

The basis of this method is to find the degree of similarity of the decay branching for two initial states i and j by taking the scalar product

$$C_{ij} = \sum_f a_{if} a_{jf} \tag{5.2.1}$$

where a_{if}^2 is the branching intensity from state i to final state f, and similarly for a_{jf}^2. In other words, a vector is formed by taking the the square root of the

Table 5.1.1: Levels in ^{190}Ir Common to (α,t), (^{3}He,d), and (d,t) Reactions

Relative Excitation Energy (keV)			Assigned l
(α,t)	(^{3}He,d)	(d,t)	
26(1)	29(2)	25.9(4)	2
84(1)	86(1)	83.0(3)	2
145(1)	147(1)	144.0(6)	0, 2
173(1)	175(2)	173.8(4)	2
184(2)	187(2)	183.2(10)	0, 2
226(1)	227(1)	225.4(10)	0, 2
269(1)	271(1)	266.8(5)	0, 2
284(1)	287(2)	284.9(7)	0, 2
314(1)	312(1)	313.4(7)	2
428(2)	425(2)	426.7(6)	0, 2
511(1)	509(2)	510.9(8)	0, 2
590(2)	592(2)	589.3(9)	0, 2
623(1)	622(1)	619.1(10)	0, 2
672(1)	671(1)	669.0(7)	0, 2
741(1)	742(2)	743.5(12)	2

branching intensities to all final states. The matrix of similarities, C, is then used in a multidimensional scaling program. Briefly, a map is formed such that for each initial state i, if $C_{if} < C_{lm}$, then $d_{ij} > d_{lm}$ where d_{ij} is the distance between the points i and j in space. If two initial states have almost identical decay properties, their corresponding points on a map will be very close together, whereas if they have no similarity at all, they will be very far apart. As the number of points increases,

the positions on the map become "locked in" in the sense that it is not possible to change any of the points.

This method has been used in the $A \simeq 20$ and $A \simeq 60$ regions with a great deal of success[67,68]. It was found that regions of different spins on the maps are clearly delineated. An attempt has been made here to use the same method to help determine unknown spins of levels in ^{192}Ir. The γ-branching intensities were those published by Kern et al[57], and levels where the branching was uncertain were not considered. The maps generated by the program[69] MINISSA can be either one or two dimensional, and are shown in Figure 5.2.1 and Figure 5.2.2. The multidimensional scaling (MDS) method has never been applied to nuclei in this mass region, and more thorough tests need to be made. However, the known spins appear to be separated from one another. Boundaries on the maps suggest spins for the unknown states, and it should be noted that the spins and γ-multipolarities in the work of Kern et al[57] are consistent with those suggested by the similarity maps, except for one spin 0^- state at 128.7 keV, which appears in the spin 1 or 2 region. The outcome of the program is very sensitive to the placement of the γ-rays, and if more spins could be included the maps would probably be clearer. The suggested spins are listed in Table 5.2.1.

Table 5.2.1: Spins for states in ^{192}Ir suggested by MDS maps.

Energy (keV)	Level Number	Spin from ref.[57]	Spin from MDS maps
118.782	24	3^-	3
128.742	23	0^-	1, 2
143.554	22	$1^-, 2^-$	1
192.933	21	2^-	2
193.509	20	$1^+, 2^+$	2
212.805	19	$(0^-), 1^-, 2^-$	2
225.916	18	2^-	2
235.758	17	1^-	1
240.900	16	$0^-, 1^-, 2^-$	2
267.126	15	$(1^-), 2^-, 3^-$	2
288.402	14	$1^-, 2^-$	2
292.374	13	$1^-, 2^-$	2
310.996	12	2^-	2
319.891	11	2^-	2
331.074	10	$2^-, (3^-)$	2
331.757	9	1^-	1
351.690	8	$2^+, 3^+, 4^+$	3
366.730	7	2^-	2
368.352	6	2^-	2
392.352	5	$1^-, 2^-, 3^-$	2
415.039	4	$1^-, 2^-$	1
418.135	3	$2^+, 3^+, 4^+$	3
489.435	2	$1^-, 2^-, (3^-)$	1
508.989	1	$1^-, 2^-, 3^-$	1

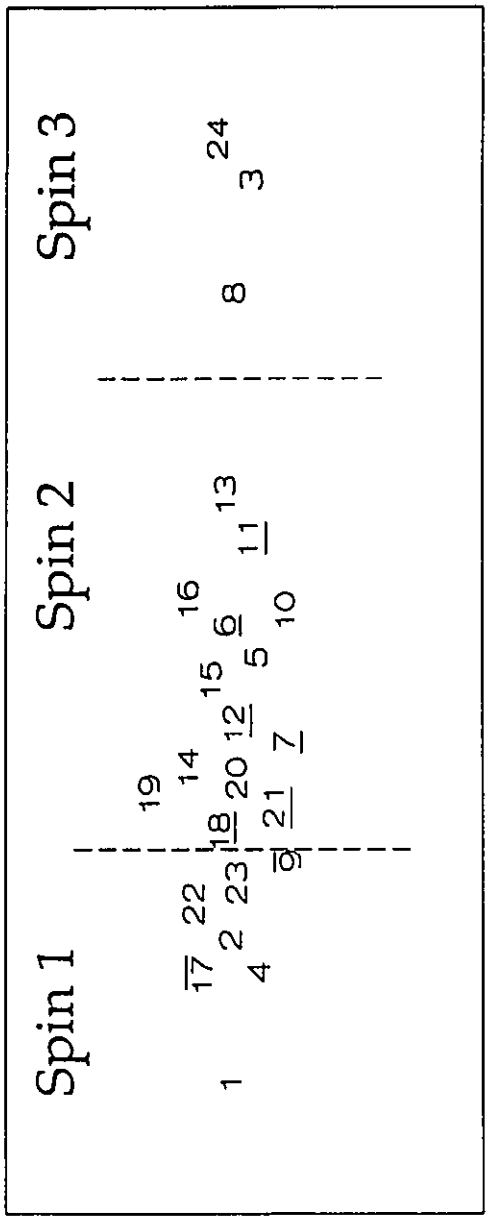

Figure 5.2.1: One-dimensional similarity plot produced by the program MINISSA. The numbers refer to levels as indicated in Table 5.2.1. States known to have spin 1 have a bar over their number, and those with spin 2 have a bar underneath. The dashed lines are suggested borders between the different spin regions.

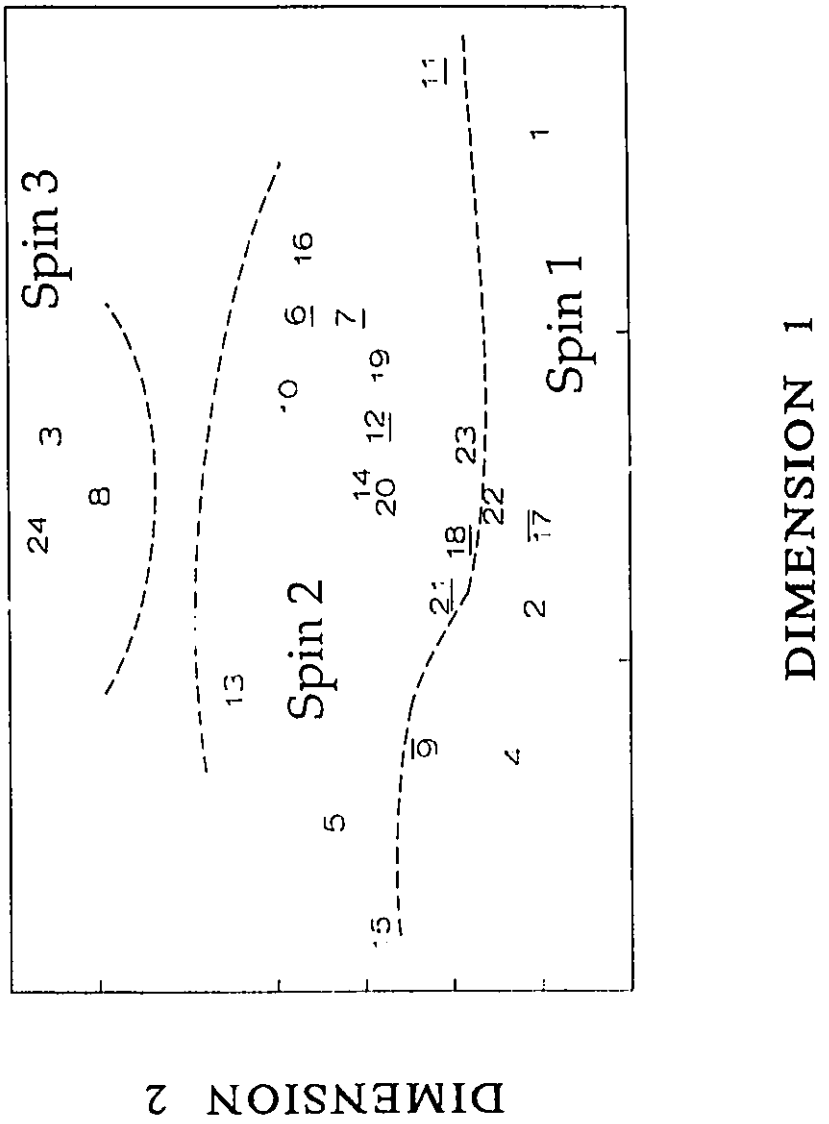

Figure 5.2.2: Two-dimensional similarity plot produced by the program MINISSA. The numbers refer to levels as indicated in Table 5.2.1. States known to have spin 1 have a bar over their number, and those with spin 2 have a bar underneath. The dashed lines are suggested borders between the different spin regions.

5.3. Interpretation in Terms of the IBFFM

Results of calculations performed by V. Paar and S. Brant[70] within the context of the interacting boson fermion fermion model (IBFFM) have been obtained. The calculations were performed with the computer code IBFFM, details of which have been described in the literature[71–73]. The Hamiltonianused in the calculations was that of Eq. (2.3.29), where the core is treated in the $SO(6)$ limit of the IBM, and valence shell proton and neutron quasiparticles are coupled to the core.

The parameters for the core were determined[57] by fitting the neighbouring even-even nuclei of Pt, and the boson space was limited to 4 bosons in order to reduce the length of the computations. Therefore, the normal $SO(6)$ parameters used to describe ^{194}Pt and ^{196}Pt, which have a total of 7 and 6 bosons, respectively, had to be renormalized. It was noted by Kern et al[57] that the truncated space reproduces the low-lying spectrum generated by the full space.

In ^{192}Ir, the proton orbitals considered were $s_{\frac{1}{2}}$, $d_{\frac{3}{2}}$, $d_{\frac{5}{2}}$, and $h_{\frac{11}{2}}$. The parameters for the IBFM(π) Hamiltonian were found by fitting the experimental properties of ^{193}Ir. The energies and occupation probabilities were determined to be 0.5, 0.0, 0.9, 0.7 MeV and 0.25, 0.62, 0.97, 0.85 for the above orbitals, respectively. From the fit to ^{193}Ir, the boson-fermion interaction strengths were determined to be $\Gamma_0^\pi = 0.55$, $\Lambda_0^\pi = 0.7$ MeV. By fitting the experimental properties of ^{193}Pt, the parameters needed for the IBFM(ν) Hamiltonian were found. The energies and occupation probabilities were 0, 0.18, 0.28, 0.73, 0.45 MeV, and 0.5, 0.6, 0.62, 0.78, 0.72 for the $p_{\frac{1}{2}}$, $p_{\frac{3}{2}}$, $f_{\frac{5}{2}}$, $h_{\frac{9}{2}}$, $i_{\frac{13}{2}}$ orbitals, respectively, and the boson-fermion interaction strengths are $\Gamma_0^\nu = 0.4$, $\Lambda_0^\nu = 0.57$ MeV. The occupation probabilities found for the orbitals differ from those obtained from the standard BCS approximation.

In order to explain the ground state spin, parity, magnetic moment and quadrupole moment, the calculations were finely tuned[57]. The magnetic moment could be reproduced only by introducing a strong mixing between the configurations $(\pi d_{\frac{5}{2}}, \nu i_{\frac{13}{2}})$ and $(\pi h_{\frac{11}{2}}, \nu p_{\frac{3}{2}})$. Usually the matrix elements between the two configurations vanish, with mixing only appearing in an "unstable" regime. The constraint

of the magnetic moment, along with the requirement that the lowest-lying positive-parity state is spin 4 and that it lie considerably below other positive-parity states, allowed values for the residual interaction strengths to be obtained. For the positive-parity states, the values determined were $V_\delta = -0.51$, $V_{\sigma\sigma} = 0.5$, $V_{\sigma\sigma\delta} = 0.05$, $V_T = -0.042$, $V_{22} = -0.8$, and $V_{44} = 0.1$ MeV for the delta, spin-spin, spin-spin-delta, tensor, quadrupole-quadrupole, and hexadecapole-hexadecapole interactions, respectively. For the negative-parity states, the same parameters were used except that the $\pi h_{\frac{11}{2}}$ and $\nu i_{\frac{13}{2}}$ orbital energies were lowered by 0.15 and 0.13 MeV, respectively, and the strengths of the spin-spin-delta and quadrupole-quadrupole residual interactions were adjusted to 0.015 and 0.3 MeV, respectively.

The same procedure was used to determine the parameters for the Hamiltonian for ^{194}Ir, except that the lowest-lying negative-parity state becomes the ground state, and the first positive-parity state is the 4^+ state at 147.1 keV.

The wave functions obtained from the calculation are very configuration mixed, often with 4 or 5 components with amplitudes of 0.4 or more. Examples of the wave functions for ^{192}Ir are presented in Table 5.3.1, which were obtained from the work of Kern et al[57]. The target wave function in zero'th order is written as $|1 \times 1d_{\frac{3}{2}}, 00; \frac{3}{2}\rangle$, where the proton is in the $d_{\frac{3}{2}}$ orbital, there are no d-bosons, and the final angular momentum is $\frac{3}{2}$. Using the wave function for the first 1^- state presented in Table 5.3.1, the spectroscopic strengths for the various j-values can be computed. Only those components of the final-state wave function that have no d-bosons contribute, and thus only the terms involving $j_\pi = d_{\frac{3}{2}}$, $j_\nu = p_{\frac{1}{2}}$, and $j_\pi = d_{\frac{3}{2}}$, $j_\nu = f_{\frac{5}{2}}$ will give non-zero spectroscopic strengths. The spectroscopic strength for pickup reactions (normalized to $(2j+1)V_j^2$ for each j and final angular momentum, I) is $(2j+1)V_j^2(\xi)^2$. The factor V_j^2 is the occupation probability for the orbit, and for $j = \frac{1}{2}$, $V_{\frac{1}{2}}^2 = 0.5$, and for $j = \frac{5}{2}$, $V_{\frac{5}{2}}^2 = 0.62$. Therefore, $S_{\frac{1}{2}}$ is calculated to be $(2 \times \frac{1}{2} + 1) \times 0.5 \times (0.48)^2 = 0.2304$, and $S_{\frac{5}{2}}$ is $(2 \times \frac{5}{2} + 1) \times 0.62 \times (0.2)^2 = 0.1488$. In the calculations received from Paar and Brant[70], the target wave function is no longer assumed to be a pure $d_{\frac{3}{2}}$ particle wave function, but involves other terms.

Therefore, another factor, the square of the amplitude for the particular proton component being considered, is introduced into the calculation. The spectroscopic strengths obtained from Paar and Brant[70] are listed in Appendix II.

Table 5.3.1: IBFFM Wave Functions for Some Low-Lying States in ^{192}Ir

I_r	j_π	j_ν	$j_{\pi\nu}$	n_d	J	$\xi[(j_\pi j_\nu)j_{\pi\nu}, n_d J; I_r]$
4_1^+	$d_{\frac{5}{2}}$	$i_{\frac{13}{2}}$	4	0	0	0.33
	$h_{\frac{11}{2}}$	$p_{\frac{3}{2}}$	4	0	0	−0.28
	$h_{\frac{11}{2}}$	$f_{\frac{5}{2}}$	4	0	0	0.26
	$d_{\frac{5}{2}}$	$i_{\frac{13}{2}}$	4	1	2	0.29
	$h_{\frac{11}{2}}$	$p_{\frac{3}{2}}$	4	1	2	−0.26
	$h_{\frac{11}{2}}$	$f_{\frac{5}{2}}$	4	1	2	0.22
	$d_{\frac{5}{2}}$	$i_{\frac{13}{2}}$	4	2	0	−0.33
	$h_{\frac{11}{2}}$	$p_{\frac{3}{2}}$	4	2	0	0.27
	$h_{\frac{11}{2}}$	$f_{\frac{5}{2}}$	4	2	0	−0.24
1_1^-	$d_{\frac{3}{2}}$	$p_{\frac{1}{2}}$	1	0	0	0.48
	$d_{\frac{3}{2}}$	$f_{\frac{5}{2}}$	1	0	0	−0.20
	$d_{\frac{3}{2}}$	$p_{\frac{1}{2}}$	1	2	0	−0.46
	$d_{\frac{3}{2}}$	$p_{\frac{1}{2}}$	2	1	2	−0.23
	$d_{\frac{3}{2}}$	$p_{\frac{3}{2}}$	3	2	2	0.23
3_1^-	$d_{\frac{3}{2}}$	$p_{\frac{1}{2}}$	1	1	2	0.25
	$d_{\frac{3}{2}}$	$p_{\frac{1}{2}}$	2	1	2	0.39
	$d_{\frac{3}{2}}$	$p_{\frac{1}{2}}$	2	3	2	−0.22
	$d_{\frac{3}{2}}$	$f_{\frac{5}{2}}$	3	0	0	0.29
	$d_{\frac{3}{2}}$	$p_{\frac{3}{2}}$	3	1	2	0.26
	$d_{\frac{3}{2}}$	$f_{\frac{5}{2}}$	3	2	0	−0.28
	$d_{\frac{3}{2}}$	$h_{\frac{9}{2}}$	5	1	2	−0.27

Table 5.3.1 -continued

I_τ	j_π	j_ν	$j_{\pi\nu}$	n_d	J	$\xi[(j_\pi j_\nu)j_{\pi\nu}, n_d J; I_\tau]$
0^-	$d_{\frac{3}{2}}$	$p_{\frac{3}{2}}$	0	0	0	0.38
	$d_{\frac{3}{2}}$	$p_{\frac{3}{2}}$	0	2	0	−0.40
	$d_{\frac{3}{2}}$	$p_{\frac{1}{2}}$	2	1	2	−0.23
	$d_{\frac{3}{2}}$	$p_{\frac{3}{2}}$	2	1	2	0.54
	$d_{\frac{3}{2}}$	$p_{\frac{3}{2}}$	2	3	2	−0.32
1_2^-	$d_{\frac{3}{2}}$	$f_{\frac{5}{2}}$	1	0	0	0.26
	$d_{\frac{3}{2}}$	$p_{\frac{1}{2}}$	1	1	2	0.37
	$d_{\frac{3}{2}}$	$f_{\frac{5}{2}}$	1	2	0	−0.24
	$d_{\frac{3}{2}}$	$p_{\frac{1}{2}}$	1	3	2	0.21
	$d_{\frac{3}{2}}$	$p_{\frac{3}{2}}$	3	1	2	0.29
2_1^-	$d_{\frac{3}{2}}$	$p_{\frac{1}{2}}$	1	1	2	0.37
	$d_{\frac{3}{2}}$	$p_{\frac{1}{2}}$	1	3	2	−0.21
	$d_{\frac{3}{2}}$	$p_{\frac{1}{2}}$	2	0	0	0.48
	$d_{\frac{3}{2}}$	$p_{\frac{1}{2}}$	2	1	2	0.24
	$d_{\frac{3}{2}}$	$p_{\frac{1}{2}}$	2	2	0	−0.45
9_1^+	$d_{\frac{5}{2}}$	$i_{\frac{13}{2}}$	9	0	0	−0.48
	$d_{\frac{5}{2}}$	$i_{\frac{13}{2}}$	9	1	2	−0.54
	$d_{\frac{5}{2}}$	$i_{\frac{13}{2}}$	9	2	0	0.47
	$d_{\frac{5}{2}}$	$i_{\frac{13}{2}}$	9	3	2	0.32

The proper normalization for the spectroscopic strengths for pickup reactions, defined as in Eq. (4.2.2), requires that for a particular j-transfer, the sum of S_j over all possible final spins is $(2j+1)V_j^2$. The strengths calculated from the Nilsson model have the proper normalization. The spectroscopic strengths obtained from the calculations of Paar and Brant[70], on the other hand, are normalized such that for *each* angular momentum value of the final nucleus, the sum of strengths is $(2j+1)V_j^2$ for pickup reactions. Therefore the strengths of Paar and Brant[70] must be renormalized so that the sum over *all* final spin values of the pickup strength is $(2j+1)V_j^2$. Once the renormalization is achieved, the experimental values of the strength can be directly compared to the calculated values. The renormalization procedure is somewhat arbitrary, since in general each j-component for each final spin I can have a different normalization. Unfortunately, this introduces 14 parameters into the strength calculations that are not predicted by the model. The procedure chosen to determine the parameters was the following: for each final angular momentum I, a normalization R_{Ij} was found by examining the experimental (d,t) strength distribution, and then matching, as closely as possible (subject to the constraint that the proper sum is obtained), the theoretical distribution for each j-component. For some spin values, such as 0^-, there was only one experimental state known in ^{192}Ir, and therefore the renormalization value used was such that the (d,t) strength to that state was reproduced. For other spins, especially 1^- and 2^-, many experimental states were known, and the renormalization values chosen were those that best reproduced the experimental strengths. Where possible, the same renormalization value was used for the same j-component for different spins. The stripping strengths obtained from Paar and Brant[70] must also be renormalized with the same parameters. If a value different from that used for the (d,t) reactions was employed, this would effectively change the U_j^2 values. Since the (d,t) strength data are more reliable and in many cases yield values for more than one j-transfer to a single state, the renormalization constants were found from these data, and

then applied to the (d,p) strengths. The renormalization values used are shown in Table 5.3.2.

Table 5.3.2: Renormalization Constants for Spectroscopic Strengths

Final Spin	$j_{\frac{1}{2}}$	$j_{\frac{3}{2}}$	$j_{\frac{5}{2}}$	$j_{\frac{9}{2}}$
0^-		0.024		
1^-	0.5	0.2	0.15	
2^-	0.5	0.55	0.15	
3^-		0.1	0.15	0.1
4^-			0.6	0.15
5^-				0.32
6^-				0.32

5.3.1 ^{192}Ir Interpretation in Terms of IBFFM

The IBFFM calculation makes predictions for both the wave functions and energies of excited states. The wave functions determine the specific properties of the levels, such as the transfer strengths, electromagnetic (EM) transition rates, etc. Cizewski et al[40] pointed out that the IBFM calculations had difficulty in predicting both the EM transition rates and the spectroscopic strengths simultaneously. Therefore, it might be expected that the IBFFM will also have these difficulties.

The calculated low-lying negative-parity states below 500 keV for ^{192}Ir are shown in Figure 5.3.1. As can be seen, there is a large number of 2^- states predicted, whereas the numbers of 0^- and 4^- states are relatively small. This agrees with the experimental situation also shown in Figure 5.3.1. There are three 1^- states that are predicted below 150 keV, and these are observed in the experiments. Above 150 keV the 1^- states that are observed become separated in energy more than predicted.

The large number of 2^- states are somewhat closer in energy than predicted, but several of these have spin assignments based on the similarity maps. If some of the states that are suggested to be 2^- are actually 1^-, then the overall agreement would improve. There are more serious discrepancies that occur, however. The calculated energies of the 3^- and 4^- states appear to be much greater than observed. For instance, the first 3^- state is predicted at 257 keV whereas experimentally it is observed at 83.8 keV. The situation is even more exaggerated for the first 4^- state (predicted at 412 keV but assigned at 66.3 keV). Figure 5.3.2, which plots E versus $I(I+1)$ for the yrast levels, illuminates this difficulty. As can be seen, the theoretical plot is approximately a straight line from spin 1 to 4, whereas the experimental curve is very different.

Table 5.3.3 presents the results of the IBFFM calculations for ^{192}Ir obtained from Paar and Brant[70]. The strengths given in the table have been renormalized using the values listed in Table 5.3.2. Figure 5.3.3 shows the predicted and experimental strength distributions for $l = 1$ and $l = 3$ transfer with the (d,t) reaction. The predicted $l = 1$ strength to low-lying 1^- states is much greater than observed, especially for the first and third 1^- levels. The lowest 2^- state has a predicted $l = 1$ strength that is consistent with the observed value to the doublet 116.5 keV, but the predictions for the next four 2^- states are a factor of approximately 2 too great. In fact, there is a general trend that the predicted $l = 1$ strengths to the low-lying states are much greater than observed, and this is best illustrated in Figure 5.3.4, which shows the sum of the $l = 1$ and $l = 3$ strength versus energy. Above 130 keV, the predicted $l = 1$ strength sum grows at a rate approximately 60% greater than the observed $l = 1$ strength. The major discrepancies for the $l = 3$ strength occur for the 4^- state at 66.3 and the 4^- or 5^- state at 256.8 keV, which have large $l = 3$ strengths, and are predicted in the IBFFM to have an energy greater than 400 keV. The predicted and observed sum of $l = 3$ strength shown in Figure 5.3.4 are approximately equal at an energy of 450 keV. While the IBFFM cannot correctly

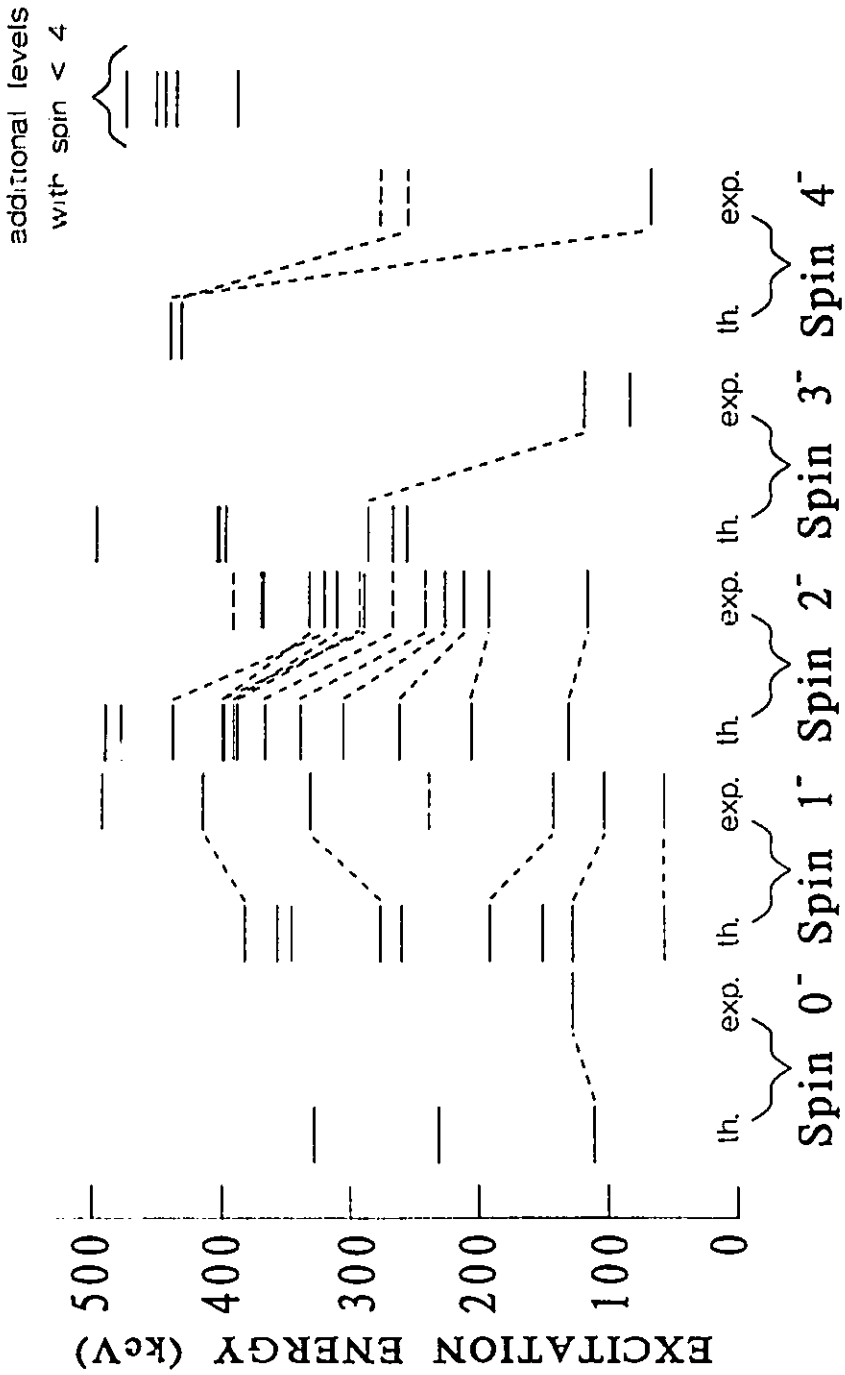

Figure 5.3.1: Predictions from the IBFFM for low-lying states and experimentally observed levels in ^{192}Ir. Only the negative-parity states with spin$\leq$4 are shown. Levels with dashed lines correspond to levels for which the spin is uncertain. The lines connecting levels are the assignments made in the present work.

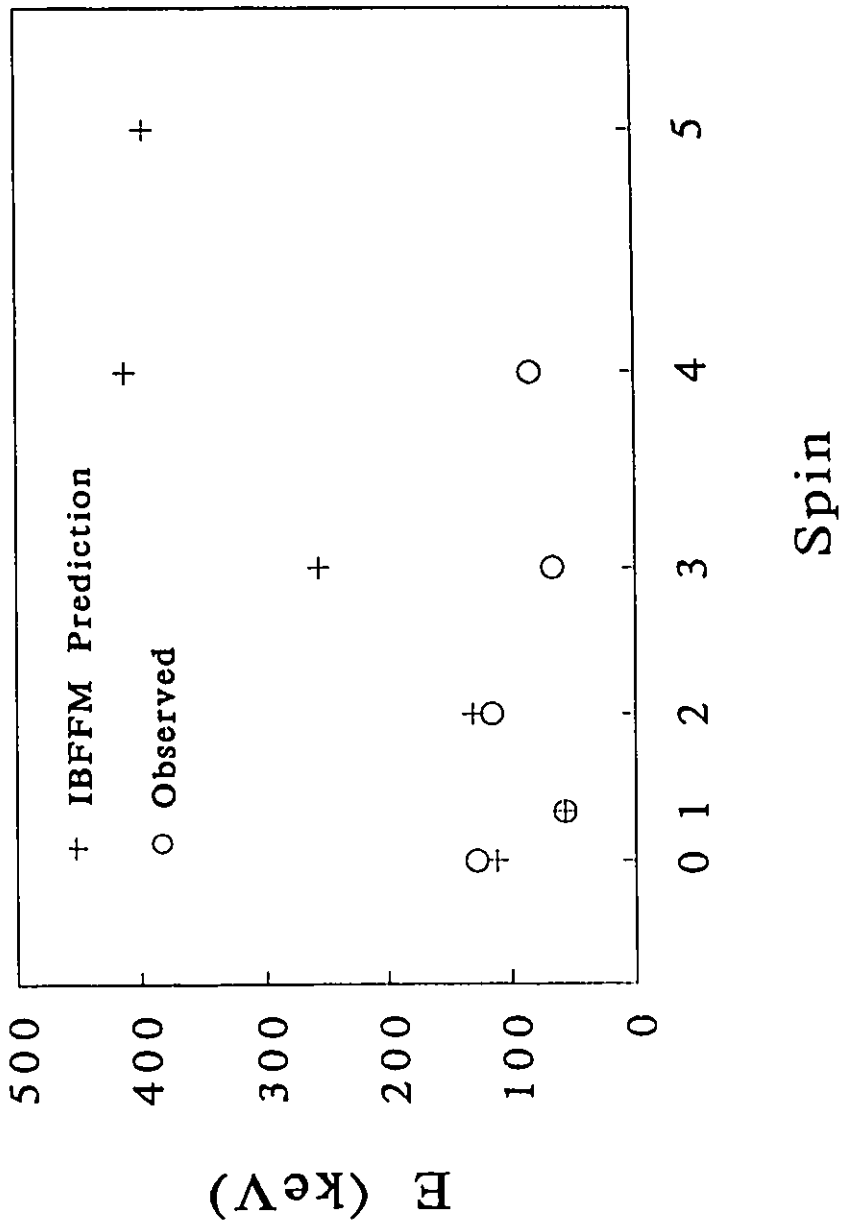

Figure 5.3.2: E versus $I(I+1)$ plot for yrast states predicted with the IBFFM and observed in ^{192}Ir.

predict the energy of states with large $l = 3$ strengths, it can reproduce the correct magnitude of total $l = 3$ strength to low-lying levels.

Table 5.3.3: IBFFM Prediction for ^{192}Ir

Energy	Spin	(d,t) Strength			(d,p) Strength		
(keV)		S_1	S_3	S_5	S_1	S_3	S_5
57	1^-	0.253	0.029		0.095	0.002	
112	0^-	0.039			0.001		
128	1^-	0.064	0.104		0.020	0.007	
131	2^-	0.334	0.048		0.171	0.007	
151	1^-	0.193	0.016		0.021	0.0008	
192	1^-	0.013	0.042		0.003	0.001	
208	2^-	0.283	0.012		0.115	0.0005	
233	0^-	0.00009			0.000003		
257	3^-	0.009	0.047	0.020	0.002	0.009	0.00005
261	1^-	0.049	0.004		0.018	0.0001	
263	2^-	0.146	0.015		0.029	0.002	
269	3^-	0.010	0.137	0.008	0.003	0.022	0.0002
277	1^-	0.161	0.0004		0.029	0.00007	
288	3^-	0.114	0.00006	0.010	0.032	0.0002	0.0002
306	2^-	0.227	0.146		0.057	0.017	
329	0^-	0.008			0.0002		
340	2^-	0.241	0.030		0.050	0.002	
347	1^-	0.009	0.022		0.003	0.001	
360	1^-	0.005	0.027		0.0006	0.001	
367	2^-	0.050	0.006		0.014	0.0001	
383	1^-	0.038	0.044		0.010	0.003	
389	2^-	0.007	0.001		0.004	0.0002	
391	2^-	0.012	0.006		0.004	0.001	

Table 5.3.3 -continued

Energy (keV)	Spin	(d,t) Strength			(d,p) Strength		
		S_1	S_3	S_5	S_1	S_3	S_5
396	5^-			0.017			0.0003
399	2^-	0.192	0.0005		0.041	0.00008	
400	2^-	0.007	0.010		0.002	0.0012	
402	3^-	0.002	0.029	0.002	0.0005	0.006	0.000004
405	3^-	0.008	0.020	0.0005	0.002	0.003	0.000004
412	4^-		0.403	0.0039		0.065	0.0007
431	11^-						
434	4^-		0.227	0.076		0.037	0.00016
438	2^-	0.082	0.066		0.026	0.007	
439	12^-						
477	2^-	0.027	0.002		0.009	0.0002	
484	6^-			0.0001			0.000001
490	2^-						
494	7^-						
497	3^-	0.008	0.055	0.016	0.002	0.007	0.00007

The predicted and observed strength distributions for the (d,p) reaction are shown in Figure 5.3.5 for both $l = 1$ and $l = 3$ transfer for final states with I^π values 0^- to 4^-. As can be seen, there are serious discrepancies for the $l = 3$ strength, with some very strong states observed but not predicted. This is best illustrated in Figure 5.3.6, which plots the sum of strengths for the (d,p) reaction for both experimental and predicted $l = 1$ and $l = 3$ transfer. The predicted $l = 1$ strength is also underestimated, but not as seriously as the $l = 3$ strength.

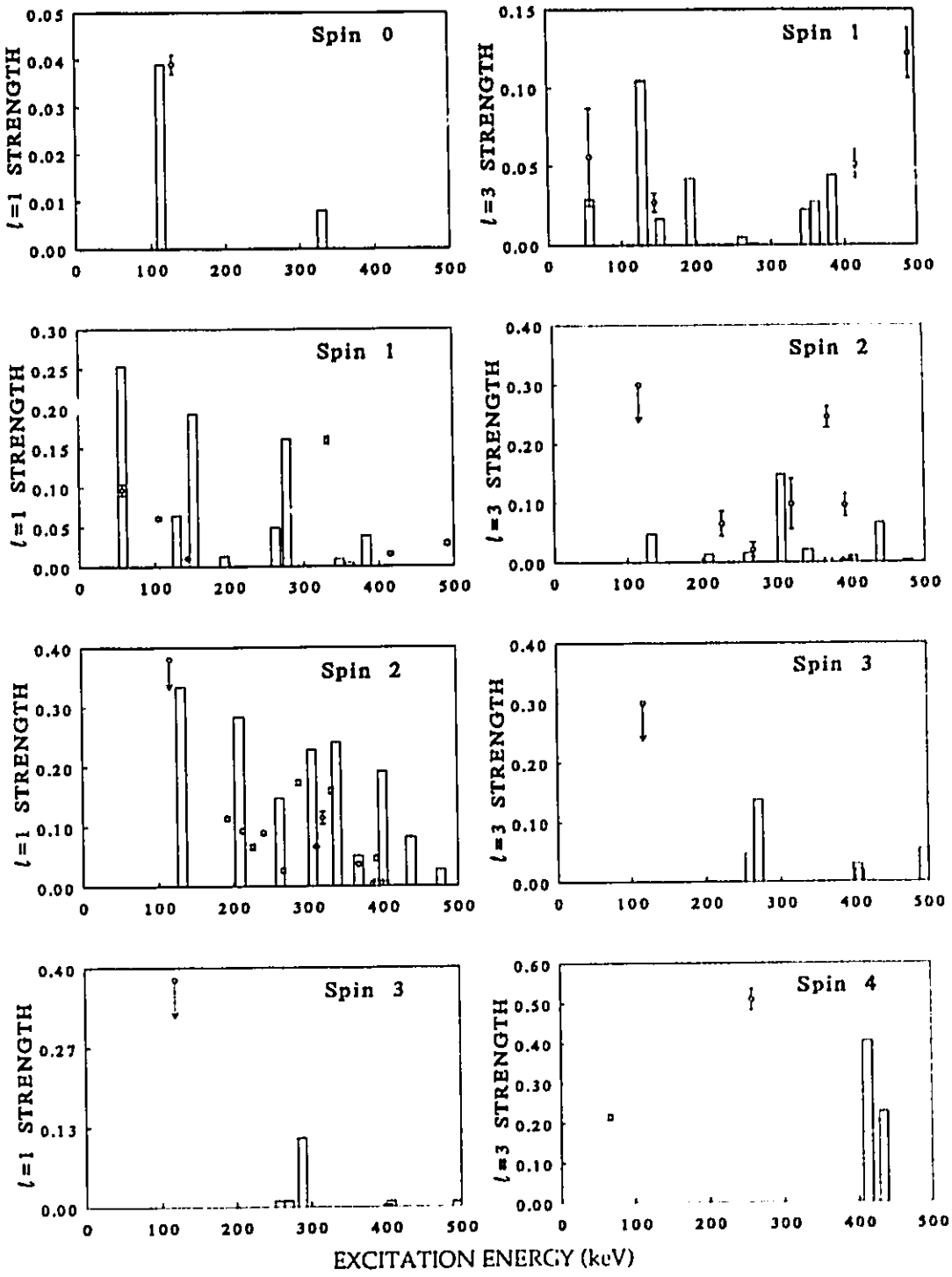

Figure 5.3.3: Predicted strengths from the IBFFM (bars) and experimental strengths (dots) for negative-parity states populated in the ^{193}Ir(d,t)^{192}Ir reaction.

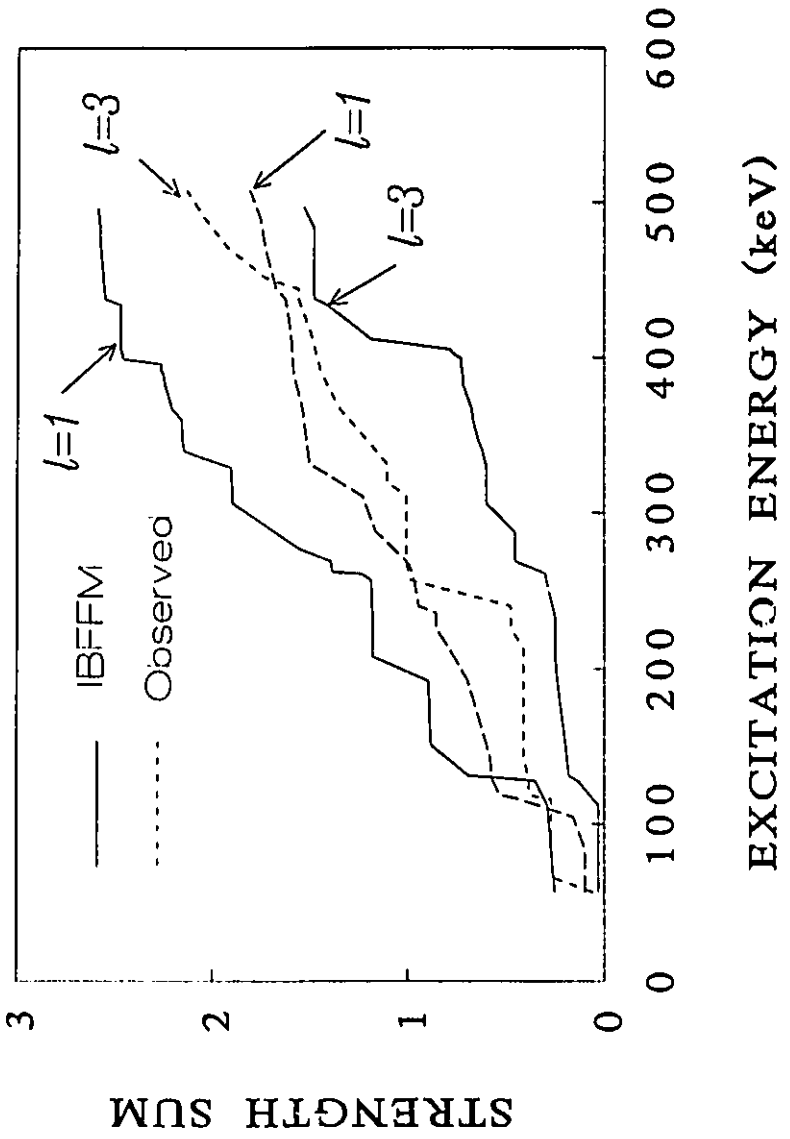

Figure 5.3.4: Sum of $l = 1$ and $l = 3$ strength predicted by the IBFFM and observed for the ^{193}Ir(d,t)^{192}Ir reaction. The predicted $l = 1$ strength grows at a rate approximately 60% greater than observed, and the discrepancies between the predicted and observed $l = 3$ strength sum arise mainly from the low-lying 4^- states.

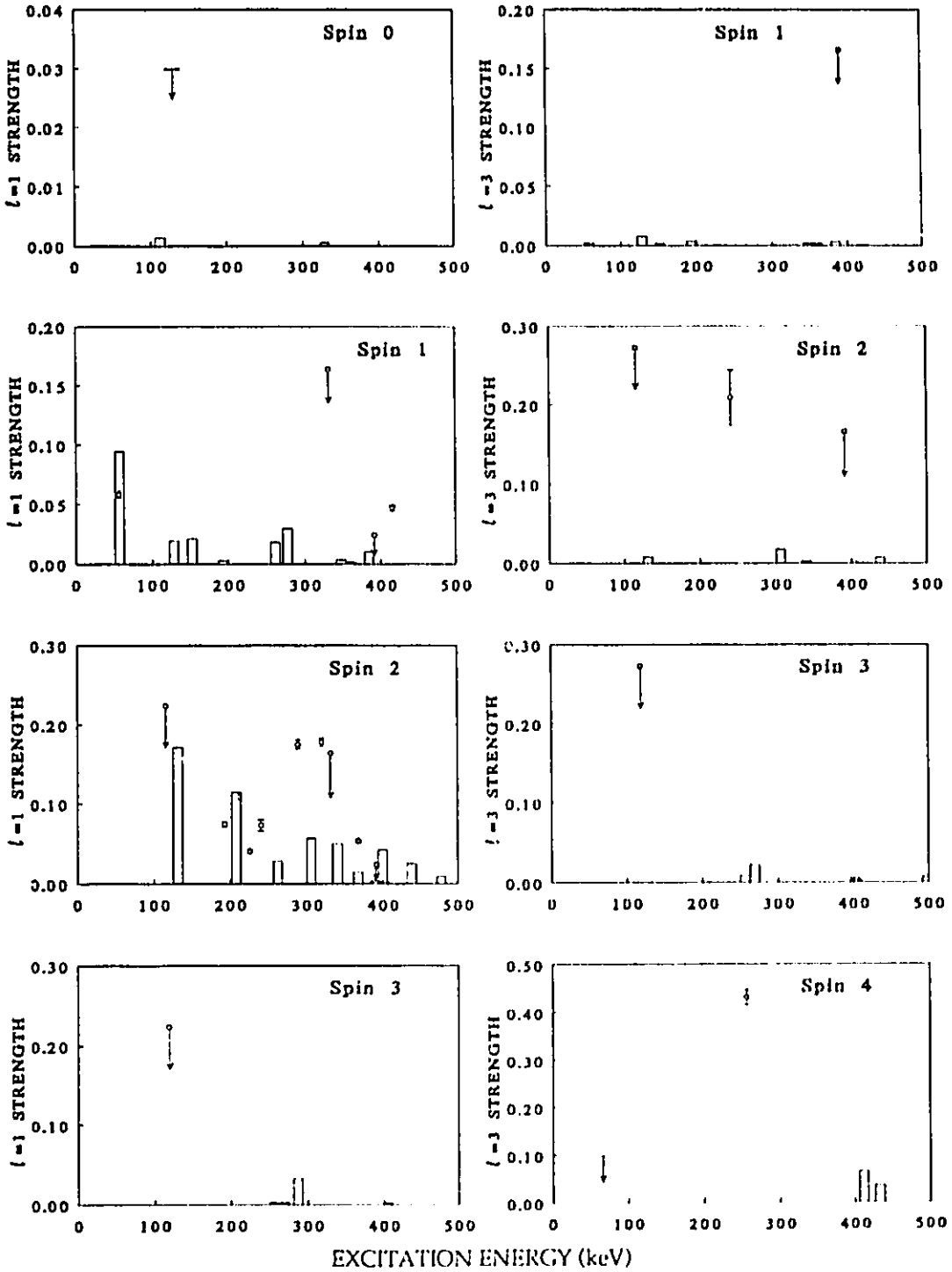

Figure 5.3.5: Predicted strengths from the IBFFM (bars) and experimental strengths (dots) for negative-parity states populated in the ^{191}Ir(d,p)^{192}Ir reaction.

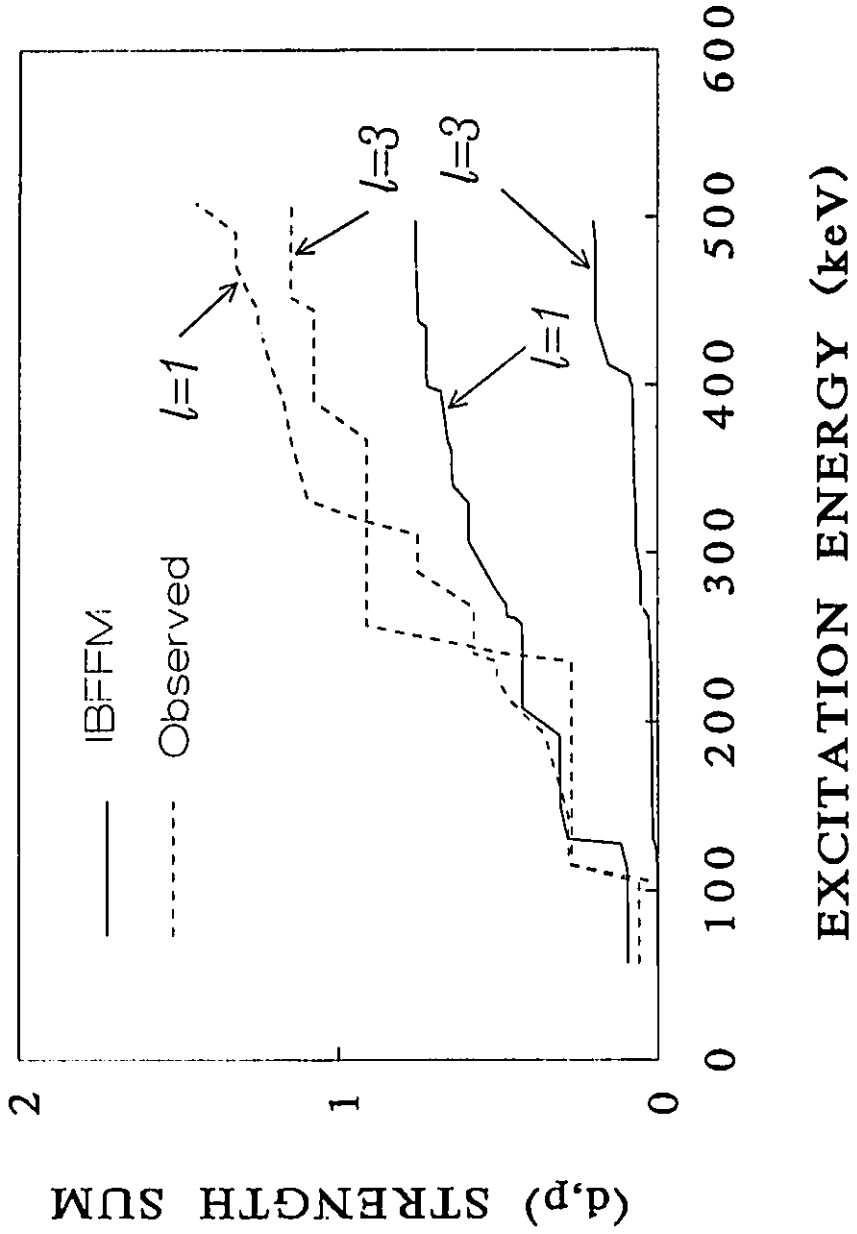

Figure 5.3.6: Sum of $l = 1$ and $l = 3$ strength predicted by the IBFFM and observed for the ^{191}Ir(d,p)^{192}Ir reaction. The observed $l = 1$ strength grows at a rate approximately 60% greater than predicted, and the predicted $l = 3$ strength is seriously underestimated.

In order to obtain good agreement between the theoretical and experimental strengths, the predicted energy and relative position of the states in the IBFFM calculation must be disregarded in some cases. For example, the first 4^- state in ^{192}Ir has a spectroscopic strength that matches the second 4^- state in the IBFFM, whereas the state at 256.8 keV, if it is a 4^- state, would be a better match to the strength predicted for the first 4^- state in the IBFFM. The assignments of predicted levels to observed ones made in this work are based primarily on the (d,p) and (d,t) strengths. However, in making assignments the relative positions of the predicted states are disregarded only in cases were it is clear that by doing so results in a significantly improved fit. In the following, only those states that require special attention, such as those where the relative positions of the predicted states must change, or are of special interest, are discussed.

The ground state in ^{192}Ir has been measured[57] to have spin and parity 4^+, and was not populated in the (d,t) or (d,p) reactions. The IBFFM parameters were adjusted[57] so that the calculation reproduces the observed spin for the ground state, and predicts that it should have approximately zero cross section, since it involves $d_{\frac{5}{2}}$ proton components and the target is primarily $d_{\frac{3}{2}}$ proton configuration.

The first 4^- state predicted in the IBFFM comes at an energy of 412 keV, approximately 346 keV higher than the first observed 4^- state at 66.3 keV. The next 4^- state is predicted at 434 keV, and has a much better strength match to the observed level at 66.3 keV, and therefore this assignment is adopted. It should be noted, however, that this match occurs for the strength values predicted when the state is at 434 keV, not when it is at 66 keV. If the parameters in the calculation were adjusted so that this state were brought down in energy, it is probable that the wave function would change significantly, thereby changing the predicted strengths considerably.

An interesting situation occurs with the 84.3 keV 3^- state. Even though the transfer of $j = \frac{3}{2}, \frac{5}{2}, \frac{7}{2}$, and $\frac{9}{2}$ would satisfy the angular momentum coupling rules, the (d,t) cross section to this state appears to be essentially that of a pure

$l = 5$ transition. The IBFFM calculation for 3^- states have essentially no $l = 5$ strength, and thus no match can be found for the state at 84.3 keV. This is clearly an inadequancy in the calculations.

The most intense peaks observed in the (d,t) and (d,p) reactions are due to an unresolved doublet of the 115.6 and 118.8 keV levels. The state at 115.6 keV is either 1^- or 2^-, while the one at 118.8 keV is known to be 3^-. In the work of Kern et al[57], the two states were resolved in the (d,p) and (d,t) spectra. At an angle of 45°, the lower member of the doublet was measured to have a (d,t) cross section approximately 61% greater, and a (d,p) cross section 54% greater, than the upper member of the doublet. Kern et al[57] favour the assignment of spin 2 for the level at 115.6 keV, and thus an appropriate candidate would be the first 2^- level predicted at 131 keV, which has (d,t) strengths of $S_1 = 0.334$, $S_3 = 0.049$, and (d,p) strengths of $S_1 = 0.171$, $S_3 = 0.007$. With this assignment, the amount of $l = 1$ strength remaining for the 118.8 keV state would be $S_1 = 0.05$, $S_3 = 0.25$ for the (d,t) reaction and $S_1 = 0.05$, $S_3 = 0.27$ for the (d,p) reaction. This does not reproduce the observations of Kern et al[57] for the cross section ratios for these states. No 3^- level predicted in the IBFFM matches the required populations exactly. However, the only reasonable candidate is the third 3^- level predicted at 288 keV, with (d,t) strengths of $S_1 = 0.114$, $S_3 = 0.00006$, and (d,p) strengths of $S_1 = 0.032$, $S_3 = 0.0002$. The predictions have an obvious discrepancy with the data in that the combined $l = 3$ strength is not reproduced.

The state at 143.5 keV was populated in the (d,t) reaction, but was not observed in the (d,p) reaction. Its (d,t) strength was $S_1 = 0.010 \pm 0.001$ and $S_3 = 0.027 \pm 0.006$. The similarity plots of the γ-ray intensities from this state, in 1 and 2 dimensions, favours a spin of 1. Adopting this, the best match in the IBFFM would be the state predicted at 192 keV, which has (d,t) strengths of $S_1 = 0.013$ and $S_3 = 0.042$. The third 1^- state in the model at 151 keV is predicted to have a large (d,t) $l = 1$ strength, and is therefore not a good candidate.

Kern et al[57] reported a level at 278.0 keV having an I^π value of 3^- or 4^-. In the (d,t) spectra, there is evidence for a weak peak at this energy with an angular distribution that would be consistent with an $l = 5$ transition with $S_5 = 0.34 \pm 0.05$. Since there are no 3^- states in the IBFFM with significant $l = 5$ strength, the model favours a spin of 4 for this state. The best candidate for this level in the IBFFM is the fourth 4^- level, which has an energy greater than 500 keV and predicts an $l = 5$ strength of $S_5 = 0.1$. Clearly, this is not a good match.

The peak observed at an energy of 288.5 keV in the spectra is due to an unresolved doublet of states at energies of 288.4 keV and 292.4 keV. However, the observed energy of the peak suggests that the lower member of the doublet dominates the cross section, and this is supported by the (d,t) spectrum shown in the work of Kern et al[57]. Both members of the doublet have either $I^\pi = 1^-$ or 2^-. The similarity plots for the 288.4 keV level favour spin 2. The most appropriate candidate in the IBFFM is the state predicted at 399 keV, with (d,t) strengths that are in excellent agreement with the observed value, but the (d,p) strength is seriously underestimated.

The state observed at 319.7 keV in both the (d,p) and (d,t) reactions has $I^\pi = 2^-$. The angular distribution for this peak in the (d,t) reaction had to be fit with both $l = 1$ and $l = 3$ curves, yielding strengths of $S_1 = 0.144 \pm 0.010$, and $S_3 = 0.098 \pm 0.043$. The (d,p) angular distribution appeared to be a pure $l = 1$ with strength $S_1 = 0.178 \pm 0.005$. The IBFFM predicts a 2^- state at 438 keV with $S_1 = 0.082$, $S_3 = 0.066$ for (d,t) strengths and $S_1 = 0.025$, $S_3 = 0.007$ for (d,p) strengths. This is a very poor match to the observed strengths, but there are no unassigned 2^- states in the IBFFM that would give a better match.

The peak at 331.7 keV, which was observed in both the (d,p) and (d,t) spectra, is due to an unresolved doublet of levels at 331.1 and 331.8 keV, with I^π values of 2^- or 3^-, and 1^-, respectively. Kern et al[57] favour the assignment of spin 2 for the former state, and the similarity plots also favour this. The (d,t) angular distribution for this peak was fit with a pure $l = 1$ DWBA curve, yielding a

strength value of $S_1 = 0.159 \pm 0.005$. The (d,p) angular distribution also resembled that of a pure $l = 1$, with the fit result giving $S_1 = 0.164 \pm 0.006$. Since the two levels lie so close together, the amount of strength to each is not known, and it is not possible to make firm assignments with states in the IBFFM. However, there are the restrictions that the sums of the predicted strengths match the observed strengths for the peak, and that they have only $l = 1$ strength. Since there is no 2^- level left unassigned that predicts significant $l = 1$ strength, it is implied that in order to match the observed strength, most of it would have to come from the spin 1^- level. The only candidate that meets this requirement and lies relatively close in energy is the 1^- level predicted at 277 keV, which gives $S_1 = 0.161$, $S_3 = 0.0004$ for (d,t) and $S_1 = 0.029$, $S_3 = 0.00007$ for (d,p) reactions. The 2^- candidate chosen is the one closest in energy to the observed state, at 400 keV, which has $S_1 = 0.007$, $S_3 = 0.010$, and $S_1 = 0.002$, $S_3 = 0.001$ for (d,t) and (d,p) reactions, respectively. While this result agrees with the observed (d,t) strength, it seriously underestimates the (d,p) strength. However, there are no other unassigned states remaining that would give better agreement with the (d,p) strength.

The next peak observed at 367.2 keV is also due to unresolved levels at 366.7 and 368.4 keV, both of which have spin 2^-. The (d,t) angular distribution appeared to be mainly $l = 3$, with strength $S_3 = 0.245 \pm 0.018$, and a small amount of $l = 1$, with $S_1 = 0.037 \pm 0.003$. The (d,p) angular distribution appears to be that of an $l = 1$ transition, with $S_1 = 0.043 \pm 0.002$. There are no candidates in the IBFFM for 2^- states that would match the observed (d,t) $l = 3$ strength.

A plot of both the experimental and theoretical energies is shown in Figure 5.3.1 where the connecting lines are based on the above assignments. Figure 5.3.7 and Figure 5.3.8 show the experimental and theoretical (d,t) strengths for $l = 1$ and $l = 3$ transitions, and Figure 5.3.9 and Figure 5.3.10 shows the (d,p) $l = 1$ and $l = 3$ strengths, respectively, based on the above assignments. It is clear that the IBFFM does not give a complete description of ^{192}Ir; it can, however, approximately reproduce the structure for some of the low-lying states. The

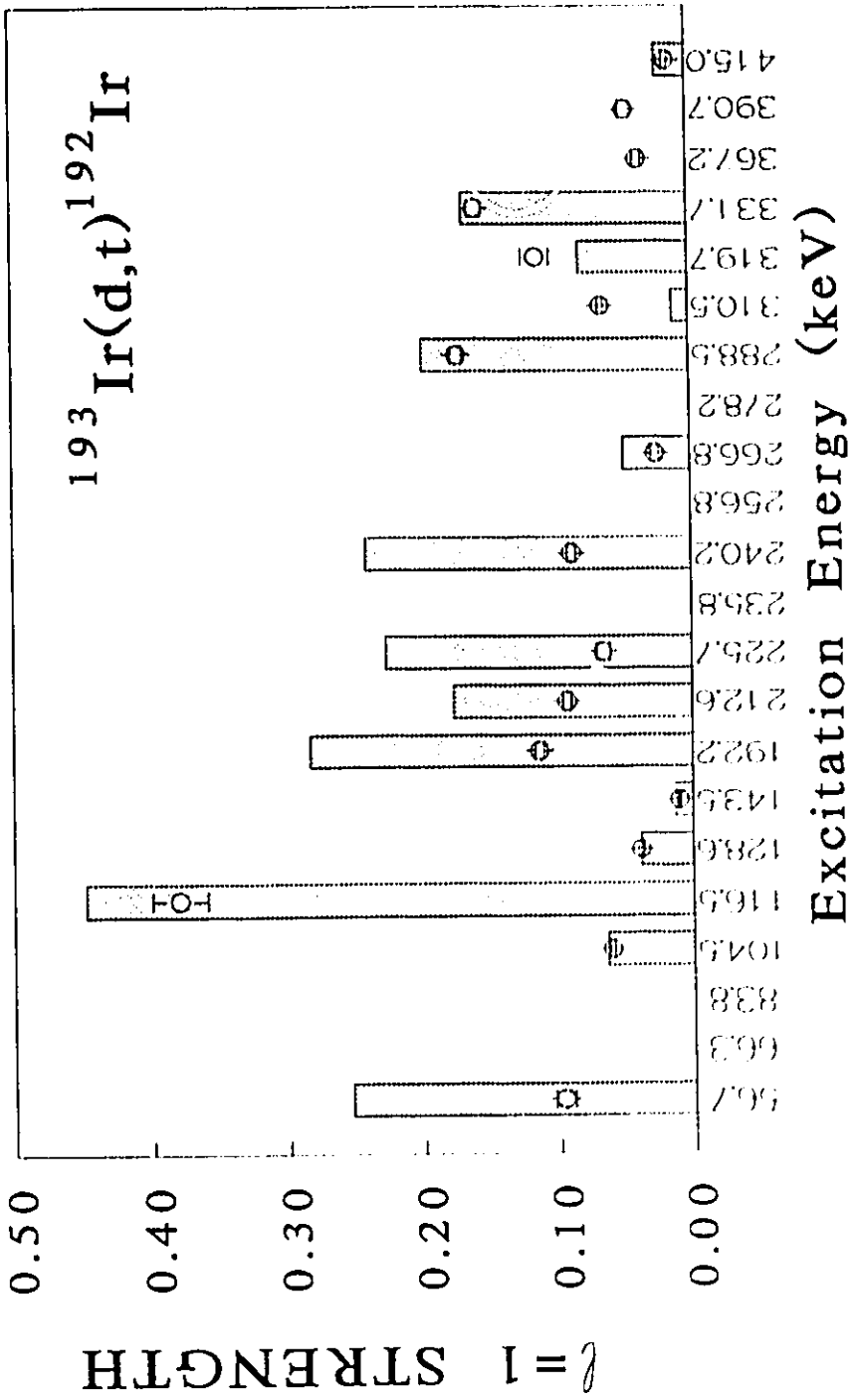

Figure 5.3.7: Predicted strengths from the IBFFM (bars) and experimental strengths (dots) for negative-parity states populated with $l = 1$ transfer in the ^{193}Ir(d,t)^{192}Ir reaction based on the assignments in Figure 5.3.1.

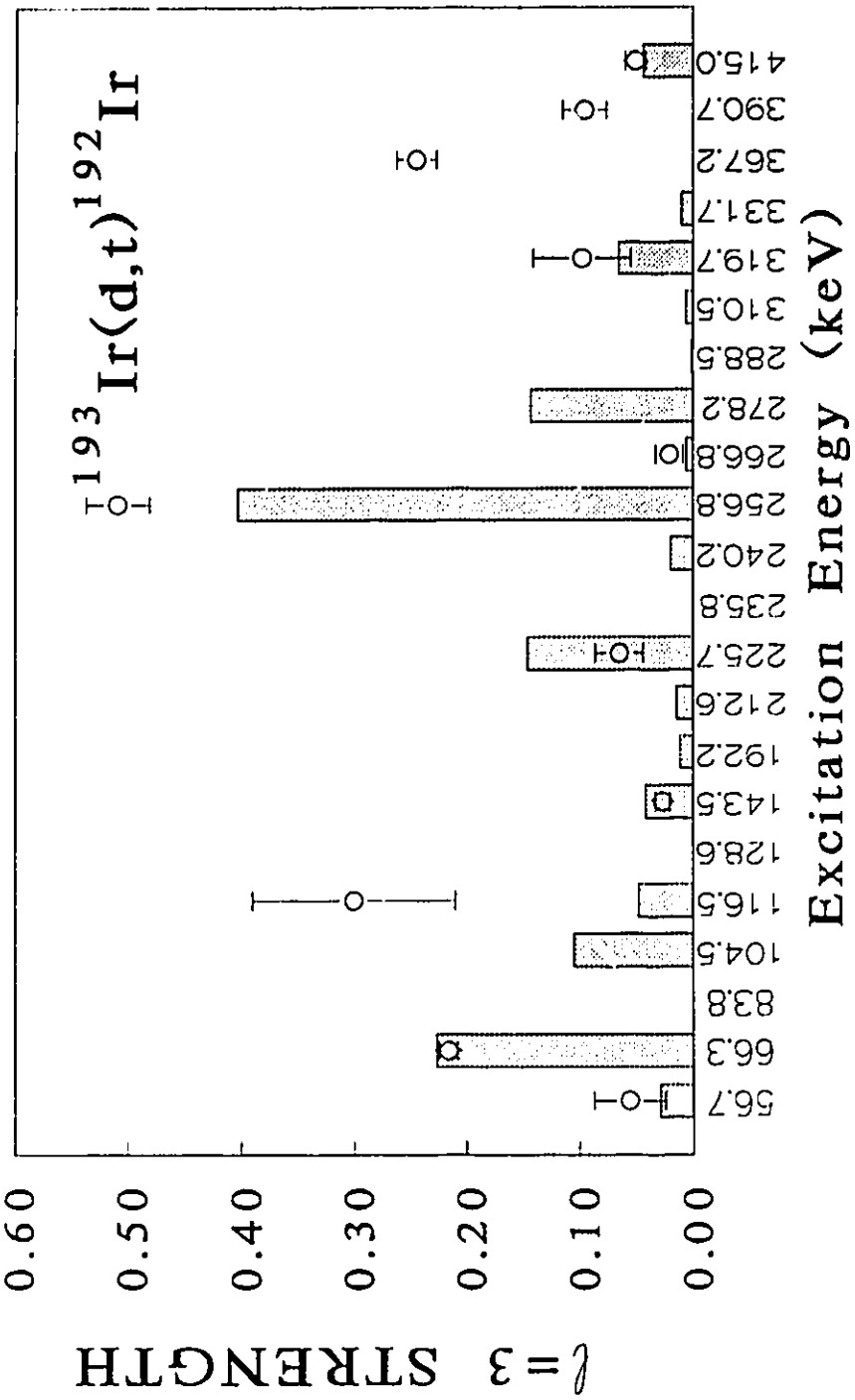

Figure 5.3.8: Predicted strengths from the IBFFM (bars) and experimental strengths (dots) for negative-parity states populated with $l = 3$ transfer in the ^{193}Ir(d,t)^{192}Ir reaction based on the assignments in Figure 5.3.1.

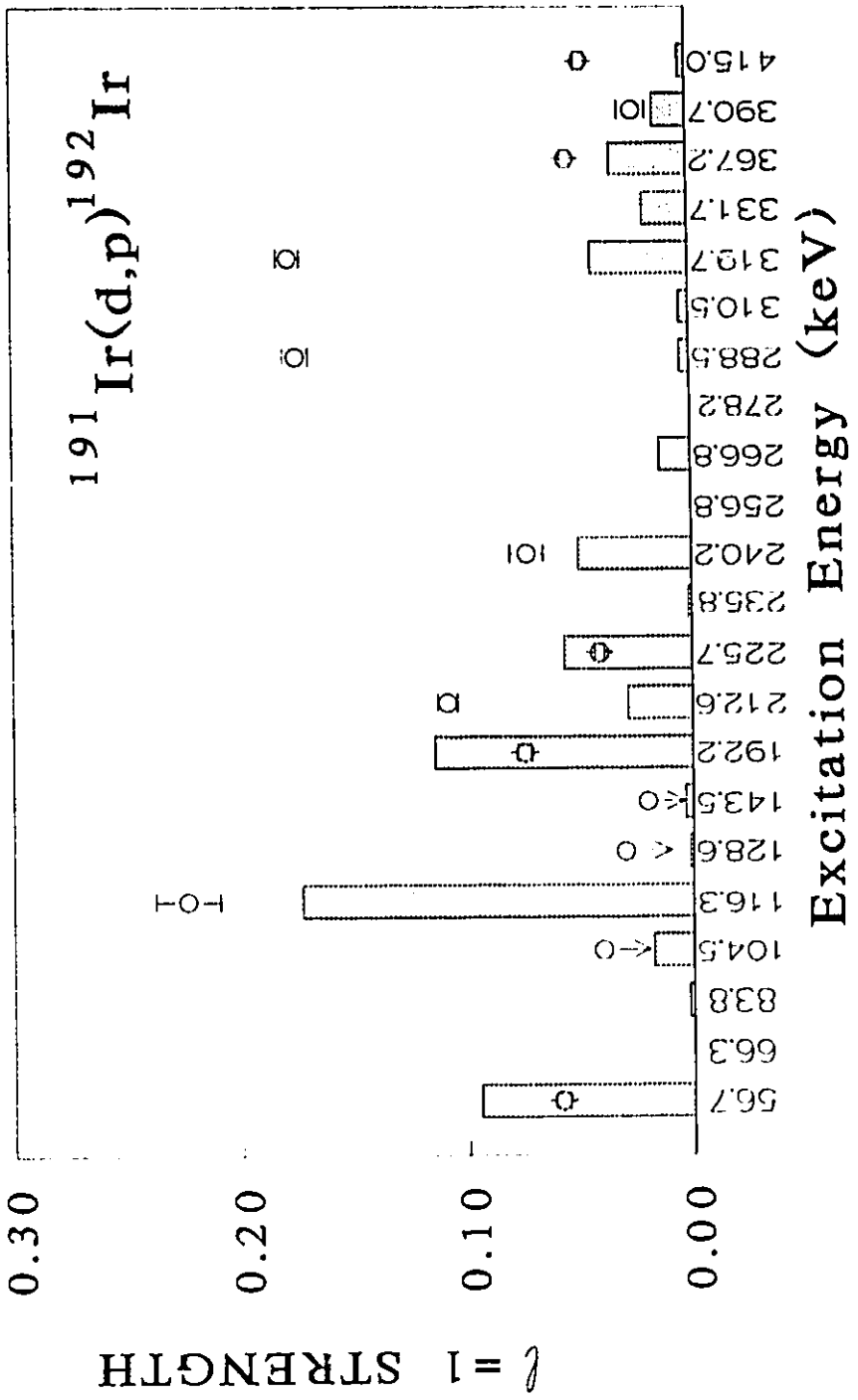

Figure 5.3.9: Predicted strengths from the IBFFM (bars) and experimental strengths (dots) for negative-parity states populated with $l = 1$ transfer in the ^{191}Ir(d,p)^{192}Ir reaction based on the assignments in Figure 5.3.1.

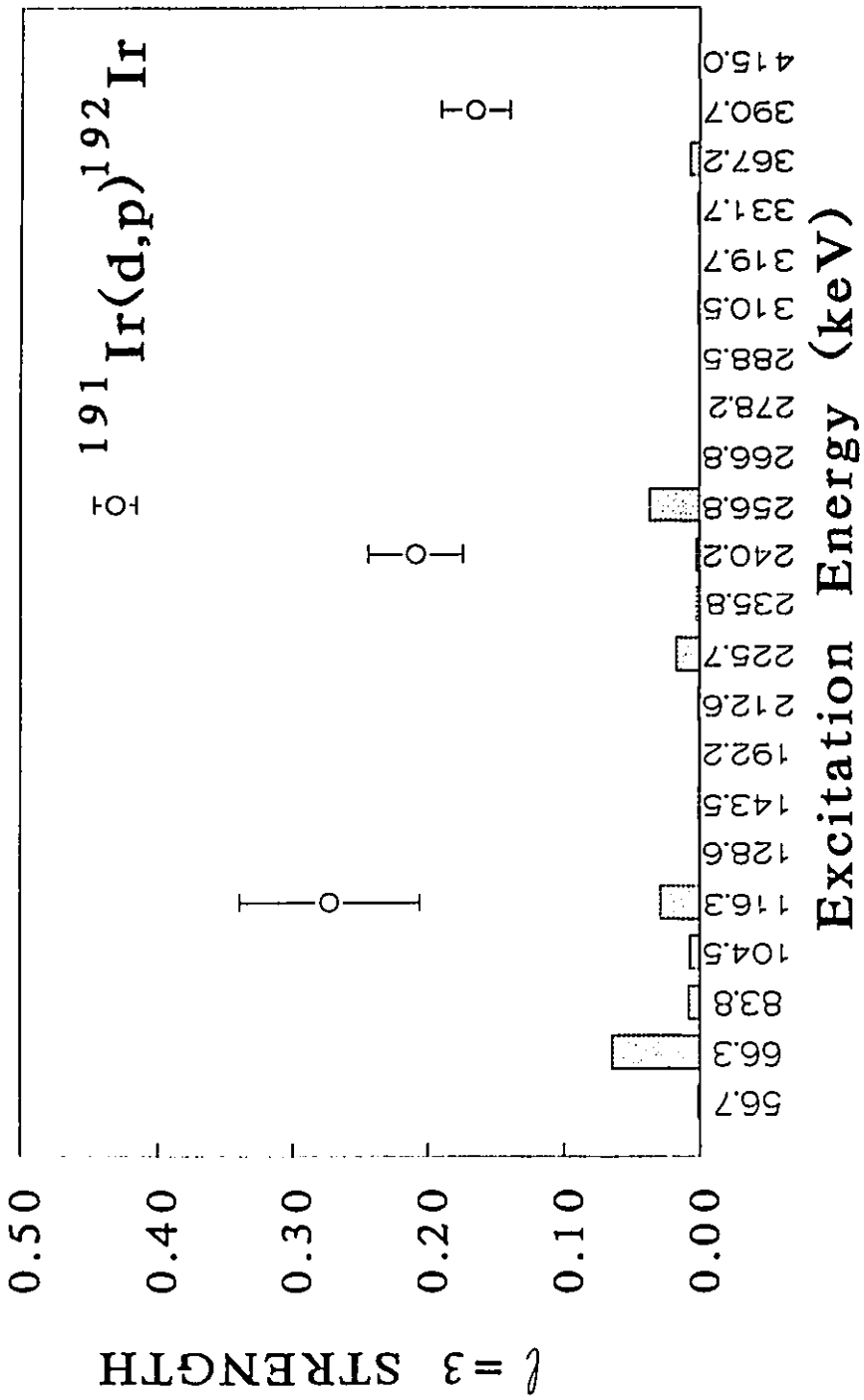

Figure 5.3.10: Predicted strengths from the IBFFM (bars) and experimental strengths (dots) for negative-parity states populated with $l = 3$ transfer in the ^{191}Ir(d,p)^{192}Ir reaction based on the assignments in Figure 5.3.1.

discrepancies of the model with the (d,p) strengths are greater than those with the (d,t) strengths, which may indicate the need to re-examine the transfer operator. The underestimation of the $l = 3$ strengths may be due to the neglect of the $f_{\frac{7}{2}}$ neutron orbital in the calculations. In ^{193}Pt, the pickup strength for $j = \frac{7}{2}$ is greater than that for $j = \frac{5}{2}$ transfer[48], and so it is expected that there is also significant $f_{\frac{7}{2}}$ transfer strength into ^{192}Ir.

5.3.2 ^{194}Ir Interpretation in Terms of IBFFM

The predictions of the IBFFM for ^{194}Ir were performed with the same program used for ^{192}Ir. Again, the (d,p) strengths listed in Appendix II obtained from Paar and Brant[70] must be renormalized. In order to minimize the number of parameters varied, the same renormalization values used for ^{192}Ir are also employed for ^{194}Ir. The IBFFM predictions for ^{194}Ir are listed in Table 5.3.4.

Table 5.3.4: IBFFM Prediction for ^{194}Ir

Energy (keV)	Spin	(d,p) Strength S_1	S_3	S_5
0	1^-	0.045	0.006	
78	0^-	0.002		
110	2^-	0.185	0.013	
112	1^-	0.056	0.010	
135	1^-	0.018	0.0003	
194	2^-	0.110	0.006	
203	1^-	0.007	0.000004	
237	0^-	0.00003		
248	4^-		0.222	0.009
250	2^-	0.006	0.010	
256	3^-	0.005	0.034	0.002
272	3^-	0.032	0.001	0.00004
274	1^-	0.043	0.0002	
287	3^-	0.002	0.021	0.007
290	2^-	0.142	0.012	
303	2^-	0.001	0.0003	
308	0^-	0.00002		
316	1^-	0.009	0.00003	
355	3^-	0.0004	0.009	0.00001
360	1^-	0.001	0.00002	
388	2^-	0.001	0.001	
398	2^-	0.005	0.00004	
399	3^-	0.001	0.0003	0.003
406	2^-	0.018	0.000001	

Table 5.3.4 -continued

Energy (keV)	Spin	(d,p) Strength S_1	S_3	S_5
430	2^-	0.019	0.002	
435	5^-			0.0006
472	1^-	0.006	0.00001	
474	11^-			
481	0^-	0.000008		
482	1^-	0.003	0.002	
484	12^-			
488	4^-		0.0008	0.0001
490	2^-	0.036	0.0003	
492	2^-	0.005	0.001	
498	3^-	0.0001	0.002	0.0005

The calculations reproduced the observed ground state spin of 1^-, and predict that it should be populated in the (d,p) reaction. This implies that the ground state has components in common with the target ground state, unlike the prediction for the ^{192}Ir ground state. The energies predicted are shown in Figure 5.3.11 along with the spins for the levels. As can be seen, up to approximately 300 keV the number of states is reproduced. The energies predicted for the 3^- and 4^- states are much closer to the observed energies than those predicted for ^{192}Ir, where the 3^- and 4^- states were observed much lower in energy than predicted. Shown in Figure 5 3.12 is the plot of energy versus $I(I+1)$ for the vrast states, both predicted and observed. The calculation approximately follows the observed states, unlike ^{192}Ir.

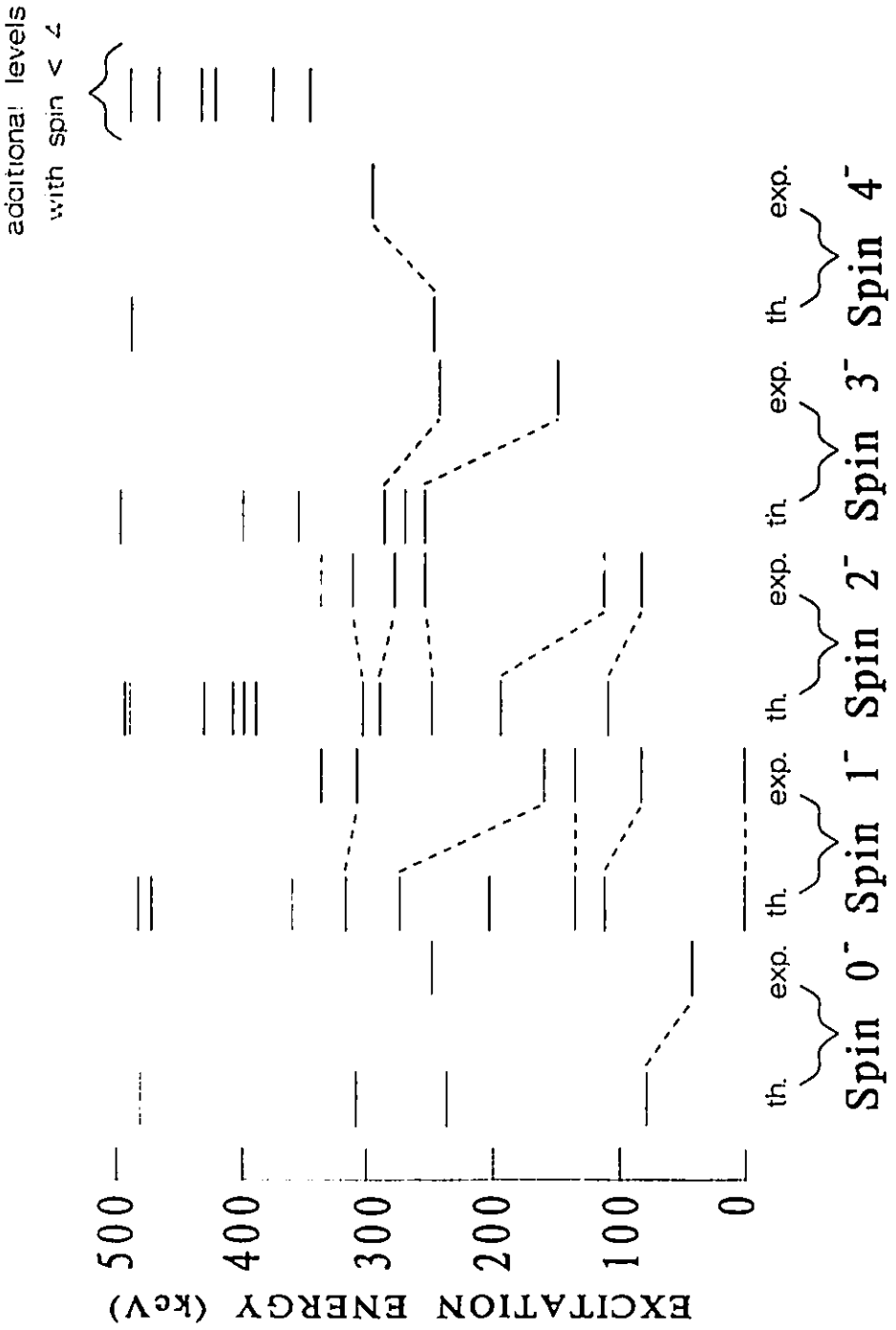

Figure 5.3.11: Predictions from the IBFFM for low-lying states and experimentally observed levels in ^{194}Ir. Only the negative-parity states with spin$\leq$4 are shown. The dashed lines correspond to levels for which the spin is uncertain. Lines connecting states are the assignments made in the present work.

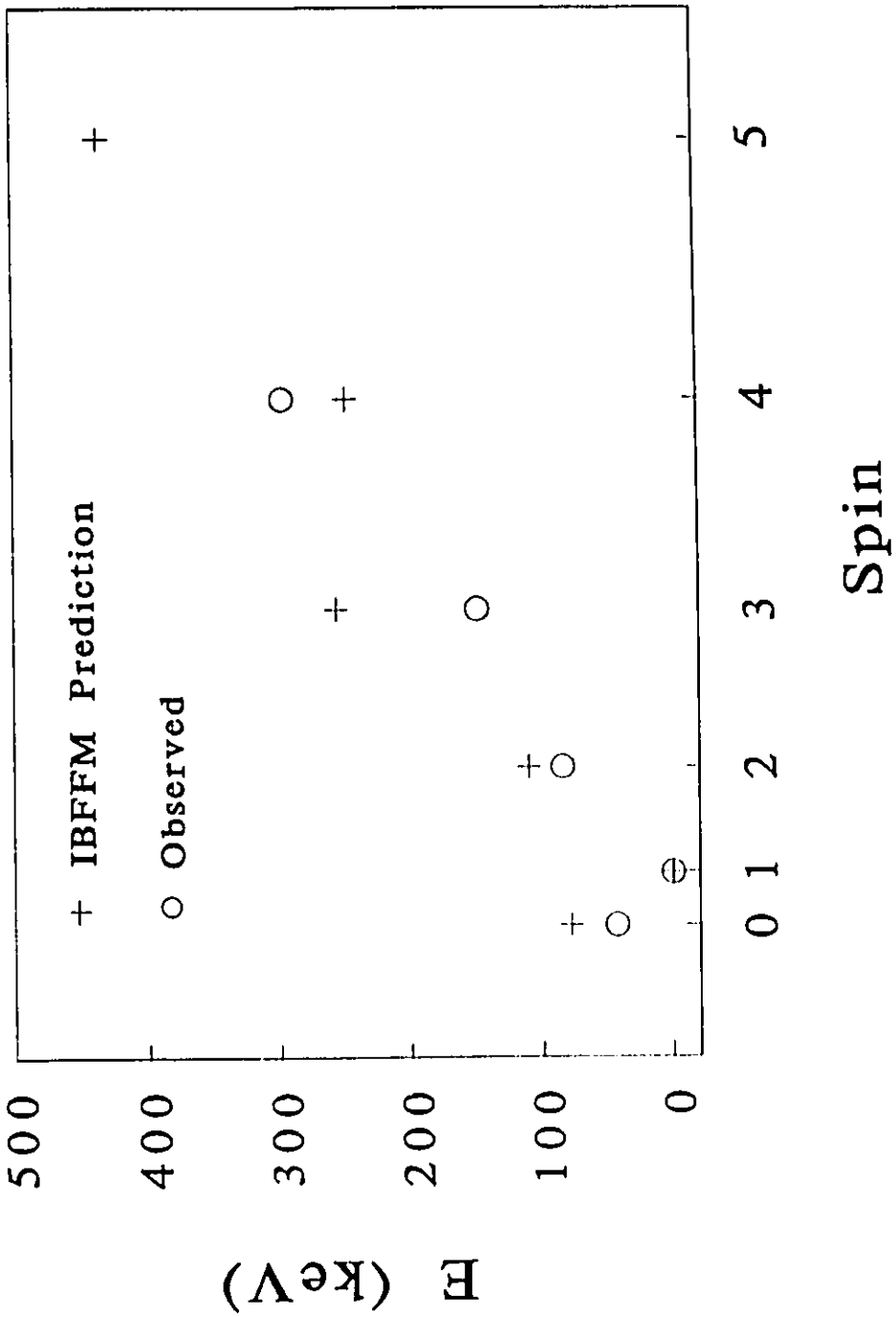

Figure 5.3.12: E versus $I(I+1)$ plot for yrast states predicted with the IBFFM and observed in ^{194}Ir.

The calculated (d,p) strengths for both $l = 1$ and $l = 3$ transfer are shown in Figure 5.3.13 along with the experimental values. As can be seen, there is only one strong $l = 3$ transition predicted contrary to the experimental results. Shown in Figure 5.3.14 are the sums of S_l for the (d,p) reaction, where the dashed lines are the observed quantities and the solid lines are calculated. The amount of $l = 3$ strength appears to be greatly underestimated, but the trend in the $l = 1$ strength is approximately reproduced up to 350 keV, where there are some rather strong $l = 1$ transitions observed.

The peak observed at 83.8 keV is due to an unresolved doublet of levels with $I^\pi = 1^-$ at 82.3 keV and 2^- at 84.3 keV. The angular distribution was fit with a pure $l = 1$ curve, yielding a value of $S_1 = 0.197 \pm 0.006$. In order to explain the observed strength the strongest spin 1 and spin 2 states must be chosen. The second 1^- state predicted at 112 keV has strength $S_1 = 0.056$, $S_3 = 0.010$, and the first 2^- state at 110 keV has $S_1 = 0.185$, $S_3 = 0.013$. This is considered to be a good match. The combination of the predicted strengths agrees nicely with the observed $l = 1$ strength, and predicts a small amount of $l = 3$ strength.

The peak at 148.7 keV has tentatively been assigned as a 3^- state by Balodis et al. It has a (d,p) angular distribution that appears to be a pure $l = 3$ curve with strength $S_3 = 0.290 \pm 0.010$. In the IBFFM calculation there are no 3^- states predicted to have this large a strength. In fact, the lowest predicted 3^- state, which occurs at an energy of 256 keV with $S_3 = 0.034$, has the greatest $l = 3$ strength of all spin 3 states. Clearly, this is a serious discrepancy with the experimental value.

The peak observed in the spectrum at 161.0 keV is due to a 1^- state. The angular distribution resembled that of a pure $l = 1$ transition, with strength $S_1 = 0.095 \pm 0.004$. The fourth 1^- state predicted in the IBFFM has essentially zero strength, and thus a much better candidate is the fifth 1^- level at 274 keV which has $S_1 = 0.043$, $S_3 = 0.0002$.

A peak observed at 244.1 keV is due to a doublet of levels at 245.1 keV, with $I^\pi = 3^-$, and 245.5 keV, with $I^\pi = 0^-$. The angular distribution resembled

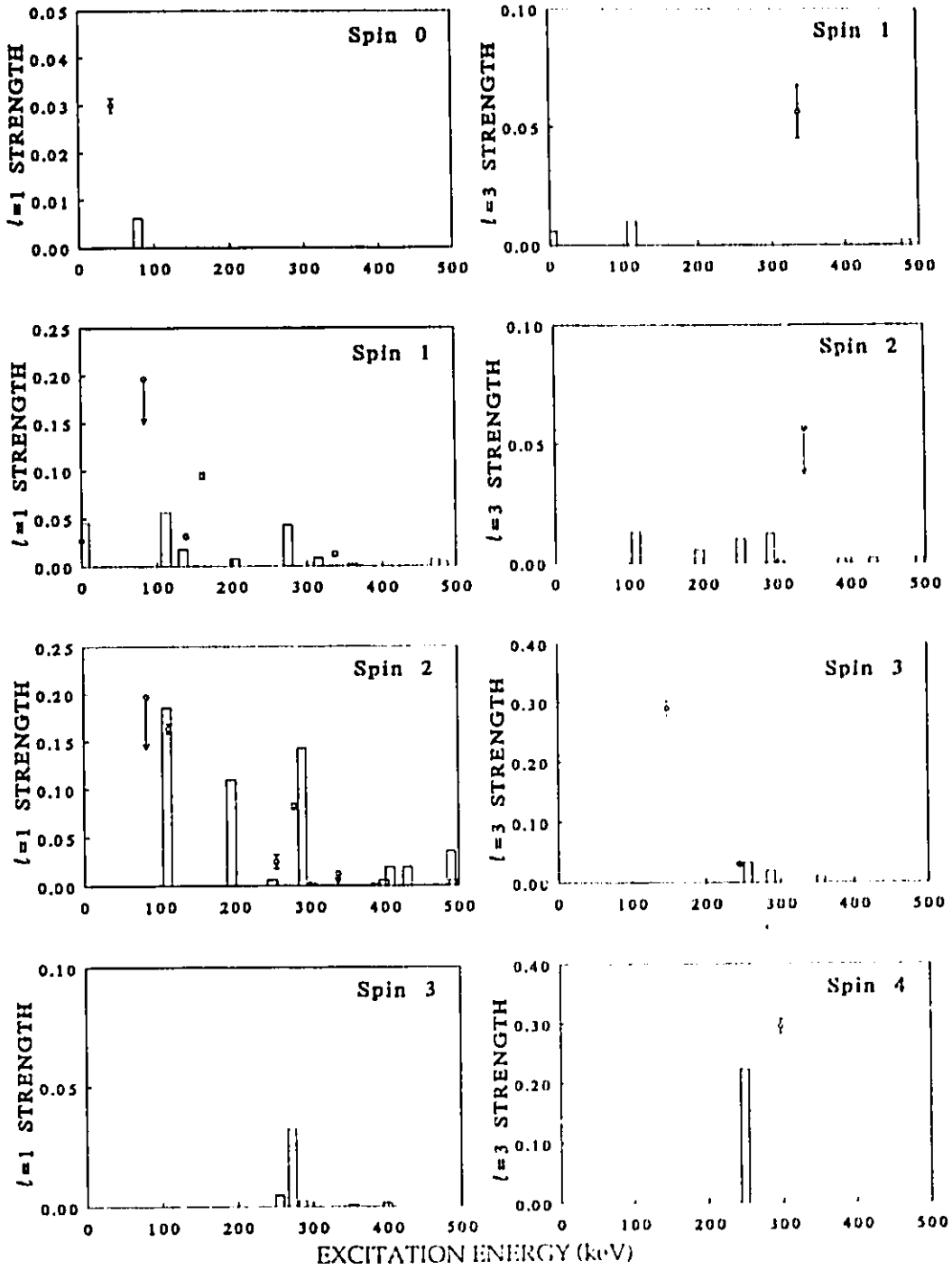

Figure 5.3.13: Predicted strengths from the IBFFM (bars) and experimental strengths (dots) for negative parity states populated in the ^{193}Ir(d,p)^{194}Ir reaction.

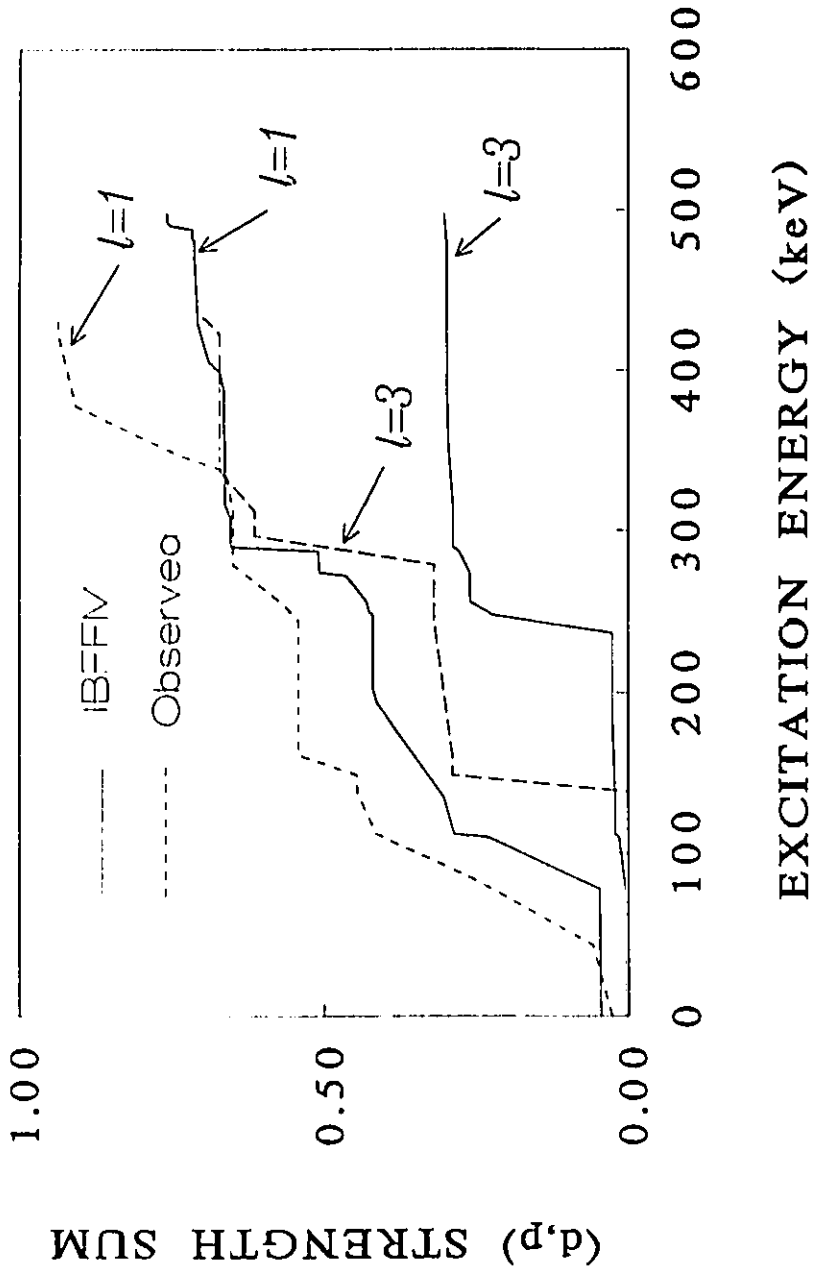

Figure 5.3.14: Sum of $l = 1$ and $l = 3$ strength predicted by the IBFFM and observed for the ^{193}Ir(d,p)^{194}Ir reaction. The observed $l = 1$ strength grows at a rate approximately 60% greater than predicted, and the predicted $l = 3$ strength is seriously underestimated.

that of the pure $l = 3$ transition, which implies that the population of the 0^- state is very small. Therefore, all of the cross section is assumed to belong to the 3^- state. The second 3^- level predicted by the IBFFM at an energy of 272 keV does not agree with the strengths, having a much larger $l = 1$ than $l = 3$ strength. The third 3^- state predicted at 287 keV has $S_1 = 0.001$, $S_3 = 0.021$, which is in better agreement with the observed strength.

Figure 5.3.11 shows the correspondence between the predicted levels and the observed levels based on the above assignments. Figure 5.3.15 and Figure 5.3.16 show the strength for $l = 1$ and $l = 3$ transitions observed with the ^{193}Ir(d,p)^{194}Ir reaction. Except for the strong $l = 3$ transition to the level at 148.7 keV, the calculations reproduce the strengths fairly well, and the energies are approximately reproduced. It appears that the IBFFM can provide a good description of ^{194}Ir for states below 300 keV. The fit might be improved with the inclusion of the $f_{\frac{7}{2}}$ neutron orbital into the calculation, as it was shown[48] that there is significant amounts of $f_{\frac{7}{2}}$ transfer strength in ^{195}Pt.

5.4. Interpretation in the Extended Supersymmetry Model

The use of extended supersymmetries as a model for odd-odd nuclei has received much attention lately. The Pt-Au region was suggested as providing likely candidates for the supermultiplet structure based on the $SO(6)$ core[49], and the group structure based on the $U(5)$ core has recently been constructed and applied to the $A \simeq 80$ region[74].

The first supermultiplet in the Pt-Au region to be examined[49] was ^{196,197}Pt, ^{197,198}Au, with a total of 6 bosons and fermions, and the model demonstrated some success in describing these[51]. However, the best candidate was expected to be the supermultiplet formed by ^{194,195}Pt, ^{195,196}Au, with a total of 7 bosons and fermions. This expectation was based on the fact that ^{194,195}Pt was the best realization of $U(6/12)$ supersymmetry[43–48], and $U(6/4)$ gave a reasonable description[75] of the

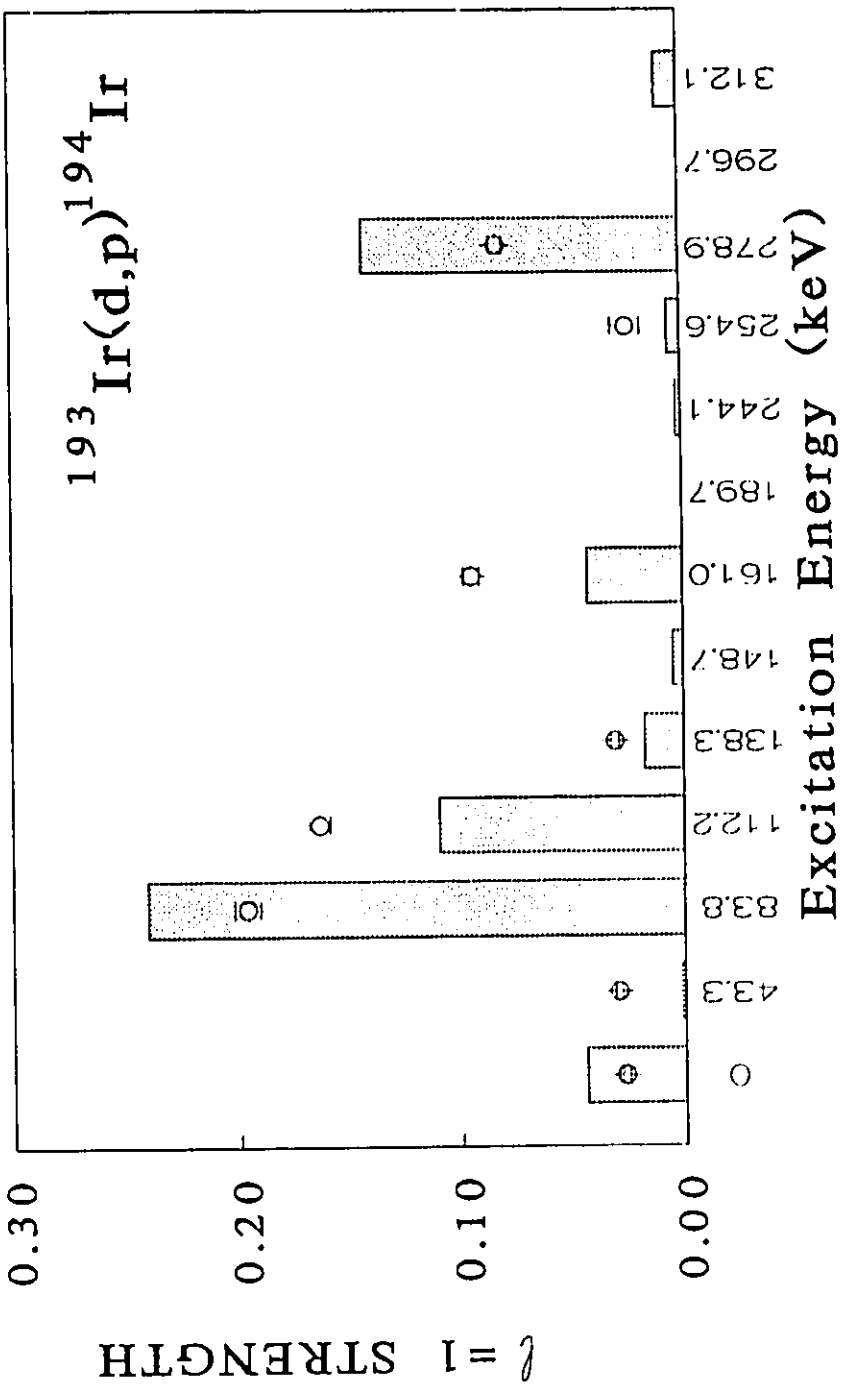

Figure 5.3.15: Predicted strengths from the IBFFM (bars) and experimental strengths (dots) for negative-parity states populated with $l = 1$ transfer in the ^{193}Ir(d,p)^{194}Ir reaction based on the assignments in Figure 5.3.11.

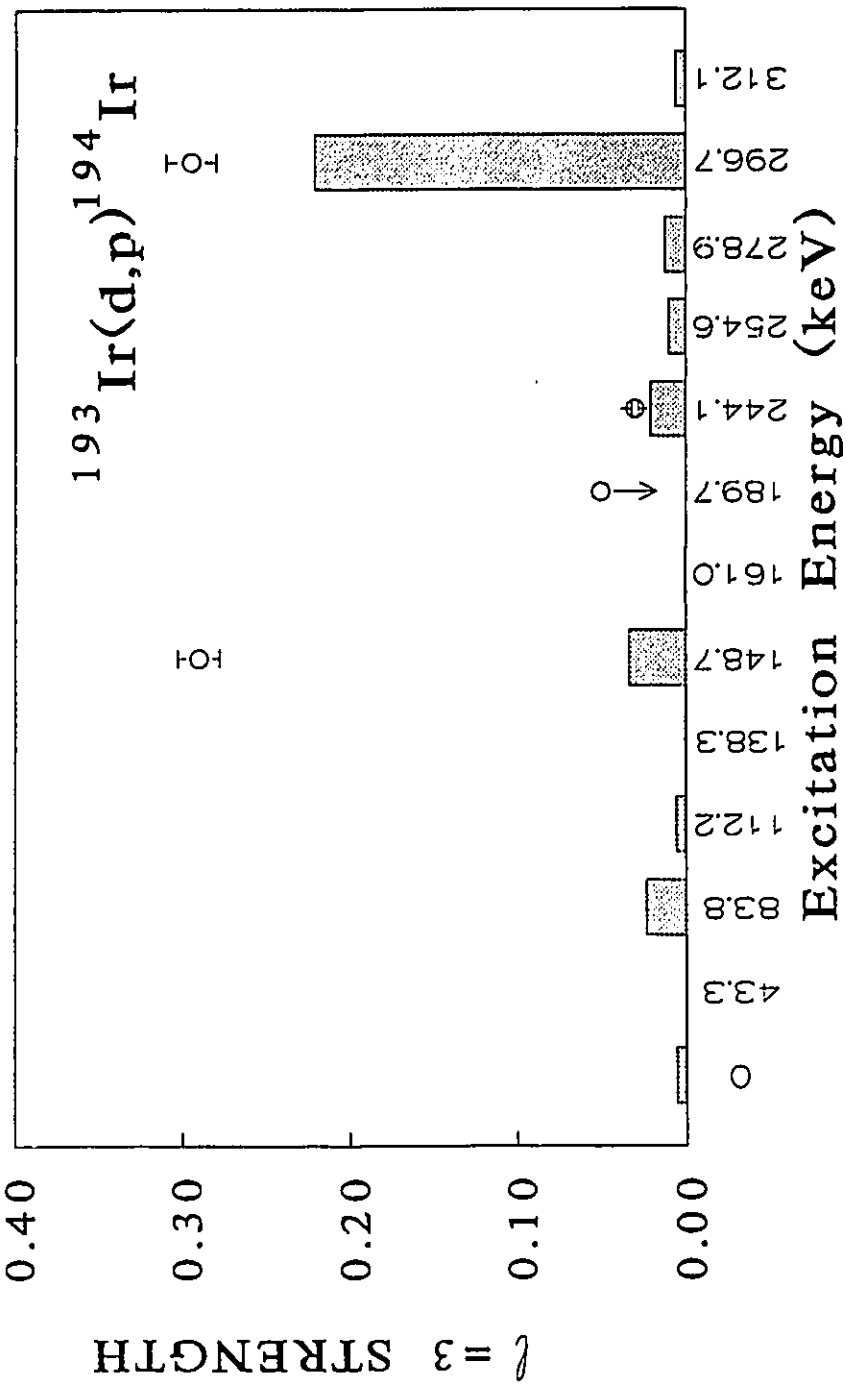

Figure 5.3.16: Predicted strengths from the IBFFM (bars) and experimental strengths (dots) for negative-parity states populated with $l = 3$ transfer in the ^{193}Ir(d,p)^{194}Ir reaction based on the assignments in Figure 5.3.11.

positive-parity states in ^{195}Au. Predictions were made for ^{196}Au, and spectroscopic strengths for ^{197}Au(d,t)^{196}Au were determined[76]. Unfortunately, the experimental spectra were recorded at only a few angles, and thus spectroscopic strengths for the different l-components could not be extracted, nor were the absolute cross sections obtained. It was possible, however, to determine which transitions were $l = 6$ and which were $l = 1$ or $l = 3$. The number of levels populated with $l = 1$ or 3 transitions (20) below 570 keV agreed very well with the theoretical predictions (22 out of 30 levels). Also, the distribution of cross sections with energy was reasonably reproduced. However, until spectroscopic strengths are determined, the success of the supersymmetry model application to ^{196}Au remains an open question.

Another candidate in the Pt-Au region for $U_\nu(6/12) \otimes U_\pi(6/4)$ sypersymmetry was suggested by Vergnes[77] to be the quartet ^{192,193}Os,^{193,194}Ir. The total number of bosons and fermions equals 8. The doublet ^{192}Os, ^{193}Ir was shown to be a good example of $U(6/4)$ supersymmetry[40]. However, problems appeared when attempting to explain the transfer strengths from the odd-A member of the supermultiplet to the even-even member[40]. In the extended supersymmetry, problems also appear when trying to fit ^{193}Os simultaneously with the other members of the supermultiplet. Jolie[76] has obtained the parameters $B = -9.3$, $B' = -24.2$, $C = 36.1$ and $D + E = 10.8$ keV for the energy eigenvalue expression

$$\begin{aligned}\mathcal{E} = {} & A\left[N_1(N_1+5) + N_2(N_2+3) + N_3(N_3+1)\right] + B\Big[\Sigma_1(\Sigma_1+4) \\ & + \Sigma_2(\Sigma_2+2) + \Sigma_3^2\Big] + B'\Big[\sigma_1(\sigma_1+4) + \sigma_2(\sigma_2+2) + \sigma_3^2\Big] \\ & + C\Big[\tau_1(\tau_1+3) + \tau_2(\tau_2+1)\Big] + DL(L+1) + EJ(J+1)\end{aligned} \tag{5.4.1}$$

from a fit to ^{192}Os and ^{193}Ir. The parameters A, and D (or E) could be obtained from a fit to either ^{193}Os or ^{194}Ir. A fit which reflects the nature of the Pt nuclei is obtained with the parameters $A = 63$, $D = -5.1$, and $E = 15.9$ keV. The negative-parity states predicted with Eq. (5.4.1) are shown in Figure 5.4.1, where the states are labelled with their respective quantum numbers. It is interesting to note that the symmetric representation, [7,0], does not come lower in energy than

the representation [6,1]. Also, there is a staggering of the levels of the same spin but differing by 1 in L. For instance, the 3^- with $L = \frac{7}{2}$ comes lower in energy than the 3^- with $L = \frac{5}{2}$. This is due to the relatively large negative value of D.

A direct comparison with the (d,p) data into ^{194}Ir cannot be made with the supersymmetry model since only the expressions for (d,t) reactions have been given. In this case, the transfer operator is a pure fermionic one, since the number of bosons does not change, and thus the only parameter involved is the occupation probability for the j-transfer in question. For a (d,p) reaction, the number of bosons decreases by one, and thus the transfer operator would be much more complicated, since it involves several terms with cross products of fermion and boson operators, and the transfer matrix elements have not been calculated.

An open question remains on the range of applicability of the extended supersymmetry model. For instance, is it possible to obtain a satisfactory description of the supermultiplet with a total of 9 bosons and fermions, namely, ^{190,191}Os, ^{191,192}Ir? It has been demonstrated[37] that the $U(6/4)$ supersymmetry is a relatively good description of ^{190}Os and ^{191}Ir as long as one does not consider the transfer strengths from ^{191}Ir to ^{190}Os[40]. The parameters $B = -20$, $B' = -25$, $C = 40$, and $D + E = 10$ keV for the energy eigenvalue equation for ^{192}Ir were obtained from the fit to ^{190}Os and ^{191}Ir in the work of Balantekin et al[37] where the $U(6/4)$ model was studied. The remaining parameters, A and D (or E), were assumed to be the same as those for ^{194}Ir. This is reasonable since the values of A for fits to different supermultiplets do not vary significantly, and the value of D reproduces the observed rotational spacing in ^{192}Ir for low-lying levels. With these parameters, the spectrum generated by Eq. (5.4.1), shown in Figure 5.4.2, resembles that of ^{194}Ir. Once again, the symmetric representation, [8,0] does not come lower in energy than the [7,1] representation. The prediction indicates that there should be 3 0^- states, 7 1^- states, 9 2^- states, 5 3^- states, and 3 4^- states, for a total of 27, below 500 keV. Experimentally, 32 negative-parity states are known below 500 keV. However, the theory predicts that only 19 states below 500 keV will be populated in the reaction,

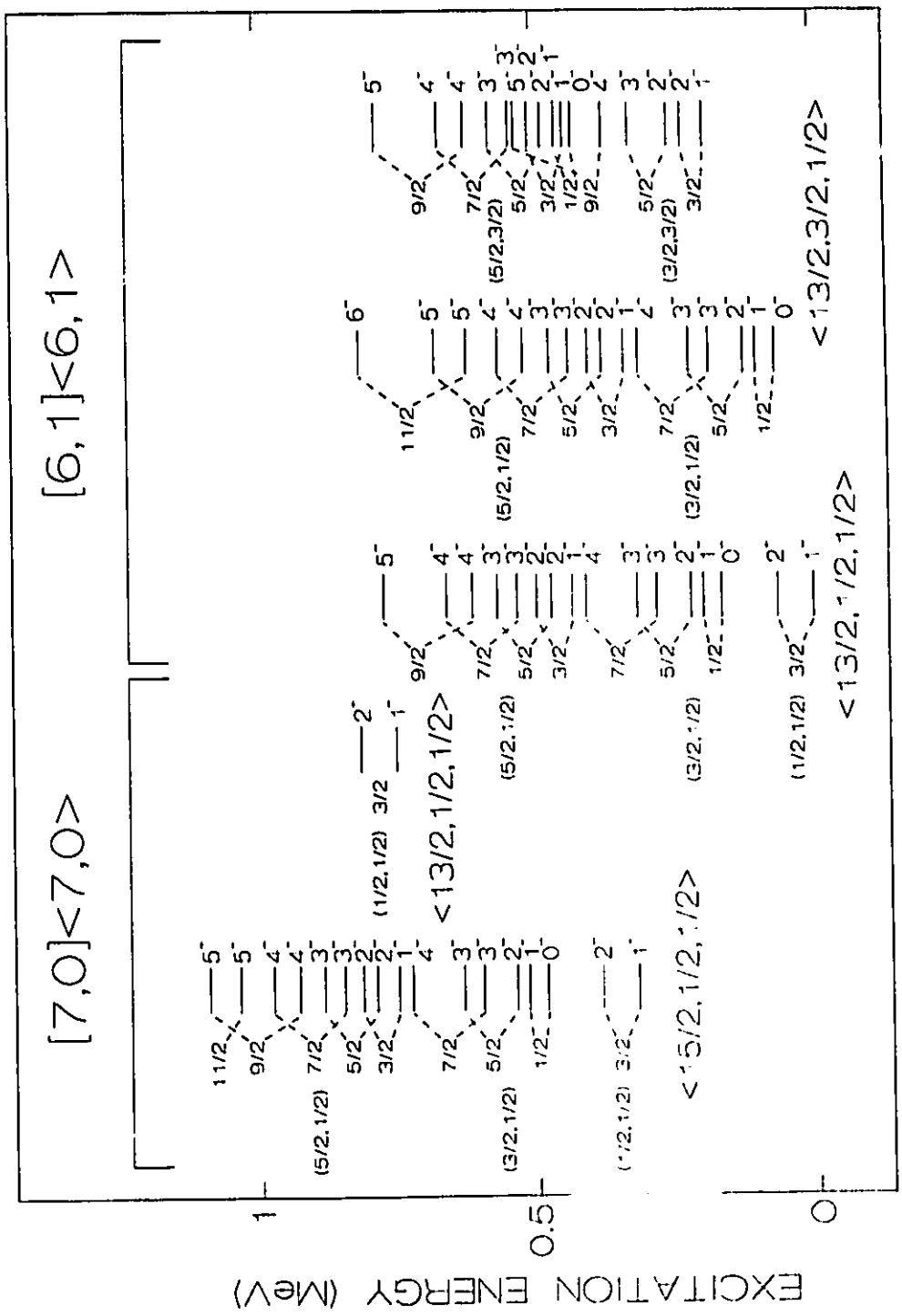

Figure 5.4.1: Predictions from the extended supersymmetry model for low-lying states in ^{194}Ir.

whereas experimentally there are at least 27 levels populated, and perhaps more, since some of the peaks are doublets.

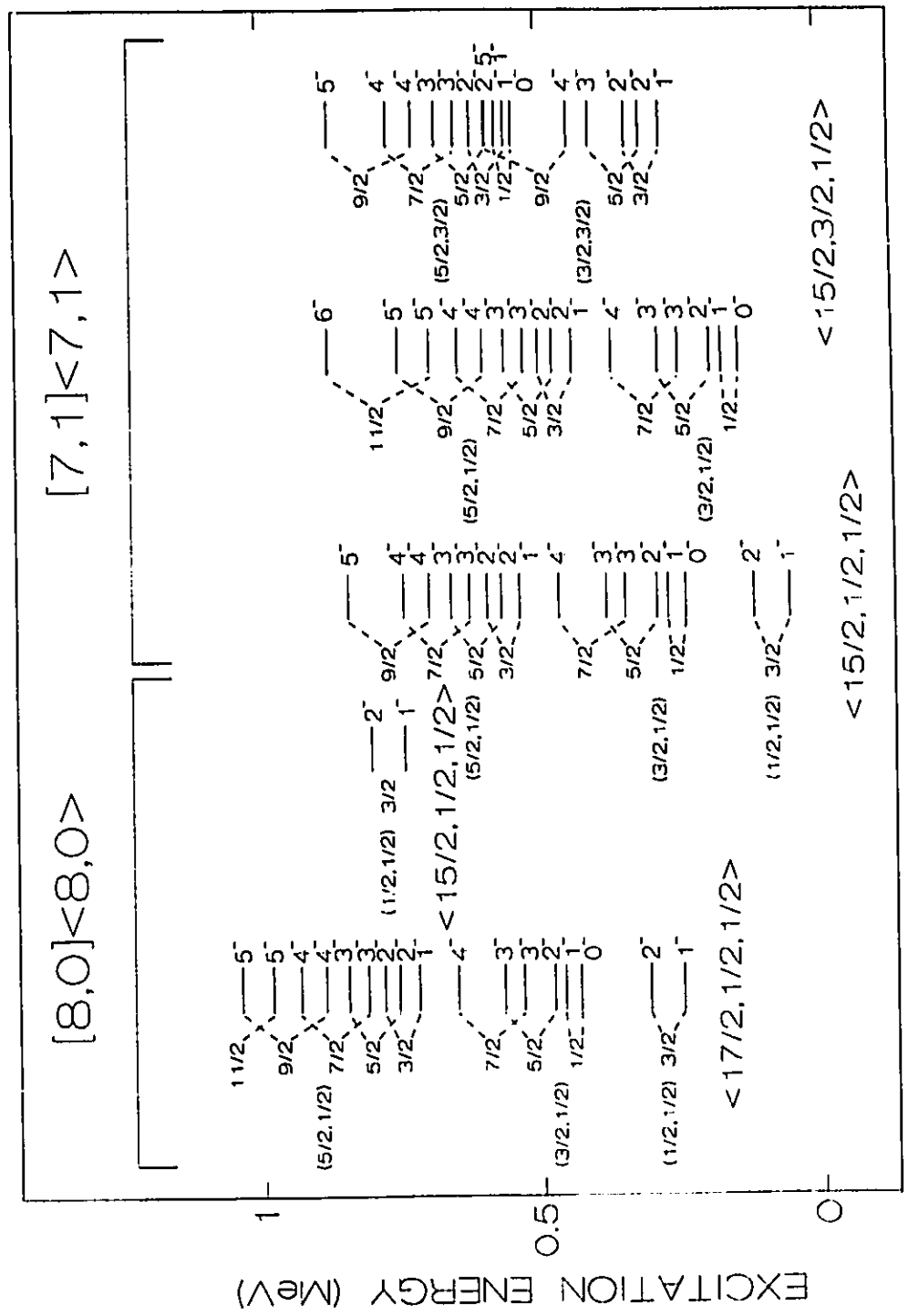

Figure 5.4.2: Predictions from the extended supersymmetry model for low-lying states in ^{192}Ir.

Table 5.4.1: Analytic Expressions for the Reduced Matrix Elements of the Fermion Transfer Operator

Final State	$\lvert\langle f\lVert T^{\dagger}_{\frac{1}{2}}\rVert\frac{3}{2}\rangle\rvert^2$	$\lvert\langle f\lVert T^{\dagger}_{\frac{3}{2}}\rVert\frac{3}{2}\rangle\rvert^2$	$\lvert\langle f\lVert T^{\dagger}_{\frac{5}{2}}\rVert\frac{3}{2}\rangle\rvert^2$
$[N+1,0]\langle N+1,0\rangle\langle N+\frac{3}{2},\frac{1}{2},\frac{1}{2}\rangle$			
$(\frac{1}{2},\frac{1}{2})\frac{3}{2}$ 1	$\frac{3(N+5)}{2(N+3)}$	$\frac{12(N+5)}{50(N+3)}$	$\frac{3(N+5)}{50(N+3)}$
$(\frac{1}{2},\frac{1}{2})\frac{3}{2}$ 2	$\frac{5(N+5)}{2(N+3)}$	$\frac{4(N+5)}{50(N+3)}$	$\frac{21(N+5)}{50(N+3)}$
$(\frac{3}{2},\frac{1}{2})\frac{1}{2}$ 0		$\frac{(N+5)(N+6)}{10(N+1)(N+3)}$	
$(\frac{3}{2},\frac{1}{2})\frac{1}{2}$ 1		$\frac{3(N+5)(N+6)}{50(N+1)(N+3)}$	$\frac{12(N+5)(N+6)}{50(N+1)(N+3)}$
$(\frac{3}{2},\frac{1}{2})\frac{5}{2}$ 2		$\frac{21(N+5)(N+6)}{50(N+1)(N+3)}$	$\frac{4(N+5)(N+6)}{50(N+1)(N+3)}$
$(\frac{3}{2},\frac{1}{2})\frac{5}{2}$ 3		$\frac{3(N+5)(N+6)}{50(N+1)(N+3)}$	$\frac{32(N+5)(N+6)}{50(N+1)(N+3)}$
$(\frac{3}{2},\frac{1}{2})\frac{7}{2}$ 3		$\frac{32(N+5)(N+6)}{50(N+1)(N+3)}$	$\frac{3(N+5)(N+6)}{50(N+1)(N+3)}$
$(\frac{3}{2},\frac{1}{2})\frac{1}{2}$ 4			$\frac{9(N+5)(N+6)}{10(N+1)(N+3)}$
$[N,1]\langle N,1\rangle\langle N+\frac{1}{2},\frac{3}{2},\frac{1}{2}\rangle$			
$(\frac{3}{2},\frac{1}{2})\frac{1}{2}$ 0		$\frac{3N(N+5)}{4(N+1)(N+4)}$	
$(\frac{3}{2},\frac{1}{2})\frac{1}{2}$ 1		$\frac{9N(N+5)}{20(N+1)(N+4)}$	$\frac{9N(N+5)}{5(N+1)(N+4)}$
$(\frac{3}{2},\frac{1}{2})\frac{5}{2}$ 2		$\frac{63N(N+5)}{20(N+1)(N+4)}$	$\frac{3N(N+5)}{5(N+1)(N+4)}$
$(\frac{3}{2},\frac{1}{2})\frac{5}{2}$ 3		$\frac{9N(N+5)}{20(N+1)(N+4)}$	$\frac{24N(N+5)}{5(N+1)(N+4)}$
$(\frac{3}{2},\frac{1}{2})\frac{7}{2}$ 3		$\frac{24N(N+5)}{5(N+1)(N+4)}$	$\frac{9N(N+5)}{20(N+1)(N+4)}$
$(\frac{3}{2},\frac{1}{2})\frac{7}{2}$ 4			$\frac{27N(N+5)}{4(N+1)(N+4)}$
$[N,1]\langle N,1\rangle\langle N+\frac{1}{2},\frac{1}{2},\frac{1}{2}\rangle$			
$(\frac{1}{2},\frac{1}{2})\frac{3}{2}$ 1	$\frac{3N}{(N+1)(N+2)^2}$	$\frac{12N(2N+5)^2}{25(N+1)(N+2)^2}$	$\frac{3N(2N+5)^2}{25(N+1)(N+2)^2}$
$(\frac{1}{2},\frac{1}{2})\frac{3}{2}$ 2	$\frac{5N}{(N+1)(N+2)^2}$	$\frac{4N(2N+5)^2}{25(N+1)(N+2)^2}$	$\frac{21N(2N+5)^2}{25(N+1)(N+2)^2}$
$(\frac{3}{2},\frac{1}{2})\frac{1}{2}$ 0		$\frac{N^2(2N+5)^2}{20(N+1)(N+2)^2}$	

Table 5.4.1 -continued

Final State	$\lvert\langle f\lVert T^{\dagger}_{\frac{1}{2}}\rVert\frac{3}{2}\rangle\rvert^2$	$\lvert\langle f\lVert T^{\dagger}_{\frac{3}{2}}\rVert\frac{3}{2}\rangle\rvert^2$	$\lvert\langle f\lVert T^{\dagger}_{\frac{5}{2}}\rVert\frac{3}{2}\rangle\rvert^2$
$(\frac{3}{2},\frac{1}{2})\frac{1}{2}$ 1		$\frac{3N^2(2N+5)^2}{100(N+1)(N+2)^2}$	$\frac{3N^2(N+5)}{25(N+1)(N+2)^2}$
$(\frac{3}{2},\frac{1}{2})\frac{5}{2}$ 2		$\frac{21N^2(2N+5)}{100(N+1)(N+2)^2}$	$\frac{2N^2(N+5)}{50(N+1)(N+2)^2}$
$(\frac{3}{2},\frac{1}{2})\frac{5}{2}$ 3		$\frac{3N^2(N+5)}{100(N+1)(N+2)^2}$	$\frac{16N^2(N+5)}{50(N+1)(N+2)^2}$
$(\frac{3}{2},\frac{1}{2})\frac{7}{2}$ 3		$\frac{32N^2(N+5)}{100(N+1)(N+2)^2}$	$\frac{3N^2(N+5)}{100(N+1)(N+2)^2}$
$(\frac{3}{2},\frac{1}{2})\frac{7}{2}$ 4			$\frac{9N^2(N+5)}{20(N+1)(N+2)^2}$

The expressions for the reduced matrix elements for the (d,t) reaction[76] are listed in Table 5.4.1. To find the spectroscopic strength, these expressions are multiplied by $V_j^2/(2I_i+1)$, where V_j^2 is the occupation probability for each j-value. Reasonable values of these were obtained from the work of Kern et al[57], and are $V^2_{\frac{1}{2}} = 0.5$, $V^2_{\frac{3}{2}} = 0.6$, and $V^2_{\frac{5}{2}} = 0.62$. The values of the spectroscopic strengths obtained are listed in Table 5.4.2, and are plotted in Figure 5.4.3 for each final spin. As can be seen, the correspondence with the experimental data is quite poor. The lowest lying 0^- state is predicted to have a large strength which is not observed, and the number of strongly populated 2^- states is not reproduced. There appears to be much more fragmentation of the strength than predicted by the model, and this may be due to the effect of the core. The supersymmetry employed here assumes that the core has good $SO(6)$ symmetry, but it is known that ^{190}Os is in a transitional region between $SU(3)$ and $SO(6)$ symmetries. A proper numerical calculation taking the mixed symmetry into account would have to be performed, but as of yet the $SU(3)$ supersymmetry limit has not been explored. An obvious extension to the model would also involve the incorporation of $f_{\frac{7}{2}}$ neutrons, the resulting group structure would be $U_\nu(6/20)\otimes U_\pi(6/4)$. The importance of $f_{\frac{7}{2}}$ neutrons was demonstrated in

Table 5.4.2: Spectroscopic Strengths Predicted for ^{193}Ir(d,t)^{192}Ir

Final State	Energy (keV)	Transfer Strength S_1	Transfer Strength S_3
[N+1,0]<N+1,0><N+$\frac{3}{2},\frac{1}{2},\frac{1}{2}$ >			
$(\frac{1}{2},\frac{1}{2})\frac{3}{2}$ 1	245	0.268	0.011
$(\frac{1}{2},\frac{1}{2})\frac{3}{2}$ 2	305	0.389	0.078
$(\frac{3}{2},\frac{1}{2})\frac{1}{2}$ 0	430	0.029	
$(\frac{3}{2},\frac{1}{2})\frac{1}{2}$ 1	460	0.018	0.073
$(\frac{3}{2},\frac{1}{2})\frac{5}{2}$ 2	480	0.123	0.024
$(\frac{3}{2},\frac{1}{2})\frac{5}{2}$ 3	570	0.018	0.193
$(\frac{3}{2},\frac{1}{2})\frac{7}{2}$ 3	535	0.187	0.018
$(\frac{3}{2},\frac{1}{2})\frac{1}{2}$ 4	655		0.272
[N,1]<N,1><N+$\frac{1}{2},\frac{3}{2},\frac{1}{2}$ >			
$(\frac{3}{2},\frac{1}{2})\frac{1}{2}$ 0	142	0.107	
$(\frac{3}{2},\frac{1}{2})\frac{1}{2}$ 1	172	0.064	0.266
$(\frac{3}{2},\frac{1}{2})\frac{5}{2}$ 2	192	0.451	0.089
$(\frac{3}{2},\frac{1}{2})\frac{5}{2}$ 3	282	0.064	0.710
$(\frac{3}{2},\frac{1}{2})\frac{7}{2}$ 3	247	0.687	0.067
$(\frac{3}{2},\frac{1}{2})\frac{7}{2}$ 4	367		0.998
[N,1]<N,1><N+$\frac{1}{2},\frac{1}{2},\frac{1}{2}$ >			
$(\frac{1}{2},\frac{1}{2})\frac{3}{2}$ 1	57	0.285	0.073
$(\frac{1}{2},\frac{1}{2})\frac{3}{2}$ 2	117	0.100	0.508
$(\frac{3}{2},\frac{1}{2})\frac{1}{2}$ 0	242	0.006	
$(\frac{3}{2},\frac{1}{2})\frac{1}{2}$ 1	272	0.004	0.017

Table 5.4.2 -continued

Final State	Energy (keV)	Transfer Strength S_1	S_3
$(\frac{3}{2},\frac{1}{2})\frac{5}{2}$ 2	292	0.029	0.006
$(\frac{3}{2},\frac{1}{2})\frac{5}{2}$ 3	382	0.004	0.045
$(\frac{3}{2},\frac{1}{2})\frac{7}{2}$ 3	347	0.044	0.004
$(\frac{3}{2},\frac{1}{2})\frac{7}{2}$ 4	467		0.063

the Pt nuclei, where large amounts of $f_{\frac{7}{2}}$ strength was found. Therefore, it can be concluded that the model would require extension before it could provide a good description of ^{192}Ir.

5.5. Interpretation in Terms of the Nilsson Model

The Nilsson model has been one of the most successful models developed for nuclear structure. It can describe a wide variety of nuclear phenomena, and is relatively easy to use. It has been applied to many of the rare-earth nuclei which have a well-defined deformed shape. In the $A \simeq 190$ transitional region, it has been applied to the Os, Ir, and Pt nuclei with varying degrees of success. Single-neutron transfer studies[78–80] showed that the Nilsson model worked reasonably well for some of the states in ^{189,191,193}Os, although there are some discrepancies, but had only limited success[81–82] in ^{195,197}Pt. Single-proton transfer studies[59] of ^{191,193,195}Ir showed that the Nilsson model was able to describe the low-lying proton states in these nuclei. One of the difficulties that the Nilsson model cannot overcome is a proper description of the core. The large number of states observed in nuclei in this region may be related to the effects of γ-soft cores and triaxiality[1,2]. For instance,

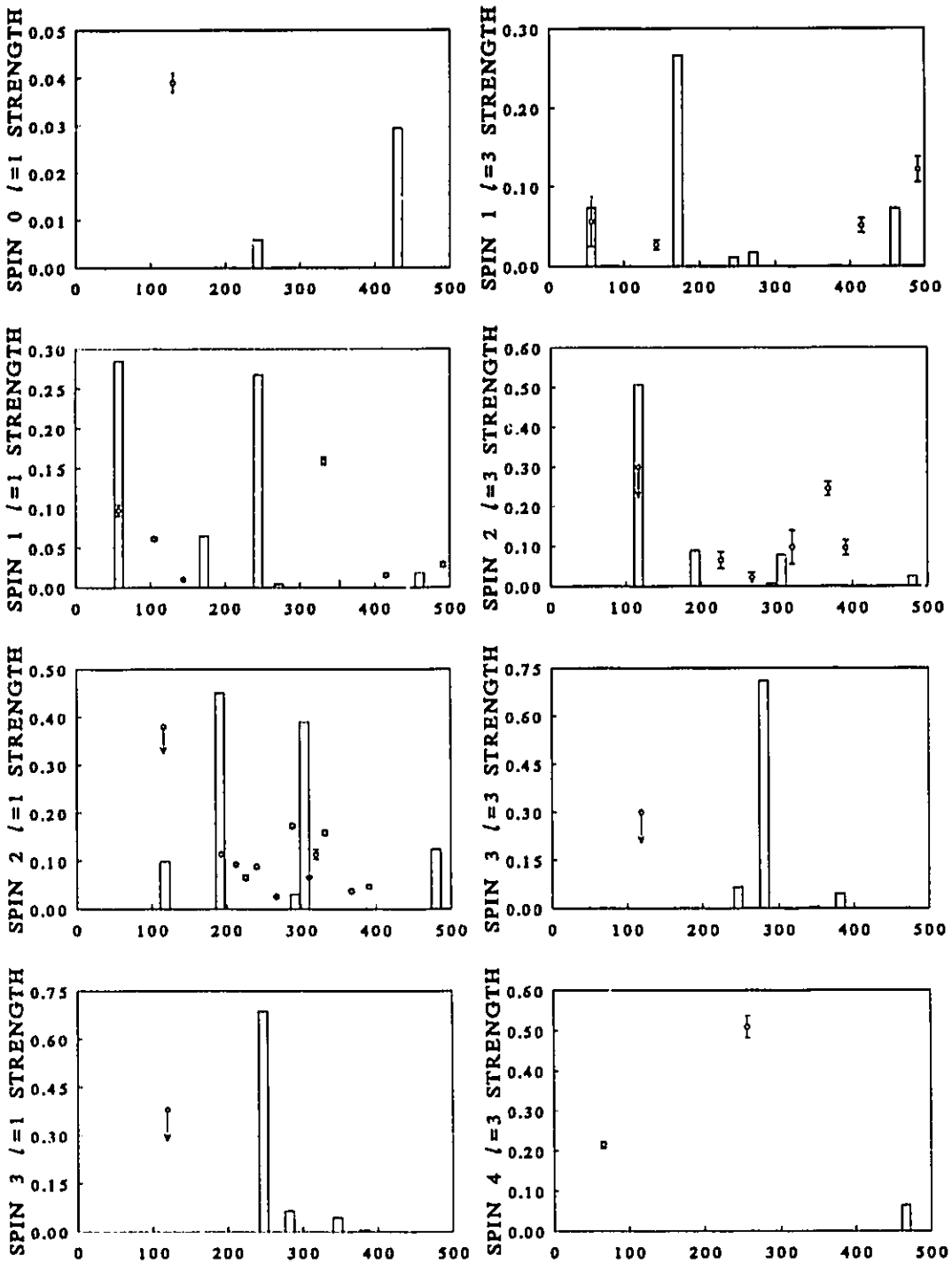

Figure 5.4.3: Strength predictions (bars) from the extended supersymmetry model for low-lying states in ^{192}Ir compared with experimentally observed values (dots) for the (d,t) reaction.

in ^{191}Os, there is a total of 22 $\frac{1}{2}^-$ and $\frac{3}{2}^-$ states found[5] below 1300 keV. The Nilsson orbitals plus the various couplings of γ- and β-vibrations can account for 9 states. It is possible that the introduction of other degrees of freedom in the core may explain these states. Not including these degrees of freedom puts a limitation on the model, but the inclusion of effects such as γ-softness introduces[83] a great deal of complication andtakes away from the simplicity of the model. Given the known limitations of the Nilsson model in explaining nuclei in the $A \simeq 190$ transitional region, a question that can be asked is the following: how well can it describe states in the odd-odd Ir nuclei?

5.5.1 Calculations

The Nilsson model calculations performed in this work employed the Hamiltonian of Eq. (2.2.56), where κ and μ were set equal to 0.0637, 0.600, respectively, for the protons and 0.0636, 0.392, respectively, for the neutrons. The quadrupole deformation, δ_2, was taken as 0.18 for all states in ^{190,192}Ir. It is possible that some of the states observed are based on different deformations, but at the present time there are no data indicating what the deformations are for individual levels, and therefore δ_2 is not used as a free parameter.

In making assignments with the Nilsson model, the similarities of population strengths to states in different nuclei were taken advantage of. For instance, many of the spins and parities of states in ^{192}Ir are known, and thus if states in ^{190}Ir were found at approximately the same energy and had similar strengths, it was considered likely that the levels had the same configurations as those in ^{192}Ir. In an analogous way, information regarding the configurations in ^{190}Ir obtained from single-proton transfer could also be applied to states in ^{192}Ir that had similar (d,t) strengths to those in ^{190}Ir. As an example, the three lowest states in ^{192}Ir were populated with $l = 1$ and 3, $l = 3$, and $l = 5$ transitions in the (d,t) reaction, and have I^π values of 1^-, 4^-, and 3^-, respectively. In ^{190}Ir, the three lowest levels populated in the (d,t) reaction have $l = 3$, $l = 1$, and $l = 5$ transitions of similar strengths

to those in ^{192}Ir, and have been assigned $I^{\pi} = 4^-$, 1^-, and 3^-, respectively. Of the three lowest levels in ^{190}Ir, only the 1^- state was populated in the (^{3}He,d) and (α,t) reactions. The cross section in the single-proton transfer to the 1^- state was small compared with the largest peaks in the spectrum, and it will be argued that a logical assignment is the $\frac{3}{2}^+[402]_\pi - \frac{1}{2}^-[510]_\nu$ band head. This is consistent with the assignment of Kern et al[57] for the corresponding 1^- state at 56.7 keV in ^{192}Ir. The lowest lying 3^- and 4^- states in ^{190}Ir, which are not populated in single-proton transfer, do not involve the $\frac{3}{2}^-[512]$ or the $\frac{1}{2}^-[510]$ neutron orbitals. Consistent with this, the presently adopted assignments for the lowest 3^- and 4^- levels in ^{192}Ir also do not involve the $\frac{3}{2}^-[512]$ or the $\frac{1}{2}^-[510]$ neutrons.

This type of comparison between levels in ^{190}Ir and ^{192}Ir was used to check the possible interpretations. However, this could only be done for low-lying levels since above ~200 keV the level density was such that it was not possible to make a correspondence between levels in the two nuclei.

In many studies of odd-odd nuclei with single-nucleon transfer reactions, the Coriolis matrix elements are calculated only between configurations involving the target orbital, which is assumed to be a pure Nilsson state. The assumption is also made that the nucleon in the odd-A target acts only as a spectator in the reaction. These assumptions are not strictly true. There can occur Coriolis mixings in the target ground state and also in the final state between different proton, and neutron, orbitals. In the present work, all low-lying configurations that have been identified have been included in the Coriolis and particle-particle coupling calculations. This has very important consequences since configurations not involving the dominant target orbital can, in some cases, have significant mixings with those involving the target orbital. Thus, states which in a first approximation would not be populated, can have significant transfer strength as a result of the admixed amplitude in the final state.

The Coriolis and particle-particle matrix elements were calculated using Eq. (2.2.65) and Eq. (2.2.67), respectively, where the C_{jl}^{Ω} coefficients were determined in the Nilsson calculation outlined above. The Coriolis attenuation factor, ρ, was set to 0.65, and the unperturbed energies of the Nilsson orbitals and their rotational parameters, $\hbar^2/2\mathcal{J}_0$, were taken as a free parameters. For each spin, I, a matrix was set up using the Nilsson wave functions as a basis, the unperturbed energies along the diagonal, and the various coupling matrix elements off diagonal. This matrix was diagonalized, and the resulting eigenvalues and eigenvectors represented the energies and wave functions of the states. Included in the calculations were the $\frac{3}{2}^+[402]_\pi \pm \frac{1}{2}^-[510]_\nu$, $\frac{3}{2}^+[402]_\pi \pm \frac{3}{2}^-[512]_\nu$, $\frac{1}{2}^+[400]_\pi \pm \frac{1}{2}^-[510]_\nu$, $\frac{1}{2}^+[400]_\pi \pm \frac{3}{2}^-[512]_\nu$, and the $-\frac{3}{2}^+[402]_\pi + \frac{9}{2}^-[505]_\nu$, $\frac{3}{2}^+[402]_\pi + \frac{5}{2}^-[503]_\nu$, $\frac{3}{2}^+[402]_\pi + \frac{7}{2}^-[503]_\nu$ configurations.

Prior to the present work, the effects of a mixed target ground state configuration on the population of final states in odd-odd nuclei had not been investigated. Thompson et al[84] had studied the effect for the ^{189}Os(d,t)^{188}Os reaction where the final states are in an even-even nucleus and the target of ^{189}Os was known to contain a mixture of the $\frac{1}{2}^-[510]_\nu$ and $\frac{3}{2}^-[512]_\nu$ orbitals. It was found that the population pattern for the two quasiparticle states in ^{188}Os could be explained only if an amplitude of $\sim$0.3 of the $\frac{1}{2}^-[510]_\nu$ orbital was admixed with the $\frac{3}{2}^-[512]_\nu$ orbital in the ^{189}Os ground state. This amplitude agreed with the findings of other studies on ^{189}Os. The demonstrated importance for ^{188}Os of the mixed target configurations suggested that it could also be important when considering odd-odd nuclei. However, the expressions developed in ref.[84] are not applicable to odd-odd nuclei.

In Appendix I, the formalism for calculating spectroscopic strengths for single-nucleon transfer to final states in odd-odd nuclei when the target has a mixed Nilsson configuration is developed in detail. The cross section is written as

$$\frac{d\sigma}{d\Omega} = \sum_{jl}\Big(\sum_{\xi\nu} a_{\xi_\nu} a_\xi P_{\nu\Omega} C_{jl}^{\nu\Omega}\Big[(I_i K_\xi j\Omega|I_f K) + (\pi_\xi)(-1)^{I_i-\frac{1}{2}}(I_i - K_\xi j\Omega|I_f K)\Big]\Big)^2 \phi_{jl} \tag{5.5.1}$$

where the subscript ξ refers to the target configuration and ν refers to the transferred nucleon. The quantity ϕ_{jl} is the single-particle cross section obtained from a DWBA calculation. The factor (π_ξ) is the parity of the target and $P_{\nu\Omega}$ is the pairing factor which is $U_{\nu\Omega}$ for stripping reactions and $V_{\nu\Omega}$ for pickup reactions. The amplitudes of the various Nilsson components in the target are a_ξ, and the amplitudes for the configurations admixed in the final state are $a_{\xi\nu}$. It should be noted that Eq. (5.5.1) reduces to the usual expression for the cross section if $a_{\xi\nu} = \delta_{\xi,t}$, where t denotes the dominant target component.

In order to investigate the effects of mixed target configurations, consider the case for single-neutron transfer reactions where there is no mixing in the final state. The target ground state wave functions are $-A(\frac{1}{2}[400]_\pi)+\sqrt{(1-A^2)}(\frac{3}{2}[402]_\pi)$ for ^{191,193}Ir. For configurations involving the $\frac{3}{2}^+[402]_\pi$ proton part, the spectroscopic strength will decrease as $(1-A^2)$ as A increases, while configurations involving the $\frac{1}{2}^+[400]_\pi$ proton part will increase as A^2. This simple dependance disappears, however, when the final states are also configuration mixed. For example, consider the final state wave function for one particular 2^- state in ^{190}Ir (labelled as the $-\frac{1}{2}^+[400]_\pi + \frac{3}{2}^-[512]_\nu$ configuration)

$$\begin{aligned}
&0.848\left(-\frac{1}{2}^+[400]_\pi + \frac{3}{2}^-[512]_\nu\right) + 0.354\left(\frac{1}{2}^+[400]_\pi - \frac{1}{2}^-[510]_\nu\right) \\
&- 0.329\left(\frac{1}{2}^+[400]_\pi + \frac{1}{2}^-[510]_\nu\right) - 0.184\left(\frac{3}{2}^+[402]_\pi - \frac{3}{2}^-[512]_\nu\right) \\
&- 0.085\left(\frac{3}{2}^+[402]_\pi + \frac{1}{2}^-[510]_\nu\right) + 0.078\left(\frac{1}{2}^+[400]_\pi + \frac{3}{2}^-[512]_\nu\right) \\
&+ 0.022\left(\frac{3}{2}^+[402]_\pi - \frac{1}{2}^-[510]_\nu\right)
\end{aligned} \tag{5.5.2}$$

as determined by Coriolis coupling calculations for ^{190}Ir with $\delta_2 = 0.18$. As can be seen in Figure 5.5.1, the dependance of the spectroscopic strengths on A no longer shows the simple form outlined above. The relative phases of the amplitudes, as well as those of the $C_{jl}^{\nu\Omega}$ values, play a very important role, and can result in constructive or destructive interference for each particular j-transfer. Figure 5.5.1 demonstrates this effect dramatically; as the amplitude of the $\frac{1}{2}^+[400]_\pi$ or the $\frac{1}{2}^-[510]_\nu$ orbital in

the target ground state increases, the strength for each j-transfer changes significantly.

For the spectroscopic strength calculations performed in this work, the target ground state wave functions were taken as $0.3(\frac{1}{2}^-[510]_\nu) + 0.95(\frac{3}{2}^-[512]_\nu)$ for ^{189}Os, as suggested in ref.[84], and $-0.125(\frac{1}{2}^+[400]_\pi) + 0.992(\frac{3}{2}^+[402]_\pi)$ for ^{191,193}Ir, as determined by Coriolis coupling calculations that reproduce the low-lying energy spectrum for these nuclei. The amplitudes $a_{\xi\nu}$ were found from the results of the Coriolis and particle-particle coupling calculations outlined above.

5.5.2 Interpretation of ^{192}Ir in Terms of the Nilsson Model

Some of the levels studied by Kern et al[57] have been interpreted in terms of the Nilsson model, as shown in Figure 5.5.2. These interpretations were based mainly on the γ-rays connecting states and transfer cross sections. The results of the single-nucleon transfer study of the present work give data complementary to those of Kern et al[57], and provide evidence for the main components in the wave functions. The low energy portion of the ^{193}Ir(d,t)^{192}Ir spectrum is shown in Figure 5.5.3, where the peaks are labelled with their dominant Nilsson configurations assigned in the present work. The Nilsson assignments are also shown in Figure 5.5.4, where a "rating" of α or β is given on the assignments for particular levels. The α rating is for levels where the assignments are certain, the β rating for levels where the assignments are tentative.

The Ground State

The ground state in ^{192}Ir has been previously assigned as having $I^\pi = 4^+$, and was not populated in the (d,t) or (d,p) reactions. The only neutron orbital that can give a 4^+ band head when coupled with the $\frac{3}{2}^+[402]$ proton is the $\frac{11}{2}^+[615]_\nu$ orbital. In single neutron transfer, this would be populated by an $l = 6$ transition, which has it maximum cross section near 50° in the (d,t) reaction. An upper limit on the ground state (d,t) cross section of 1 μb/sr can be given at this angle, which

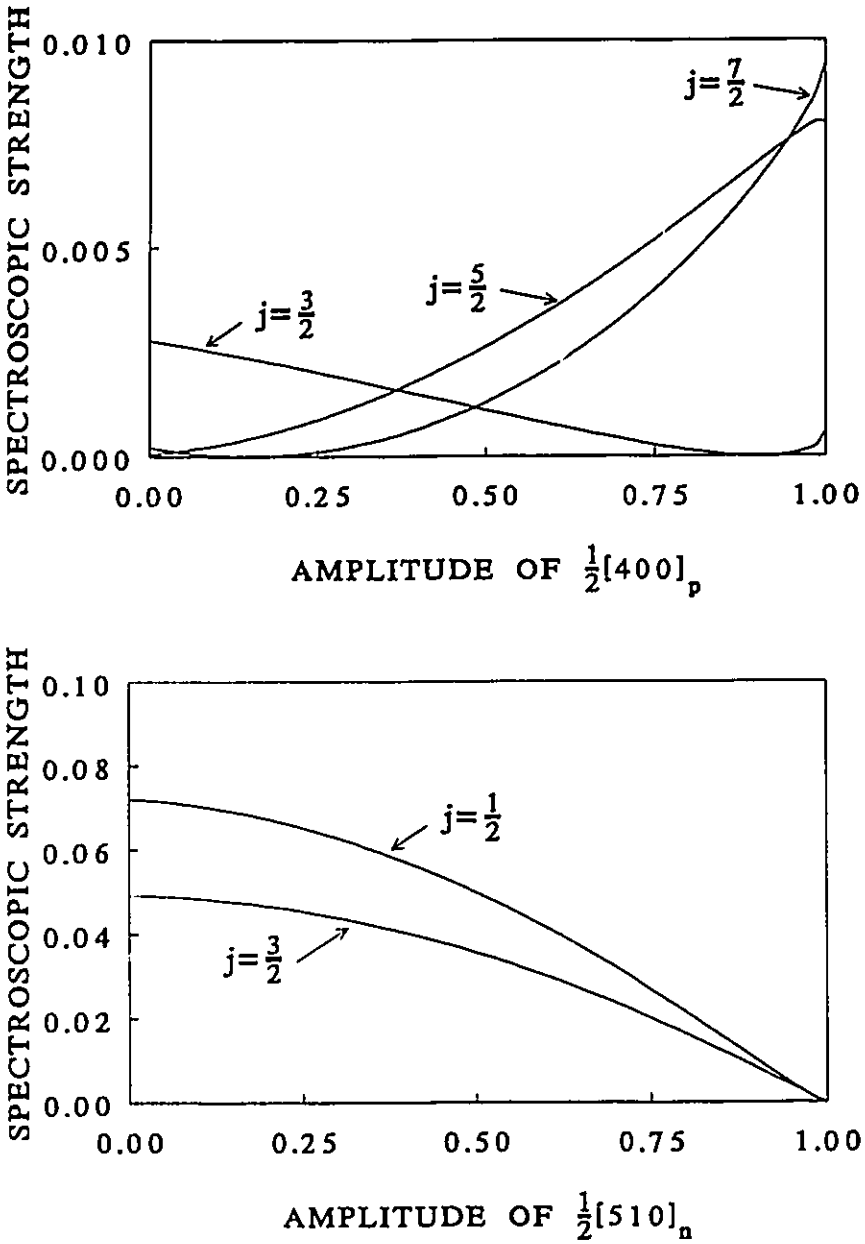

Figure 5.5.1: Spectroscopic strengths for single-neutron transfer (top) and single-proton transfer (bottom) as a function of the admixed amplitude. The final state wave function used was that described in the text for a particular 2^- state in ^{190}Ir.

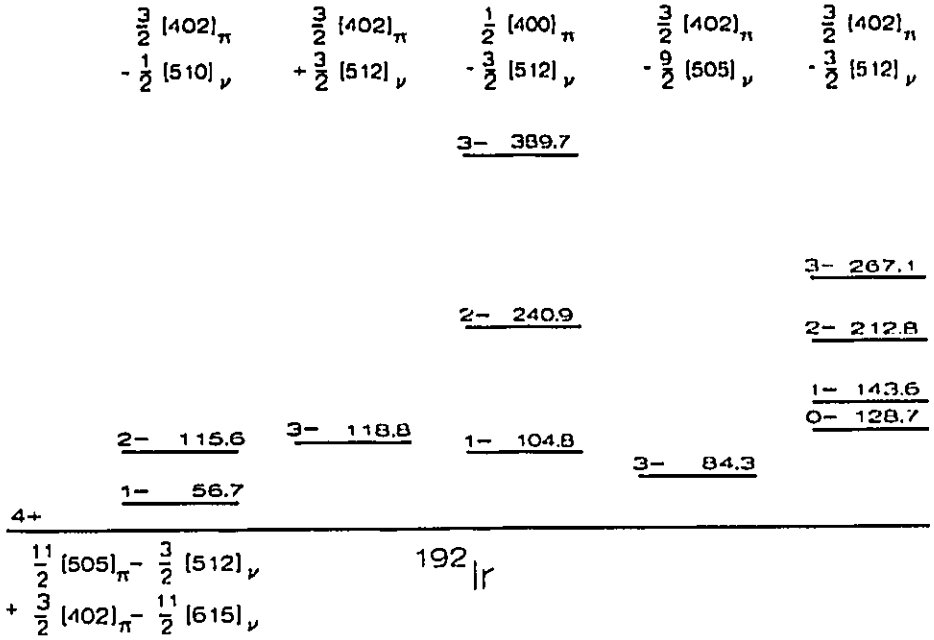

Figure 5.5.2: Interpretation of levels in ^{192}Ir in the Nilsson model as suggested in ref.[57].

yields an upper limit on the strength of $S_6 < 0.02$. This is well above the calculated value of $S_6 = 0.001$ for this configuration. In the work of Kern et al[57], the ground state is assigned as a mixture of the $\frac{11}{2}^-[505]_\pi - \frac{3}{2}^-[512]_\nu$ and $-\frac{3}{2}^+[402]_\pi + \frac{11}{2}^+[615]_\nu$ configurations based on the analysis of the magnetic moment. Therefore, as with the IBFFM calculation, in order to explain the static properties of the ground state, configurations must be mixed for which the coupling matrix elements usually considered, i.e. the Coriolis or particle-particle coupling matrix elements, vanish.

The $\frac{3}{2}^+[402]_\pi \pm \frac{1}{2}^-[510]_\nu$ Orbitals

The $\frac{1}{2}^-[510]$ neutron orbital forms[85] the ground state in ^{181}Hf, ^{183}W, and ^{185,187}Os, and also occurs at low energies in ^{183}Hf, ^{185,187}W, and ^{189,191,193}Os. It

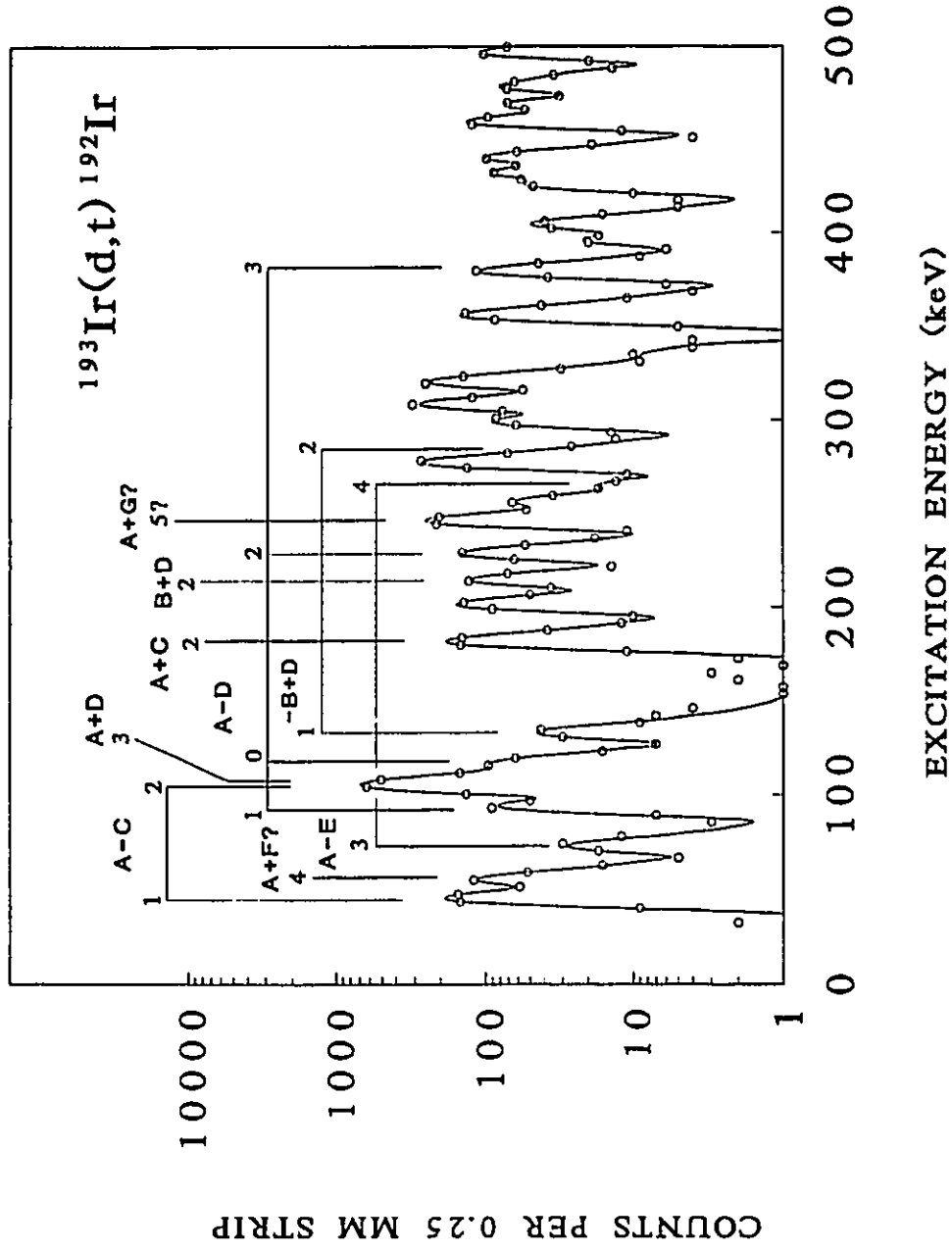

Figure 5.5.3: Low energy portion of the ^{193}Ir(d,t)^{192}Ir spectrum obtained at 45° with a beam energy of 18 MeV. The peaks are labelled with their dominant Nilsson configurations where A=$\frac{3}{2}^+[402]_\pi$, B=$\frac{1}{2}^+[400]_\pi$, C=$\frac{1}{2}^-[510]_\nu$, D=$\frac{3}{2}^-[512]_\nu$, E=$\frac{9}{2}^-[505]_\nu$, F=$\frac{5}{2}^-[503]_\nu$, and G=$\frac{7}{2}^-[503]_\nu$.

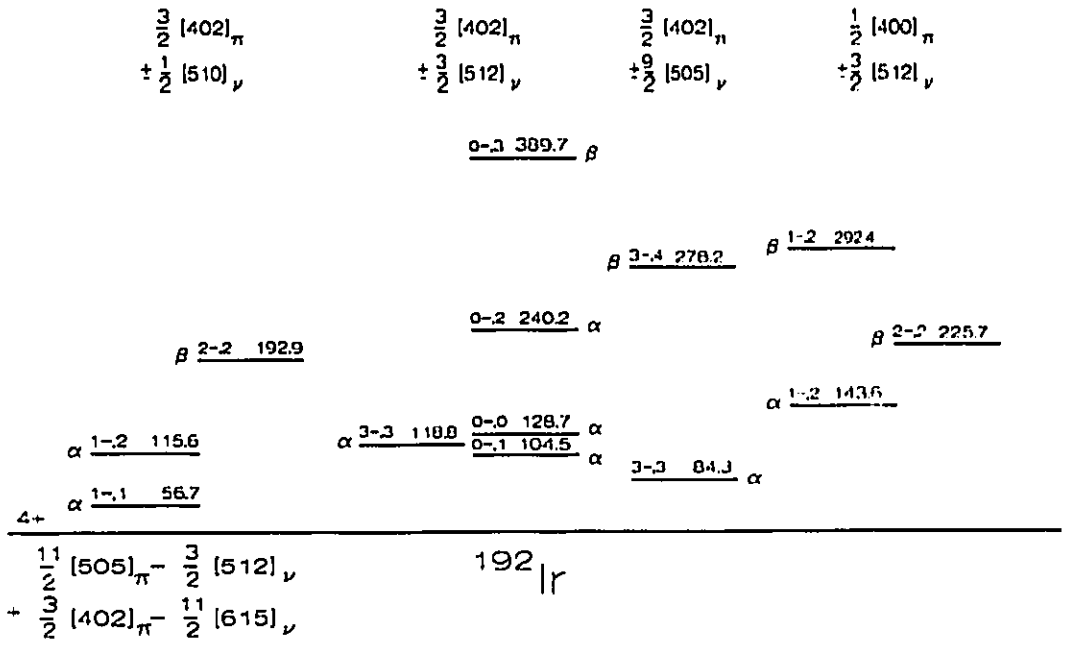

Figure 5.5.4: Interpretation of levels in ^{192}Ir in the Nilsson model as suggested in the present work. The α ratings are for levels where the assignments are definite, the β ratings are for tentative assignments.

is therefore expected to be present at low energies in ^{192}Ir. It can couple to the $\frac{3}{2}^+[402]_\pi$ orbital to form $K^\pi = 1^-$ and 2^- bands, with the $K^\pi = 1^-$ band head expected to lie lower in energy from the Gallagher-Moszkowski[17] rule. With a deformation of $\delta_2 = 0.18$, the wave function for the $\frac{1}{2}^-[510]$ neutron orbital contains $j = \frac{3}{2}$ and $j = \frac{5}{2}$ components with amplitudes of 0.67 and 0.61, respectively. Therefore, the spectroscopic strength to rotational band members based on this neutron configuration should have both $l = 1$ and $l = 3$ components.

The 1^- state at 56.7 keV was assigned by Kern et al[57] as the $\frac{3}{2}^+[402]_\pi - \frac{1}{2}^-[510]_\nu$ band head, with the 2^- member at 115.6 keV. The assignment of the 2^- member was based on the strong $M1 + E2$ γ-decay to the 1^- band head, and also on its large single-neutron transfer cross section. This assignment is adopted in

the present work. The results of the calculations described above are presented in Table 5.5.1 and Table 5.5.2, where the experimental strengths are listed along with the theoretical ones, and shown in Figure 5.5.5 and Figure 5.5.6 for the (d,t) and (d,p) reactions, respectively. Both the (d,t) and (d,p) strengths to the 1^- member of the $K^\pi = 1^-$ band are well reproduced. The 2^- band member is predicted to have almost equal amounts of $l = 1$ and $l = 3$ strength. Unfortunately, it is part of an unresolved doublet, and thus the strengths to each level were not determined. However, when an attempt was made to deconvolve the doublet in the (d,t) spectra, the results indicated that the lower member had ~70% more cross section than the upper member. This is consistent with the results of Kern et al[57] where the two levels were resolved. If the assumption is made that both the $l = 1$ and $l = 3$ strengths are divided between the two unresolved members in the same ratio as the cross sections, the resulting strengths are $S_1 \simeq 0.24$, $S_3 \simeq 0.18$ for the 2^- state and $S_1 \simeq 0.14$, $S_3 \simeq 0.12$ for the upper member of the doublet. The strengths predicted to the 2^- state are far less than the values obtained from the deconvolution of the doublet.

Table 5.5.1: Experimental and Predicted Spectroscopic (d,t) Strength for States in ^{192}Ir Assigned in the Nilsson Model

Nilsson Configuration	Energy (keV)	$l=1$ Strength			$l=3$ Strength		
		Observed	Predicted		Observed	Predicted	
			Pure[a])	Mixed[b])		Pure[a])	Mixed[b])
$\frac{3}{2}^+[402]_\pi \pm \frac{1}{2}^-[510]_\nu$							
$K^\pi = 1^-, I = 1$	56.7	0.097(7)	0.084	0.081	0.056(31)	0.013	0.013
$I = 2$	115.6	<0.38[c])	0.106	0.106	<0.30[c])	0.097	0.095
$I = 3$			0.040	0.042		0.152	0.151
$I = 4$						0.079	0.081
$K^\pi = 2^-, I = 2$	192.9	0.114(3)	0.122	0.113		0.014	0.020
$I = 3$			0.097	0.111		0.031	0.030
$I = 4$						0.091	0.095
$\frac{3}{2}^+[402]_\pi \pm \frac{3}{2}^-[512]_\nu$							
$K^\pi = 3^-, I = 3$	118.8	<0.38[c])	0.112	0.110	<0.30[c])	0.142	0.140
$I = 4$						0.050	0.049
$K^\pi = 0^-, I = 0$	128.6	0.039(2)	0.029	0.029			
$I = 1$	104.5	0.061(2)	0.054	0.054	<0.04	0.045	0.043
$I = 2$	240.2	0.089(3)	0.011	0.012		0.060	0.055
$I = 3$	389.7	<0.046	0.031	0.030	<0.096	0.162	0.163
$I = 4$						0.005	0.005
$\frac{1}{2}^+[400]_\pi \pm \frac{3}{2}^-[512]_\nu$							
$K^\pi = 1^-, I = 1$	143.5	0.010(1)	0.000	0.002	0.027(6)	0.000	0.000
$I = 2$	292.4	<0.173	0.019	0.013		0.034	0.032
$I = 3$			0.002	0.002		0.000	0.000
$I = 4$						0.031	0.017

Table 5.5.1 -continued

Nilsson Configuration	Energy (keV)	$l=1$ Strength			$l=3$ Strength		
		Observed	Predicted		Observed	Predicted	
			Pure[a])	Mixed[b])		Pure[a])	Mixed[b])
$\frac{1}{2}^+[400]_\pi \pm \frac{3}{2}^-[512]_\nu$							
$K^\pi = 2^-, I = 2$	225.7	0.066(5)	0.049	0.055	0.065(21)	0.009	0.002
$I = 3$			0.001	0.000		0.004	0.000
$I = 4$						0.000	0.010
$\frac{1}{2}^+[400]_\pi \pm \frac{1}{2}^-[510]_\nu$							
$K^\pi = 1^-, I = 1$	(235.8)		0.000	0.002		0.0004	0.0005
$I = 2$			0.015	0.023		0.004	0.005
$I = 3$			0.021	0.007		0.013	0.008
$I = 4$						0.015	0.020
$K^\pi = 0^-, I = 0$			0.001	0.001			
$I = 1$			0.000	0.000		0.000	0.001
$I = 2$			0.001	0.000		0.002	0.003
$I = 3$			0.000	0.000		0.000	0.000
$I = 4$						0.002	0.003
$\frac{3}{2}^+[402]_\pi \pm \frac{5}{2}^-[503]_\nu$							
$K^\pi = 4^-, I = 4$	66.3				0.216(8)	0.283	0.277
$\frac{3}{2}^+[402]_\pi \pm \frac{7}{2}^-[503]_\nu$							
$K^\pi = 5^-, I = 5$	256.7				0.509(28)	0.480	0.472

Table 5.5.1 -continued

Nilsson Configuration	Energy (keV)	$l = 5$ Strength Observed	Predicted Pure[a])	Predicted Mixed[b])
$\frac{3}{2}^+[402]_\pi \pm \frac{9}{2}^-[505]_\nu$				
$K^\pi = 3^-, I = 3$	83.8	0.553(38)	0.496	0.488
$I = 4$	278.2	0.34(5)	0.191	0.188

[a]) Calculated with the target ground state assumed to be pure $\frac{3}{2}^+[402]_\pi$.

[b]) Calculated with the target ground state assumed to be $0.992(\frac{3}{2}^+[402]_\pi) - 0.125(\frac{1}{2}^+[400]_\pi)$.

[c]) Total strength for the unresolved doublet is given.

The 3^- member of the $K^\pi = 1^-$ band would be expected to lie below 300 keV but there are no obvious candidates. The state at 257 keV was not populated in the ARC measurements, and is probably a 4^- or 5^- state. The state at 267.1 keV could have a spin of 3, however the similarity plots favour a spin of 2 and its cross section is much too small for it to be a reasonable candidate for the 3^- member of the band. Therefore, the higher spin members of the band are not assigned.

The $K = 2$ band was not identified in the work of Kern et al[57], and it is suggested in the present work that the 2^- state at 192.9 keV is the band head. This state was populated with a strong $l = 1$ transition, and also has a very strong $M1$ γ-transition to the 1^- state at 56.7 keV, and a weaker γ-transition to the 2^- state at 115.6. The $K = 2^-$ band head is expected to be populated with a strong $l = 1$ transition (the $l = 3$ component is much smaller) in both the (d,t) and (d,p) reactions. The level at 192.9 keV has (d,t) and (d,p) $l = 1$ strengths that match the predicted strengths extremely well. The levels observed at 212.6 and 240.2 keV

Table 5.5.2: Experimental and Predicted Spectroscopic (d,p) Strength for States in ^{192}Ir Assigned in the Nilsson Model

Nilsson Configuration	Energy (keV)	$l=1$ Strength			$l=3$ Strength		
		Observed	Predicted		Observed	Predicted	
			Pure[a])	Mixed[b])		Pure[a])	Mixed[b])
$\frac{3}{2}^+[402]_\pi \pm \frac{1}{2}^-[510]_\nu$							
$K^\pi = 1^-, I = 1$	56.7	0.058(3)	0.076	0.073		0.011	0.011
$I = 2$	115.6	<0.224(14)	0.057	0.057	<0.27(7)	0.052	0.050
$I = 3$			0.027	0.028		0.101	0.101
$I = 4$						0.052	0.054
$K^\pi = 2^-, I = 2$	192.9	0.075(3)	0.066	0.060		0.008	0.011
$I = 3$			0.065	0.074		0.021	0.020
$I = 4$						0.060	0.062
$\frac{3}{2}^+[402]_\pi \pm \frac{3}{2}^-[512]_\nu$							
$K^\pi = 3^-, I = 3$	118.8	<0.38(2)	0.075	0.073	<0.30(9)	0.095	0.093
$I = 4$						0.033	0.031
$K^\pi = 0^-, I = 0$	128.6	<0.03	0.019	0.019			
$I = 1$	104.5	<0.04	0.036	0.036		0.022	0.020
$I = 2$	240.2	0.073(7)	0.008	0.009	0.21(4)	0.031	0.028
$I = 3$	389.7	<0.024	0.021	0.020	<0.165	0.108	0.109
$I = 4$						0.003	0.003
$\frac{1}{2}^+[400]_\pi \pm \frac{3}{2}^-[512]_\nu$							
$K^\pi = 1^-, I = 1$	143.5	<0.02	0.000	0.001		0.000	0.000
$I = 2$	292.4	<0.175	0.012	0.008		0.016	0.015
$I = 3$			0.001	0.000		0.003	0.000
$I = 4$						0.020	0.011

Table 5.5.2 -continued

Nilsson Configuration	Energy (keV)	$l=1$ Strength			$l=3$ Strength		
		Observed	Predicted		Observed	Predicted	
			Pure[a])	Mixed[b])		Pure[a])	Mixed[b])
$\frac{1}{2}^+[400]_\pi \pm \frac{3}{2}^-[512]_\nu$							
$K^\pi = 2^-, I = 2$	225.7	0.041(2)	0.026	0.029		0.004	0.001
$I = 3$			0.000	0.000		0.002	0.000
$I = 4$						0.000	0.005
$\frac{1}{2}^+[400]_\pi \pm \frac{1}{2}^-[510]_\nu$							
$K^\pi = 1^-, I = 1$	(235.8)		0.000	0.001		0.000	0.000
$I = 2$			0.008	0.013		0.002	0.002
$I = 3$			0.014	0.005		0.009	0.005
$I = 4$						0.010	0.013
$K^\pi = 0^-, I = 0$			0.000	0.000			
$I = 1$			0.000	0.000		0.000	0.001
$I = 2$			0.001	0.000		0.001	0.002
$I = 3$			0.000	0.000		0.000	0.000
$I = 4$						0.001	0.002
$\frac{3}{2}^+[402]_\pi \pm \frac{5}{2}^-[503]_\nu$							
$K^\pi = 4^-, I = 4$	66.3				<0.1	0.659	0.653
$\frac{3}{2}^+[402]_\pi \pm \frac{7}{2}^-[503]_\nu$							
$K^\pi = 5^-, I = 5$	256.7				0.431(15)	0.210	0.202

Table 5.5.2 -continued

Nilsson Configuration	Energy (keV)	$l = 5$ Strength Observed	Predicted Pure[a])	Predicted Mixed[b])
$\frac{3}{2}^+[402]_\pi \pm \frac{9}{2}^-[505]_\nu$				
$K^\pi = 3^-$, $I = 3$	83.8	<0.25	0.265	0.262

[a]) Calculated with the target ground state assumed to be pure $\frac{3}{2}^+[402]_\pi$.

[b]) Calculated with the target ground state assumed to be $0.992(\frac{3}{2}^+[402]_\pi) - 0.125(\frac{1}{2}^+[400]_\pi)$.

also would be appropriate matches to the predicted (d,t) strengths, but are poorer matches for the predicted (d,p) strengths. Unfortunately, the higher spin members of this band were not identified.

The $\frac{3}{2}^+[402]_\pi \pm \frac{3}{2}^-[512]_\nu$ Orbitals

The $\frac{3}{2}^-[512]$ neutron orbital forms[85] the ground state of ^{183}Hf, ^{185,187}W, and ^{189,193}Os, and therefore should lie low in energy in ^{192}Ir. It can couple to the $\frac{3}{2}^+[402]$ proton orbital to form both a $K = 3$ and a $K = 0$ band, with the $K = 3$ band expected to lie lower in energy from the Gallagher-Moszkowski rule. With the value of δ_2 used in this work, the $\frac{3}{2}^-[512]$ neutron orbital is calculated to have an amplitude of 0.4 for $j = \frac{3}{2}$ and 0.8 for the $j = \frac{5}{2}$ components, respectively. Thus, the population of states involving this neutron orbital will contain both $l = 1$ and $l = 3$ components.

In the work of Kern et al[57], the $K^\pi = 3^-$ band head was assigned at 118.8 keV, while the $K^\pi = 0^-$ band head was assigned at 128.7 keV, with the 1^-, 2^-, and 3^- members at 143.6, 212.8, and 267.1 keV, respectively. In the present study, the $K^\pi = 3^-$ band head assignment of Kern et al[57] was adopted. The 3^- state at

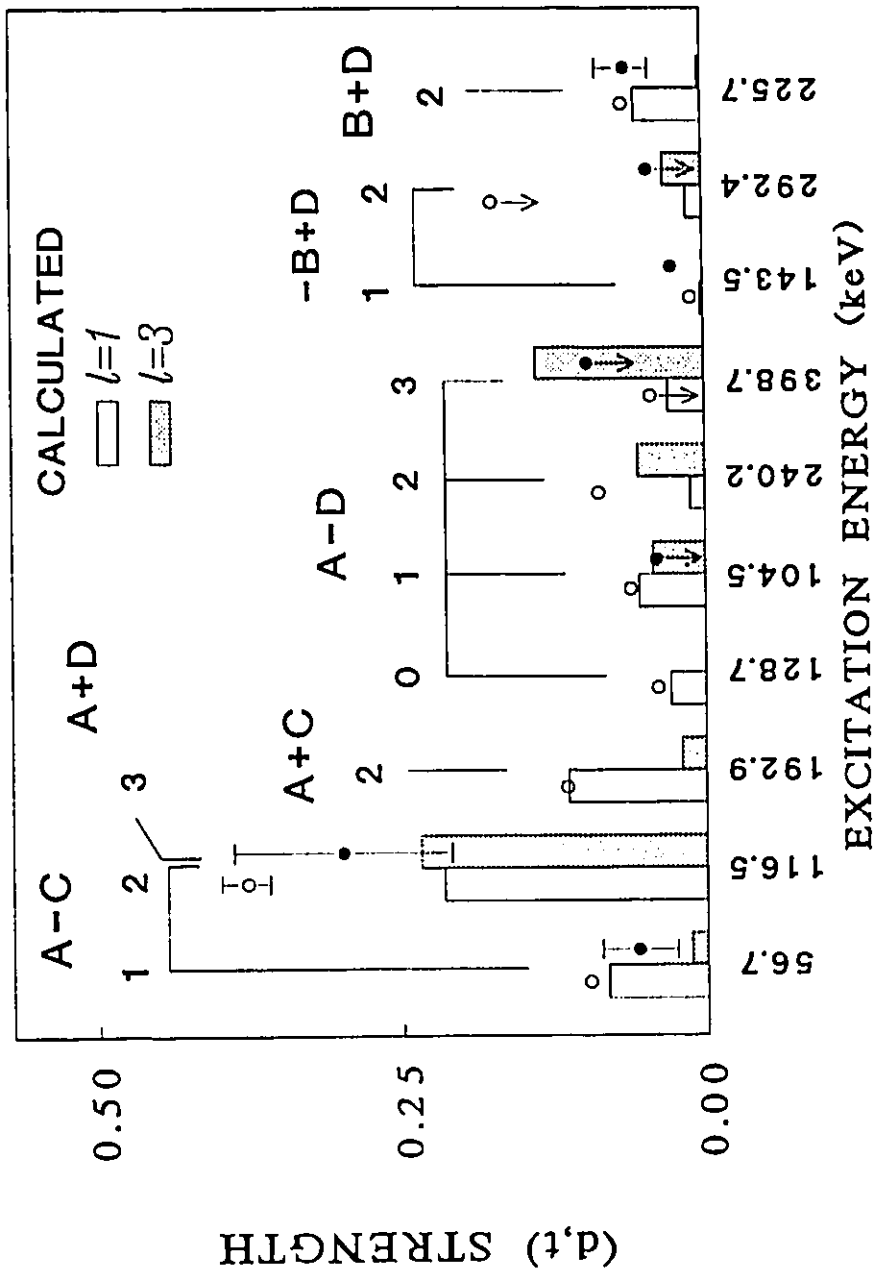

Figure 5.5.5: Strengths observed in the ^{193}Ir(d,t)^{192}Ir reaction (dots) compared with Nilsson model predictions (bars) taking into account Coriolis coupling and effects of mixed target ground states. The states are labelled with their dominant Nilsson configuration, with A=$\frac{3}{2}^{+}[402]_{\pi}$, B=$\frac{1}{2}^{+}[400]_{\pi}$, C=$\frac{1}{2}^{-}[510]_{\nu}$, and D=$\frac{3}{2}^{-}[512]_{\nu}$. Data points with arrows are upper limits, and those with no error bars have an uncertainity smaller than the size of the data point. The theoretical strengths shown for the doublet at 116.5 keV are the sums of the strengths predicted to each member.

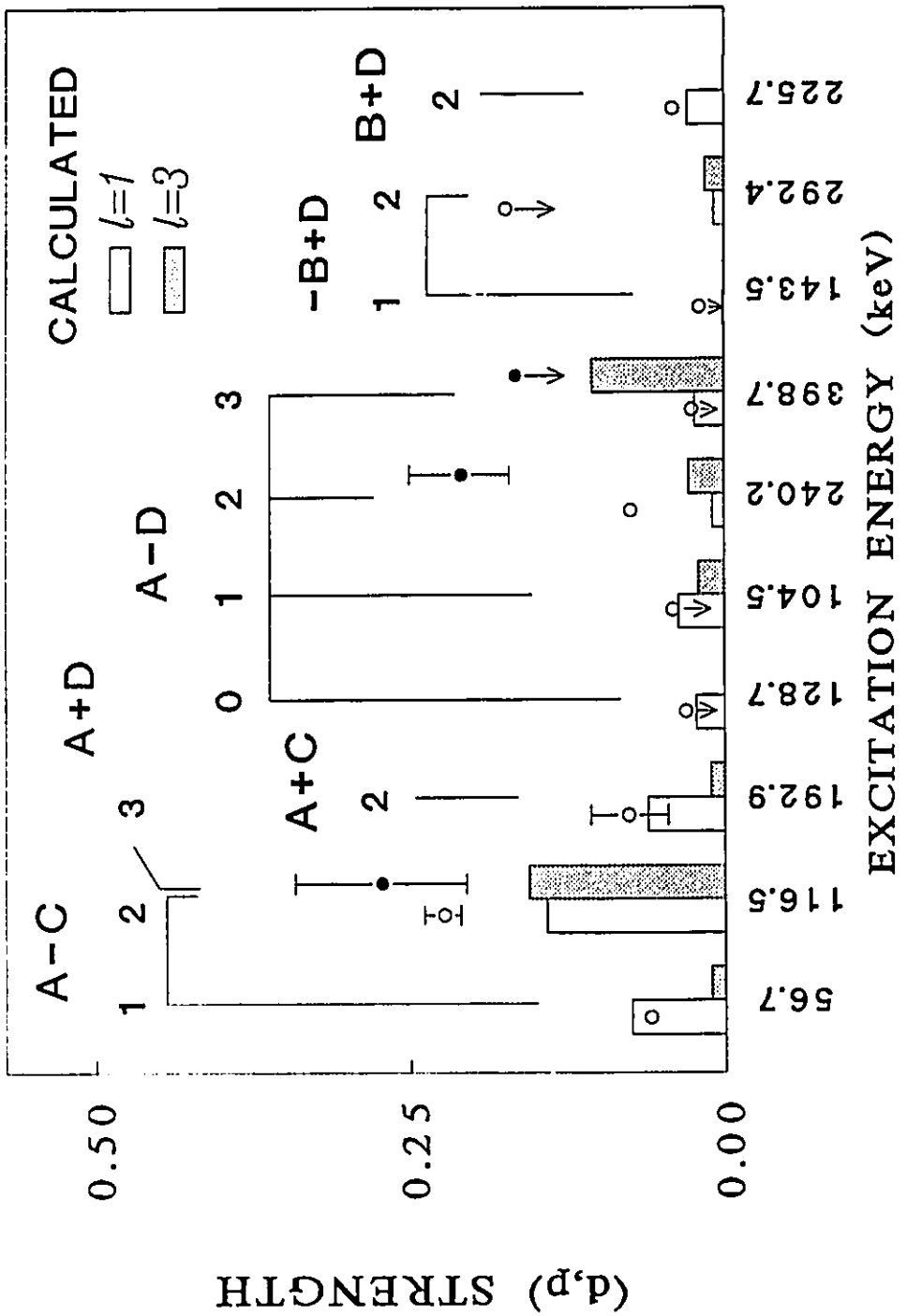

Figure 5.5.6: Strengths observed in the ^{191}Ir(d,p)^{192}Ir reaction (dots) compared with Nilsson model predictions (bars). See caption to Figure 5.5.5.

118.8 keV was populated strongly in the (d,t) reactions with both $l = 1$ and $l = 3$ transitions, and also in the (d,p) reactions. The calculations indicate that the state should be populated with $l = 1$ and 3 transitions of comparable strength.

The combined (d,t) strength predicted for the doublet at 116.6 keV, based on the above assignments, is $S_1 = 0.216$, $S_3 = 0.235$. For the (d,p) reaction, the predicted strength to the doublet is $S_1 = 0.115$, $S_3 = 0.143$. Therefore, the calculations account for $\sim 67\%$ of the observed strength.

The higher spin members of the $K^\pi = 3^-$ band have not been assigned. Assuming that the rotational parameter is between 20 and 35 keV, the 4^- member of the band would be expected between 280 and 400 keV. A possible candidate for the 4^- member is the state at 256.7 keV. However, its energy is rather low, and its strength is much too great. It is possible that the 4^- member is part of an unresolved doublet, as there are several peaks between 300 and 400 keV that have significant $l = 3$ strength.

The $K^\pi = 0^-$ band is expected to exhibit a strong Newby shift[86], with the 1^-member actually lying lower in energy than the 0^- state. The only known spin 0 state in ^{192}Ir is at 128.7 keV. It is populated with an $l = 1$ transition with $S_1 = 0.039 \pm 0.002$ in the (d,t) reaction, and has an upper limit of $S_1 < 0.03$ in the (d,p) reaction. The spin 0 state of the $K^\pi = 0^-$ band is calculated to have a (d,t) strength of $S_1 = 0.029$, and this agrees well with the experimental result. Kern et al[57] had assigned the 1^- member at 143.6 keV, but this state is too weakly populated in the (d,t) reactions, with $S_1 = 0.010 \pm 0.001$ and $S_3 = 0.027 \pm 0.006$, to belong to the $K^\pi = 0^-$ band. The 1^- state at 104.5 keV has an $l = 1$ (d,t) strength of 0.061 ± 0.002, which agrees much better with the predicted value of $S_1 = 0.054$, and is the only reasonable candidate for the 1^- member. It is also predicted to have a small $l = 3$ component, but a fit to the angular distribution with both $l = 1$ and $l = 3$ curves was not favoured by the $F\chi$ statistic. An upper limit of $S_3 = 0.04$ was determined for this state, which is just below the value of 0.043 predicted. There are several possible candidates for the 2^- member of the band, but the 240.9 keV

level is preferred. It has a strong γ-transition to the 1^- level at 104.5 keV, a large transfer strength, and a spin of 2 is favoured by the similarity plots. By considering the γ-decay characteristics, the 3^- member of the band is assigned at 389.7 keV. These last three states were assigned by Kern et al[57] as the $-\frac{1}{2}^+[400]_\pi + \frac{3}{2}^-[512]_\nu$ configuration. However, the predicted strengths for this configuration are much less than observed for the levels at 104.5 and 240.9 keV.

The $\frac{3}{2}^+[402]_\pi \pm \frac{9}{2}^-[505]_\nu$ Orbitals

The $\frac{9}{2}^-[505]$ neutron orbital occurs[85] at low excitation energy in ^{189}Os and forms the ground state in ^{191}Os, and is therefore expected at low excitation energy in ^{192}Ir. This orbital originates from the $h_{\frac{9}{2}}$ shell, and thus its wave function is dominated by the $j = \frac{9}{2}$ component. The coupling to the $\frac{3}{2}^+[402]$ proton orbital would give rise to $K^\pi = 6^-$ and $K^\pi = 3^-$ bands, with the $K^\pi = 6^-$ band head expected to lie lower in energy. These orbitals would be populated in single-neutron transfer reactions with $l = 5$ transitions, since the wave functions remain rather pure.

A strong $l = 5$ transition was observed at 84.3 keV in the (d,t) reaction. This state was determined to have $I^\pi = 3^-$ by Kern et al[57], and therefore it becomes the logical candidate for the $-\frac{3}{2}^+[402]_\pi + \frac{9}{2}^-[505]_\nu$ configuration. The expected strength for the $K = 3$ band head is $S_5 = 0.488$, which is in excellent agreement with the value $S_5 = 0.553 \pm 0.038$ observed. The 4^- member of the $K = 3^-$ band may be located at 278 keV, where a level was reported by Kern et al[57] to have either $I^\pi = 3^-$ or 4^-. In the (d,t) spectra there is evidence of a very weak peak at this energy, but only a partial angular distribution could be obtained since at many angles impurities causes it to be obscured. The angular distribution that is obtained is consistent with that of an $l = 5$ transition, with a strength of $S_5 = 0.34 \pm 0.05$. This is a factor of two greater than would be expected for the 4^- member, but it gives a reasonable rotational parameter of $\simeq$25 keV for the band and is the only higher spin state in the work of Kern et al[57] that decays to the 84.3 keV band head.

From the Gallagher-Moszkowski rule, the $K^\pi = 6^-$ band head is expected to lie lower in energy than the $K^\pi = 3^-$ band head. However, it is very unlikely that the $K = 6$ band head lies lower than 161 keV since it would probably then be in the decay path of the spin 9 isomer. As well, the $K = 6$ band head, expected to be populated with a strong $l = 5$ transition, was not detected in the (d,t) reaction below 200 keV. Therefore, there must be some coupling mechanism not accounted for in the present work that causes the Gallagher-Moszkowski rule to be broken.

The $\frac{1}{2}^+[400]_\pi \pm \frac{3}{2}^-[512]_\nu$ Orbitals

The $\frac{1}{2}^+[400]$ proton orbital has been identified[59,85] in ^{191,193}Ir at low excitation energies (82 and 73 keV, respectively), and coupling to the $\frac{3}{2}^-[512]$ neutron orbital will give low-lying $K^\pi = 1^-$ and 2^- bands. Kern et al[57] assigned the $-\frac{1}{2}^+[400]_\pi + \frac{3}{2}^-[512]_\nu$ configuration to the levels at 104.8 keV (1^-), 240.9 keV (2^-), and 389.7 keV (3^-). However, the present work has reassigned these levels to the $\frac{3}{2}^+[402]_\pi - \frac{3}{2}^-[512]_\nu$ configuration. Since the $\frac{1}{2}^+[400]_\pi$ amplitude in the target wave function is much smaller than that of the $\frac{3}{2}^+[402]_\pi$ orbital, it is predicted that configurations based on the $\frac{1}{2}^+[400]$ proton are only weakly populated, unless there is extreme final state mixing with orbitals based on the $\frac{3}{2}^+[402]$ proton.

The level at 143.6 keV has either $I^\pi = 1^-$ or 2^-, and the value of 1 is favoured by the similarity plots. In ^{190}Ir, a level at a relative excitation energy of 144.0 keV is populated with similar (d,t) strengths to the state at 143.6 keV in ^{192}Ir. Based on this similarity, it is considered likely that the two states have the same configuration. The level at 144.0 keV in ^{190}Ir was populated quite strongly in the single-proton transfer reactions, and thus the $\frac{3}{2}^-[512]_\nu$ orbital, which is the major component of the ground state of the target of ^{189}Os, is the dominant neutron component. Since the states are also weakly populated in the single-neutron transfer reactions, the most likely configuration is $-\frac{1}{2}^+[400]_\pi + \frac{3}{2}^-[512]_\nu$. Assuming an amplitude of 0.125 for the $\frac{1}{2}^+[400]_\pi$ orbital in the ^{193}Ir ground state (this value is the result of Coriolis mixing calculations which reproduce the low-lying spectrum of

^{193}Ir), the predicted strengths to the band head in ^{192}Ir are $S_1 = 0.002$, $S_3 = 0.0004$. While these values are far less than observed for the state at 143.6 keV, there could be additional mixings with states not included in the calculations, that would increase the strength.

The 2^- band member would be expected between 200 and 280 keV, and is probably weakly populated. There are several candidates that meet these requirements. For instance, the state at 267.1 keV has an I^π value of (1^-), 2^-, or 3^-, with the similarity plots favoring the spin 2 assignment, and is populated weakly in the (d,t) reactions. There is also a 1^- or 2^- state at 292.4 keV, again the similarity plots favoring a spin of 2, that is part of an unresolved doublet in the (d,t) and (d,p) reactions at 288.5 keV. The other level in the doublet has an energy of 288.4 keV, and thus the 292.4 keV state is weakly populated. The 143.5 keV state is not fed by a γ-transition from the level at 267.1 keV, but is fed from the 292.4 keV level. Therefore, the 292.4 keV level is tentatively assigned as the 2^- member of the $K^\pi = 1^-$ band.

The $K^\pi = 2^-$ band based on the $\frac{1}{2}^+[400]_\pi + \frac{3}{2}^-[512]_\nu$ configuration would also be weakly populated unless there is a significant amount of mixing with a configuration based on the $\frac{3}{2}^+[402]_\pi$ orbital. Such a situation may occur if the unperturbed states are situated close in energy. The Gallagher-Moszkowski splitting is expected[87] to be on the order of 100 keV, so the $K^\pi = 2^-$ band head should be between 200 and 280 keV. Once again, there are several states that would be candidates, such as the 212.8 keV level (similarity plots favour spin 2), the 225.9 2^- level, the 267.1 keV level (again, similarity plots favour spin 2), and the 288.4 and 292.4 keV levels, both of which are favoured to have spin 2 from the similarity plots. The level at 288.4 keV is too strongly populated to be a reasonable choice, since a strength of $S_1 = 0.173 \pm 0.005$ would require the dominant component to be built on the $\frac{3}{2}^+[402]_\pi$ orbital, and the level at 292.4 keV was assigned as the 2^- member of the $K^\pi = 1^-$ band. Calculations indicate that the $K^\pi = 2^-$ band head may become very configuration mixed if placed near to other 2^- states, and have (d,t)

strengths of $S_1 = 0.055$, $S_3 = 0.002$, and (d,p) strengths of $S_1 = 0.029$, $S_3 = 0.001$. The 2^- level at 225.7 keV is the best overall match, as it has (d,t) strengths of $S_1 = 0.066 \pm 0.005$, $S_3 = 0.065 \pm 0.021$, and (d,p) strength of $S_1 = 0.033 \pm 0.002$. The state at 212.6 keV is populated as strongly in the (d,p) reactions as in the (d,t) reactions, and has an $l = 1$ strength that is much larger than predicted. Unfortunately, no higher spin members of the band can be assigned at this time.

The $\frac{1}{2}^+[400]_\pi \pm \frac{1}{2}^-[510]_\nu$ Orbitals

It is expected that weakly populated $K^\pi = 1^-$ and $K^\pi = 0^-$ bands based on the the $\frac{1}{2}^+[400]_\pi \pm \frac{1}{2}^-[510]_\nu$ orbitals should exist at low energies. From the Gallagher-Moszkowski rule, the $K^\pi = 1^-$ configuration should lie lower in energy. A possible assignment for this state is the tentative 1^- level at 235.8 keV, which was not observed in the present work. Calculations indicate that the (d,t) strength to the $K^\pi = 1^-$ band head would be $S_1 = 0.002$, $S_3 = 0.0005$, which would make its detection by single-nucleon transfer practically impossible. It is not possible at this time to assign the higher spin members or the $K^\pi = 0^-$ band.

Possible Interpretation for the 4^- State at 66.3 keV
the Probable 4^- or 5^- State at 257.6 keV

The peak observed at 66.3 keV was populated with a pure $l = 3$ transition in the (d,t) reactions with strength $S_3 = 0.216 \pm 0.008$. As discussed previously, the value $I^\pi = 4^-$ is favoured for this state. An examination of the Nilsson diagram indicates that there are two possible configurations that yield a $K^\pi = 4^-$ band which would be populated with essentially pure $l = 3$ transitions; the $\frac{1}{2}^+[400]_\pi + \frac{7}{2}^-[503]_\nu$ and $\frac{3}{2}^+[402]_\pi + \frac{5}{2}^-[503]_\nu$ configurations. The $\frac{7}{2}^-[503]_\nu$ orbital has been identified[85] as a hole state at low excitation energies in ^{187,189,191}Os. The $\frac{5}{2}^-[503]_\nu$ orbital has been identified[85] as a particle state in ^{187}W and ^{187}Os at approximately 600 keV, but it may fall rapidly in energy with increasing neutron number. The $\frac{1}{2}^+[400]_\pi + \frac{7}{2}^-[503]_\nu$

configuration would not be expected to be populated strongly in the single-neutron transfer reactions since the amplitudes of the $\frac{1}{2}^+[400]_\pi$ orbital in the targets are small. The $\frac{3}{2}^+[402]_\pi + \frac{5}{2}^-[503]_\nu$ configuration is predicted to have a (d,t) strength of $S_3 \simeq 0.28$ assuming a $V^2 = 0.3$. While the (d,t) strength can be approximately reproduced with this configuration, the (d,p) strength cannot. The predicted (d,p) strength is $S_3 \simeq 0.65$, but an upper limit for the $l = 3$ strength to the level at 66.3 keV is $S_3 < 0.1$. A mixture of the $\frac{3}{2}^+[402]_\pi + \frac{5}{2}^-[503]_\nu$ and $\frac{1}{2}^+[400]_\pi + \frac{7}{2}^-[503]_\nu$ configurations would be necessary to reproduce the strength. However, the particle-particle coupling matrix element is only 1.6 keV, and thus the extreme mixing that would be required can not be reproduced in the present work.

A strong $l = 3$ transition was observed to populate the level at 257.6 keV, with $S_3 = 0.509 \pm 0.028$ in the (d,t) reaction and $S_3 = 0.431 \pm 0.015$ in the (d,p) reaction. As explained in a previous section, this state is probably 4^- or 5^- since it was not observed in the ARC experiments of Kern et al[57]. Possible interpretations for this state would be the $I = 4, K^\pi = 4^-$, $\frac{3}{2}^+[402]_\pi + \frac{5}{2}^-[503]_\nu$ configuration or the $I = 5, K^\pi = 5^-$, $\frac{3}{2}^+[402]_\pi + \frac{7}{2}^-[503]_\nu$ configuration. Since it was shown above that the $K^\pi = 4^-$ configuration may be needed to explain the 4^- state at 66.3 keV, the only state left that could explain the strength is the $K^\pi = 5^-$, $\frac{3}{2}^+[402]_\pi + \frac{7}{2}^-[503]_\nu$ configuration. As seen in Table 5.5.1 and Table 5.5.2, this configuration can approximately reproduce the (d,t) strength, but underestimates the (d,p) strength by a factor of 2.

The suggested assignments for the 66.3 and 256.7 keV levels must be considered as spectulative, since there are problems reproducing the observed strengths, and the spin of the 256.7 keV level is not known.

5.5.3 Interpretation of ^{190}Ir in Terms of the Nilsson Model

The nuclear structure of ^{190}Ir is virtually unknown, even though it lies next to the stable nuclei ^{191}Ir and ^{189}Os. The ground state is known to decay with a half life of 11.78 days, and 2 isomeric levels exist at 26.3 and 175 keV. The ground

state was assigned 4^+, with the possible configuration[62] of $-\frac{3}{2}^+[402]_\pi + \frac{11}{2}^+[615]_\nu$. The isomeric levels were assigned I^π values of 7^+ ($\frac{3}{2}^+[402]_\pi + \frac{11}{2}^+[615]_\nu$) and 11^- ($\frac{11}{2}^-[505]_\pi + \frac{11}{2}^+[615]_\nu$), respectively. Until the present experiments were performed, this was the extent of knowledge concerning the structure of levels in ^{190}Ir.

The single-neutron transfer experiments were performed on a target of ^{191}Ir which has $I^\pi = \frac{3}{2}^+$. The dominant component in the wave function of the target is the $\frac{3}{2}^+[402]_\pi$ orbital, and thus the strongest peaks resulting from the (d,t) reaction should have this proton configuration. However, Coriolis coupling calculations for ^{191}Ir indicate that there is an admixture of the $\frac{1}{2}^+[400]_\pi$ orbital in the ground state, with an amplitude of 0.125 and opposite phase to the $\frac{3}{2}^+[402]_\pi$ orbital. Because of this, and Coriolis coupling of different configurations in the final state, it is expected that states will be populated that have the $\frac{1}{2}^+[400]_\pi$ orbital as their dominant proton configuration. The single-proton transfer experiments were performed on a target of ^{189}Os that has $I^\pi = \frac{3}{2}^-$. The dominant component in the wave function of the target is the $\frac{3}{2}^-[512]_\nu$ orbital, but, once again, Coriolis mixing introduces another orbital, $\frac{1}{2}^-[510]_\nu$, into the wave function. The amplitude of this admixed orbital is approximately 0.3, and it has the same phase as the $\frac{3}{2}^-[512]_\nu$ orbital. Therefore, the strongest peaks observed in the proton-transfer spectra involve the $\frac{3}{2}^-[512]$ neutron, but there should also be weaker peaks that involve the $\frac{1}{2}^-[510]$ neutron part of the configuration. The low-energy portions of the ^{191}Ir(d,t)^{190}Ir and ^{189}Os(α,t)^{190}Ir spectra, shown in Figure 5.5.7 and Figure 5.5.8, have the peaks labelled with the dominant Nilsson configurations determined in this work. The Nilsson assignments are also shown in Figure 5.5.9, where the ratings α or β have been used to express the confidence in the assignments.

The levels that are below 400 keV relative excitation energy and populated in *both* the single-neutron and single-proton transfer reactions are listed in Table 5.5.3. In a simple Nilsson picture without any configuration mixing in the target ground state or in the final state, only 5 levels would be expected to be populated in common: the spin 0 to 3 members of the $K^\pi = 0^-$ band and the $K^\pi = 3^-$

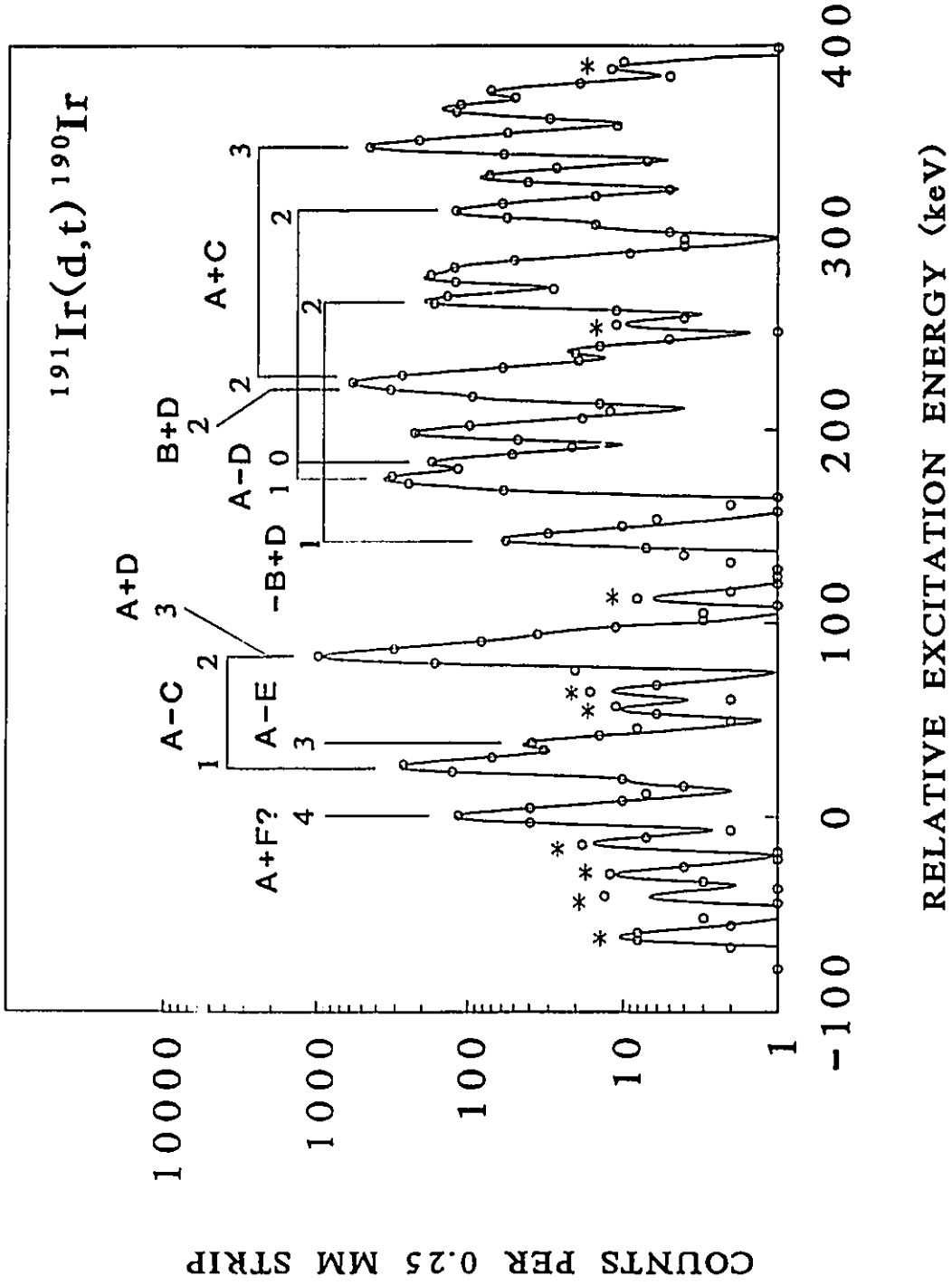

Figure 5.5.7: Low energy portion of the ^{191}Ir(d,t)^{190}Ir spectrum obtained at 45° with a beam energy of 18 MeV. The peaks are labelled with their dominant Nilsson configurations where A=$\frac{3}{2}^+[402]_\pi$, B=$\frac{1}{2}^+[400]_\pi$, C=$\frac{1}{2}^-[510]_\nu$, D=$\frac{3}{2}^-[512]_\nu$, E=$\frac{9}{2}^-[505]_\nu$, and F=$\frac{5}{2}^-[503]_\nu$.

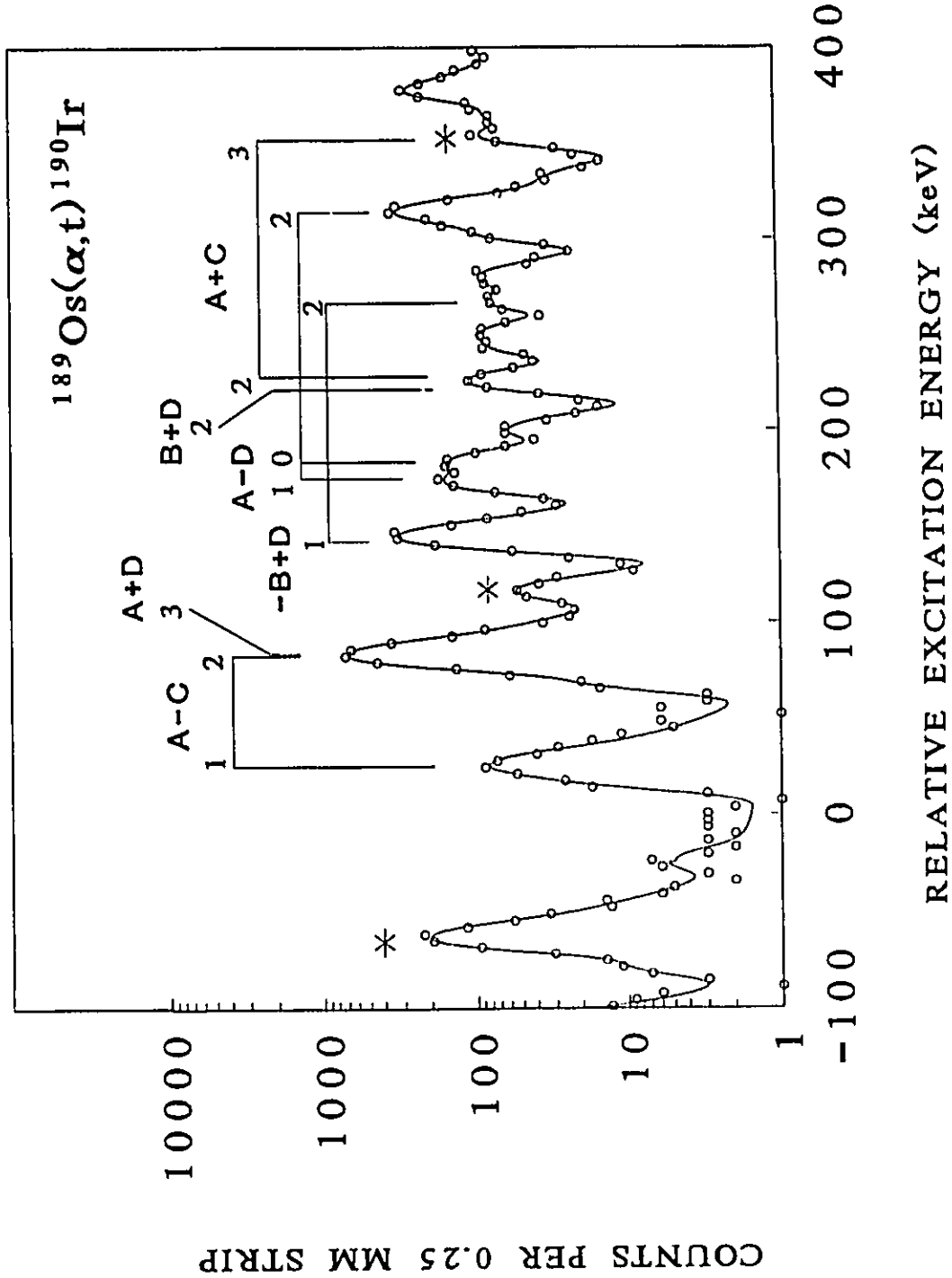

Figure 5.5.8: Low energy portion of the ^{189}Os(α,t)^{190}Ir spectrum obtained at 50° with a beam energy of 30 MeV. See caption to Figure 5.5.7.

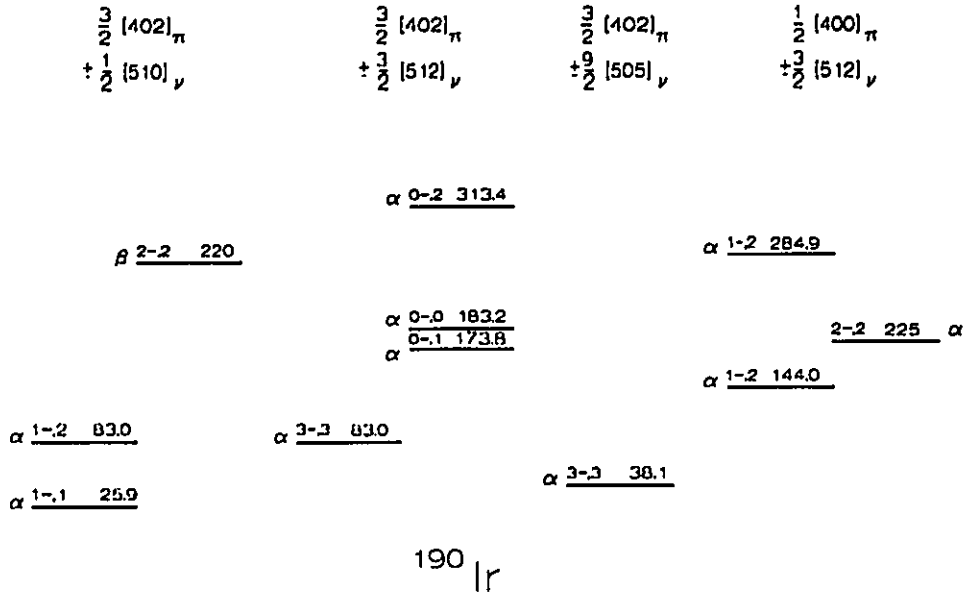

Figure 5.5.9: Interpretation of levels in ^{190}Ir in the Nilsson model as suggested in the present work. The α ratings are for levels where the assignments are definite, the β ratings are for tentative assignments.

band head of the $\frac{3}{2}^{+}[402]_{\pi} \pm \frac{3}{2}^{-}[512]_{\nu}$ configuration. However, there are 9 peaks (two of which are probably doublets) below 320 keV that appear to be populated in common in the single-proton and single-neutron transfer reactions. This is strong evidence for a large amount of configuration mixing in ^{190}Ir. As will be seen below, the Coriolis and particle-particle coupling, as well as the effect of mixing in the ground states of the targets, can account for all but one of the low-lying levels populated in both single-proton and single-neutron transfer. This illustrates the need to take a proper account of the various mixings, and demonstrates that the simple Nilsson model can approximately describe some of the low-lying structure of ^{190}Ir.

In the discussion below, all references to energies in ^{190}Ir refer to relative excitation energies, and the (^{3}He,d) cross sections are those at an angle of 35°. The

Table 5.5.3: Levels Populated in Common in Both the Single-Neutron and Single-Proton Transfer Below 400 keV

Relative Excitation Energy (keV)	Single-Neutron Transfer Strength		(^{3}He,d) Cross Section
	S_1	S_3	
25.9	0.089(3)		3.7(9)
83.0	0.224(14)	0.224(59)	35(4)
144.0	0.019(1)		28(3)
173.8	0.055(4)	0.323 (31)	6.0(14)
183.2	0.045(2)		12(2)
198.9	0.062(4)	0.044(18)	4.9(8)
225.4	<0.187	<0.313	13.4(17)
266.8	0.074(2)		9.5(14)
284.9	0.021(4)	0.020(13)	8.4(16)
313.4	0.021(2)	0.130(14)	16(2)

results of the calculations are listed in Table 5.5.4 and Table 5.5.5, and can be seen in Figure 5.5.10 and Figure 5.5.11, for the (d,t) strengths and single-proton transfer cross sections, respectively.

Table 5.5.4: Experimental and Predicted Spectroscopic (d,t) Strength for States in ^{190}Ir Assigned in the Nilsson Model

Nilsson Configuration	Energy (keV)	$l=1$ Strength			$l=3$ Strength		
		Observed	Predicted		Observed	Predicted	
			Pure[a])	Mixed[b])		Pure[a])	Mixed[b])
$\frac{3}{2}^+[402]_\pi \pm \frac{1}{2}^-[510]_\nu$							
$K^\pi = 1^-, I = 1$	25.9	0.089(3)	0.086	0.084		0.013	0.012
$I = 2$	83.0	<0.224[c])	0.119	0.119	<0.224[c])	0.089	0.088
$I = 3$			0.039	0.041		0.151	0.150
$I = 4$						0.080	0.079
$K^\pi = 2^-, I = 2$	220	<0.187[c])	0.119	0.121	<0.313(53)	0.022	0.015
$I = 3$	347.8	0.121(8)	0.117	0.128	0.116(34)	0.085	0.081
$I = 4$						0.069	0.079
$\frac{3}{2}^+[402]_\pi \pm \frac{3}{2}^-[512]_\nu$							
$K^\pi = 3^-, I = 3$	83.0	<0.224[c])	0.112	0.110	<0.224[c])	0.142	0.140
$I = 4$						0.050	0.049
$K^\pi = 0^-, I = 0$	183.2	0.045(2)	0.029	0.029			
$I = 1$	173.8	<0.055[c])	0.052	0.054	<0.323[c])	0.073	0.066
$I = 2$	313.4	0.021(2)	0.028	0.022	0.130(14)	0.135	0.129
$I = 3$			0.007	0.006		0.104	0.118
$I = 4$						0.037	0.032
$\frac{1}{2}^+[400]_\pi \pm \frac{3}{2}^-[512]_\nu$							
$K^\pi = 1^-, I = 1$	144.0	0.019(1)	0.0004	0.000		0.0005	0.003
$I = 2$	284.9	0.021(4)	0.000	0.0003	0.020(13)	0.003	0.002
$I = 3$			0.013	0.018		0.004	0.009
$I = 4$						0.010	0.003

Table 5.5.4 -continued

Nilsson Configuration	Energy (keV)	$l=1$ Strength			$l=3$ Strength		
		Observed	Predicted		Observed	Predicted	
			Pure[a])	Mixed[b])		Pure[a])	Mixed[b])
$\frac{1}{2}^+[400]_\pi \pm \frac{3}{2}^-[512]_\nu$							
$K^\pi = 2^-, I = 2$	225.0	0.066(5)	0.086	0.075	0.065(21)	0.012	0.021
$I = 3$			0.007	0.008		0.002	0.003
$I = 4$						0.001	0.005
$\frac{1}{2}^+[400]_\pi \pm \frac{1}{2}^-[510]_\nu$							
$K^\pi = 1-, I = 1$			0.0003	0.002		0.0008	0.0003
$I = 2$			0.005	0.011		0.003	0.005
$I = 3$			0.026	0.012		0.031	0.022
$I = 4$						0.027	0.031
$K^\pi = 0^-, I = 0$			0.001	0.001			
$I = 1$			0.001	0.000		0.003	0.009
$I = 2$			0.006	0.003		0.022	0.026
$I = 3$			0.004	0.001		0.019	0.011
$I = 4$						0.001	0.000
$\frac{3}{2}^+[402]_\pi + \frac{5}{2}^-[503]_\nu$							
$K^\pi = 4^-, I = 4$	0			0.100(8)	0.283	0.277	

Table 5.5.4 -continued

Nilsson Configuration	Energy (keV)	$l=5$ Strength Observed	Predicted Pure[a])	Predicted Mixed[b])
$-\frac{3}{2}^+[402]_\pi + \frac{9}{2}^-[505]_\nu$				
$K^\pi = 3^-, I = 3$	38.1	0.325(24)	0.496	0.488

[a]) Calculated with the target ground state assumed to be pure $\frac{3}{2}^+[402]_\pi$.

[b]) Calculated with the target ground state assumed to be $0.992(\frac{3}{2}^+[402]_\pi) - 0.125(\frac{1}{2}^+[400]_\pi)$.

[c]) Total strength for the unresolved doublet is given.

The $\frac{3}{2}^+[402]_\pi \pm \frac{3}{2}^-[512]_\nu$ Configurations

In *both* single-neutron and single-proton transfer reactions, levels due to the $\frac{3}{2}^+[402]_\pi \pm \frac{3}{2}^-[512]_\nu$ configurations are expected to be the most strongly populated ones . The $K^\pi = 3^-$ band is expected to be below the $K^\pi = 0^-$ band. The $K^\pi = 0^-$ band may have a strong Newby shift as in ^{192}Ir, such that the 1^- member lies lower in energy than the 0^- member.

Since the $K^\pi = 3^-$ band head is expected to be the lowest energy peak which is strongly populated in both single-proton and single-neutron transfer reactions, a likely candidate is the peak at 84 keV. However, its (d,t) strength appears too large to be explained by the spin 3 state. There is a great similarity in the (d,t) strengths between the peak at 84 keV in ^{190}Ir and the peak at 116.6 keV in ^{192}Ir. This latter peak was attributed to a doublet, and one of the members was assigned as the $K^\pi = 3^-$ band head. It is suggested that the peak at 84 keV in ^{190}Ir is also a doublet. The $K = 3^-$ band head is predicted to have (d,t) strengths of $S_1 = 0.136$, $S_3 = 0.114$ and a (^{3}He,d) cross section of 22 μb/sr. This would account for half of

Table 5.5.5: Experimental and Predicted Single-Proton Transfer Cross Sections for States in ^{190}Ir Assigned in the Nilsson Model

Nilsson Configuration	Energy (keV)	(^{3}He,d) Cross Section (μb/sr) at $\theta = 35°$			(α,t) Cross Section (μb/sr) at $\theta = 50°$		
		Observed	Predicted		Observed	Predicted	
			Pure[a])	Mixed[b])		Pure[a])	Mixed[b])
$\frac{3}{2}^+[402]_\pi \pm \frac{1}{2}^-[510]_\nu$							
$K^\pi = 1^-, I = 1$	25.9	3.7(9)	0.0	0.5	7.3(9)	0.0	1.0
$I = 2$	83.0	<35[c])	0.0	1.0	<57[c])	0.0	1.8
$I = 3$			0.0	0.7		0.0	0.5
$K^\pi = 2^-, I = 2$	220	<13.4[c])	0.7	1.7	<8.5[c])	0.7	1.2
$I = 3$	347.8		0.0	0.5		0.0	0.5
$\frac{3}{2}^+[402]_\pi \pm \frac{3}{2}^-[512]_\nu$							
$K^\pi = 3^-, I = 3$	83.0	<35[c])	24	22	<57[c])	47	42
$K^\pi = 0^-, I = 0$	183.2	12(2)	7.0	6.3	10(1)	13.3	12
$I = 1$	173.8	<6.0[c])	7.2	6.6	<11[c])	13.3	12
$I = 2$	313.4	16(2)	3.1	2.3	31(4)	5.3	4.3
$I = 3$			2.5	2.3		2.4	2.2
$\frac{1}{2}^+[400]_\pi \pm \frac{3}{2}^-[512]_\nu$							
$K^\pi = 1^-, I = 1$	144.0	28(3)	22.3	18.3	35(4)	17.5	14.1
$I = 2$	284.9	8.4(16)	9.5	8.4	7.1(10)	9.3	8.2
$I = 3$			2.6	2.4		2.0	1.8
$K^\pi = 2^-, I = 2$	225.0	13.4(17)[c])	17.5	17.8	8.5(10) [c])	12.5	13.9
$I = 3$			4.2	3.9		3.0	2.7

Table 5.5.5 -continued

Nilsson Configuration	Energy (keV)	(^{3}He,d) Cross Section (μb/sr) at $\theta = 35°$		(α,t) Cross Section (μb/sr) at $\theta = 50°$	
		Observed	Predicted	Observed	Predicted
			Pure[a]) Mixed[b])		Pure[a]) Mixed[b])
$\frac{1}{2}^+[400]_\pi \pm \frac{1}{2}^-[510]_\nu$					
$K^\pi = 1^-$, $I = 1$		0.3	2.6	0.2	1.9
$I = 2$		3.7	1.6	4.8	2.9
$I = 3$		0.0	0.6	0.0	0.6
$K^\pi = 0^-$, $I = 0$		0.0	0.0	0.0	0.0
$I = 1$		0.6	1.6	0.9	1.2
$I = 2$		1.5	1.6	2.1	2.6
$I = 3$		0.0	0.5	0.0	0.4

[a]) Calculated with the target ground state assumed to be pure $\frac{3}{2}^-[512]_\nu$.

[b]) Calculated with the target ground state assumed to be $0.95(\frac{3}{2}^-[512]_\nu)+0.3(\frac{1}{2}^-[510]_\nu)$.

[c]) Total cross section for the unresolved doublet is given.

the observed (d,t) strength and $\simeq$63% of the observed (^{3}He,d) cross section. Higher spin states of the $K^\pi = 3^-$ band cannot be assigned at the present time.

The level populated at an energy of 173.8 keV is suggested to be due to a doublet, with one of the levels due to the 1^- member of the $K^\pi = 0^-$ $\frac{3}{2}^+[402]_\pi - \frac{3}{2}^-[512]_\nu$ configuration. This is predicted to have (d,t) strengths of $S_1 = 0.054$, $S_3 = 0.066$, and since it is believed that the experimental strength is due to two levels, it is quite possible that the other member of the doublet is populated with a strong, almost pure $l = 3$ transition. Such transitions are observed in ^{192}Ir, and

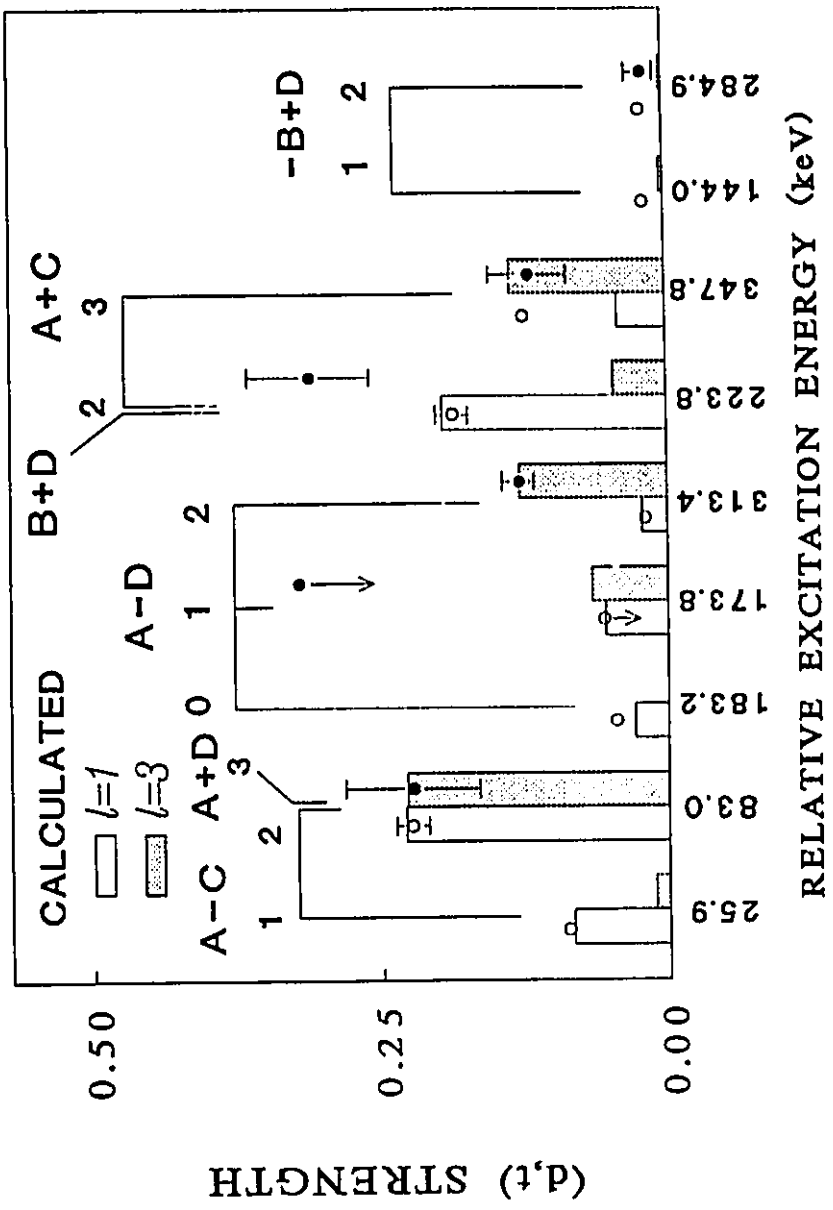

Figure 5.5.10: Strengths observed in the ^{191}Ir(d,t)^{190}Ir reaction (dots) compared with Nilsson model predictions (bars) taking into account Coriolis coupling and effects of configuration mixed target ground state. The states are labelled with their dominant Nilsson configuration, with A=$\frac{3}{2}^{+}[402]_{\pi}$, B=$\frac{1}{2}^{+}[400]_{\pi}$, C=$\frac{1}{2}^{-}[510]_{\nu}$, and D=$\frac{3}{2}^{-}[512]_{\nu}$. Data points with arrows are upper limits, and those with no error bars have an uncertainity smaller than the size of the data point. The theoretical strengths shown for the doublets at 83.0 and 223.8 keV are the sums of the strengths predicted to each member.

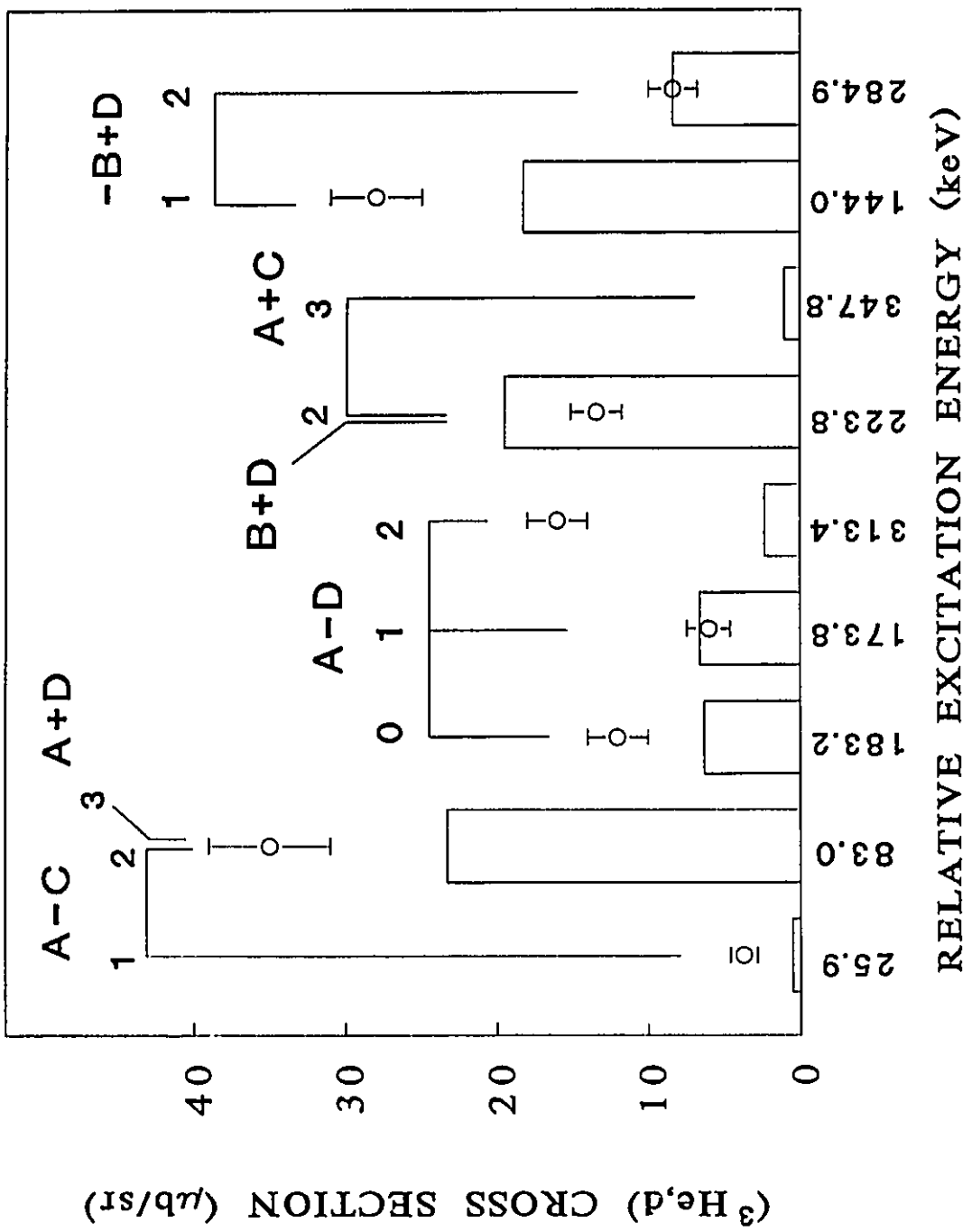

Figure 5.5.11: Cross sections observed in the ^{189}Os(^{3}He,d)^{190}Ir reaction (dots) compared with Nilsson model predictions (bars). See caption to Figure 5.5.10.

are expected in ^{190}Ir as well. The calculated (^{3}He,d) cross section of 5.0 μb/sr is in reasonable agreement with the observed cross section.

The 0^- member of the $K^\pi = 0^-$ band is assigned at 183.2 keV. This level was populated in both the single-neutron transfer, with a pure $l = 1$ transition, and single-proton transfer reactions. The predicted strength and cross section to this level are in excellent agreement with the observations, as listed in Table 5.5.4 and Table 5.5.5, and as can be seen in Figure 5.5.10 and Figure 5.5.11.

The 2^- member of the $K^\pi = 0^-$ band may lie at 313.4 keV. This level is populated strongly in the single-proton transfer reactions ((^{3}He,d) cross section of 16 ± 2 μb/sr), and has a relatively large $l = 3$ strength, with a much smaller $l = 1$ strength ($S_1 = 0.021 \pm 0.002$, $S_3 = 0.130 \pm 0.014$) in the (d,t) reactions. The calculations indicate that this state should have a (^{3}He,d) cross section of 2.0 μb/sr, and (d,t) strengths of $S_1 = 0.022$, $S_3 = 0.129$. While the proton transfer strength is greatly underestimated, the (d,t) strengths are in excellent agreement with the observations. It may be possible that the proton-transfer cross section to this peak is due to an unresolved doublet.

The $\frac{3}{2}^+[402]_\pi \pm \frac{1}{2}^-[510]_\nu$ Configurations

The level at 26 keV is populated with a strong $l = 1$ transition in the (d,t) reactions. Therefore, it must have the $\frac{3}{2}^+[402]$ orbital as its dominant proton component. This level is also populated in the (α,t) and (^{3}He,d) reactions with a relatively small cross section, as expected if the dominant neutron configuration were $\frac{1}{2}^-[510]$. The coupling of these two orbitals gives rise to two bands, a $K^\pi = 1^-$ and a $K^\pi = 2^-$ band, and since the $K^\pi = 1^-$ band is expected lower in energy due to the Gallagher-Moszkowski rule, it is assigned at 26 keV. The predicted (d,t) strength is $S_1 = 0.084$, $S_3 = 0.012$, which is in excellent agreement the observed values of $S_1 = 0.089$ and no $l = 3$ strength found. The calculated (^{3}He,d) cross section is 0.54 μb/sr, which is much less then the value of 3.7 μb/sr observed.

The 2^- member of the $K^\pi = 1^-$ band would be expected to be populated in the (d,t) reactions with $S_1 = 0.119$, $S_3 = 0.088$, and to have (^{3}He,d) cross section of 1.0 μb/sr. The only possible candidate in the experimental spectrum below 170 keV would be one of the levels at 84 keV. The peak at 84 keV, which is believed due to a doublet, is populated with $S_1 = 0.224 \pm 0.014$, $S_3 = 0.224 \pm 0.059$ in the (d,t) reaction, and has a (^{3}He,d) cross section of 35 ± 4 μb/sr. The similarity of the (d,t) strengths of the 84 keV peak in ^{190}Ir to those of the peak at 116.3 keV in ^{192}Ir supports the assignment of the spin 2 member of the $K^\pi = 1^-$ band to one of the levels in the doublet. The other member of the doublet is believed due to the the $K^\pi = 3^-$ band head discussed above. The total predicted (d,t) strength and (^{3}He,d) cross section to the doublet is $S_1 = 0.255$, $S_3 = 0.202$, and 23 μb/sr, respectively. This is in excellent agreement with the observations considering that there are other 2^- and 3^- states within a few hundred keV that are not included in the calculations, and coupling with these states could change the strengths.

The $K^\pi = 2^-$ band head of the $\frac{3}{2}^+[402]_\pi + \frac{1}{2}^-[510]_\nu$ configuration is expected to lie about 100 keV above the $K^\pi = 1^-$ band head. A possible candidate for the $K^\pi = 2^-$ band head is the level at approximately 220 keV which is part of a strongly populated doublet in the (d,t) reaction, and was obscured in the single-proton transfer reactions as it was not resolved from the much stronger peak due to the level at 225 keV. The predicted (d,t) strengths are $S_1 = 0.121$ and $S_3 = 0.015$, which is approximately 60% of the observed $l = 1$ population of the doublet but only 5% of the $l = 3$ strength. The calculated (^{3}He,d) cross section is 1.7 μb/sr, which is consistent with the observation that the level is obscured by the much stronger peak at 225 keV.

The $\frac{1}{2}^+[400]_\pi \pm \frac{3}{2}^-[512]_\nu$ Configurations

Configurations involving the $\frac{1}{2}^+[400]$ proton orbital should be weakly populated in the (d,t) reactions unless there is significant mixing with states involving the $\frac{3}{2}^+[402]$ proton orbital. In the single-proton transfer reactions, strongly populated

levels probably involve the $\frac{3}{2}^-[512]_\nu$ orbital, since it is the dominant configuration in the target ground state. There are several levels observed that are populated weakly in the (d,t) reactions and strongly in the single-proton transfer reactions, and these have been assigned as the $\frac{1}{2}^+[400]_\pi \pm \frac{3}{2}^-[512]_\nu$ configurations.

The state observed at 144.0 keV is assigned as the $K^\pi = 1^-$ band head, with the 2^- member assigned at 284.9 keV. Both of these levels were populated relatively weakly in the (d,t) reactions, and strongly in the single-proton transfer reactions. The observed (d,t) strengths are much stronger than predicted. However, the calculations are sensitive to the placement of other 2^- levels. The (^{3}He,d) cross sections are reproduced quite well. It is possible that additional mixings not accounted for in the present work could increase the (d,t) strengths while not seriously affecting the single-proton transfer cross sections.

The $K^\pi = 2^-$ band head is expected to lie higher in energy than the $K^\pi = 1^-$ band head from the Gallagher-Moszkowski rule. The expected splitting is on the order of 100 keV or so, and thus the $K^\pi = 2^-$ band head should be at an energy of approximately 240 keV. Calculations performed with the band head placed at this energy indicate that the (d,t) strengths may become quite large, with $S_1 = 0.075$ and $S_3 = 0.021$, due to mixings with the $\frac{3}{2}^+[402]_\pi + \frac{1}{2}^-[510]_\nu$ configuration discussed above. A possible candidate for the $K^\pi = 2^-$ band head is the level at 225 keV, which appears to be populated strongly in the single-proton transfer reactions, and forms part of a strongly populated doublet with a level at 220 keV in the (d,t) reactions. The total (d,t) strength predicted to the doublet is $S_1 = 0.196$ and $S_3 = 0.036$, which agrees well with the total $l = 1$ strength but seriously underestimates the $l = 3$ strength. The (^{3}He,d) cross section is predicted to be 8.1 μb/sr which is in good agreement with the observed cross section of 13.4 μb/sr, especially when considering that the level at 220 keV, which is not resolved, is predicted to contribute 1.7 μb/sr.

Other Configurations

Information can be obtained on other configurations that are not populated in the proton transfer reactions. For instance, the level at a relative excitation energy of 0 keV was populated in the (d,t) reactions with an $l = 3$ transition of strength $S_3 = 0.100 \pm 0.008$, and thus the spin values can range from 1^- to 5^-. An upper limit of $S_1 < 0.004$ was determined for this level. This state may be similar in nature to the level at 66.3 keV in ^{192}Ir, which was populated with a pure $l = 3$ transition of strength $S_3 = 0.216$. The spin of the 66.3 keV level in ^{192}Ir was argued to be 4^-, and it is suggested that this may also be the spin of the 0 keV level in ^{190}Ir. If this is indeed the case, the only configurations available to explain the strength would be a mixture of the $\frac{1}{2}^+[400]_\pi + \frac{7}{2}^-[503]_\nu$ and $\frac{3}{2}^+[402]_\pi + \frac{5}{2}^-[503]_\nu$ configurations. However, the degree of mixing required can not be explained by the coupling mechanisms accounted for in this work.

The level at 38.1 keV can be assigned as the $\frac{3}{2}^+[402]_\pi \pm \frac{9}{2}^-[505]_\nu$ band since it was not populated in the single-proton transfer reactions, and was populated in the (d,t) experiments with a pure $l = 5$ transition. It is uncertain whether this is the $K = 3^-$ or $K = 6^-$ band head, since it is expected that the $K = 6^-$ band head is lower in energy. In ^{192}Ir the state populated at 83.8 keV is the $K = 3^-$ band head, with the $K = 6^-$ band head higher than 161 keV. The $l = 5$ strength observed to the level at 38.1 keV in ^{190}Ir is an excellent match to the strength expected for the $K = 3^-$ band head, and thus, as in ^{192}Ir, the assignment $I^\pi = 3^-$ of the $-\frac{3}{2}^+[402]_\pi + \frac{9}{2}^-[505]_\nu$ configuration is adopted.

5.5.4 States in ^{194}Ir

At the present time it is very difficult to make assignments of bands in ^{194}Ir. This is due to two main reasons.

1. The lack of experimental data. A large collaboration[61] similar to that which worked on ^{192}Ir has been studying ^{194}Ir, but their results are

not yet available. Some of the spins for low-lying states have been determined [61], but many others are only tentative.

2. The nuclear shape is uncertain. ^{193}Os appears to have a prolate shape, whereas ^{195}Pt has an oblate shape. It is possible that many states in ^{194}Ir are built on an oblate core, and that there are coexisting prolate configurations.

The Nilsson model interpretation of states in ^{193}Os populated with single-neutron transfer reactions experiences some difficulty. Some of the largest peaks observed in the spectra cannot be assigned Nilsson configurations. For instance, a peak at 234 keV in the ^{192}Os(d,p) spectrum has the second largest cross section observed, and has been tentatively assigned[78] as a spin $\frac{3}{2}$ triaxial state. Single-neutron transfer studies[81] of ^{195}Pt demonstrated that oblate shapes with large γ-fluctuations are needed to explain the levels observed.

Nilsson calculations performed with a prolate shape can reproduce the spectroscopic strengths for only a few states in ^{194}Ir. Other states have much different spectroscopic strengths than predicted or require that the Gallagher-Moszkowski rule be broken.

The ground state has $I^\pi = 1^-$ and a similar (d,p) population to that of the 1^- state at 56.7 keV in ^{192}Ir. Therefore a logical assignment is the $\frac{3}{2}^+[402]_\pi - \frac{1}{2}^-[510]_\nu$ configuration, with the 2^- member of the band assigned at 84.3 keV. The $K^\pi = 2^-$ band head may be located at 112.2 keV, since the expected Gallagher-Moszkowski splitting is on the order of 100 keV.

The $K^\pi = 0^-$ band head based on the $\frac{3}{2}^+[402]_\pi - \frac{3}{2}^-[512]_\nu$ configuration may be assigned to the state at 43.2 keV, since it has a similar (d,p) strength as the 0^- state at 128.3 keV in ^{192}Ir. The 1^- member of the band can be located at 82.3 keV. However, there are several problems associated with this interpretation. For instance, in ^{190,192}Ir, the 1^- member of the $K^\pi = 0^-$ band was assigned lower in energy than the 0^- member. An alternative assignment for the 1^- member of the $K^\pi = 0^-$ band would be the ground state, as this would preserve the Newby

shift. The 2^- state at 84.3 keV would then be assigned as a band head, since it would have too small a rotational parameter to be part of the $K^\pi = 0^-$ band. The state at 112.2 keV could be assigned as the 2^- member of the $K^\pi = 0^-$ band. Therefore, none of the proposed assignments are unique, and until more properties of these states are known, it is impossible to say which of the above interpretations is correct. The second problem associated with the interpretation of the 0^- state at 43.2 keV is that the $K^\pi = 3^-$ band head is expected to be lower in energy than the $K^\pi = 0^-$ band. However, the lowest known 3^- state occurs at 148.9 keV, which would violate the Gallagher-Moszkowski rule by $\sim$ 100 keV, and is populated with a strong $l = 3$ transition in the (d,p) reactions. The $K^\pi = 3^-$ band head is expected to be populated with both $l = 1$ and $l = 3$ transitions of almost equal strength.

The difficulties and ambiguities outlined above continue for other states in ^{194}Ir thus making comparisons with the Nilsson model assuming a prolate shape practically impossible.

Spectroscopic strength calculations for ^{194}Ir assuming an oblate core cannot be performed at the present time. The target of ^{193}Ir has a prolate shape, and therefore, when deriving expressions for the (d,t) spectroscopic strength, the integration over the proton configurations does not yield 1 (as in the case of the final nucleus having the same shape as the target) but will result in a sum over the components in the wave function. The assumption that the proton wave function does not change significantly is not a valid one, and ignoring the effect would alter the calculations much more than mixed target ground states, or, in many cases, Coriolis mixing. Also, it is not clear that the transfer operator would retain its simple form. Since the core changes shape, the effect is probably more than just altering the wave function of the proton, the transfer operator itself may no longer have a simple form.

5.6. χ^2_ν Tests for the Transfer Strengths

In the IBFFM comparison with the experimental data, a total of 14 renormalization parameters were applied to the spectroscopic strengths obtained from Paar and Brant[70]. These parameters were determined from an examination of the strength distribution for each j-transfer to final states with angular momentum I_f. In view of the renormalization, it is necessary to establish goodness-of-fit criteria to test the significance of the ability of the models to reproduce the data. The goodness-of-fit test used in this work is the χ^2_ν defined in ref.[48], where

$$\chi^2_\nu = \frac{1}{\nu}\sum_i \frac{(S_i - S_{th})^2}{\sigma_i^2} \qquad (5.6.1)$$

where ν is the number of degrees of freedom. The test was performed for each reaction where the results could be interpretated in terms of the IBFFM. As a comparison, the test was also performed for the Nilsson model interpretation of ^{192}Ir.

In order to have a meaningful χ^2_ν value, the uncertainties σ_i must be determined for each strength, and should include the statistical uncertainty as determined from the least-squares fitting procedure, as well as the systematic uncertainty introduced by the DWBA calculation. For states that have strengths that are 5–10% of the largest strength observed in the reaction, the reaction mechanism may have significant contributions from mulitstep processes which are not described by the DWBA calculations. For strong transitions it has been found that the reproducibility of relative strengths is typically within 5–10%. Therefore, a reasonable estimate of the systematic uncertainty is approximately 10% of the largest strength observed in the reaction[48]. The uncertainty for each data point was $\sigma_i = \sqrt{\sigma^2_{i_{fit}} + (0.1S^g_l)^2}$ where S^g_l is the largest strength observed in the reaction for the particular value of l.

The number of degrees of freedom used in the test is the number of strengths minus the number of parameters. The spectroscopic strengths calculated with the IBFFM depend on the wave function for the state and the renormalization

constants, but all of the model parameters were fixed by fitting neighbouring nuclei or determined by the energy and static properties of the lowest-lying positive and negative-parity state. Therefore, the only parameters that were fitted to the strengths were the renormalization parameters in Table 5.3.2, and these were determined from only the (d,t) strengths into ^{192}Ir. Since the theoretical states were allowed to be shifted in energy to match the experimental levels, this was considered as a "parameter" that was fitted to the data. For the IBFFM, all states were included in the χ^2_ν tests up to an energy of 331.7 keV for the ^{191}Ir(d,p) and ^{193}Ir(d,t) reactions, and 312 keV for the ^{193}Ir(d,p) reaction. The energy cutoff was used because above these energies, there were many states that were not interpretated in the model. It should be noted that two levels in ^{192}Ir populated with $l = 5$ transitions, at 83.8 and 278.2 keV, which were not interpretated in the model, were included in the χ^2_ν test. As well, for the interpretated states all the theoretical strengths were included regardless of whether strength was observed for that particular l-value. Included in the χ^2_ν test for the Nilsson model were all states which were interpretated, including the states at 66.3 and 256.7 keV. No constants in the Nilsson model were allowed to vary in order to get a better fit. However, as with the IBFFM, the predicted states were allowed to be shifted in energy to correspond to the observed states, and thus the number of fitted parameters is considered to be 1. The results of the χ^2_ν test for each reaction and model are listed in Table 5.6.1. As can be seen, the χ^2_ν values are large for both models, implying that neither model gives an acceptable fit. The values for the Nilsson model χ^2_ν would increase greatly if all the states below 300 keV which were not interpretated in the model were also included in the calculation.

One drawback in the IBFFM calculations is the absence of the $f_{\frac{7}{2}}$ neutron orbitals, even though in the neighbouring odd-Pt isotopes, significant amounts of $j = \frac{7}{2}$ strength were observed[48]. In the χ^2_ν test for the present case, states populated with $j = \frac{7}{2}, l = 3$ transfer should not be included, but at the present time there is

Table 5.6.1: Results of χ^2_ν test for ^{192,194}Ir

Reaction	No. of data points[a])	No. of fitted parameters	ν	χ^2_ν
IBFFM				
^{193}Ir(d,t)	36	10	26	23
^{191}Ir(d,p)	30	1	29	5.6
^{193}Ir(d,p)	23	1	22	5.0
Nilsson Model				
^{193}Ir(d,t)	21	1	20	2.9
^{191}Ir(d,p)	19	1	18	4.2

[a]) Includes upper limits to on experimental strengths

no available experimental information to distinguish states populated with $j = \frac{5}{2}$ or $j = \frac{7}{2}$ from each other.

Chapter 6.
Conclusions

The experiments performed in the present work have provided many new results concerning the structure of odd-odd iridium nuclei. The most important results stem from the precision that was obtained in the extraction of spectroscopic strengths from the angular distributions. This was due to two main factors. Firstly, the quality of the data was high. The resolutions obtained in the reactions were impressive. In the (d,t) reactions, for instance, the FWHM of 4.5 keV obtained for some spectra corresponds to ~1 part in 3700 for $\Delta E/E$ or ~1 part in 7400 for $\Delta p/p$ where p is the particle momentum. Recall that in Chapter 3 it was stated that for a 1 mm wide beam spot on target, the value of $p/\Delta p$ could obtain a value of 5000. The beam spot widths obtained in the present work were less than 1 mm, but the value of $\Delta p/p$ for the (d,t) reaction is probably close to the theoretical limit. These impressive resolutions were obtained for nearly all spectra for the (d,t) angular distributions. Furthermore, large numbers of angles were included in the angular distributions, thus yielding a highly reliable and precise set of data. The second important factor was the analysis procedure. Instead of quoting cross sections and merely noting the dominant component in the angular distribution, a least squares procedure was used to determine the spectroscopic factors for one, and in many cases, two l-components.

Large numbers of levels were observed with the single-nucleon transfer reactions. In the single-neutron transfer experiments, all the levels observed had negative parity, and most of the angular distributions could be fitted with an $l = 1$ and/or an $l = 3$ component. However, in both ^{190}Ir and ^{192}Ir, a low-lying level populated with an $l = 5$ transition was observed. In the single-proton transfer experiments into ^{190}Ir, ratios of (^{3}He,d) and (α,t) cross sections provided information regarding the transferred l-value, and the dominant components transferred were $l = 0$ and $l = 2$. A large number of levels appeared to be populated in both the

single-proton and single-neutron transfer experiments into ^{190}Ir, indicating a large amount of configuration mixing in this nucleus.

For the first time in medium to heavy nuclei, the multi-dimensional scaling method has been employed on the branching intensities of γ-rays. The MDS method has been demonstrated to be sensitive to spin in the light mass regions. Using the intensities published by Kern et al[57] for ^{192}Ir, the method appears to have success in separating out the various spins. All of the known spin 1, 2, and 3 states were separated in the similarity maps from each other, and states with unknown spin were assigned as belonging to one of the clusters. However, the method is sensitive to the correct placement of the γ-rays originating from each state, and it is possible that some of the γ-transitions placed by Kern et al [57] are incorrect.

The results of the experiments have been compared with three different models. Two of these models, the IBFFM and the SUSY model, are based on extensions of the IBM. The third model was a simple Nilsson model approach.

The IBFFM calculations for ^{192}Ir and ^{194}Ir were performed by Paar and Brant, and coupled two fermions to an $SO(6)$ core of the IBM. The calculations were performed numerically since no limiting symmetry, other than that of the core, was employed. The results of the calculations predict that the wave functions are very configuration mixed, with a large number of levels observed in single-neutron transfer that are populated with both $l = 1$ and $l = 3$ transitions. This was observed, and the number of states lying below 500 keV in excitation energy was approximately reproduced. However, while this is an encouraging result, there remain many problems with the IBFFM interpretation. The predicted energies of the first 3^- and 4^- states in ^{192}Ir are predicted are much too high. The 3^- state at 84.3 keV in ^{192}Ir was observed to be populated with a strong $l = 5$ transition, but no 3^- states in the IBFFM calculation are predicted to have significant $l = 5$ strength. In fact, it is a general trend that the calculations have trouble reproducing the spectroscopic strengths to individual states. This was clearly illustrated in the previous chapter in Figure 5.3.7, Figure 5.3.8, Figure 5.3.9, Figure 5.3.10 for ^{192}Ir.

The calculations for ^{194}Ir appear to be more successful in reproducing the energies and strengths of individual levels. However, the amount of $l = 3$ strength is greatly underestimated.

The $U_\nu(6/12)\otimes U_\pi(6/4)$ supersymmetry prediction for ^{194}Ir cannot be tested in the present work since the expressions for single-nucleon transfer in which the number of bosons changes, as in the (d,p) reactions of this study, have not been worked out. However, expressions are given for the spectroscopic strengths for (d,t) reactions, and thus the model can be tested with the experimental data for ^{192}Ir. The particular supersymmetry limit employed assumed that the core has $SO(6)$ symmetry, but this may not be the case for ^{192}Ir. The supermultiplet containing ^{192}Ir also contains ^{190,191}Os and ^{191}Ir. It has been pointed out by Jolie that ^{190}Os is in a transitional region between the $SU(3)$ limit and the $SO(6)$ limit, and thus it would be very surprising if the extended supersymmetry gave a good description for ^{192}Ir. As was demonstrated in the previous chapter, the extended supersymmetry model does not provide a good description for ^{192}Ir, and thus the quartet of ^{190,191}Os and ^{191,192}Ir is not a candidate for ESUSY.

The Nilsson model calculations show some promising results, but there is an indication for the need of a more complicated treatment. The neutron orbitals expected to be populated at low-excitation energies, namely the $\frac{1}{2}^-[510]_\nu$ and the $\frac{3}{2}^-[512]_\nu$ orbitals, have very similar spectroscopic strengths, especially when the effects of Coriolis mixing are taken into account. In ^{192}Ir, there are many levels populated in the single-neutron transfer reactions which have strengths that would be a suitable match to the predicted strengths for the two orbitals mentioned above. The problem of the identification of rotational bands whose neutron part is based on these orbitals is furthermore compounded by the fact that the spin > 2 members were not identified. In ^{190}Ir, the results of the proton transfer experiment are very useful in the identification of configurations, since in ^{189}Os the $\frac{3}{2}^-[512]$ neutron

forms the ground state. The success of the calculations in reproducing the single-proton transfer cross sections and the (d,t) spectroscopic strengths for configurations that were assigned is very impressive.

The $-\frac{3}{2}^+[402]_\pi + \frac{9}{2}^-[505]_\nu$ configuration has been identified in both ^{190}Ir and ^{192}Ir at low excitation energies. Interestingly, the $K^\pi = 3^-$ band comes lower in energy than the $K^\pi = 6^-$ band, and thus the Gallagher-Moszkowski rule is broken for this configuration. The results of the present calculations which take into account the Coriolis and particle-particle coupling, cannot reproduce this. A strong $l = 3$ transition at 66.3 keV in ^{192}Ir and at 0 keV relative excitation energy in ^{190}Ir have been assigned $I^\pi = 4^-$. These levels are very interesting since in the simple Nilsson model only a mixture of the $\frac{3}{2}^+[402_\pi + \frac{5}{2}^-[503]_\nu$ and $\frac{1}{2}^+[400]_\pi + \frac{7}{2}^-[503]_\nu$ band heads could explain the strength. However, the mixing between these two configurations is expected to be quite small, and the calculations of the present work cannot account for the degree of mixing required to explain the spectroscopic strengths.

Configurations based on the $\frac{1}{2}^+[400]$ proton and the $\frac{1}{2}^-[510]$ and $\frac{3}{2}^-[512]$ neutron orbitals have been tentatively identified. The population of configurations in single-neutron transfer reactions involving the $\frac{1}{2}^+[400]_\pi$ orbital occurs because of Coriolis mixing in both the target and the final states. The formalism needed to deal with mixed target ground states was developed. It was found that a proper treatment of Coriolis mixing in the final states has more effect on the single-neutron transfer strengths than mixed target ground states. The single-proton transfer cross sections into ^{190}Ir show the effects of the relatively large amplitude (0.3) of the $\frac{1}{2}^-[510]_\nu$ orbital mixed with the $\frac{3}{2}^-[512]_\nu$ orbital in the ^{189}Os ground state. However, more information regarding ^{190}Ir needs to be obtained.

It is possible that a more sophisticated treatment of levels within the Nilsson model would better reproduce the levels observed in the reactions. If one assumes a constant deformation, the number of available 1^- and 2^- states are depleted before all of the observed 1^- and 2^- levels can be accounted for. If the deformation changes with excitation energy, this might account for some of the complexity of the level

scheme since a new degree of freedom is introduced. However, at the present time there is no specific information regarding the deformation of individual levels.

Clearly more work needs to be performed on the odd-odd iridium isotopes. On the experimental side, more level spins must be determined. It would also be useful to have knowledge of the nuclei at higher spin, since the band structure may be illuminated in this way. On the theoretical side, a proper treatment of odd-odd nuclei in the transitional region within the context of the geometrical model would be useful, and would provide guidance as to the complex nature of states. This work would be very difficult, and a complete set of experimental data would have to be in place in order to justify the huge theoretical effort needed. It is the hope of the author that the present work will form an essential part of the experimental knowledge on odd-odd iridium isotopes.

Appendix I.
Effects of Mixed Target Ground States

In this appendix, the formulas for the population of a rotational band member in an odd-odd final nucleus by single-nucleon transfer from an odd nucleus with a mixed ground state configuration is derived. These expressions have never appeared in the literature, although similar expressions for the case where the final states are in an even-even nucleus were given some time ago by Thompson et al[84].

The cross section is defined as

$$\frac{d\sigma}{d\Omega} = \sum_{jl} S_{jl}\phi_l \qquad (I.1)$$

where I_i is the target spin, and I_f is the final nuclear spin. The spectroscopic strength is

$$S_{jl} = \frac{(2I_f+1)}{(2I_i+1)} \mid \beta_{jl}|^2 \qquad (I.2)$$

where

$$\beta_{jl} = \sum_{m,M_i} (jmI_iM_i|I_fM_f) \langle \Psi_{I_fM_f}|T^{\dagger}_{jlm}|\Psi_{I_iM_i}\rangle \qquad (I.3)$$

for stripping reactions, and

$$\beta_{jl} = \sum_{m,M_i} (-1)^{j-m} (j-mI_iM_i|I_fM_f) \langle \Psi_{I_fM_f}|T_{jlm}|\Psi_{I_iM_i}\rangle \qquad (I.4)$$

for pickup reactions. The $T^{\dagger}_{jlm}$ and T_{jlm} operators are the creation and annihilation operators for a nucleon in an orbit with quantum numbers jlm. These refer to quantities for the transferred particle.

The wave function for the target, $|\Psi_{I_iM_i}\rangle$ is assumed to have various Nilsson components such that

$$|\Psi_{I_iM_i}\rangle = \sum_{\xi} a_{\xi} \left(\frac{2I_i+1}{16\pi^2}\right)^{\frac{1}{2}} \left[D^{I_i*}_{M_iK_{\xi}}(\theta_j)\,|\chi_{K_{\xi}}\rangle + (-1)^{I_i-\frac{1}{2}}(\pi_{\xi})\,\mathcal{D}^{I_i*}_{M_i-K_{\xi}}(\theta_j)\,|\chi_{-K_{\xi}}\rangle\right] \qquad (I.5)$$

where π_ξ is the parity of the odd nucleon, and the rotation axis is taken to be perpendicular to the intrinsic $\hat{z}$-axis. The sum over ξ is performed over the various Nilsson orbitals, with amplitude a_ξ, that are present in the ground state. It should be noted that the target wave function is assumed to have no admixture of β or γ phonons present. These assumptions will also be made for the final states in the residual nucleus. Thus, the final state wave function will be written as

$$|\Psi_{I_f M_f}\rangle = \sum_{\delta_\pi \delta_\nu} a_{\delta_\pi \delta_\nu} \left(\frac{2I_f+1}{16\pi^2}\right)^{\frac{1}{2}} \left[\mathcal{D}^{I_f *}_{M_f K_\delta}(\theta_j)\,|\chi_{\Omega_{\delta_\pi}}\rangle|\chi_{\Omega_{\delta_\nu}}\rangle \right. \\ \left. - (-1)^{I_f}(\pi_{\delta_\pi})(\pi_{\delta_\nu})\,\mathcal{D}^{I_f *}_{M_f -K_\delta}(\theta_j)\,|\chi_{-\Omega_{\delta_\pi}}\rangle|\chi_{-\Omega_{\delta_\nu}}\rangle\right] \tag{I.6}$$

where is sum is over the two-quasiparticle components, $\delta_\pi \delta_\nu$ with amplitude $a_{\delta_\pi \delta_\nu}$ present in the wave function.

The single-particle wave functions are in the intrinsic frame, therefore the creation and annihilation operators should also be transformed into this frame. The transformation is accomplished by applying the rotational matrices to the operators as would be done for any other tensor of rank m. Therefore,

$$T^\dagger_{jlm} = \sum_\Omega \mathcal{D}^{j *}_{m\Omega}(\theta_j)\, T^{\dagger\prime}_{jl\Omega} \tag{I.7a}$$

$$T_{jlm} = \sum_\Omega \mathcal{D}^{j}_{m\Omega}(\theta_j)\, T'_{jl\Omega} \tag{I.7b}$$

where $T^{\dagger\prime}$, T' are the creation and annihilation operators in the intrinsic frame. To introduce the Nilsson model, the basis must be changed from the spherical jlm basis, i.e.,

$$T^{\dagger\prime}_{jl\Omega} = \sum_\nu C^{\nu\Omega}_{jl} T^{\dagger\prime}_{\nu\Omega} \tag{I.8a}$$

$$T'_{jl\Omega} = \sum_\nu C^{\nu\Omega}_{jl} T'_{\nu\Omega} \tag{I.8b}$$

where $C^{\nu\Omega}_{jl}$ are the expansion coefficients for the Nilsson wave function onto the spherical basis, and the summation is performed over all Nilsson configurations.

At this point it is convenient to make a Bogolyubov-Valatin transformation to the quasiparticle basis

$$T^{\dagger\prime}_{\nu\Omega} = U_{\nu\Omega}\alpha^{\dagger\prime}_{\nu\Omega} - V_{\overline{\nu\Omega}}\alpha^{\prime}_{\overline{\nu\Omega}} \tag{I.9a}$$

$$T^{\prime}_{\nu\Omega} = U_{\nu\Omega}\alpha^{\prime}_{\nu\Omega} - V_{\overline{\nu\Omega}}\alpha^{\dagger\prime}_{\overline{\nu\Omega}} \tag{I.9b}$$

where the bar over the quantities $\nu\Omega$ means that these are in time-reversed orbits, and $\alpha^{\prime}$ and $\alpha^{\dagger\prime}$ are the quasiparticle creation and annihilation operators. It is possible to express the time-reversed operators in terms of the forward projecting operators, and the relations are

$$\alpha^{\dagger\prime}_{\overline{\nu\Omega}} = (-1)^{\Omega-\frac{1}{2}}\,\alpha^{\dagger\prime}_{\nu-\Omega} \tag{I.10a}$$

$$\alpha^{\prime}_{\overline{\nu\Omega}} = (-1)^{\Omega-\frac{1}{2}}\,\alpha^{\prime}_{\nu-\Omega} \tag{I.10b}$$

with the condition that

$$V_{\overline{\nu\Omega}} = -V_{\nu\Omega} \tag{I.11}$$

Therefore, the transfer operators become

$$T^{\dagger}_{jlm} = \sum_{\Omega} \mathcal{D}^{j\,*}_{m\Omega}(\theta_j) \sum_{\nu} C^{\nu\Omega}_{jl}\left[U_{\nu\Omega}\alpha^{\dagger\prime}_{\nu\Omega} + V_{\nu\Omega}(-1)^{\Omega-\frac{1}{2}}\,\alpha^{\prime}_{\nu-\Omega}\right] \tag{I.12a}$$

$$T_{jlm} = \sum_{\Omega} \mathcal{D}^{j}_{m\Omega}(\theta_j) \sum_{\nu} C^{\nu\Omega}_{jl}\left[U_{\nu\Omega}\alpha^{\prime}_{\nu\Omega} + V_{\nu\Omega}(-1)^{\Omega-\frac{1}{2}}\,\alpha^{\dagger\prime}_{\nu-\Omega}\right] \tag{I.12b}$$

The Nilsson wave functions for the target nucleus can be written in terms of a creation operator acting on the quasiparticle vacuum,

$$|\chi_{K_\xi}\rangle = \alpha^{\dagger\prime}_{\xi K_\xi}|0\rangle \tag{I.13}$$

and similarly for the wave functions for the final nuclear state.

If we first consider pickup reactions, i.e. (d,t) reactions, then the expression for the spectroscopic amplitude becomes

$$\beta_{jl} = \sum_{m_i M_i} (-1)^{j-m} \left(j - m I_i M_i | I_f M_f\right) \langle 0 | \Bigg[\sum_{\delta_\pi \delta_\nu} a_{\delta_\pi \delta_\nu} \left(\frac{2I_f+1}{16\pi^2}\right)^{\frac{1}{2}} \times \left[\mathcal{D}^{I_f}_{M_f K_\delta}(\theta_j)\, \alpha^{I}_{\Omega_{\delta_\pi}} \alpha^{I}_{\Omega_{\delta_\nu}} - (-1)^{I_f} (\pi_{\delta_\pi})(\pi_{\delta_\nu})\, \mathcal{D}^{I_f}_{M_f -K_\delta}(\theta_j)\, \alpha^{I}_{-\Omega_{\delta_\pi}} \alpha^{I}_{-\Omega_{\delta_\nu}} \right] \Bigg] \times \left[\sum_{\Omega} \mathcal{D}^{j}_{m\Omega}(\theta_j) \sum_{\nu} C^{\nu\Omega}_{jl} \left[U_{\nu\Omega} \alpha^{I}_{\nu\Omega} + V_{\nu\Omega} (-1)^{\Omega - \frac{1}{2}} \alpha^{\dagger I}_{\nu -\Omega} \right] \right] \times \left[\sum_{\xi} a_\xi \left(\frac{2I_i+1}{16\pi^2}\right)^{\frac{1}{2}} \left[\mathcal{D}^{I_i *}_{M_i K_\xi}(\theta_j)\, \alpha^{\dagger I}_{\xi K_\xi} + (-1)^{I_i - \frac{1}{2}} (\pi_\xi)\, \mathcal{D}^{I_i *}_{M_i -K_\xi}(\theta_j)\, \alpha^{\dagger I}_{\xi -K_\xi} \right] \right] |0\rangle \tag{I.14}$$

When evaluating the above expression, terms involving three annihilation operators disappear since there must be the same number of creation as there are annihilation operators. Therefore the term $U_{\nu\Omega}\alpha^{I}_{\nu\Omega}$ disappears. The remaining terms involve

$$\alpha^{I}_{\Omega_{\delta_\pi}} \alpha^{I}_{\Omega_{\delta_\nu}} V_{\nu\Omega} \alpha^{\dagger I}_{\nu -\Omega} \alpha^{\dagger I}_{\xi K_\xi} \tag{I.15a}$$

$$\alpha^{I}_{-\Omega_{\delta_\pi}} \alpha^{I}_{-\Omega_{\delta_\nu}} V_{\nu\Omega} \alpha^{\dagger I}_{\nu -\Omega} \alpha^{\dagger I}_{\xi K_\xi} \tag{I.15b}$$

$$\alpha^{I}_{\Omega_{\delta_\pi}} \alpha^{I}_{\Omega_{\delta_\nu}} V_{\nu\Omega} \alpha^{\dagger I}_{\nu -\Omega} \alpha^{\dagger I}_{\xi -K_\xi} \tag{I.15c}$$

$$\alpha^{I}_{-\Omega_{\delta_\pi}} \alpha^{I}_{-\Omega_{\delta_\nu}} V_{\nu\Omega} \alpha^{\dagger I}_{\nu -\Omega} \alpha^{\dagger I}_{\xi -K_\xi} \tag{I.15d}$$

and are evaluated as follows:

$$\langle 0_\pi | \alpha^{I}_{\Omega_{\delta_\pi}} \alpha^{\dagger I}_{\xi K_\xi} | 0_\pi \rangle \langle 0_\nu | \alpha^{I}_{\Omega_{\delta_\nu}} V_{\nu\Omega} \alpha^{\dagger I}_{\nu -\Omega} | 0_\nu \rangle = V_{\nu\Omega} \delta_{\delta_\pi \xi} \delta_{\Omega_{\delta_\pi} K_\xi} \delta_{\delta_\nu \nu} \delta_{\Omega_{\delta_\nu} -\Omega} \tag{I.16a}$$

$$\langle 0_\pi | \alpha^{I}_{-\Omega_{\delta_\pi}} \alpha^{\dagger I}_{\xi K_\xi} | 0_\pi \rangle \langle 0_\nu | \alpha^{I}_{-\Omega_{\delta_\nu}} V_{\nu\Omega} \alpha^{\dagger I}_{\nu -\Omega} | 0_\nu \rangle = V_{\nu\Omega} \delta_{\delta_\pi \xi} \delta_{-\Omega_{\delta_\pi} K_\xi} \delta_{\delta_\nu \nu} \delta_{-\Omega_{\delta_\nu} -\Omega} \tag{I.16b}$$

$$\langle 0_\pi | \alpha^{I}_{\Omega_{\delta_\pi}} \alpha^{\dagger I}_{\xi -K_\xi} | 0_\pi \rangle \langle 0_\nu | \alpha^{I}_{\Omega_{\delta_\nu}} V_{\nu\Omega} \alpha^{\dagger I}_{\nu -\Omega} | 0_\nu \rangle = V_{\nu\Omega} \delta_{\delta_\pi \xi} \delta_{\Omega_{\delta_\pi} -K_\xi} \delta_{\delta_\nu \nu} \delta_{\Omega_{\delta_\nu} -\Omega} \tag{I.16c}$$

$$\langle 0_\pi | \alpha^{I}_{-\Omega_{\delta_\pi}} \alpha^{\dagger I}_{\xi -K_\xi} | 0_\pi \rangle \langle 0_\nu | \alpha^{I}_{-\Omega_{\delta_\nu}} V_{\nu\Omega} \alpha^{\dagger I}_{\nu -\Omega} | 0_\nu \rangle = V_{\nu\Omega} \delta_{\delta_\pi \xi} \delta_{-\Omega_{\delta_\pi} -K_\xi} \delta_{\delta_\nu \nu} \delta_{-\Omega_{\delta_\nu} -\Omega} \tag{I.16d}$$

where δ is a Kronecker delta function. There are also integrals involving the products of three rotational matrices, and these are evaluated as follows:

$$\int d\theta_j \mathcal{D}^{I_f}_{M_f K_\delta} \mathcal{D}^{j}_{m\Omega} \mathcal{D}^{I_i *}_{M_i K_\xi} =$$

$$(-1)^{M_i+M_f-K_\xi-K_\delta}\frac{8\pi^2}{2I_f+1}\left(I_i-M_ijm|I_f-M_f\right)\left(I_i-K_\xi j\Omega|I_f-K_\delta\right) \quad (I.17a)$$

$$\int d\theta_j \mathcal{D}^{I_f}_{M_f-K_\delta}\mathcal{D}^{j}_{m\Omega}\mathcal{D}^{I_i*}_{M_iK_\xi} =$$

$$(-1)^{M_i+M_f-K_\xi+K_\delta}\frac{8\pi^2}{2I_f+1}\left(I_i-M_ijm|I_f-M_f\right)\left(I_i-K_\xi j\Omega|I_fK_\delta\right) \quad (I.17b)$$

$$\int d\theta_j \mathcal{D}^{I_f}_{M_fK_\delta}\mathcal{D}^{j}_{m\Omega}\mathcal{D}^{I_i*}_{M_i-K_\xi} =$$

$$(-1)^{M_i+M_f+K_\xi-K_\delta}\frac{8\pi^2}{2I_f+1}\left(I_i-M_ijm|I_f-M_f\right)\left(I_iK_\xi j\Omega|I_f-K_\delta\right) \quad (I.17c)$$

$$\int d\theta_j \mathcal{D}^{I_f}_{M_f-K_\delta}\mathcal{D}^{j}_{m\Omega}\mathcal{D}^{I_i*}_{M_i-K_\xi} =$$

$$(-1)^{M_i+M_f+K_\xi+K_\delta}\frac{8\pi^2}{2I_f+1}\left(I_i-M_ijm|I_f-M_f\right)\left(I_iK_\xi j\Omega|I_fK_\delta\right) \quad (I.17d)$$

Collecting all terms together, the expression for the spectroscopic amplitude becomes

$$\begin{aligned}\beta_{jl} = \sum_{m,M_i}(-1)^{j-m+M_i+M_f}&\left(\frac{(2I_i+1)^{\frac{1}{2}}}{2\left(2I_f+1\right)^{\frac{1}{2}}}\right)\left(j-mI_iM_i|I_fM_f\right)\\
&\times\left(I_i-M_ijm|I_f-M_f\right)\sum_{\delta_\pi\delta_\nu}a_{\delta_\pi\delta_\nu}\sum_{\nu}\sum_{\xi}\sum_{\Omega}a_{xi}V_{\nu\Omega}C^{\nu\Omega}_{jl}\delta_{\delta_\pi\xi}\delta_{\delta_\nu\nu}(-1)^{\Omega-\frac{1}{2}}\\
&\Big[(-1)^{-K_\xi-K_\delta}\left(I_i-K_\xi j\Omega|I_f-K_\delta\right)\delta_{\Omega_{\delta_\pi}K_\xi}\delta_{\Omega_{\delta_\nu}-\Omega}\\
&-(-1)^{I_f+K_\delta-K_\xi}\left(\pi_{\delta_\pi}\right)\left(\pi_{\delta_\nu}\right)\left(I_i-K_\xi j\Omega|I_fK_\delta\right)\delta_{-\Omega_{\delta_\pi}K_\xi}\delta_{-\Omega_{\delta_\nu}-\Omega}\\
&+(-1)^{I_i-\frac{1}{2}+K_\xi-K_\delta}\left(\pi_\xi\right)\left(I_iK_\xi j\Omega|I_f-K_\delta\right)\delta_{\Omega_{\delta_\pi}-K_\xi}\delta_{\Omega_{\delta_\nu}-\Omega}\\
&-(-1)^{I_f+K_\delta+I_i-\frac{1}{2}+K_\xi}\left(\pi_{\delta_\pi}\right)\left(\pi_{\delta_\nu}\right)\left(\pi_\xi\right)\left(I_iK_\xi j\Omega|I_fK_\delta\right)\delta_{-\Omega_{\delta_\pi}-K_\xi}\delta_{-\Omega_{\delta_\nu}-\Omega}\Big]\end{aligned} \quad (I.18)$$

Some simplifications can now be made. The factor $(-1)^{-m+M_i+M_f}$ is always 1 for allowed values of m, M_i, and using

$$\begin{aligned}\left(I_i-M_ijm|I_f-M_f\right) &= (-1)^{I_i+j-I_f}\left(jmI_i-M_i|I_f-M_f\right)\\ &= \left(j-mI_iM_i|I_fM_f\right)\end{aligned} \quad (I.19)$$

then

$$\sum_{m,M_i}\left(j-mI_iM_i|I_fM_f\right)\left(j-mI_iM_i|I_fM_f\right)=1 \quad (I.20)$$

There are two distinct situations that must be dealt with. First, where $K_\delta = |K_\xi + \Omega_{\delta_\nu}|$, and secondly where $K_\delta = |K_\xi - \Omega_{\delta_\nu}|$. Considering the first case, this is satisfied only by the first and fourth terms, and the spectroscopic amplitude becomes

$$\left(\frac{2I_i+1}{2I_f+1}\right)^{\frac{1}{2}} \sum_{\xi\nu} a_{\xi\nu} a_\xi V_{\nu\Omega} C^{\nu\Omega}_{jl}(\pi_\nu)(-1)^{j+I_i-I_f} \left(I_i K_\xi j \Omega_\nu | I_f K_\delta\right) \qquad (I.21)$$

Considering the second case, this is satisfied only by the second and third terms, and the spectroscopic amplitude becomes

$$\left(\frac{2I_i+1}{2I_f+1}\right)^{\frac{1}{2}} \sum_{\xi\nu} a_{\xi\nu} a_\xi V_{\nu\Omega} C^{\nu\Omega}_{jl}(\pi_\nu)(\pi_\xi)(-1)^{j+\frac{1}{2}-I_f} \left(I_i - K_\xi j \Omega_\nu | I_f K_\delta\right) \qquad (I.22)$$

Combining these two equations together gives the desired result

$$\begin{aligned}\beta_{jl} = &\left(\frac{2I_i+1}{2I_f+1}\right)^{\frac{1}{2}} \sum_{\xi\nu} a_{\xi\nu} a_\xi U_{\nu\Omega} C^{\nu\Omega}_{jl}(\pi_\nu)(-1)^{j+I_i-I_f} \\ &\times \left[\left(I_i K_\xi j \Omega_\nu | I_f K_\delta\right) + (\pi_\xi)(-1)^{I_i-\frac{1}{2}} \left(I_i - K_\xi j \Omega_\nu | I_f K_\delta\right)\right]\end{aligned} \qquad (I.23)$$

For stripping reactions the equation for the spectroscopic amplitude becomes

$$\begin{aligned}\beta_{jl} = \sum_{m,M_i} &\left(jmI_iM_i | I_fM_f\right) \langle 0 | \left[\sum_{\delta_\pi\delta_\nu} a_{\delta_\pi\delta_\nu} \left(\frac{2I_f+1}{16\pi^2}\right)^{\frac{1}{2}} \left[\mathcal{D}^{I_f}_{M_f K_\delta}(\theta_j)\, \alpha^{\dagger}_{\Omega_{\delta_\pi}} \alpha^{\dagger}_{\Omega_{\delta_\nu}}\right.\right. \\ &\left. - (-1)^{I_f}(\pi_{\delta_\pi})(\pi_{\delta_\nu}) \mathcal{D}^{I_f}_{M_f -K_\delta}(\theta_j)\, \alpha^{\dagger}_{-\Omega_{\delta_\pi}} \alpha^{\dagger}_{-\Omega_{\delta_\nu}}\right]\Big] \\ &\left[\sum_\Omega \mathcal{D}^{j*}_{m\Omega}(\theta_j) \sum_\nu C^{\nu\Omega}_{jl}\left[U_{\nu\Omega}\alpha^{\dagger l}_{\nu\Omega} + V_{\nu\Omega}(-1)^{\Omega-\frac{1}{2}} \alpha^{l}_{\nu-\Omega}\right]\right] \\ &\left[\sum_\xi a_\xi \left(\frac{2I_i+1}{16\pi^2}\right)^{\frac{1}{2}} \left[\mathcal{D}^{I_i *}_{M_i K_\xi}(\theta_j)\, \alpha^{\dagger l}_{\xi K_\xi}\right.\right. \\ &\left.\left. + (-1)^{I_i-\frac{1}{2}}(\pi_\xi)\, \mathcal{D}^{I_i *}_{M_i -K_\xi}(\theta_j)\, \alpha^{\dagger l}_{\xi -K_\xi}\right]\right] |0\rangle\end{aligned} \qquad (I.24)$$

When evaluating the above expression, terms involving three creation operators disappear since there must be the same number of creation as there are annihilation

operators. Therefore the term $V_{\nu\Omega}\alpha^{\dagger I}_{\nu-\Omega}$ disappears. The remaining terms involve

$$\alpha^{I}_{\Omega_{\delta_\pi}}\alpha^{I}_{\Omega_{\delta_\nu}}U_{\nu\Omega}\alpha^{\dagger I}_{\nu\Omega}\alpha^{\dagger I}_{\xi K_\xi} \tag{I.25a}$$

$$\alpha^{I}_{-\Omega_{\delta_\pi}}\alpha^{I}_{-\Omega_{\delta_\nu}}U_{\nu\Omega}\alpha^{\dagger I}_{\nu\Omega}\alpha^{\dagger I}_{\xi K_\xi} \tag{I.25b}$$

$$\alpha^{I}_{\Omega_{\delta_\pi}}\alpha^{I}_{\Omega_{\delta_\nu}}U_{\nu\Omega}\alpha^{\dagger I}_{\nu\Omega}\alpha^{\dagger I}_{\xi-K_\xi} \tag{I.25c}$$

$$\alpha^{I}_{-\Omega_{\delta_\pi}}\alpha^{I}_{-\Omega_{\delta_\nu}}U_{\nu\Omega}\alpha^{\dagger I}_{\nu\Omega}\alpha^{\dagger I}_{\xi-K_\xi} \tag{I.25d}$$

and are evaluated as follows:

$$\langle 0_\pi|\alpha^{I}_{\Omega_{\delta_\pi}}\alpha^{\dagger I}_{\xi K_\xi}|0_\pi\rangle\langle 0_\nu|\alpha^{I}_{\Omega_{\delta_\nu}}U_{\nu\Omega}\alpha^{\dagger I}_{\nu\Omega}|0_\nu\rangle = U_{\nu\Omega}\delta_{\delta_\pi\xi}\delta_{\Omega_{\delta_\pi}K_\xi}\delta_{\delta_\nu\nu}\delta_{\Omega_{\delta_\nu}\Omega} \tag{I.26a}$$

$$\langle 0_\pi|\alpha^{I}_{\Omega_{\delta_\pi}}\alpha^{\dagger I}_{\xi-K_\xi}|0_\pi\rangle\langle 0_\nu|\alpha^{I}_{\Omega_{\delta_\nu}}U_{\nu\Omega}\alpha^{\dagger I}_{\nu\Omega}|0_\nu\rangle = U_{\nu\Omega}\delta_{\delta_\pi\xi}\delta_{\Omega_{\delta_\pi}-K_\xi}\delta_{\delta_\nu\nu}\delta_{\Omega_{\delta_\nu}\Omega} \tag{I.26b}$$

$$\langle 0_\pi|\alpha^{I}_{-\Omega_{\delta_\pi}}\alpha^{\dagger I}_{\xi K_\xi}|0_\pi\rangle\langle 0_\nu|\alpha^{I}_{-\Omega_{\delta_\nu}}U_{\nu\Omega}\alpha^{\dagger I}_{\nu\Omega}|0_\nu\rangle = U_{\nu\Omega}\delta_{\delta_\pi\xi}\delta_{-\Omega_{\delta_\pi}K_\xi}\delta_{\delta_\nu\nu}\delta_{-\Omega_{\delta_\nu}\Omega} \tag{I.26c}$$

$$\langle 0_\pi|\alpha^{I}_{-\Omega_{\delta_\pi}}\alpha^{\dagger I}_{\xi-K_\xi}|0_\pi\rangle\langle 0_\nu|\alpha^{I}_{-\Omega_{\delta_\nu}}U_{\nu\Omega}\alpha^{\dagger I}_{\nu\Omega}|0_\nu\rangle = U_{\nu\Omega}\delta_{\delta_\pi\xi}\delta_{-\Omega_{\delta_\pi}-K_\xi}\delta_{\delta_\nu\nu}\delta_{-\Omega_{\delta_\nu}\Omega} \tag{I.26d}$$

The integrals involving the products of three rotational matrices are evaluated as follows:

$$\int d\theta_j \mathcal{D}^{I_f}_{M_f K_\delta}\mathcal{D}^{j*}_{m\Omega}\mathcal{D}^{I_i*}_{M_i K_\xi} =$$

$$(-1)^{M_i+M_f-\Omega-K_\xi-K_\delta}\frac{8\pi^2}{2I_f+1}\left(I_i-M_i jm|I_f-M_f\right)\left(I_i-K_\xi j-\Omega|I_f-K_\delta\right) \tag{I.27a}$$

$$\int d\theta_j \mathcal{D}^{I_f}_{M_f -K_\delta}\mathcal{D}^{j*}_{m\Omega}\mathcal{D}^{I_i*}_{M_i K_\xi} =$$

$$(-1)^{M_i+M_f-\Omega-K_\xi+K_\delta}\frac{8\pi^2}{2I_f+1}\left(I_i-M_i jm|I_f-M_f\right)\left(I_i-K_\xi j-\Omega|I_f K_\delta\right) \tag{I.27b}$$

$$\int d\theta_j \mathcal{D}^{I_f}_{M_f K_\delta}\mathcal{D}^{j*}_{m\Omega}\mathcal{D}^{I_i*}_{M_i -K_\xi} =$$

$$(-1)^{M_i+M_f-\Omega+K_\xi-K_\delta}\frac{8\pi^2}{2I_f+1}\left(I_i-M_i jm|I_f-M_f\right)\left(I_i K_\xi j-\Omega|I_f-K_\delta\right) \tag{I.27c}$$

$$\int d\theta_j \mathcal{D}^{I_f}_{M_f -K_\delta}\mathcal{D}^{j*}_{m\Omega}\mathcal{D}^{I_i*}_{M_i -K_\xi} =$$

$$(-1)^{M_i+M_f-\Omega+K_\xi+K_\delta}\frac{8\pi^2}{2I_f+1}\left(I_i-M_i jm|I_f-M_f\right)\left(I_i K_\xi j-\Omega|I_f K_\delta\right) \tag{I.27d}$$

Collecting all terms together, the expression for the spectroscopic amplitude becomes

$$\begin{aligned}\beta_{jl} = \sum_{m,M_i} (-1)^{m+M_i+M_f} & \left(\frac{(2I_i+1)^{\frac{1}{2}}}{2\,(2I_f+1)^{\frac{1}{2}}}\right) (jmI_iM_i|I_fM_f) \\ & \times (I_i - M_ij - m|I_f - M_f) \sum_{\delta_\pi\delta_\nu} a_{\delta_\pi\delta_\nu} \sum_\nu \sum_\xi \sum_\Omega a_\xi U_{\nu\Omega} C_{jl}^{\nu\Omega} \delta_{\delta_\pi\xi}\delta_{\delta_\nu\nu} \\ & \Big[(-1)^{-\Omega-K_\xi-K_\delta} (I_i - K_\xi j - \Omega|I_f - K_\delta)\, \delta_{\Omega_{\delta_\pi}K_\xi}\delta_{\Omega_{\delta_\nu}-\Omega} \\ & - (-1)^{I_f-\Omega+K_\delta-K_\xi} (\pi_{\delta_\pi})(\pi_{\delta_\nu}) (I_i - K_\xi j - \Omega|I_fK_\delta)\, \delta_{-\Omega_{\delta_\pi}K_\xi}\delta_{-\Omega_{\delta_\nu}-\Omega} \\ & + (-1)^{I_i-\frac{1}{2}-\Omega+K_\xi-K_\delta} (\pi_\xi) (I_iK_\xi j - \Omega|I_f - K_\delta)\, \delta_{\Omega_{\delta_\pi}-K_\xi}\delta_{\Omega_{\delta_\nu}-\Omega} \\ & - (-1)^{I_f-\Omega_i+K_\delta+I_i-\frac{1}{2}+K_\xi} (\pi_{\delta_\pi})(\pi_{\delta_\nu})(\pi_\xi) \\ & (I_iK_\xi j - \Omega|I_fK_\delta)\, \delta_{-\Omega_{\delta_\pi}-K_\xi}\delta_{-\Omega_{\delta_\nu}-\Omega}\Big]\end{aligned} \tag{I.28}$$

The same simplifications made for the expression for pickup reactions can now be made. The factor $(-1)^{m+M_i+M_f}$ is always 1 for allowed values of m, M_i, and using

$$\begin{aligned}(I_i - M_ij - m|I_f - M_f) &= (-1)^{I_i+j-I_f} (j - mI_i - M_i|I_f - M_f) \\ &= (jmI_iM_i|I_fM_f)\end{aligned} \tag{I.29}$$

then

$$\sum_{m,M_i} (jmI_iM_i|I_fM_f)\,(jmI_iM_i|I_fM_f) = 1 \tag{I.30}$$

Again, there are two distinct situations that must be dealt with. First, where $K_\delta = |K_\xi + \Omega_{\delta_\nu}|$, and secondly where $K_\delta = |K_\xi - \Omega_{\delta_\nu}|$. Considering the first case, this is satisfied only by the first and fourth terms, and the spectroscopic amplitude becomes

$$\left(\frac{2I_i+1}{2I_f+1}\right)^{\frac{1}{2}} \sum_{\xi\nu} a_{\xi\nu}a_\xi U_{\nu\Omega} C_{jl}^{\nu\Omega} (-1)^{I_i+j-I_f} (I_iK_\xi j\Omega_\nu|I_fK_\delta) \tag{I.31}$$

Considering the second case, this is satisfied only by the second and third terms, and the spectroscopic amplitude becomes

$$\left(\frac{2I_i+1}{2I_f+1}\right)^{\frac{1}{2}} \sum_{\xi\nu} a_{\xi\nu}a_\xi U_{\nu\Omega} C_{jl}^{\nu\Omega} (\pi_\xi) (-1)^{j-\frac{1}{2}-I_f} (I_i - K_\xi j\Omega_\nu|I_fK_\delta) \tag{I.32}$$

Combining these two equations together gives the desired result

$$\beta_{jl} = \left(\frac{2I_i+1}{2I_f+1}\right)^{\frac{1}{2}} \sum_{\xi\nu} a_{\xi\nu} a_\xi U_{\nu\Omega} C^{\nu\Omega}_{jl} (-1)^{j+I_i-I_f} \left[(I_i K_\xi j \Omega_\nu | I_f K_\delta) + (\pi_\xi)(-1)^{I_i-\frac{1}{2}} (I_i - K_\xi j \Omega_\nu | I_f K_\delta)\right] \tag{I.23}$$

Only one of the terms in each of the expressions for β_{jl} are non-zero at any one time. An interesting case develops when there is appreciable mixing of the $K_> = |K_\xi + \Omega_\nu|$ and $K_< = |K_\xi - \Omega_\nu|$ terms in a single state. This situation arises when the Nilsson amplitudes are large, and, in the case where the mixing is caused by Coriolis coupling, this occurs only when $K_> = K_< + 1$, i.e. for $\Omega_\nu = \frac{1}{2}$ transfer. The two K terms can either add or subtract from one another, depending upon the parity and spin of the target state.

Appendix II.
IBFFM Spectroscopic Strengths

The strengths listed in this appendix are those obtained from V. Paar and S. Brant[70]. The pickup strengths listed here, S_j, are normalized to $(2j+1)V_j^2$ for each j-value and final angular momentum, I. When renormalized with the values R_{Ij} presented in Table 5.3.2, they are normalized such that the sum over all final spins of $S_j = R_{Ij}S_j$ is $(2j+1)V_j^2$. The strengths are related to the cross section by

$$\frac{d\sigma}{d\Omega}\Big)_{exp} = \sum_j S_j N \frac{d\sigma}{d\Omega}\Big)_{DWBA} \qquad (II.1)$$

for pickup reactions. For stripping reactions the strengths listed here are normalized to U_j^2 for each j-transfer and final angular momentum, I. When renormalized with the values R_{Ij}, the resulting strengths are related to the cross section by

$$\frac{d\sigma}{d\Omega}\Big)_{exp} = \sum_j \left(\frac{2I_f+1}{2I_i+1}\right) R_{Ij}S_j N \frac{d\sigma}{d\Omega}\Big)_{DWBA} \qquad (II.2)$$

In order to facilitate the comparisons with the data, the factor $(2I_f+1)/(2I_i+1)$ has been incorporated into the definition of the strength such that

$$S_j = \left(\frac{2I_f+1}{2I_i+1}\right) R_{Ij}S_j \qquad (II.3)$$

The strengths S_l are listed in Chapter 5, where the strengths for different j-values but the same l-value have been summed.

Table II.1: Strengths Obtained from Paar and Brant for the ^{193}Ir(d,t)^{192}Ir and ^{191}Ir(d,p)^{192}Ir Reactions

Spin	(d,t) Strength				(d,p) Strength			
	$S_{\frac{1}{2}}$	$S_{\frac{3}{2}}$	$S_{\frac{5}{2}}$	$S_{\frac{9}{2}}$	$S_{\frac{1}{2}}$	$S_{\frac{3}{2}}$	$S_{\frac{5}{2}}$	$S_{\frac{9}{2}}$
0		1.2922				0.1852		
0		0.0031				0.0005		
0		0.2628				0.0291		
0		0.00004				0.0009		
0		0.0122				0.0019		
0		0.0255				0.0147		
0		0.0147				0.004		
0		0.0073				0.0022		
0		0.0038				0.0009		
0		0.0101				0.0098		
0		0.0395				0.0134		
0		0.0017				0.0009		
1	0.5053	0.0038	0.1944		0.2527	0.00001	0.0122	
1	0.0928	0.09	0.6963		0.0464	0.0126	0.0653	
1	0.0016	0.9626	0.1069		0.0008	0.1387	0.0091	
1	0.0064	0.0483	0.2791		0.0032	0.0095	0.0216	
1	0.0978	0.0018	0.0291		0.0489	0.00005	0.0009	
1	0.0615	0.6528	0.0028		0.0325	0.1143	0.0006	
1	0.0159	0.0047	0.1462		0.0079	0.0017	0.0105	
1	0.0028	0.0176	0.1784		0.0013	0.0006	0.0128	
1	0.0343	0.1062	0.2937		0.0172	0.0231	0.0181	
1	0.0022	0.0042	0.1226		0.0011	0.0006	0.0089	
1	0.0008	0.0141	0.0113		0.0004	0.0023	0.0011	
1	0.0008	0.0014	0.0211		0.0004	0.0006	0.0008	

Table II.1 -continued

Spin	(d,t) Strength				(d,p) Strength			
	$S_{\frac{1}{2}}$	$S_{\frac{3}{2}}$	$S_{\frac{5}{2}}$	$S_{\frac{9}{2}}$	$S_{\frac{1}{2}}$	$S_{\frac{3}{2}}$	$S_{\frac{5}{2}}$	$S_{\frac{9}{2}}$
2	0.4804	0.1704	0.3242		0.2402	0.0304	0.0375	
2	0.2867	0.2544	0.0787		0.1433	0.0363	0.0026	
2	0.0004	0.2658	0.0987		0.0002	0.0417	0.0082	
2	0.0132	0.4013	0.9749		0.0065	0.0764	0.0926	
2	0.0026	0.4366	0.1346		0.0013	0.0713	0.0113	
2	0.0095	0.0823	0.0392		0.0048	0.0154	0.0007	
2	0.0069	0.0063	0.0088		0.0035	0.0028	0.0008	
2	0.0002	0.0222	0.0426		0.0001	0.0058	0.0069	
2	0.108	0.3412	0.003		0.0039	0.0592	0.0004	
2	0.0005	0.0118	0.0671		0.0002	0.0023	0.0062	
2	0.0087	0.1413	0.4393		0.0044	0.0333	0.0368	
2	0.0137	0.0375	0.0108		0.0068	0.0062	0.001	
3		0.0896	0.3147	0.1975		0.0108	0.0324	0.0003
3		0.1025	0.9136	0.0783		0.0152	0.0845	0.0009
3		1.1419	0.0004	0.1027		0.1808	0.0006	0.0009
3		0.0197	0.1929	0.019		0.0027	0.0218	0.00002
3		0.0844	0.1332	0.0492		0.0136	0.0117	0.00002
3		0.0757	0.3644	0.1587		0.0107	0.027	0.0004
3		0.056	0.2095	0.0448		0.0104	0.0193	0.0046
3		0.0259	0.0249	0.0353		0.0039	0.0044	0.0046
3		0.234	0.0325	0.0004		0.0387	0.0019	0.0042
3		0.0136	0.0438	0.1366		0.0015	0.003	0.0079
3		0.0118	0.0704	0.3312		0.0036	0.0083	0.0047
3		0.000002	0.0034	0.0826				

Table II.1 -continued

Spin	(d,t) Strength				(d,p) Strength			
	$S_{\frac{1}{2}}$	$S_{\frac{3}{2}}$	$S_{\frac{5}{2}}$	$S_{\frac{9}{2}}$	$S_{\frac{1}{2}}$	$S_{\frac{3}{2}}$	$S_{\frac{5}{2}}$	$S_{\frac{9}{2}}$
4			0.6718	0.026			0.0479	0.0017
4			0.3775	0.5052			0.0271	0.0004
4			0.0033	0.2942			0.00004	0.0033
4			0.2395	0.5051			0.0199	0.0052
4			0.1521	0.6939			0.0113	0.0046
4			0.1811	0.0002			0.0099	0.0006
4			0.2613	0.222			0.0276	0.0014
4			0.0167	0.2565			0.0008	0.0058
4			0.0472	0.2758			0.0047	0.015
4			0.0034	0.0964			0.00002	0.0052
4			0.0289	0.7254			0.0044	0.0215
4			0.0002	0.0007			0.00009	0.000006
5				0.0518				0.0004
5				0.4432				0.0003
5				0.7552				0.0073
5				0.7938				0.017
5				0.0057				0.0001
5				0.0969				0.0002
5				0.4531				0.0148
5				0.0745				0.0015
5				0.0681				0.0027
5				0.0051				0.0001
5				0.5761				0.0181
5				0.2854				0.0122

Table II.1 -continued

Spin	(d,t) Strength				(d,p) Strength			
	$S_{\frac{1}{2}}$	$S_{\frac{3}{2}}$	$S_{\frac{5}{2}}$	$S_{\frac{9}{2}}$	$S_{\frac{1}{2}}$	$S_{\frac{3}{2}}$	$S_{\frac{5}{2}}$	$S_{\frac{9}{2}}$
6				0.0004				0.00001
6				4.3995				0.0422
6				0.0253				0.0029
6				0.1132				0.0015
6				0.0042				0.000000
6				0.1355				0.0013
6				0.0022				0.000000
6				0.0213				0.0002
6				0.0316				0.0017
6				0.1076				0.0069
6				0.0748				0.0043
6				0.009				0.001

Table II.2: Strengths Obtained from Paar and Brant for the ^{193}Ir(d,p)^{194}Ir Reaction

Spin	(d, p) Strength			
	$S_{\frac{1}{2}}$	$S_{\frac{3}{2}}$	$S_{\frac{5}{2}}$	$S_{\frac{9}{2}}$
0		0.2091		
0		0.0035		
0		0.003		
0		0.0011		
0		0.0007		
0		0.028		
0		0.0012		
0		0.00002		
0		0.0002		
0		0.00006		
0		0.019		
0		0.00001		
1	0.1184	0.0021	0.0506	
1	0.1489	0.0011	0.09	
1	0.0047	0.1063	0.0026	
1	0.0035	0.0401	0.00004	
1	0.0854	0.0749	0.0019	
1	0.0143	0.0224	0.0003	
1	0.0028	0.0007	0.0002	
1	0.0067	0.0231	0.0001	
1	0.0078	0.0022	0.0175	
1	0.0008	0.0076	0.0085	
1	0.0004	0.0006	0.0049	
1	0.01	0.0091	0.0004	

Table II.2 -continued

Spin	(d,p) Strength			
	$S_{\frac{1}{2}}$	$S_{\frac{3}{2}}$	$S_{\frac{5}{2}}$	$S_{\frac{9}{2}}$
2	0.2304	0.0595	0.0714	
2	0.149	0.0242	0.0297	
2	0.0011	0.0074	0.0545	
2	0.0047	0.2028	0.0659	
2	0.0016	0.0002	0.0015	
2	0.0018	0.00001	0.0075	
2	0.0011	0.0068	0.0002	
2	0.0045	0.0222	0.00001	
2	0.00005	0.0271	0.0101	
2	0.0005	0.0517	0.0014	
2	0.006	0.0024	0.0067	
2	0.0054	0.0135	0.0032	
3		0.0263	0.1281	0.0103
3		0.1852	0.0038	0.0002
3		0.0131	0.0795	0.0036
3		0.002	0.0357	0.00006
3		0.0068	0.0012	0.017
3		0.0008	0.0066	0.0026
3		0.0322	0.0027	0.0015
3		0.0004	0.0004	0.0097
3		0.0118	0.0027	0.0046
3		0.0001	0.0065	0.0006
3		0.0082	0.0004	0.0000
3		0.0003	0.0209	0.0003

Table II.2 -continued

Spin	(d, p) Strength			
	$S_{\frac{1}{2}}$	$S_{\frac{3}{2}}$	$S_{\frac{5}{2}}$	$S_{\frac{9}{2}}$
4			0.1645	0.017
4			0.0006	0.0002
4			0.0143	0.0055
4			0.0003	0.0063
4			0.0054	0.009
4			0.0002	0.000009
4			0.0066	0.0005
4			0.0049	0.00003
4			0.0002	0.00001
4			0.00005	0.00009
4			0.0009	0.0006
4			0.000009	0.0007
5				0.0003
5				0.0082
5				0.0123
5				0.0138
5				0.0008
5				0.0031
5				0.00002
5				0.0004
5				0.0003
5				0.0006
5				0.0002
5				0.00004

Table II.2 -continued

Spin	(d,p) Strength			
	$S_{\frac{1}{2}}$	$S_{\frac{3}{2}}$	$S_{\frac{5}{2}}$	$S_{\frac{9}{2}}$
6				0.000003
6				0.0002
6				0.0233
6				0.0003
6				0.0033
6				0.0068
6				0.0025
6				0.0001
6				0.0001
6				0.00002
6				0.0014
6				0.0001

References

1. M.T. McEllistrem in *Proceedings of the Internal Conference on High Spin Physics and Gamma-Soft Nuclei*, ed. by J.X. Saladin, R.A. Sorensen, and C.M. Vincent, pub. World Scientific.
2. H.J. Wollersheim in *Proceedings of the Internal Conference on High Spin Physics and Gamma-Soft Nuclei*, ed. by J.X. Saladin, R.A. Sorensen, and C.M. Vincent, pub. World Scientific.
3. R.D. Bagnell, Y. Tanaka, R.K. Sheline, D.G. Burke, and J.D. Sherman, Phys. Lett. 66B, 129 (1977).
4. D.G. Burke, M.A.M. Shahabuddin and R.N. Boyd, Phys. Lett. 78B, 48 (1978).
5. H.G. Borner, R.F. Casten, I. Forster, D. Lieberz, P. von Brentano, S.J. Robinson, T. von Egidy, G. Hlawatsch, H. Lindner, P. Geltenbort, F.Hoyler, H.Faust, G. Colvin, W.R. Kane and M. MacPhail, Nucl. Phys. A534, 255 (1991).
6. P.O. Hess, J. Maruhn, and W. Greiner, J. Phys. G7, 737 (1981).
7. A. Arima and F. Iachello, Phys. Rev. Lett. 35, 1069 (1975).
8. J.A. Cizewski, R.F. Casten, G.J. Smith, M.L. Stelts, W.R. Kane, H.G. Borner, and W.F. Davidson, Phys. Rev. Lett. 40, 167 (1978).
9. C.S. Lim, R.H. Spear, M.P. Fewell, and G.J. Gyapong, Nucl. Phys. A548, 308 (1992).
10. F.T. Baker, A. Sethi, V. Penumetcha, G.T. Emery, W.P. Jones, M.A. Grimm, and W.L. Witten, Phys. Rev. C32, 2212 (1985).
11. J.M. Eisenberg and W. Greiner, *Nuclear Models, vol.1* (1987) North Holland, Amsterdam, The Netherlands.
12. M.A. Preston and R.K. Bhaduri, *Structure of the Nucleus* (1975) Addison-Wesley Pub., Reading, Mass. USA.
13. R.F. Casten, *Nuclear Structure from a Simple Perspective* (1990) Oxford University Press, New York, USA.

14. P. Ring and P. Schuck, *The Nuclear Many-Body Problem* (1980), Springer-Verlag, Germany.

15. B.E. Chi, Nucl. Phys. 83, 97 (1966).

16. A.K. Jain, J. Kvasil, R.K. Sheline, and R.W. Hoff, Phys. Rev. C40, 432 (1989).

17. C.J. Gallagher Jr. and S.A. Moszkowski, Phys. Rev. 111, 1282 (1958).

18. P.C. Sood and R.N. Singh, Nucl. Phys. A373, 519 (1982).

19. D. Elmore and W.P. Alford, Nucl. Phys. A273, 1 (1976).

20. N.D. Newby, Phys. Rev. 125, 2063 (1962).

21. P.C. Sood and R.S. Ray, Pramana-J. Phys. 27, 537 (1986).

22. S. Brant, V. Paar, and D. Vretenar, Z. Phys. A319, 355 (1984).

23. T. Hubsch and V. Paar, Z. Phys. A319, 111 (1984).

24. R.F. Casten and D.D. Warner, Rev. Mod. Phys. 60, 389 (1988).

25. A. Arima and F. Iachello, Phys. Rev. C14, 761 (1976).

26. F. Iachello and O. Scholten, Phys. Rev. Lett. 43, 679 (1979).

27. F. Iachello and S. Kuyucak, Anns. Phys. 136, 19 (1981).

28. F. Iachello and O. Scholten, Phys. Rev. Lett. 43, 679 (1976).

29. F. Iachello, Phys. Rev. Lett. 44, 772 (1980).

30. R. Bijker and A.E.L. Dieperink, Nucl. Phys. A379, 221 (1982).

31. S. Brant and V. Paar, Z. Phys. A329, 151 (1988).

32. T. Hubsch and V. Paar, Z. Phys. A327, 287 (1987).

33. V. Paar, D.K. Sunko, and D. Vretenar, Z. Phys. A327, 291 (1987).

34. V. Lopac, S. Brant, V. Paar, O.W.B. Schult, H. Seyfarth, and A.B. Balantekin, Z. Phys. A323, 491 (1986).

35. J. Vervier and R.V.F. Janssens, Phys. Lett. 108B, 1 (1982).

36. A.B. Balantekin, I. Bars, and F. Iachello, Nucl. Phys. A370, 284 (1981).

37. A.B. Balantekin, I. Bars, and F. Iachello, Phys. Rev. Lett. 47, 19 (1981).

38. M. Vergnes, G. Rotbard, J. Kalifa, G. Berrier-Rosin, J. Vernotte, R. Seltz, and D.G. Burke, Phys. Rev. Lett. 46, 584 (1981).

39. J. Cizewski, D.G. Burke, R.E. Brown, J.W. Sunier, and E.R. Flynn, Phys. Rev. Lett. 46, 1264 (1981).

40. J. Cizewski, D.G. Burke, E.R. Flynn, R.E. Brown, and J.W. Sunier, Phys. Rev. C27, 1040 (1983).

41. J.A. Cizewski in *Interacting Bose-Fermi Systems in Nuclei*, ed. by F. Iachello, pub. Plenum Pub. (1981).

42. D.D. Warner and A.M. Bruce, Phys. Rev. C30, 1066 (1984).

43. A. Mauthofer, K. Stelzer, Th.W. Elze, Th. Happ, G. Eckert, T. Faestermann, A. Frank, and P. Van Isacker, Phys. Rev. C34, 1958 (1986).

44. D.D. Warner, Phys. Rev.Lett. 52, 259 (1984).

45. M. Vergnes, G. Berrier-Rosin, and R. Bijker, Phys. Rev. C28, 360 (1983).

46. D.D. Warner, R.F. Casten, M.L. Stelts, H.G. Borner, and G. Barreau, Phys. Rev. C26, 1921 (1983).

47. R.F. Casten, D.D. Warner, G.M. Gawdy, N. Rofail, and K.P. Leib, Phys. Rev. C27, 1310 (1983).

48. D.G. Burke and G. Kajrys, Nucl. Phys. A517, 1 (1990).

49. P. Van Isacker, J. Jolie, K. Hyede, and A. Frank, Phys. Rev. Lett. 54, 635 (1985).

50. P. Van Isacker, J.Math. Phys. 28, 957 (1987).

51. D.D. Warner, R.F. Casten, and A. Frank, Phys. Lett. 180B, 207 (1986).

52. B. Elbeck and P.O. Tjøm, in Adv. in Nucl. Phys. 3, 259 (1969).

53. J.E. Spencer and H. Enge, Nucl. Instm. Meth. 49, 181 (1967).

54. D.G. Burke and C.R. Hirning, private communication (1992).

55. P.R. Bevington, *Data Reduction and Error Analysis for the Physical Sciences*, McGraw-Hill Book Company, U.S.A., (1969).

56. A.H. Wapstra, G. Audi, and R. Hoekstra, At. Data Nucl. Data Tables 39, 281 (1988).

57. J. Kern, A. Raemy, W. Beer, J.-Cl. Dousse, W. Schwitz , M.K. Balodis, P.T. Prokofjev, N.D. Kramer, L.I. Simonova, R.W. Hoff, D.G. Gardner, M.A. Gardner, R.F. Casten, R.L. Gill, R. Eder, T. von Egidy, E. Hagn, P. Hungerford, H.J. Scheerer, H.H. Schmidt, E. Zech, A. Chalupka, A.V. Murzin, V.A. Libman, I.V. Kononenko, C. Coceva, P. Giacobbe, I.A. Kondurov, Yu.E. Loginov, P.A. Sushkov, S. Brant, and V. Paar, Nucl. Phys. A534, 77 (1991).

58. P.D. Kunz, Computer program DWUCK4, University of Colorado (1974), unpublished.

59. R.H. Price, D.G. Burke, and M.W. Johns, Nucl. Phys. A176, 388 (1971).

60. M.A.M. Shahabuddin, J.C. Waddington, and D.G. Burke, Nucl. Phys. A307, 239 (1978).

61. M.K. Balodis et al, private communication (1992).

62. B. Singh, Nucl. Data Sheets 61, 243 (1990).

63. S.W. Yates, J.C. Cunnane, P.J. Daly, R. Thompson, and R.K. Sheline, Nucl. Phys. A222, 276 (1974).

64. P.C. Sood and R.K. Sheline, At. Data Nucl. Data Tbl. 43, 259 (1989).

65. B. Harmatz and T.H. Handley, Nucl. Phys. 56, 1 (1964).

66. M. Schrader, K. Bucholz, and H.V. Klapdor, Nucl. Phys. A123, 173 (1973).

67. J.A. Cameron, Can. J. Phys. 62, 115 (1984).

68. G.U. Din and J.A. Cameron, Phys. Rev. C45, 2147 (1992).

69. E.E. Roskan, MDS(X) program series. Distributed by A.P.M. Coxan, C.L. Jones, and S.K. Tagg, University College, Cardiff, Wales..

70. S. Brant and V. Paar, private communication (1990).

71. S. Brant, V. Paar, D.K. Sunko, and D. Vretenar, Phys. Rev. C37, 830 (1988).

72. U. Mayerhofer, T. von Egidy, P. Durner, G. Hlawatsch, J. Klora, H. Lindner, S. Brant, H. Seyfarth, V. Paar, V. Lopac, J. Kopecky, D.D. Warner, R.E. Chrien, and S. Pospisil, Nucl. Phys. A492, 1 (1989).

73. R.A. Meyer, K.V. Marsh, H. Seyfarth, S. Brant, M Bogdanovic, and V. Paar, Phys. Rev. C41, 1172 (1990).

74. J. Jolie, U. Mayerhofer, T. von Egidy, H. Hiller, I. Klora, H. Lindner, and H. Trieb, Phys. Rev. C43, R16 (1991).

75. J. Wood, in *Interacting Bose-Fermi Systems in Nuclei*, ed F. Iachello, Plenum Pub., New York (1981).

76. J. Jolie, U. Mayerhofer, T. von Egidy, H. Hiller, J. Klora, H. Lindner, and H. Tribe *Proc. 7'th Int. Symp. on Capture γ-ray Spectroscopy*, Asilomar 14-19.10.1990, AIP Conf. Proc. ed. R.W. Hoff, AIP New York USA.

77. M. Vergnes, in *Nuclear Structure, Reactions, and Symmetries*, ed. R.A. Meyer and V. Paar, World Scientific (1987).

78. D. Benson Jr., P. Kleinheinz, R.K. Sheline, and E.B. Shera, Phys. Rev. C14, 2095 (1976).

79. D. Benson Jr., P. Kleinheinz, R.K. Sheline, and E.B. Shera, Z. Phys. A281, 145 (1977).

80. D. Benson Jr., P. Kleinheinz, R.K. Sheline, and E.B. Shera, Z. Phys. A285, 405 (1978).

81. Y. Yamazaki and R.K. Sheline, Phys. Rev, C14, 531 (1976).

82. Y. Yamazaki, R.K. Sheline, and E.B. Shera. Phys. Rev. C17, 531 (1978).

83. S.E. Larsson, Phys. Scripta 8, 17 (1975).

84. R.C. Thompson, A. Ikeda, P. Kleinheinz, R.K. Sheline, and P.J. Daly, Phys. Lett. 55B, 447 (1975).

85. A.K. Jain, R.K. Sheline, P.C. Sood, and K. Jain, Rev. Mod. Phys. 62, 393 (1990).

86. P.C. Sood, private communication (1992).

87. J. Kern, W. Beer, S. Brant, R.F. Casten, A Chalupka, C. Coceva, J.-Cl. Dousse, R. Eder, T. von Egidy, D.G. Gardner, M.A. Gardner, P. Giacobbe, R.L. Gill, E. Hagn, R.W. Hoff, P. Hungerford, I.A. Kondurov, I.V. Kononenko, N.D. Kramer, V.A. Libman, Yu.E. Loginov, V. Murzin, V. Paar, P.T. Prokofjev, A. Reamy, H.J. Scheerer, H.H. Schmidt, W. Schwitz, L.I. Simonova, P.A. Sushkov, and E. Zech, in *Proc. 7'th Int. Symp. on Capture γ-ray Spectroscopy*, Asilomar 14-19.10.1990, AIP Conf. Proc. ed. R.W. Hoff, AIP New York USA.